Development of a macro-element of foundations under dynamic load : Application in the case of soils reinforced by rigid inclusions

Yuxiang Shen

INSTITUT POLYTECHNIQUE DE PARIS

NNT : 2023IPPAE019

Thèse de doctorat

ENSTA

IP PARIS

Development of a macro-element of foundations under dynamic load: Application in the case of soils reinforced by rigid inclusions

Thèse de doctorat de l'Institut Polytechnique de Paris
préparée à l'École nationale supérieure de techniques avancées

École doctorale n°626 École doctorale de l'Institut Polytechnique de Paris (EDIPP)
Spécialité de doctorat : Mécanique des fluides et des solides, acoustique

Thèse présentée et soutenue à Paris, le 18 décembre 2023, par

YUXIANG SHEN

Composition du Jury :

Alain Pecker Professeur, École Nationale des Ponts et Chaussées	Président
Panagiotis Kotronis Professeur, École Centrale de Nantes	Rapporteur
Stéphane Grange Professeur, INSA Lyon	Rapporteur
Ioannis Anastasopoulos Professeur, École Polytechnique Fédérale de Zurich	Examinateur
Sandra Escoffier Chargée de recherche, Université Gustave Eiffel	Examinatrice
Jean-François Semblat Professeur, ENSTA Paris	Directeur de thèse
Jesús Pérez-Herreros Terrasol (Setec)	Co-encadrant de thèse
Fahd Cuira Terrasol (Setec)	Co-encadrant de thèse, invité
Sébastien Burlon Terrasol (Setec)	Co-encadrant de thèse, invité

Per aspera ad astra

Acknowledgements

I am deeply grateful to all those who have contributed to completing my thesis.

Foremost, I extend my sincere appreciation to the executive board of Terrasol for their invaluable support throughout this endeavour. I am profoundly grateful for their mentorship and the opportunities they have afforded me to grow both professionally and personally.

My heartfelt thanks go to my thesis supervisor, Professor Jean-François Semblat, and the supervisory team comprising Fahd Cuira, Jesús Pérez-Herreros, and Sébastien Burlon. Their scientific expertise, generosity, and unwavering support have been indispensable. I am deeply grateful for their profound impact on my academic and professional growth.

Special thanks are extended to Jesús Pérez-Herreros, also my team manager at Terrasol. His availability, trust, insightful ideas, and continuous encouragement have greatly enriched my research journey, enabling me to explore various facets of the subject matter.

I am grateful to Professor Alain Pecker, who graciously chaired the thesis jury and meticulously examined the work, adding significant value to its evaluation. Special gratitude is extended to Professor Panagiotis Kotronis and Professor Stéphane Grange for their willingness to serve on the thesis follow-up committee and for their thorough review of the manuscript. Furthermore, I thank Doctor Sandra Escoffier and Professor Ioannis Anastasopoulos for agreeing to assess this thesis.

I owe a debt of gratitude to Professor Yujun Cui from École Nationale des Ponts et Chaussées for affording me the opportunity to study in France, as well as for his invaluable advice and guidance throughout my academic journey in the country. Additionally, Monsieur Vincent Desvignes, my tutor from Ponts Alumni, provided invaluable professional and personal guidance. Their encouragement has been instrumental in shaping my academic and professional development, for which I am profoundly thankful.

I would also like to extend my gratitude to my colleagues at Terrasol and to my friends. Your unwavering support has been invaluable to me throughout this journey. Your presence has made a significant difference, and I am truly grateful for your continued support and friendship.

My deepest appreciation is reserved for my family in China, especially my grandparents and parents, for their unwavering support, encouragement, and love. I am acutely aware of the sacrifices they have made due to my absence over the years, and I remain forever indebted to them.

Abstract

The dynamic response of a rigid inclusion-reinforced foundation represents a complex Soil-Structure Interaction (SSI) problem. Considering the limited existing studies, there is a clear necessity to explore the SSI phenomena involved in the response of such foundations under seismic conditions and to enhance the corresponding design methodologies.

Building upon insights gained from a limited number of dynamic experimental and numerical studies, this research focuses on the dynamic SSI phenomena of foundations reinforced by rigid inclusions. The study aims to provide a better understanding of the seismic behaviour of such foundations using several complementary approaches, including various numerical models, resolution strategies, and analytical analyses. The effects of inertial and kinematic interaction phenomena on the response of both the overall foundation and individual elements within the system (e.g., rigid inclusions, load transfer platform, etc.) are examined in detail.

The seismic bearing capacity of foundations reinforced by rigid inclusions is further investigated, using the kinematic exterior approach within the framework of yield design theory. A multi-subsystem analytical approach based on the kinematic exterior approach is introduced and validated through FEM analyses. The evolution of the reduction factors associated with load eccentricity, load inclination, and soil inertia is also explored for several configurations of the reinforcement in terms of coverage area ratio.

A novel macro-element for rigid inclusion-reinforced foundations under seismic loading is developed and numerically validated. It allows the modelling of both the linear and non-linear response of the foundation, including uplift, sliding and loss of bearing capacity mechanisms. The validated macro-element model is used to perform a parametric study using a lumped mass model and the Incremental Dynamic Analysis (IDA) of a 22-storey building, demonstrating the effectiveness and usefulness of the proposed approach in a performance-based design approach.

This research is conducted within the framework of the French National Project ASIRI+ and French National Research (ANR) Project ASIRIplus_SDS.

Key words: Macro-element, Foundation, Rigid inclusion, Dynamic soil-structure interaction, Bearing capacity, Seismic loading, ASIRI+

Résumé

La réponse dynamique d'une fondation renforcée par inclusions rigides représente un problème complexe d'Interaction Sol-Structure (ISS). Cependant, le nombre d'études s'intéressant à ce type de fondations reste encore limité, et il est nécessaire d'explorer davantage les phénomènes d'ISS impliqués dans leur réponse sous l'action des séismes et d'améliorer les méthodes d'analyse correspondantes.

Sur la base des connaissances acquises à partir des études expérimentaux et numériques disponibles à ce jour, ce travail de recherche s'intéresse aux phénomènes d'ISS dynamique des fondations renforcées par inclusions rigides. L'étude vise à fournir une meilleure compréhension du comportement sismique de ce type de fondation en utilisant plusieurs approches complémentaires comprenant divers modèles numériques, stratégies de résolution et approches analytiques. Les effets des phénomènes d'interaction inertiel et cinématique à la fois sur la réponse globale de la fondation et sur la réponse des différents éléments du système (i.e., inclusions rigides, matelas de répartition, etc.) sont examinés en détail.

La capacité portante sismique des fondations renforcées par inclusions rigides est étudiée en utilisant l'approche cinématique par l'extérieur dans le cadre de la théorie du calcul à la rupture. Une approche analytique permettant d'explorer plusieurs mécanismes de rupture de la fondation est proposée et validée par des analyses numériques en éléments finis. L'évolution des facteurs de réduction associés à l'excentrement et l'inclinaison de la charge ainsi qu'à l'inertie du sol est également explorée pour plusieurs configurations de renforcement en termes du taux de substitution.

Un nouveau macro-élément pour les fondations renforcées par inclusions rigides sous chargement sismique est développé et validé numériquement. Il permet la modélisation de la réponse linéaire et non-linéaire de la fondation, incluant les mécanismes de décollement, de glissement et de perte de la capacité portante. Ce modèle est ensuite utilisé pour conduire une étude paramétrique à l'aide d'un modèle de structure simplifiée et l'analyse dynamique incrémentale d'une tour R+22, démontrant l'efficacité et l'utilité de l'approche proposée dans une démarche de conception parasismique basée sur la performance.

Cette recherche est menée dans le cadre du Projet National français ASIRI+ et du projet ANR ASIRIplus_SDS.

Mots clés: Macro-élément, Fondation, Inclusions rigides, Interaction dynamique soil-structure, Capacité portante, Chargement sismique, ASIRI+

Contents

General introduction

Background and motivation

General context

Earthquakes are typically associated with faults, which are areas of reduced mechanical strength capable of accommodating the deformations resulting from the movement of tectonic plates. The majority of seismic activity occurs along the boundaries of major tectonic plates, where the relative movements between these plates are most significant (IRSN, 2012). Figure 1 provides an intuitive visualisation of seismic activity, illustrating epicentre locations and magnitudes worldwide. Seismic activity is notably concentrated around the Circum-Pacific seismic zone and Alpine-Himalayan seismic zone.

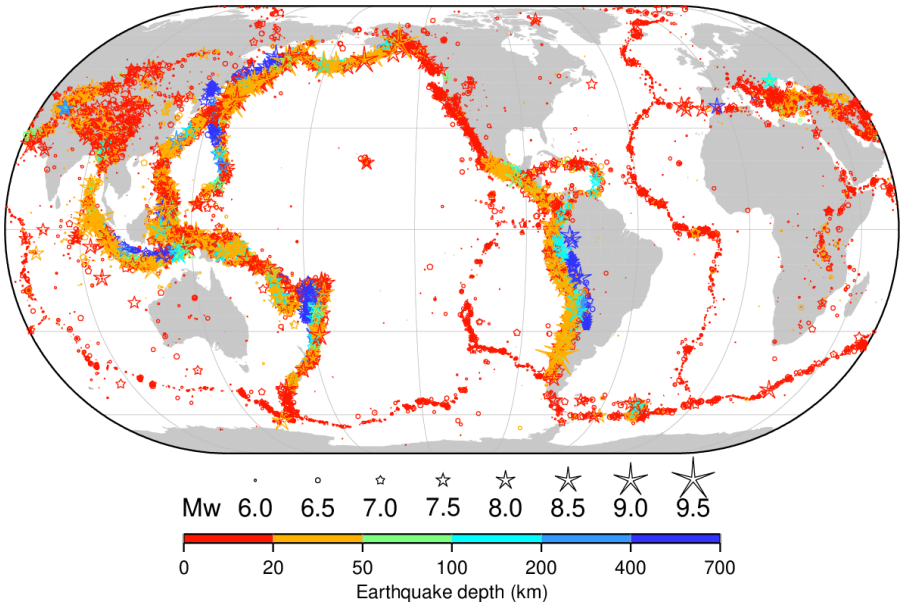

Fig. 1. Earthquake map showing about 69 000 earthquakes between 1904 and 2019 (International Seismological Centre, 2023)

Earthquakes constitute a formidable natural disaster due to their suddenness and destructive potential. While most earthquakes result in structural damage, exceptionally rare seismic events have led to catastrophic building collapses and human casualties. Therefore, ensuring the seismic safety of building structures is of paramount importance.

The design objectives in current building codes address life safety, control damage in minor and moderate earthquakes, and prevent collapse in a major earthquake (Ghobarah, 2001). For minor earthquakes, the goal is to minimise structural damage, and engineers typically rely on equivalent linear elasticity models without extensively exploring local

non-linear behaviours. This approach is particularly applicable in regions with low to moderate seismic risks, where the focus is on characterising structural responses within the elastic framework. Conversely, with major earthquakes, it becomes essential to employ methods that can account for non-linear phenomena, as these can have a substantial impact on structural responses and performance.

Employing rigid inclusions for soil reinforcement stands as a practical, cost-effective, and time-efficient technique, enabling the use of shallow foundations on compressible soils. Since 1990, the use of vertical rigid inclusions for soil reinforcement has experienced remarkable growth and evolution, making significant contributions to various civil engineering structures.

This innovative technique necessitates the formulation of dedicated guidelines and codes to ensure its safe and efficient implementation. Addressing this demand, the French Government sponsored the ASIRI (*Amélioration des Sols par Inclusions RIgides*) national project, conducting substantial research from 2005 to 2011.

The outcomes of the project were comprehensively documented in a publication entitled "*Recommendations for the Design, Construction, and Control of Rigid Inclusion Ground Improvements*". The provided recommendations offer valuable insights into the behaviour of foundations reinforced with rigid inclusions. They delve into the diverse interaction mechanisms that occur between the soil, inclusions and load transfer platform (LTP), drawing from both experimental and numerical research.

Continuing the endeavours initiated by the ASIRI National Project, a subsequent project named ASIRI+ was initiated in 2019. This project seeks to explore uncharted areas that were previously untouched. These unexplored topics encompass geosynthetic reinforcement, traffic loads, and dynamic and seismic loads.

In seismic design, accounting for the impacts of Soil-Structure Interaction (SSI) or Soil-Foundation-Structure Interaction (SFSI) is essential. While extensive research has explored soil reinforcement by rigid inclusions under vertical static loading in the past two decades (ASIRI, 2012), their behaviour during dynamic and seismic loading has not yet received the same attention. Consequently, the understanding of the mechanisms controlling foundation response and performance under seismic loads remains limited. Further research is therefore needed to refine design practices and accelerate the use of rigid inclusion soil improvement within seismic conditions.

Motivation and problem statement

The adoption of rigid inclusions for soil reinforcement has gained interest owing to their potential to enhance the foundation's bearing capacity, reduce settlement, and strengthen

overall stability. Grasping the SSI phenomena governing such foundations under seismic loading is pivotal to ensuring their secure and reliable performance in earthquake-prone areas.

In practice, the seismic design of rigid inclusion-reinforced foundations has predominantly rested upon the pseudo-static approaches introduced by the ASIRI national project (ASIRI, 2012). However, the viability of these widely employed calculation methods in seismic contexts remains uncertain. Consequently, it becomes imperative to investigate the difference between the results derived from a simplified pseudo-static model and a sophisticated dynamic model. This exploration also extends to scrutinising the potential for improving the proposed pseudo-static calculation approach.

The increase of bearing capacity by rigid inclusion improvement necessitates quantification, yet a practical method is absent. Additionally, the consideration of soil inertia becomes crucial in seismic scenarios. In the context of rigid inclusion ground improvement, the quantification of reinforcement effects using yield design theory (Salençon, 1983) serves as a pivotal motivation for this research.

Furthermore, the dynamic response of structures founded on the rigid inclusion improved foundation presents a complex SSI issue that requires the use of adapted computational methods. Within the performance design framework, contemporary design codes like Eurocode 8 (AFNOR, 2007) acknowledge the SSI influence and non-linear energy dissipation during intense earthquakes (Pérez-Herreros, 2020).

The most direct approach, known as the global approach, involves modelling the soil, foundation elements, and superstructure to consider the non-linear behaviour of the foundation system. However, this method is computationally demanding. To reduce complexity and computational costs, the concept of a macro-element, initially introduced by Nova and Montrasio (1991) and later effectively applied to both shallow foundations and deep foundations, allows for the consolidation of linear and non-linear SSI effects within a multi-directional non-linear element. The macro-element incorporates a non-linear constitutive law defined in terms of generalised forces and displacements, operating within the framework of plasticity or hypo-plasticity theory, capable of coupling linear and non-linear dynamic behaviours (Pérez-Herreros, 2020).

Within this context, the primary objective of this doctoral work is to explore both linear and non-linear aspects of soil-structure interaction in rigid inclusion-reinforced foundations under seismic loading. Ultimately, the goal is to create a macro-element model capable of representing these behaviours.

Therefore, the research intends to address the following fundamental aspects:

- Review of existing experimental and numerical studies

A comprehensive review of existing experimental and numerical studies in the literature offers valuable insights into the behaviour of rigid inclusion-reinforced foundations under various loading conditions. Several studies have already been conducted in the existing literature, and in some cases, insights from studies related to other foundation systems can be extrapolated and applied to the rigid inclusions. Nonetheless, an important gap persists between research-oriented investigations and their practical application in engineering applications.

- Linear SSI behaviour

  This study focuses on investigating the SSI behaviour of rigid inclusion-reinforced foundations within the linear domain. The study explores the effects of inertial and kinematic interaction, aiming to understand the dynamic response of the system when subjected to seismic loading. This analysis is expected to provide valuable insights into the linear behaviour of such foundations and their response to ground motion induced by earthquakes.

- Seismic bearing stability

  The exploration into the non-linear domain begins with an evaluation of seismic bearing stability through the implementation of the yield design theory. Specifically, the kinematic exterior approach (or kinematic external approach) of the yield design theory will be employed to establish a stability domain. The objective of this approach is to provide a comprehensive understanding of the failure mechanism that foundations on rigid inclusions may experience under seismic loads and the associated bearing capacity.

- Macro-element development and validation

  The primary emphasis is placed on the development of a macro-element model that precisely portrays the behaviour of rigid inclusion-reinforced foundations and encompasses the SSI effects identified through linear analysis and yield design. This macro-element is expected to offer an efficient tool for analysing the response of such foundation systems under seismic loading. The research also encompasses the incorporation of numerical modelling to validate the proposed macro-element approach. Parametric studies can be conducted using the macro-element model to gain a comprehensive understanding of the SSI effects on such foundations.

Thesis outline

This dissertation is structured into four distinct parts.

Part I focuses on the literature review, constituting a vital cornerstone for the work. It furnishes an overview of rigid inclusion ground improvement and the dynamic SSI problem concerning this foundation type. A thorough examination of existing literature concerning rigid inclusion-reinforced foundations is undertaken. This review encompasses both experimental and numerical studies, highlighting the advances made in comprehending the behaviour of these foundations under seismic load. Furthermore, various calculation approaches commonly employed in this context are introduced and evaluated, with their respective strengths and weaknesses. Additionally, the significance of the yield design theory is emphasised in this review.

Part II of the dissertation delves into the linear exploration of SSI, with a specific emphasis on inertial and kinematic effects within the linear domain. It begins with a study on ground motion modification resulting from kinematic interaction effects. Subsequently, kinematic forces within rigid inclusions are investigated, followed by an analysis of dynamic impedance functions for foundations on rigid inclusions through a comparative study. The exploration of inertial interaction effects is further pursued by examining the inertial forces within rigid inclusions. Additionally, cross-calculations are performed between direct dynamic analyses employing a complete model and conventional engineering approaches, serving to validate the conventional methodologies and to explore avenues for their improvement.

Part III explores the application of yield design theory to evaluate the seismic bearing capacity of the reinforced foundations. The potential failure mechanisms are proposed. The results of the analytical approach are validated with the numerical studies. Some numerical applications of the kinematic exterior approach are realised to explore the bearing capacity problem for the rigid inclusion-reinforced foundation.

Part IV of the dissertation shifts its focus to the non-linear SSI behaviour. The development of a macro-element, encompassing linear and non-linear aspects of the SSI, is elaborated. Furthermore, a numerical validation process is undertaken. The comprehensive parametric studies using macro-element are realised. This part of the dissertation provides valuable insights into the non-linear dynamic behaviour characterising these foundations and effectively validates the proposed macro-element methodology.

Concluding the dissertation, a general conclusion encapsulates the pivotal discoveries and contributions of the study. It further contemplates their implications for engineering practice. This section also aspires to stimulate future research aimed at advancing the understanding and analysis of SSI under seismic conditions for rigid inclusion-reinforced foundations.

Part I

Literature review

Introduction

Rigid inclusion ground reinforcement has gained considerable attention over time. Existing literature has primarily focused on the vertical behaviour of foundations on rigid inclusion-improved soil, as demonstrated in the ASIRI French national project (ASIRI, 2012). Limited attention has been given to the response of such foundations with inclusions under seismic loading. In the following three chapters, the existing work is presented regarding three main axes: basic concepts, experimental observations and numerical analyses.

Chapter 1 offers an overview of the key interaction mechanisms within a ground improvement system reinforced with rigid inclusions. It also highlights significant applications of rigid inclusions in real engineering cases, including the Rio–Antirrio Bridge. Additionally, this chapter introduces significant dynamic SSI effects and analyses them in the context of rigid inclusion-reinforced foundations.

Chapter 2 explores the experimental studies conducted on foundations positioned on soil reinforced with rigid inclusions. Dynamic SSI has been studied through a range of experimental methods, including shaking table tests, centrifuge tests, and in-situ tests. These experiments have been conducted in various configurations, both with and without the presence of a superstructure. The main experimental test observations are summarised.

Lastly, Chapter 3 examines several numerical methods reported in the literature that can be used to investigate dynamic SSI, with a special emphasis on the macro-element approach, which serves as the primary objective of this study. This chapter also highlights the importance of yield design theory as an effective approach for studying the seismic stability of foundations on soil reinforced with rigid inclusions.

1 Rigid inclusion reinforcement and dynamic soil-structure interaction

1.1 Rigid inclusion ground improvement

1.1.1 General concept

In engineering practice, shallow foundations are typically preferred if they can satisfactorily meet both stability and settlement criteria. If either one or both of these criteria cannot be met, a possible approach is to opt for pile foundations, where piles are designed to carry the entire load and provide stiffness to the foundation.

The concept of a foundation with rigid inclusions involves a shallow foundation reinforced by vertical rigid elements, known as inclusions, which reduce the foundation settlement while enhancing its vertical bearing capacity. The materials used for inclusions, such as concrete and steel, are significantly stiffer than the surrounding soil. This is the main reason why they are named "rigid" inclusions. Various foundation types are depicted in Figure 1.1.

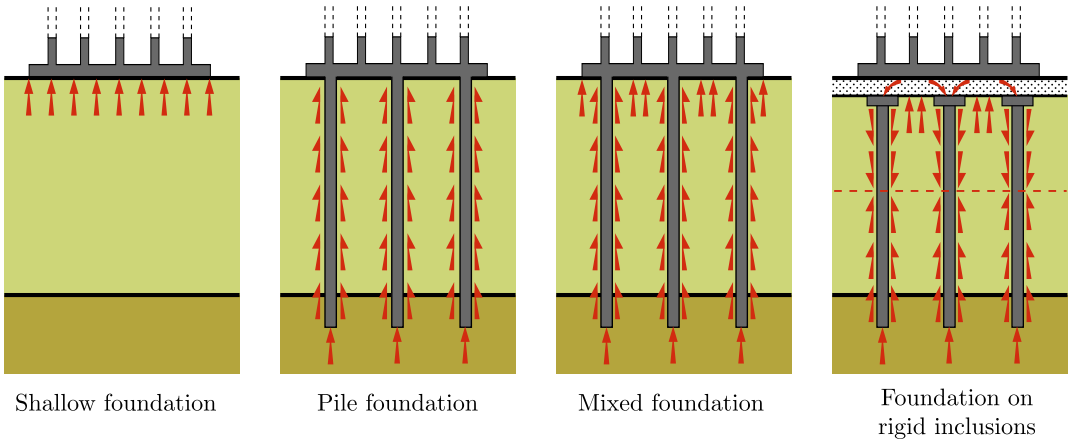

Fig. 1.1. Illustration of the load transfer mechanism in various foundation types

It is important to note that there is no direct connection between the shallow foundation and the inclusions. Instead, a gravel layer is introduced as a load transfer platform (LTP) within the inclusion-reinforced foundation system. This load transfer platform, commonly known as "mattress" or "cushion", is a crucial component of this reinforced foundation

system. This layer of gravel, placed between the shallow foundation and the inclusions, must be well-compacted to achieve a high modulus. A minimum thickness is always necessary to ensure effective load transfer between the inclusions and the soil, while also reducing the stresses of the superstructure (ASIRI, 2012). Additionally, when a gravel platform is present, the non-linear mechanism at the interface is usually governed by a sliding mechanism. This sliding mode has the potential to improve the seismic performance of the structure by acting as a filter for the seismic loads that are effectively transmitted to the structure.

Inclusions are particularly suitable for structures with a large footprint that impose distributed loads on the soil (ASIRI, 2012). This technique finds application in various scenarios, including:

- Foundations of industrial and commercial buildings;
- Storage reservoirs, treatment plant basins and facilities;
- Highway embankments or railway embankments designed for high-speed trains.

In the literature, several research studies can be found that apply the same concept as inclusion ground improvement but under different names, such as "cushioned pile raft foundation", "disconnected pile raft foundation", "insulated pile foundation", "unattached pile foundation", "rigid pile composite foundation", "pile-reinforced composite foundation" and so on. The aforementioned studies are presented in Chapters 2 and 3.

1.1.2 Principal interaction mechanisms

The response of foundation on soil reinforced by rigid inclusions encompasses a series of intricate mechanisms that extend from the supported structure to the underlying substrate. These mechanisms include the interaction between the structure, the foundation, the LTP, and the inclusion. The two primary mechanisms of foundation on rigid inclusions are outlined in the following.

Mechanisms developed at the granular transfer platform

The inclusion-reinforced foundation system incorporates a granular layer positioned between the soft soil and the foundation, as depicted in Figure 1.2. This granular layer exhibits significantly higher stiffness and resistance compared to surrounding soil, resulting in reduced settlement and increased bearing capacity. Importantly, during an earthquake, this layer serves as an energy fuse (Pecker, 2023b). When the shear force in the layer exceeds a specific value due to friction, controlled sliding occurs, as shown in Figure 1.3. This mechanism prevents the foundation from overturning due to a loss of

bearing capacity and instead allows for controlled displacement within the well-designed granular layers.

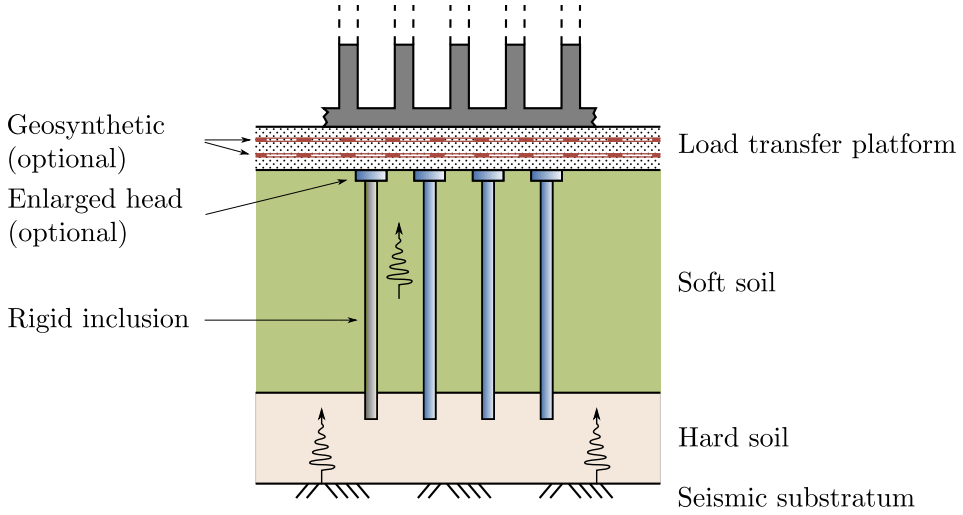

Fig. 1.2. Scheme of a foundation on rigid inclusions under seismic loading

The sliding behaviour observed in the inclusion-reinforced foundation system effectively limits the seismic load transmitted to the superstructure while filtering the inertial load transmitted to the rigid inclusions with the effect of fuse (Pecker, 2023b).

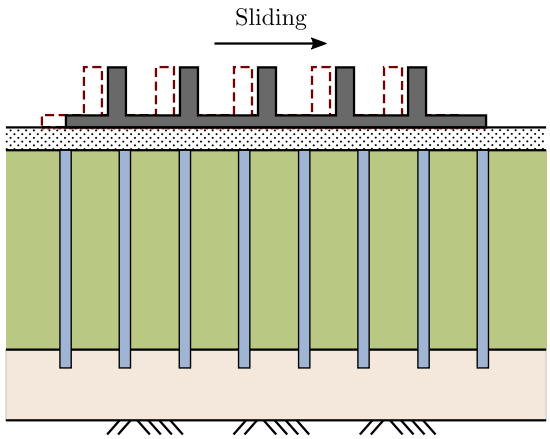

Fig. 1.3. Sliding behaviour of a rigid inclusion-reinforced foundation

The thickness of the LTP and the embedment of the inclusion head within the LTP significantly influence the performance of the reinforced foundation, particularly in facilitating the transfer of horizontal forces through the LTP. Han *et al.* (2016) has shown that the thickness of LTP is a crucial factor in seismic attenuation, with a thicker LTP exhibiting a more effective seismic absorption effect.

Interaction at the interface between the soft soil and the inclusions

The main role of the inclusions is to transfer the gravitational load from the structure to the bearing stratum, thereby reducing settlement and improving bearing capacity. Unlike conventional pile foundations, where the load is not primarily transferred through the head of inclusions but also using the skin friction generated between the inclusion and the surrounding soil due to differential settlement, as shown in Figure 1.4.

The soft soil can be divided into two distinct zones based on their shaft friction (ASIRI, 2012). In the upper zone, there is a phenomenon known as negative friction, where the soil experiences greater settlement compared to the inclusions. In contrast, the lower zone of the soft soil exhibits a different shaft friction. Here, the inclusions settle more than the surrounding soil, causing a positive friction. Between these two zones, a neutral point can be identified (Frank *et al.*, 2021). This neutral point represents a location within the soil where there is no relative movement between the inclusions and the surrounding soil.

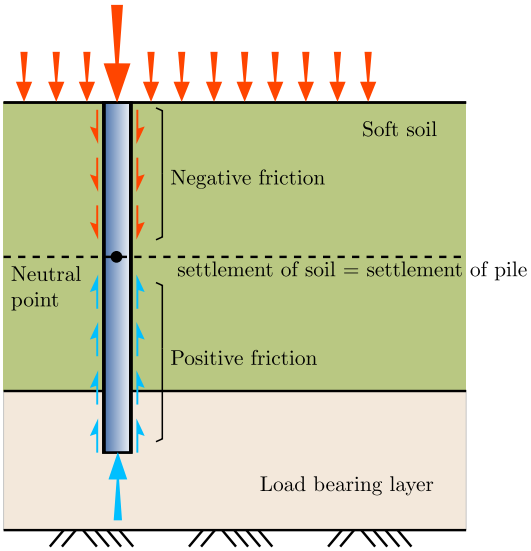

Fig. 1.4. Schema of positive and negative friction

Negative skin friction has an adverse effect on pile foundations as it reduces their load-carrying capacity. Conversely, negative friction for rigid inclusions is not considered a harmful force because it helps to alleviate stress levels within the compressible soil.

The lateral behaviour of a rigid inclusion is similar to that of a pile, with the key distinction being the lack of a connection at the head of the rigid inclusion. This absence of connection prevents a significant concentration of force at the head of the rigid inclusion.

1.1.3 Remarkable applications of rigid inclusions to real projects

The application of this ground improvement technique has experienced significant growth in recent years. The literature showcases several notable applications of rigid inclusions in real projects with complicated geotechnical environments, such as the Rio-Antirrio Bridge (Garnier and Pecker, 1999; Pecker, 2004, 2006; Pecker and Teyssandier, 2009; Pecker, 2023b), the Izmit Bay Bridge (Steenfelt *et al.*, 2015), the ICEDA project (Mattsson *et al.*, 2013), and the 1915 Çanakkale Bridge (Giannakou *et al.*, 2019; Arıoğlu, 2021; Kroon *et al.*, 2021). These projects serve as successful examples of the foundation on rigid inclusions, highlighting its effectiveness as a viable solution even in challenging engineering contexts characterised by favourable soil properties, substantial water depths, and significant seismic activity.

Rio-Antirrio Bridge

The famous Rio-Antirrio Bridge successfully employed this reinforcement technique. The bridge is situated near Patras, approximately 250 km west of Athens in Greece (Garnier and Pecker, 1999). The construction commenced in 1998 and was completed in the summer of 2004.

The Rio-Antirrio Bridge is a cable-stayed bridge consisting of three spans, with a total length of 2 290 m. The three central spans are 560 m in length each and are extended by two adjacent spans (Pecker, 2023b). The bridge pier foundations are located at a significant water depth of approximately 65 m. The soil in the area primarily comprises alluvial deposits. The local seismic design motion is characterised by a high peak ground acceleration of 0.48 g at the seabed level (Garnier and Pecker, 1999).

The bridge foundation comprises a gravity caisson with a diameter of 90 m at the seabed level. The height of each pylon reaches approximately 220 m, with 65 m of it submerged beneath the water.

The permanent load borne by a single pier amounts to approximately 800 MN. Furthermore, the occurrence of an earthquake generates a horizontal shear force of 600 MN and an overturning moment of 20 000 MN.m on the bridge (Pecker, 2004).

The structural performance criteria permit the foundation to sustain permanent displacements following a seismic event, as long as these displacements are controlled and do not hinder the bridge's future functionality (Pecker, 2023b). Given this context, a shallow foundation becomes a feasible option. To address the challenges posed by the weak soil conditions, soil reinforcement utilising inclusions was implemented. A total of 270 steel tubes with a diameter of 2 m and a thickness of 20 mm were driven to depths of either 25 m or 30 m, following a square pattern with dimensions of 7 m $\times$ 7 m (ASIRI, 2012).

It is worth noting that the rigid inclusions are not directly connected to the bridge foundation. Instead, a free-draining gravel bed layer is placed between the top of the inclusions and the pier footing, as depicted in Figure 1.5. This layer allows for uplift and sliding of the footing during earthquakes. The foundation's excellent seismic performance has been demonstrated at full scale during a real earthquake with a moment magnitude $M_W = 6.5$ that occurred in Greece. Through the analysis of the data and comprehensive inspections after the seismic event, the bridge's behaviour remained well within the serviceability limit states, with no permanent damages observed (Papanikolas *et al.*, 2010).

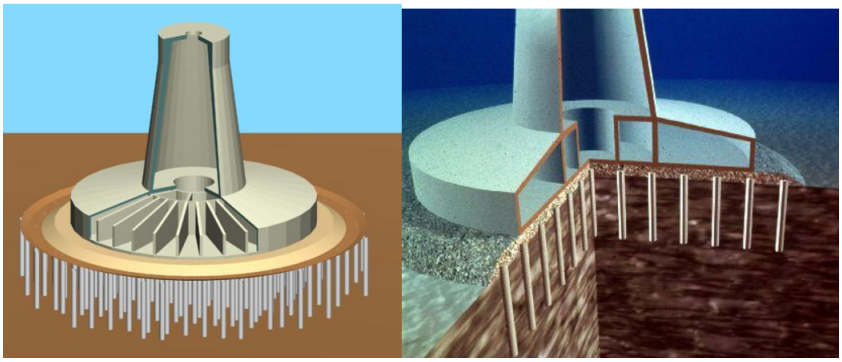

Fig. 1.5. Foundation of a bridge pile (Pecker and Teyssandier, 2009)

Nuclear waste storage facility project: ICEDA

The ICEDA (*Installation de Conditionnement et d'Entreposage de Déchets Activés*) nuclear waste storage facility was constructed at the Bugey nuclear power station site in France. The site is located in a seismic area with 0.24 g as the design earthquake peak ground acceleration (Pecker, 2023b).

This facility was designed to accommodate the conditioning and storage of radioactive waste from 9 decommissioned reactors. Its overall dimensions are 130 m in length and 60 m in width. To enhance the soil's strength, a total of 300 reinforced concrete inclusions with a diameter of 1 m were installed in a rectangular pattern with spacing ranging from 3 m to 6 m (Mattsson *et al.*, 2013). These inclusions, ranging from 35 m to 55 m long, traverse a compressible clay layer and are extended down to the substratum. Figure 1.6 illustrates the cross-section of the structure and the inclusion-reinforced soil. Notably, this project marks the first application of the rigid inclusion reinforcement technique in a nuclear installation in France (Mattsson *et al.*, 2013).

As part of the installation project, two full-scale experimental tests were conducted to verify the design and gain insights into the static and dynamic behaviour of rigid inclusions. In the static experimental tests, a 10 m embankment was constructed on a concrete foundation slab supported by 9 inclusions (Mattsson *et al.*, 2013). The dynamic

tests involved forced vibration tests conducted on two concrete slabs (Okyay *et al.*, 2012). Further details on the dynamic in-situ tests can be found in Section 2.4.

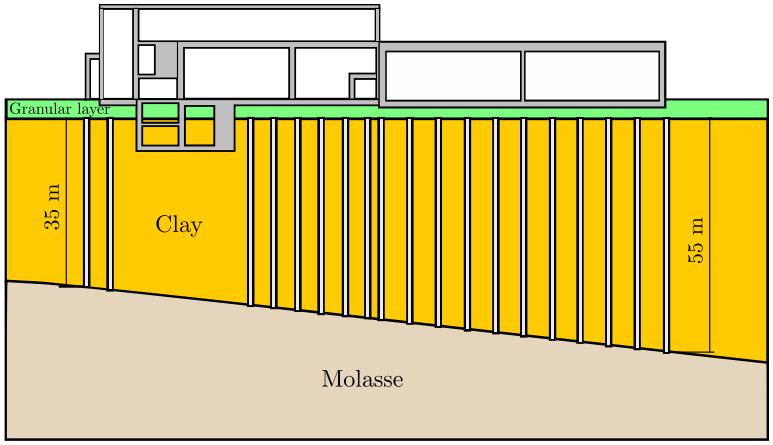

Fig. 1.6. ICEDA buildings on reinforced soil by rigid inclusions (Mattsson *et al.*, 2013)

1915 Çanakkale bridge

The 1915 Çanakkale Bridge, which crosses the Çanakkale strait, is situated approximately 200 km southwest of Istanbul. This remarkable structure holds today the distinction of being the longest suspension bridge in the world. With a total bridge length of 3 563 m, it comprises a main span measuring 2 023 m and two side spans of 770 m. The bridge features two primary towers known as the European and Anatolian towers (Giannakou *et al.*, 2019).

The foundations of the towers consist of gravity caissons, measuring approximately 83 m by 74 m supported by soil reinforced with steel pipe inclusions 2.5 m in diameter, as shown in Figure 1.7. At the European tower location, a total of 203 inclusions with lengths up to 46 m were driven, while at the Anatolian tower location, 165 inclusions with lengths of 21 m were installed (Kroon *et al.*, 2021).

The use of inclusion improvement results in a significant reduction of settlement for the European tower, with an estimated reduction of about 80 % compared to the case without rigid inclusions, while the embedment of rigid inclusions in the gravel LTP also enhances the lateral resistance of the foundation against ship impacts and seismic events (Kroon *et al.*, 2021). The gravel bed positioned beneath the caisson acts as a "plastic hinge", facilitating the development of inelastic deformation and energy dissipation (Pecker, 2004).

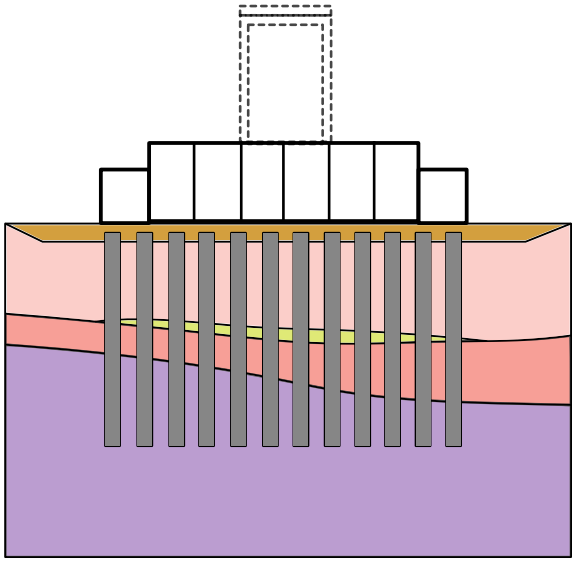

Fig. 1.7. Ground improvement by inclusions for tower foundations (Kroon *et al.*, 2021)

1.2 Dynamic soil-structure interaction

Dynamic SSI phenomena encompass the interaction effects between the surrounding soil and the structure, rendering them an inseparable entity. Consequently, the dynamic behaviour of the structure is influenced by the rigidity of the soil, leading to a distinct response from that of a fixed-base solution. The soil movements during dynamic excitation also undergo a modification due to the presence of the structure and foundation element, deviating from the response observed in a free field.

The interaction effect can be classified into two categories based on its origin: kinematic interaction and inertial interaction. Another significant phenomenon in dynamic SSI is energy dissipation. During dynamic excitation, energy is dissipated within the soil-structure system due to various mechanisms.

1.2.1 Kinematic interaction effect

The kinematic interaction phenomenon is a significant mechanism of SSI that arises from the difference in rigidity between the soil and the foundation elements. This effect becomes apparent when comparing the free field ground motion and the ground motion with foundation elements. It is observed that the ground motion modification occurs not only at the ground surface but also at various depths within the soil.

In the case of reinforcement by rigid inclusions, the presence of the rigidity contrast can be of a nature to:

- Affect the propagation of seismic waves and alter the incident seismic action on the supported structure (amplitude and frequency content);
- Induce additional solicitation (bending moment, shear force) in the rigid inclusions, in addition to those related to the natural vibration of the supported structure.

1.2.2 Inertial interaction effect

During seismic loading, the mass of the superstructure generates inertial forces, making it the source of vibrations that are transmitted to the soil and foundation elements. This phenomenon, resulting from the presence of the structural mass, is referred to as inertial interaction. The generated inertial forces can vary in magnitude and direction depending on the characteristics of the earthquake and the structural response of the building.

As another consequence of the inertial interaction phenomenon, the soil-foundation system cannot be treated as a fixed base, but rather as a flexible base, as depicted in Figure 1.8. The stiffness and damping characteristic of the foundation under inertial loading exhibit a significant frequency dependence, and a novel mechanism of energy radiation dissipation also emerges.

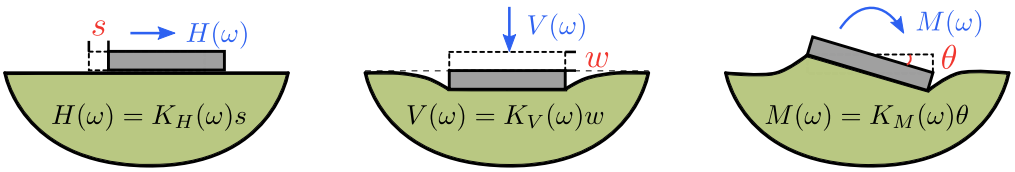

Fig. 1.8. Dynamic impedances of a shallow foundation

In the case of rigid inclusions, the effects generated by inertial interaction can be summarised as follows:

- A change in the support conditions of the structure, resulting in variations in dynamic impedances as a function of load frequency;
- Additional stresses within the inclusions, generating bending and shear forces, which often become decisive from a design point of view.

Compared with pile foundations, in most cases of reinforcement using rigid inclusions, the presence of LTP, allows the disconnection between the footing and the inclusions, which has an impact on the dynamic impedances and the inertial force transfer mechanism.

1.2.3 Energy dissipation

In a SSI analysis, it is commonly assumed that the soil behaviour at a distance from the superstructure and foundation can be approximated as linear elastic or equivalent linear elastic. Nonlinear effects, if present, typically occur in the zone near the structure and at the soil-foundation interface. The energy dissipation within the soil-foundation system under seismic loads can be classified into three main categories based on their underlying mechanisms, as illustrated in Figure 1.9.

- Viscous material damping of soil, represented by mechanism (I) in Figure 1.9;
- Hysteretic damping due to irreversible behaviour, represented by mechanism (II) in Figure 1.9;
- Radiation damping, represented by mechanism (III) in Figure 1.9.

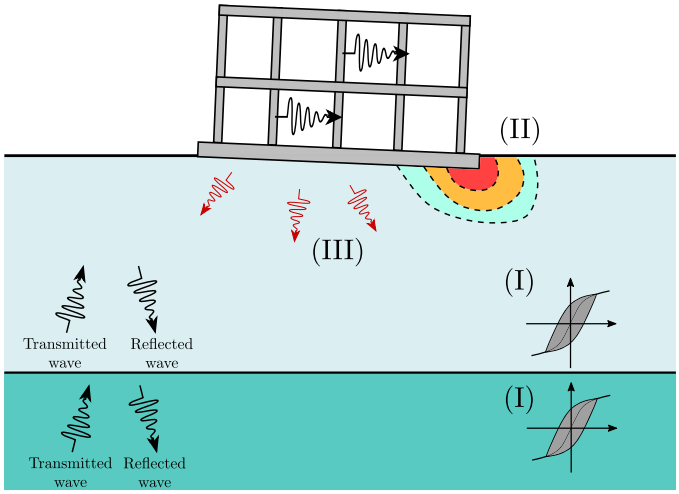

Fig. 1.9. Different energy dissipation mechanisms

Viscous damping is an inherent characteristic of soil and is dependent on the level of strain. Due to the curved stress-strain behaviour exhibited by most soils, the damping factor can be quantified by the area enclosed within the hysteresis loop of the soil stress-strain curve (Seed and Idriss, 1970). To approximate this hysteretic stress-strain relationship, a visco-elastic behaviour is commonly employed, utilising a secant modulus and an equivalent linear damping ratio (Gazetas, 1991b).

Hysteretic damping, as a type of material damping, is not influenced by frequency and is related to energy dissipation resulting from the plasticity of the soil and the interaction between the foundation and the surrounding soil. It should be noted that if the foundation-soil system remains within the linear elastic range, the contribution of hysteretic damping tends to diminish. For the rigid inclusion-reinforced foundation, the sliding mechanism between the foundation and the LTP can be a source of energy dissipation.

Radiation damping, a form of geometric damping, is associated with the transmission of seismic waves from the structure to the soil at an infinite distance. It is influenced by various factors, including the geometry of the foundation-soil-contact area, the characteristics of the structure, and the properties of the underlying soil deposits (Celebi, 2000).

1.3 Summary

This chapter provided an overview of the principal interaction mechanisms within a rigid inclusion-reinforced foundation. In contrast to pile foundations, negative friction in the context of inclusion-reinforced foundations is not a harmful phenomenon. The incorporation of the LTP enables a controlled displacement sliding mechanism. Moreover, this chapter presented notable applications of this technique, highlighting the potential and advantages of employing the rigid inclusion soil improvement technique.

Furthermore, the chapter summarised the dynamic phenomena SSI within inclusion-reinforced foundations. These phenomena include kinematic interaction, inertial interaction, and energy dissipation.

2 Literature review: Experimental dynamic SSI studies

2.1 Interest of experimental studies

Numerous experimental studies have been conducted to investigate the static interaction phenomena of inclusion-reinforced foundations through small-scale tests and full-scale tests (Low *et al.*, 1994; van Eekelen *et al.*, 2003; Jenck, 2005; Briançon and Andromeda, 2008; Briançon *et al.*, 2010; Okyay, 2010).

The number of dynamic and seismic studies is relatively limited due to several reasons. Firstly, experimental studies with dynamic and seismic excitation are associated with high costs. The required equipment, materials, and testing procedures contribute to the overall expense. Secondly, considerable preparation time is necessary to properly set up the experiments, which can further hinder the execution of a large number of studies. Finally, the complexity of the tests themselves poses challenges, making it difficult to conduct many experimental investigations.

However, experimental studies on dynamic SSI offer numerous invaluable advantages and substantially contribute to our comprehension of this complex phenomenon in the context of rigid inclusion-reinforced foundation. In contrast to numerical investigations, experimental studies provide a more realistic representation of the behaviour and response of soil-foundation-structure systems under dynamic loading conditions. Furthermore, the comparison between experimental and numerical results facilitates the evaluation of the accuracy and dependability of numerical models.

In the experimental research, it becomes evident that several studies employ the same concept of inclusion ground improvement but use different names to describe it. These names include "cushioned pile raft foundation", "disconnected pile raft foundation", "insulated pile foundation", "unattached pile foundation", "rigid pile composite foundation", "pile-reinforced composite foundation" and so on.

Among these configurations, some incorporate a designed LTP, often referred to as a cushion or simply a gravel layer. In certain cases, the foundations are directly positioned on the top of the piles (inclusions). However, in other studied configurations, there exists a gap between the heads of piles (inclusions) and the foundation. Within this gap, the same type of soil is present as in the surroundings of the piles (inclusions).

2.2 Shaking table tests

Shaking table tests are widely recognised as one of the primary techniques for evaluating the seismic performance of structures. Several studies concerning the rigid inclusion seismic behaviour have been conducted with the help of shaking table devices.

Azizkandi *et al.* (2018) have conducted shaking table tests to investigate the dynamic behaviour of both disconnected and connected pile rafts. The models are filled with dry Firoozkuh siliceous sand, which has a relative density of 60 %. In the connected pile raft model, a square aluminium raft is rigidly connected to four hollow aluminium piles. Conversely, in the disconnected pile raft model, a granular LTP is placed between the raft and the heads of the piles.

The results of the tests reveal that the connected pile raft exhibits smaller displacements during the lateral cyclic loading, and ultimately, the residual displacement is also reduced compared to the disconnected pile raft foundation. In the case of a disconnected pile raft, the piles experience significantly smaller moments and lateral shear forces compared to the connected configuration.

Furthermore, in the connected pile raft, the piles contribute much more effectively to the lateral bearing mechanism, accounting for approximately 50 % of the lateral cyclic loading. Conversely, in the disconnected pile raft foundation, the disconnected piles primarily bear less than 15 % of the lateral loading during the cyclic loading. Both connected and disconnected pile foundations effectively mitigate the ground settlement compared to the free ground during the excitation.

In the study conducted by Nakagawa *et al.* (2018), the seismic behaviour of a building with an insulated pile foundation, which is equivalent to a foundation reinforced by rigid inclusions, is examined. In contrast to the rigid inclusion-reinforced foundation, the investigated insulated pile foundation is installed in the sand without a designed LTP layer, even when the foundation is not directly positioned on the piles.

Two scaled models are installed within the shear box. One model represents a pile foundation where 16 piles are connected to the slab while the other model consists of 16 insulated piles, as depicted in Figure 2.1. The piles are simulated using aluminium tubes. The shaking table is utilised to provide lateral in-plane input motion, which corresponds to the design response spectrum defined in the Building Standard Code in Japan. The peak amplitudes of the input motion are varied between 25 % and 200 % (six amplitude levels).

The investigation reveals that the building response and the stresses near the pile heads are reduced due to the pile insulation. In cases where the amplitude of the input motion is large, the rocking motion plays a significant role in the response of the insulated pile foundation system, as illustrated in Figure 2.2. Additionally, it is observed that the forces

exerted on piles at different positions are similar during small-intensity earthquakes. However, distinct differences in the forces between piles at different positioned piles in the insulated pile raft foundation are observed during strong earthquakes due to the more pronounced inertial force (Nakagawa *et al.*, 2020).

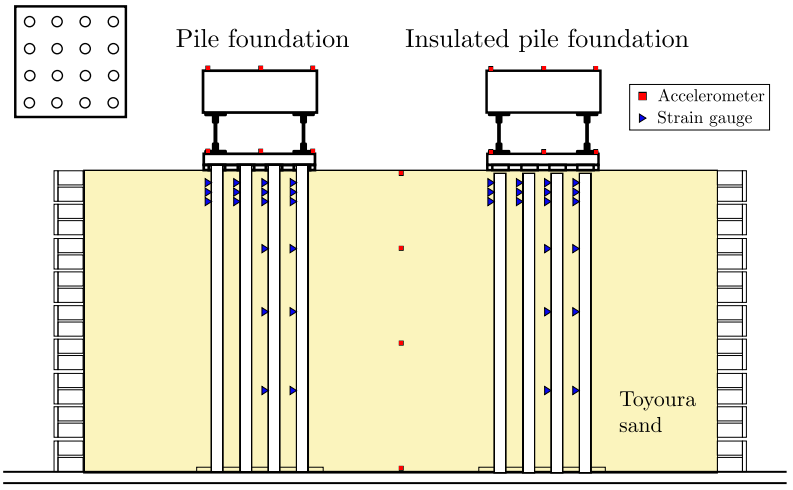

Fig. 2.1. Experimental models scheme (Nakagawa *et al.*, 2018)

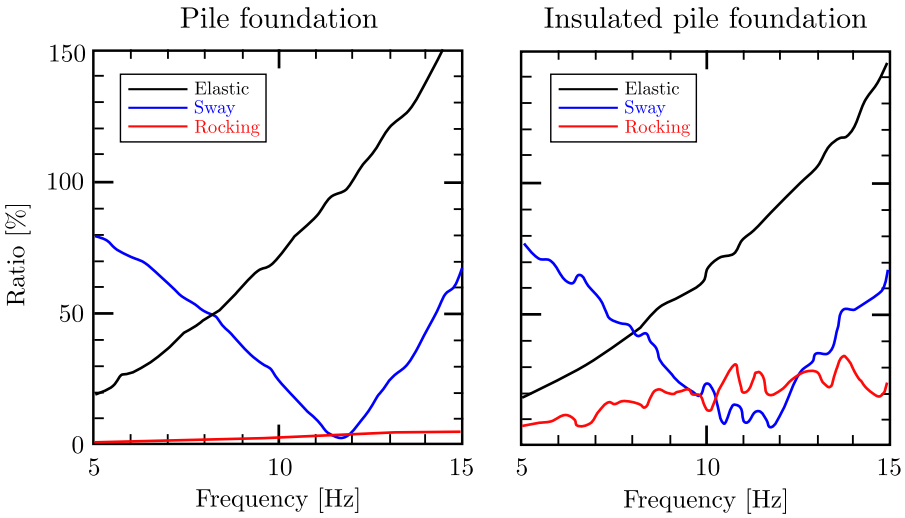

Fig. 2.2. Estimated ratio of sway, rocking and elastic deformation to the total motion for: (a) pile foundation and (b) disconnected pile foundation (Nakagawa *et al.*, 2018)

The study conducted by Kashiwa *et al.* (2020) aims to investigate the bearing mechanisms of insulated existing pile foundations. The motivation behind this study is to reuse the existing underground piles in the design of a new building. Shaking table tests have been conducted on various foundation configurations. The existing piles (representing inclusions) are modelled using 16 aluminium piles embedded in dry sandy soil.

The input motion for the shaking table tests is a sinusoidal wave with varying frequencies of from 4 Hz to 20 Hz, changing every 2 Hz. The natural frequency of the superstructure is 12 Hz. The motion amplitudes are set at 1.0, 2.0, 4.0 and 6.0 m/s^2. The detailed specimen is illustrated in Figure 2.3. Accelerometers have been installed on the mass and

the base foundation to measure horizontal and vertical acceleration. Displacement gauges are used to capture the story drift, as well as horizontal and vertical displacement of the mass and the base foundation.

Several interesting conclusions are drawn from the shaking table tests. It is found that the residual rotation of the foundation with existing piles is significantly smaller than the model without piles, particularly during tests with large input amplitudes. The decline in the overturning moment occurs significantly earlier than the skeleton curve representing rigid body overturning, indicating that the local non-linearity surrounding the insulated pile foundation notably influences the dynamic response of the superstructure.

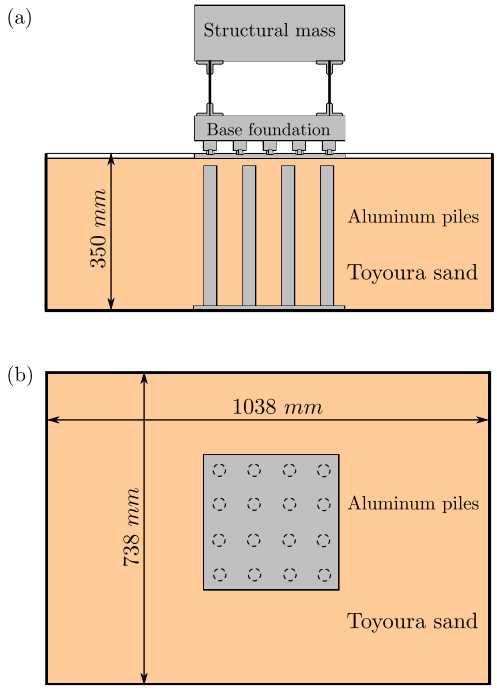

Fig. 2.3. Shaking table test layout: (a) Existing piles model and (b) Plan view of rigid rank (Kashiwa *et al.*, 2020)

Lin *et al.* (2022) have conducted a shaking table test to study the seismic behaviour of a composite foundation consisting of rigid and sub-rigid piles. This type of foundation, commonly known as a CM pile composition foundation, has been applied to many practical engineering scenarios. It is composed of C piles (rigid), M piles (sub-rigid), and the LTP layer.

The term "C pile" primarily refers to rigid, long piles such as concrete piles. "M pile" denotes semi-rigid piles, including cement mixing piles or cement mortar mixing piles. The underlying design principle aims to enhance bearing capacity and reduce foundation settlement by capitalising on both C and M piles. The C piles not only serve to increase the bearing capacity but also transfer loads to the deep foundation through its pile body, consequently reducing deformation within the compressed layer. The primary role of M

piles is to improve the bearing capacity through shaft friction, reinforce the soil between piles, and increase the frictional resistance of the C pile body.

The pile group is arranged in a 4 × 4 pattern, as shown in Figure 2.4. The results of the shaking table test reveal that the acceleration response strength at the pile heads surpasses that at the pile tips. Furthermore, as the excitation peak value increases, the peak strain of the piles also rises. The distribution of peak strain along the length of rigid piles is altered with changes in excitation amplitude. Conversely, the distribution of peak strain in sub-rigid piles displays relatively less variation.

The test configuration is particularly noteworthy due to the utilisation of a mixture of two families of varying lengths in reinforcement. Typically, in reinforcement practices, inclusions of the same length are commonly employed. However, in these tests, the innovative approach using inclusions from two different length families is adopted.

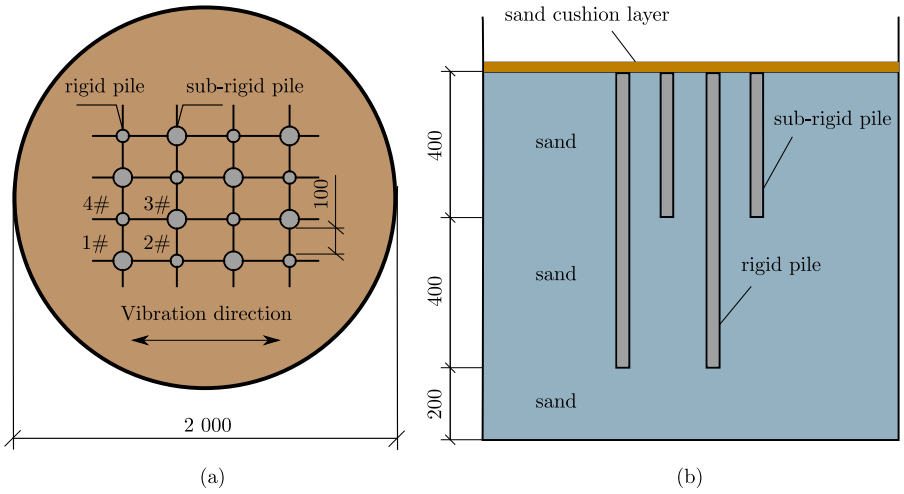

Fig. 2.4. Layout of test model: (a) plan view and (b) sectional view, in mm (Lin *et al.*, 2022)

Yang *et al.* (2023) have conducted a series of scaled 1-g shaking table tests to investigate the seismic response of a nuclear power station supported by disconnected pile raft foundations in clay soil. The research involves analysing the non-linearity of the soil, the isolation effect of the LTP, as well as the displacement of the structure and the bending moments of inclusions. The objective of the study is to explore the influence of different types of gravel LTP type on the response of the reinforced foundation system under earthquake excitation.

The structural model is scaled down to 1/10 of the Chinese III generation nuclear power station and supported by a group of 4 × 3 aluminium tube piles. The clay used in the tests was obtained from the Nanjing sampling site. Three types of 0.5 m thick LTP are selected for investigation. The first type, referred to as cushion A, consists of a well-graded gravel LTP with a D_{50} particle size of 3.5 mm and a size range of 2 mm to 10 mm. LTP B is a mixture of two types of gravel particles in a 3:1 ratio, with the larger proportion ranging from 2 mm to 5 mm, and the smaller proportion ranging from 5 mm to 10 mm. The final

type, LTP C, exclusively comprises gravel particles ranging from 2 mm to 5 mm. During the test, the system is subjected to a white noise excitation with a magnitude of 0.05 g, as well as three earthquake excitations, including two natural and one artificial ground motion, each with varying intensities.

The conclusions drawn from the study emphasise the importance of considering not only the characteristics of the inclusions but also the properties of the LTP material. The fundamental frequency determined through white noise excitation indicates that LTP A and LTP B, which include a mixture of small and large particle sizes, exhibit superior isolation efficiency compared to LTP C. It is noteworthy that the measured peak acceleration and absolute displacement consistently exhibit the highest values in the case involving LTP C. Additionally, the maximum bending moment occurs at the midpoint of the piles, it is independent of the location of the piles. This study highlights the impact of the granular composition of the LTP, with well-graded and gap-graded gravel LTP performing better than the single small-size gravel.

2.3 Centrifuge tests

The behaviour of soils is contingent upon their load history and the level of stress to which they are exposed. Reproducing the same state of stress is, therefore, an essential requirement for simulating the real behaviour of a full-scale structure, referred to as the "prototype", at the reduced scale model level. Centrifuge modelling achieves this by amplifying the body forces applied to the small-scale model.

Geotechnical centrifuge modelling stands out as a reliable and effective technique for investigating the seismic effects on structures with a reduced-scale model. It has been extensively employed to investigate the seismic behaviour of both shallow foundations and pile foundations (Chatzigogos *et al.*, 2005; Li, 2014; Pérez-Herreros, 2020).

In recent years, numerous tests involving rigid inclusions have also been conducted. Garnier and Pecker (1999) have conducted centrifuge tests at Gustave Eiffel University (UGE) in Nantes to validate an innovative foundation concept for the Rio-Antirrio Bridge. The primary objectives of these centrifuge tests are to estimate the ultimate bearing capacity of the foundation under a combination of monotonically increasing horizontal force and overturning moment and to assess the behaviour of the foundation under various cyclic loads. Additionally, the study aims to identify the failure mechanism of the foundation under these combined loads.

Three tests are conducted at 100 g using a 1/100 scaled model. The prototype model features a circular footing with a 30 m radius supported by rigid inclusions measuring 8.5 m in length and 0.67 m in diameter. Clay samples are collected from the area

around the bridge pier. On top of the clay layer, a 1.2 m thick ballast LTP layer made of Fontainebleau sand is placed.

Various parameters are measured during the tests, including pore pressure at different locations below the foundation, soil settlement, water table level, applied loads, and bending moment in the inclusions. The vertical load V is kept constant through the tests. A cyclic horizontal force T is applied at a constant height above the footing, generating an overturning moment $T.h$. A cyclic additional overturning moment M is produced by a movable mass. At the end of the tests, the model is subjected to monotonically increasing shear force until failure, with a constant M/V ratio (Pecker, 2003).

These centrifuge tests reveal that the ultimate bearing capacity is not degraded, even when the cyclic amplitude arrives at 75 % of the failure load. The displacement does not increase with the number of cycles. An equivalent damping ratio of 20 % is detected during the tests (Garnier and Pecker, 1999).

At the same time, five centrifuge preliminary tests have been conducted in the CEA-CESTA centrifuge laboratory in Bordeaux with different configurations in terms of number of inclusions, soil strength and vertical load. The sample is monotonically loaded with any prior cyclic loads until a significant geometric change occurs, and the failure loads are underestimated (Garnier and Pecker, 1999) The results of the centrifuge test confirm the theoretical predictions in terms of failure load. Figure 2.5 showed the correspondence of the three test results in Nantes and five tests performed in Bordeaux.

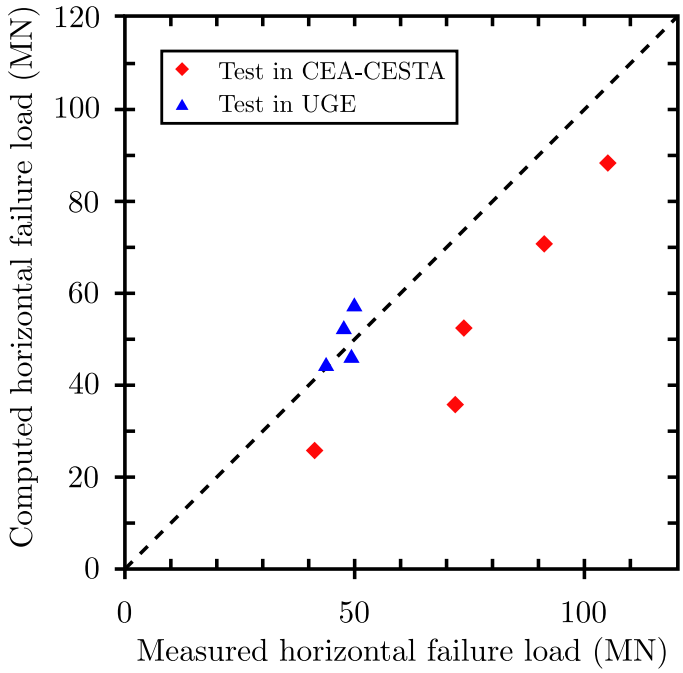

Fig. 2.5. Comparison of predicted and measured failure loads (Pecker, 2003)

A rocking foundation can be considered as a type of seismic isolation system that allows a foundation to rock during an earthquake. The benefits of a rocking foundation include the

reduction of structural damage and the improvement of structure seismic performance. The rocking behaviour of unattached pile foundations was investigated by Allmond and Kutter (2014). The studied configuration involves a footing directly positioned on the piles, which are not connected to the footing. Unlike the conventional configuration for a rigid inclusion-improved foundation, there is no sand or granular layer between the piles and the raft. Unattached pile raft foundations offer the advantage of reducing residual rotations and settlements while still benefiting from the advantages of a rocking foundation. The study concludes that a shear key connection is essential for unattached pile rocking foundations. Without a shear key, the large sliding displacement appears unexpectedly and results in the movement of the piles.

To benefit from the advantages of a rocking foundation while reducing the settlements, Loli *et al.* (2015) have conducted a study on the rocking behaviour of shallow foundations on unconnected piles. Different to the configuration studied by Allmond and Kutter (2014), a uniform intermediate sandy layer is introduced between the pile and the raft in this study. Three dynamic centrifuge tests have been performed using a 1/50 scaled bridge pier, as depicted in Figure 2.6. The seismic sequence considered in the study involves a strong earthquake followed by several lower-magnitude motions aftershocks, such as the Rinaldi motion (1994 Northridge earthquake). Based on the recorded time-history data, it is observed that the maximum acceleration of the rocking-isolated pier on unconnected piles is lower compared to conventional design approaches. This hybrid foundation design results in reduced permanent rotation and settlement.

Park *et al.* (2017) have examined the dynamic SSI behaviour of a storage tank with three different types of foundations: a shallow foundation, a pile foundation, and a disconnected pile foundation. The investigations have been carried out through centrifuge model tests using poorly graded clean silica sandy soil. For the model of the slab with disconnected piles, the slab is directly placed on the top of the piles without any distance between the pile heads and the slab. The primary focus of the study is placed on the analysis and comparison of the response exhibited by the structure with different types of foundations. It can be observed that the peak acceleration is more significantly amplified in the case where a shallow foundation is employed, while it is less amplified in the case of a slab with connected piles. The response of the tank on the slab with disconnected piles fails between the response of these two configurations.

Influenced by the concept of rocking foundations, the study conducted by Ha *et al.* (2019) aims to investigate the behaviour of unconnected pile foundations under various conditions. The research focuses on understanding the influence of different factors, including the pile tip and head conditions, the rigidity of the LTP and the shaking level. All pile foundations are installed in dry sand in a 3×3 pattern with a centre-to-centre distance of 3.5 times the pile diameter. Three earthquake records are utilised as input motion. The findings reveal that the disconnected pile foundation effectively reduces the seismic load on the structure. Moreover, the rotational damping of the disconnected pile foundation

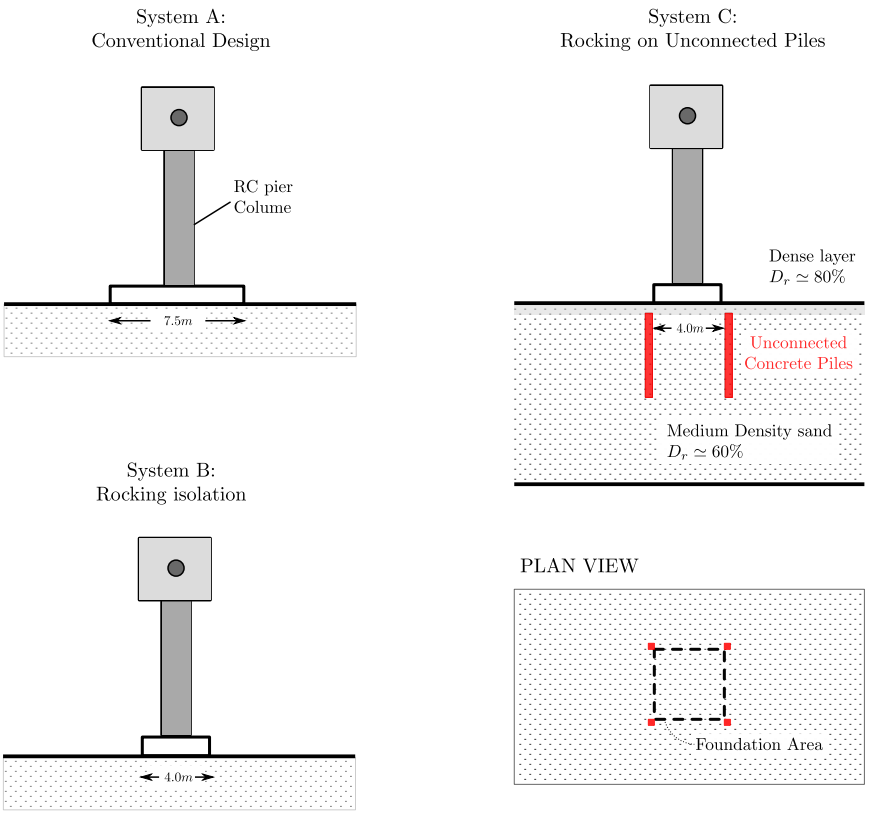

Fig. 2.6. Three foundation solutions for a bridge pier (Loli *et al.*, 2015)

is found to be comparable to that of a shallow foundation. The study also examines the rotational stiffness, which is found to depend on the fixation condition of the pile tip and head. Additionally, the stiffness is observed to degrade as the rotation angle increases due to the uplift mechanism.

In the study conducted by Ko *et al.* (2019), the seismic behaviour of disconnected pile raft foundations is analysed through dynamic centrifuge tests, with a specific focus on modelling bridge piers and comparing them to connected piled rafts. Two types of piles made of different materials, including aluminium and steel, are employed to assess the influence of pile material on the system response. The centrifugal acceleration used in the tests is set at 50 g.

The model ground consists of dry silica sand, which is poured into a shear beam box. The structural model adopts a SDOF configuration, comprising a lumped mass at the top connected to a thin supporting plate through two thin steel plates. Aluminium and steel piles are employed to simulate pre-stressed high-strength concrete and steel pipe piles, respectively. Two natural earthquakes, the Ofunato and Hachinohe earthquakes, are selected as input motions. The Ofunato earthquake represents a short-period-dominated signal, while the Hachinohe earthquake represents a long-period-dominated signal.

The findings indicate that the seismic response of the disconnected piled foundation decreases as the peak ground acceleration at the LTP increases, primarily due to the sliding

behaviour between the raft and the transfer platform. Furthermore, when compared to connected pile foundations, the disconnected pile foundations exhibit larger permanent settlements and foundation rotations. Additionally, the bending moments of the piles are also reduced as a result of the disconnection of the piles.

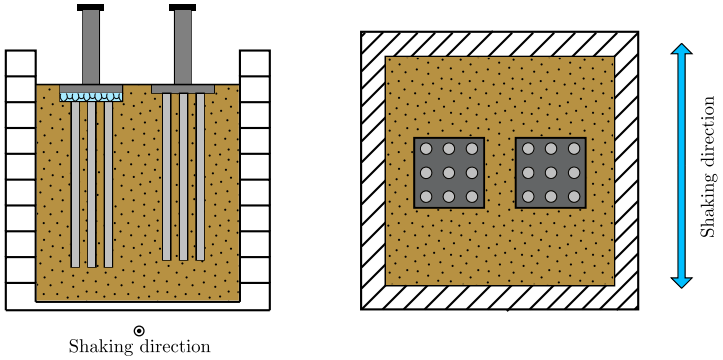

Fig. 2.7. Comparison of predicted and measured failure loads (Ko *et al.*, 2019)

Liang *et al.* (2021) have conducted dynamic centrifuge tests to assess the non-linear behaviour of a cushioned pile raft foundation, which shares the same concepts as a foundation reinforced by rigid inclusions. In the case of the cushioned pile raft, the raft remains unconnected to the piles. Gravels are placed above the piles and are meticulously compacted to establish the LTP layer, referred to as the cushion in their study. They have also examined the isolation effect of a granular LTP. The model consists of a superstructure and a foundation comprising a 3 $\times$ 3 pile group embedded in soft clay. The tests are conducted under different earthquake motions with various intensities. To measure the response of the system, multiple sensors are deployed, including those to measure the acceleration and residual displacement of the superstructure as well as the bending moments in the superstructure columns and inclusions. A comparison is made between the foundation on rigid inclusions and the pile foundation. The results reveal that the foundation on rigid inclusions achieves a significant reduction in bending moment in the superstructure compared to the pile foundation. Furthermore, the presence of the LTP facilitates effectively dissipating earthquake energy and reduces the seismic excitation transmitted to the superstructure, particularly during high-intensity earthquakes.

Yang *et al.* (2022) have conducted a series of sixteen dynamic centrifuge tests using a 50 g centrifuge test model to investigate the seismic response of nuclear power stations supported by disconnected pile raft foundation, which follows the same concept as foundation reinforced by rigid inclusions. The study specifically focuses on exploring the effect of gravel LTP thickness on the system's response.

The tests are conducted within a laminar shear model box. Shanxi kaolin clay and Fujian standard sand are used as the soil materials in the experiments. The foundation system consists of twelve aluminium piles with a diameter of 0.7 m, arranged in a 4 $\times$ 3 pattern and spaced at 2.45 m intervals. It is worth noting that the configuration examined in this research corresponds to a form of floating inclusion reinforcement, where the tips of the

piles are not embedded in a support layer. A well-graded gravel LTP layer is incorporated between the piles and the raft. Two different LTP thicknesses are tested: Case A (0.7 m) and Case B (1.4 m). During the dynamic centrifuge tests, the system is subjected to white noise excitation, as well as two natural ground motions and one artificial ground motion.

The study's finding confirms the effectiveness of the gravel LTP in providing seismic isolation effect. Specifically, Case A demonstrates a better performance compared to Case B. Consequently, the article recommends using an LTP thickness equal to the diameter of the inclusions. Additionally, the results reveal that the bending moments experienced by the corner and edge piles are significantly higher compared to the inner piles.

2.4 In-situ tests and instrumented foundation

The in-situ tests aim to obtain the actual seismic response records of the instrumented structure through the global seismic monitoring network and a large number of sensors placed on the structure. In some cases, the in-situ tests also involve steady-state forced vibration or the controlled detonation of pre-embedded explosives to simulate earthquake excitation.

As part of the ICEDA project, EDF (*Electricité de France*) has conducted a series of forced vibration tests on two experimental plots to investigate the vertical and horizontal dynamic response of inclusion-reinforced foundations. The objective of these tests is to assess the practical methods under real-site conditions and validate the adopted methodology for the numerical calculations (Okyay *et al.*, 2012).

The in-situ tests included 14 cone penetration tests and 3 pressiometer tests to gather information about the soil properties. In addition, oedometer and triaxial tests are conducted in the laboratory. The shear modulus of the soil layers is determined using cross-hole tests, and the concrete modulus is determined from compression tests on concrete specimens.

Two slabs measuring 11 m $\times$ 11 m $\times$ 1.2 m are subjected to testing. One slab is placed on non-reinforced soil, while the other is on soil reinforced with nine inclusions. A machine equipped with a rotating unbalance is installed at the centre of each slab. Excitation is applied in both the horizontal and vertical directions, ranging from 2 Hz to 20 Hz. The vertical and horizontal dynamic responses of the reinforced foundation are measured and compared with numerical calculations (EDF, 2008b; Okyay, 2010; Vandeputte *et al.*, 2010; Okyay *et al.*, 2012). The experimental transfer functions recorded on both slabs indicate that the inclusion reinforcement has no impact on the horizontal direction, whereas the rigid inclusions do reduce the vertical displacement at the centre of the slab.

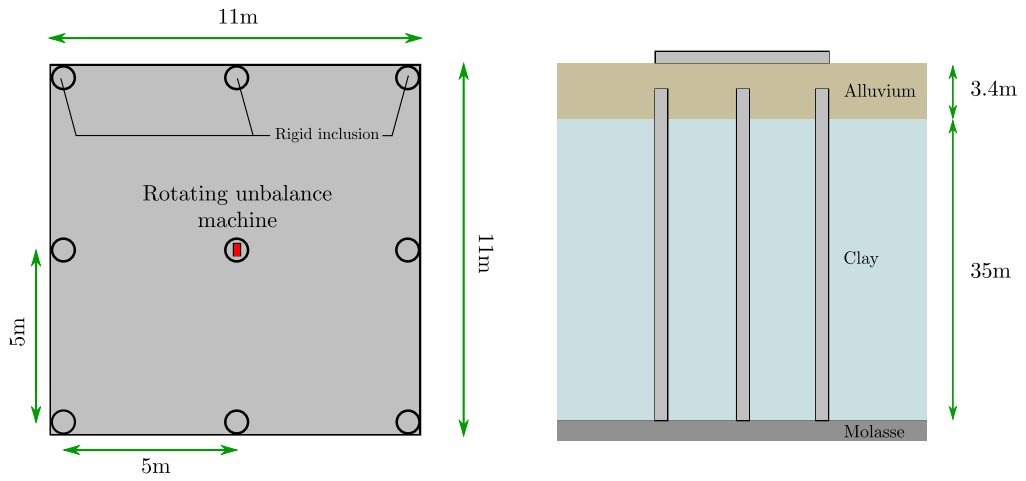

Fig. 2.8. Configuration of inclusion-reinforced slab (EDF, 2008a)

Sekiguchi *et al.* (2015) have conducted a study on the potential reuse of existing concrete piles as foundations for new buildings, referred to as insulated pile foundations. The foundation concept is similar to foundations reinforced by rigid inclusions. Three types of foundations, namely pile foundation, shallow foundation, and insulated pile foundation, are installed on the actual ground. Their behaviour is monitored during 56 earthquakes that occurred between June 18, 2013, and February 28, 2015, including 8 earthquakes with a peak ground acceleration exceeding 0.1 m/s^2 at the free field.

The piles used in the study are steel pipes with a diameter of 101.6 mm while reinforced concrete blocks serve as the superstructure. In the insulated pile foundation, a thin layer of sand is placed between the concrete blocks and the top of the insulated piles. Additionally, a geotextile is installed on the top of the insulated piles. To measure the system responses during earthquakes, three-component accelerometers are placed at the top of the superstructure, at the free field, and at a depth of -10 m below the ground level. Strain gauges are also installed at the pile heads to measure the stresses. The experimental foundation models and sensor placements can be seen in Figure 2.9.

Seismic observations reveal that the peak response accelerations of the insulated pile foundation are lower than those of the other two foundations, both in the horizontal and vertical directions. The stress at the pile heads is significantly reduced due to the insulation of the piles compared to the pile foundation.

From the time histories of bending moment and axial force at the pile heads, it is evident that the bending moment and axial force of the pile foundation fluctuate in response to seismic ground motion. However, in the case of the insulated pile foundation, the variations in bending moment and axial force are less pronounced. Additionally, it is noteworthy that the stress resulting from the inertia force of the superstructure is less concentrated at the pile heads of the insulated pile foundation compared to the pile foundation.

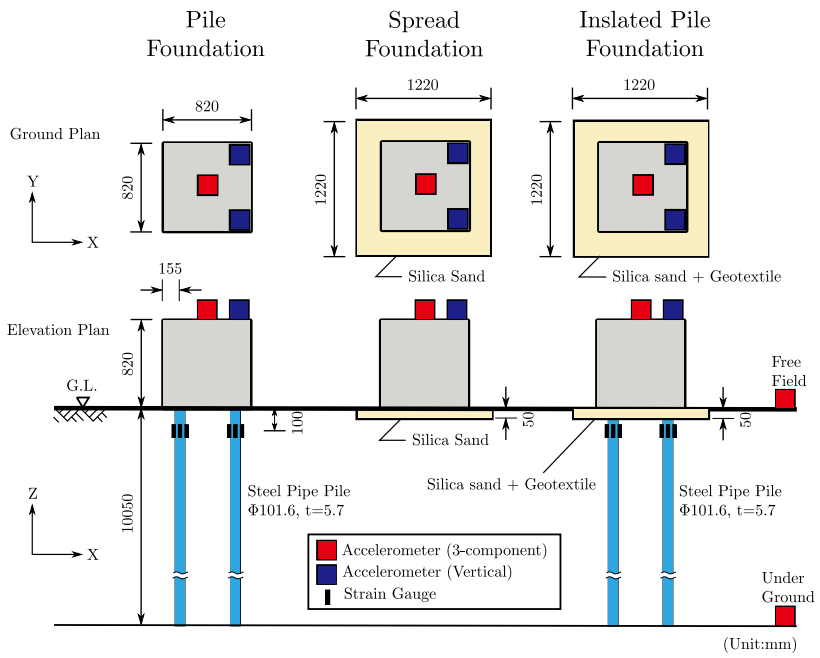

Fig. 2.9. Experimental model scheme (Sekiguchi *et al.*, 2015)

2.5 Key observations from experimental studies

The primary objective of this review is to comprehensively evaluate the behaviour and performance of these foundations under dynamic or seismic loading conditions. The aim is to offer valuable insights into their performance.

From the experimental research, several key observations can be drawn:

- **Permanent settlement and rotation of foundations**

  Rigid inclusion ground improvement is a technique for reinforcing the foundation, known for its capacity to reduce settlement under static loads. From cited experimental studies, it has been observed that the presence of rigid inclusions can effectively mitigate both settlement and permanent rotation of foundations during seismic excitation when compared to cases without reinforcement (Allmond and Kutter, 2014; Loli *et al.*, 2015). The shaking table tests conducted by Azizkandi *et al.* (2018) further demonstrate that the foundation on rigid inclusions exhibits a smaller settlement compared to the free ground during the excitation.

  However, it should be noted that foundations reinforced by rigid inclusions exhibit larger permanent settlements and foundation rotations when compared to conventional pile foundations (Ko *et al.*, 2019).

- **Forces at heads of inclusions**

Clearly, due to the insulation of rigid inclusions with foundations, the forces acting on the heads of the inclusions are supposed to be considerably diminished. In the case of foundations on rigid inclusions, these inclusions experience significantly reduced bending moments and lateral shear forces at the heads (Sekiguchi *et al.*, 2015; Azizkandi *et al.*, 2018; Nakagawa *et al.*, 2018; Ko *et al.*, 2019).

Moreover, it should be noted that the concentration of inertial forces resulting from the mass of the superstructure is less pronounced at the heads of rigid inclusions when compared to pile foundations (Sekiguchi *et al.*, 2015).

- **Stiffness of foundations**

  The stiffness of the inclusion-reinforced foundation is also assessed through experimental research. The in-situ experiments conducted within the framework of the ICEDA project indicate that inclusion reinforcement does not affect the horizontal direction, but enhances vertical stiffness (EDF, 2008a).

  Additionally, it is observed that the rotational stiffness degrades as the rotation angle increases, due to the uplift mechanism and non-linearity near the foundation (Park *et al.*, 2017; Nakagawa *et al.*, 2018).

- **Isolation effect and characteristic of LTP**

  A significant phenomenon observed is the isolation effect of such a foundation during seismic excitation. The disconnection between rigid inclusions and the foundation leads to a substantial reduction in the seismic response of the superstructure, as evident in studies by Allmond and Kutter (2014), Loli *et al.* (2015), and Nakagawa *et al.* (2018).

  Moreover, the presence of LTP introduces a sliding behaviour of the foundation, as observed in the study conducted by Ko *et al.* (2019). Liang *et al.* (2021) demonstrates that the gravel LTP can achieve a notable reduction in bending moments within the superstructure, particularly during high-intensity earthquakes. These studies collectively confirm that the presence of LTP effectively facilitates the dissipation of earthquake energy and reduces the seismic excitation transmitted to the superstructure.

  The effectiveness of the isolation effect depends on the characteristics of LTP. In the studies carried out by Yang *et al.* (2022, 2023), it is recommended that the thickness of LTP matches the diameter of rigid inclusions and a well-graded granular composition of LTP is deemed necessary to ensure a favourable isolation effect.

2.6 Summary

This chapter presents a literature review dedicated to the experimental investigation of rigid inclusion-reinforced foundations. Encouragingly, many experimental studies have been conducted in this field in recent years (within the past ten years). The findings from these studies represented crucial contributions to our understanding of the behaviour and performance of inclusion-reinforced foundations subjected to seismic loading conditions. However, there remains a significant gap in current research compared to studies on shallow foundations and pile foundations.

These studies have typically focused on comparing the performance of pile foundations and inclusion-reinforced foundations. Some studies highlighted the effects of the raft-inclusion discontinuity on reducing the seismic response of the structural and foundation elements and examined the isolation effect resulting from the presence of gravel LTP.

However, most of the studies have investigated the behaviour of the structure-foundation-soil system, which involves a combination of inertial and kinematic interactions.

3 Literature review: Numerical dynamic SSI studies

3.1 Interest of numerical studies

The high cost associated with experimental approaches often restricts their application in the study of dynamic SSI problems. Consequently, numerical methods are frequently preferred alternatives.

Classical numerical modelling methodologies, which are commonly used to study the dynamic SSI problem for different superstructures and foundations, can also be utilised for structures founded on rigid inclusion reinforced soil.

Multiple approaches do not provide global information but instead focus on addressing specific problems, such as bearing capacity and the response of rigid inclusions. These approaches, along with their variations and adaptations for the study of foundations on rigid inclusions, are also interesting.

In practical applications, these methodologies are implemented using a variety of numerical modelling techniques, including the finite element method, the finite difference method, the hybrid method combining the finite element method and boundary integral equation, among others.

3.2 General dynamic SSI numerical approach

3.2.1 Direct approach

Modelling the structure, the foundation and the volume of surrounding soil may be the most intuitive approach to analysing the dynamic SSI problem. This approach, known as the global approach or direct approach, involves solving the dynamic equation coupling the soil, the foundation and the superstructure in either the time or frequency domain. It allows for simultaneous determination of the response of both the soil and the structure (Brûlé and Cuira, 2018). Furthermore, it enables the consideration of radiation effect and energy dissipation effects in the soil volume, which is explicitly modelled (Pérez-Herreros, 2020). To achieve this, it is necessary to accurately model the boundaries of the model

and to use suitable constitutive laws. Numerical approaches like the spectral element method, boundary element method, finite element method, and finite volume method can be employed to model seismic wave propagation in the soil (Semblat, 2011).

When using the global approach in the time domain, the analysis can incorporate the non-linear behaviour of the structure, uplift and sliding of the foundation, as well as the inelastic phenomena and the heterogeneity of the soil. Typically, the resolution technique relies on commonly used numerical modelling approaches such as the finite element method, including classical algorithms like the time integration Newmark method (Pecker, 2023a).

The global approach has several drawbacks. One challenge in solving dynamic SSI problem is the treatment of boundary conditions (Pecker, 2023a). To account for the semi-infinite nature of the soil deposit and prevent the reflection of waves, absorbing boundaries need to be introduced into the model. Additionally, boundary elements can significantly reduce soil volume that needs to be modelled. However, they should be placed at a sufficient distance away from any structural element to avoid interference (Romo-Organista *et al.*, 1980).

Another challenge is to simulate the non-linear behaviour, which increases the complexity of the models. Configuring the non-linear constitutive laws requires extensive calibration and validation work.

There are certain limitations on the mesh size of the numerical model. The maximum mesh size should satisfy a criterion that depends on the maximum frequency of interest and the characteristics of the soil being modelled. To accurately simulate the transmission of high-frequency waves, the maximum size of the mesh elements should not exceed 1/5 or even 1/8 of the wavelength. Furthermore, due to the time-consuming nature of direct approach analyses, they are not suitable for performing exhaustive parametric studies.

When conducting numerical studies, the analysis of the dynamic SSI response for structures supported by shallow foundations on reinforced soil by rigid inclusions poses a complex problem. It necessitates the utilisation of appropriate numerical modelling techniques, including finite element method (Rangel-Núñez *et al.*, 2008; Okyay *et al.*, 2012; Han *et al.*, 2016; Messioud *et al.*, 2016; Saadatinezhad *et al.*, 2021), finite difference method (Mánica Malcom *et al.*, 2016; López Jiménez *et al.*, 2019), and the hybrid method combining the finite element method and boundary integral equation (Shen *et al.*, 2021, 2022a,b,c).

3.2.2 Sub-structuring approach

The sub-structuring approach, which utilises the superposition theorem, is commonly employed in the analysis of SSI due to its simplicity and efficiency. This approach involves decomposing the global model into sub-systems.

In this approach, the Kausel superposition theorem (Kausel *et al.*, 1978) is one of the most widespread and commonly applied, allowing for the step-by-step analysis of the SSI problem, assuming linearity. The sub-structuring approach based on this superposition theorem involves three successive steps, as depicted in Figure 3.1.

1. Calculation of kinematic interaction to determine the seismic action exerted at the base of the structure;
2. Calculation of dynamic impedance functions;
3. Calculation of structural responses, considering dynamic impedance functions and seismic action exerted at the base of the structure.

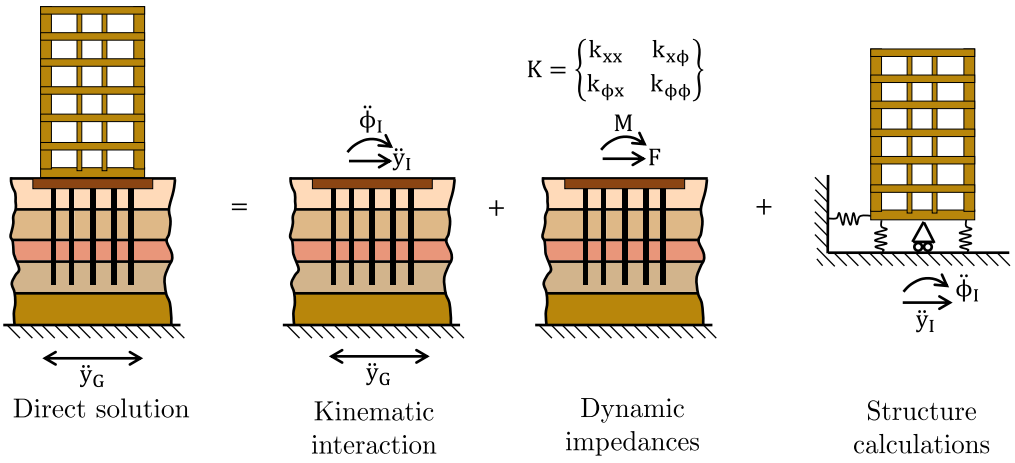

Fig. 3.1. Sub-structuring approach in three steps (Kausel *et al.*, 1978)

The initial two steps of the sub-structuring approach can be executed in the frequency domain, while the calculation of structural responses, incorporating SSI effects, can be carried out in the frequency domain or in the time domain to account for the non-linear behaviour of the superstructure.

However, the substructuring approach does have some limitations. The superposition theorem assumes that the entire system remains in a linear elastic state, which means that the local inelastic behaviour cannot be simulated. Non-linear behaviour in the soil is approximated using equivalent linear visco-elastic constitutive laws. The soil characteristics are determined through iterative interactions based on stiffness degradation curves and damping curves to ensure compatibility with the mean shear strain level resulting from the applied dynamic excitation intensity.

Additionally, similar to the global approach, the mesh size in the sub-structuring approach needs to adhere to certain criteria based on the maximum frequency of calculation and the characteristics of the soil.

3.2.3 Macro-element approach

This hybrid approach integrates both the global approach and the substructuring approach to leverage the respective strengths of each method, as depicted in Figure 3.2. In this approach, a macro-element is positioned at the foundation base to consider the non-linearity within the soil-foundation system. The primary objective of this study is to develop a macro-element for foundation reinforced by rigid inclusions. To gain a comprehensive understanding of a macro-element, it is important to delve into the specifics of macro-elements for different types of foundations.

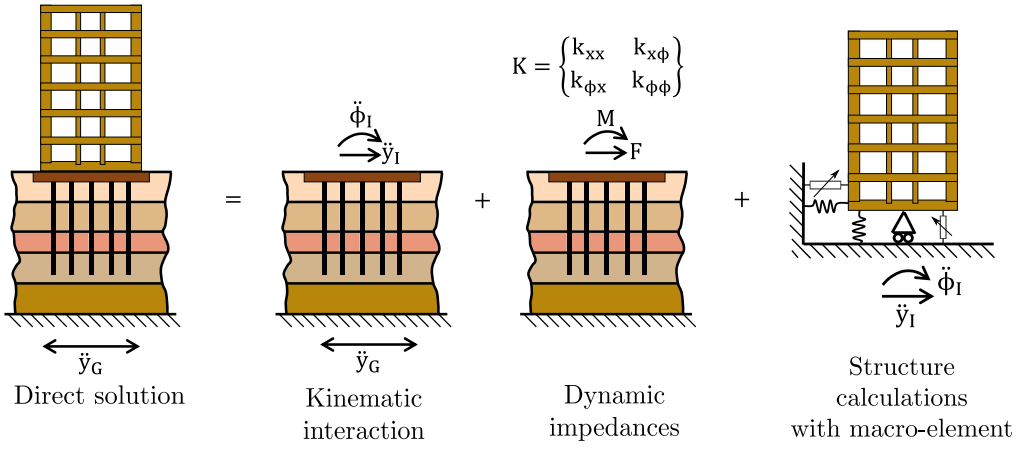

Fig. 3.2. Macro-element approach based on the substructuring approach

This hybrid approach aims to partition the SSI effect into two distinct mechanisms: linear interaction in the far field sub-domain and non-linear interaction in the near field sub-domain, as depicted in Figure 3.3. This approach supposes that the far field, located at a significant distance from the foundation and superstructure, exhibits only linear elastic behaviour governed by dynamic impedances. All potential non-linearities are concentrated in the near field under the assumption of this approach, which encompasses interface non-linear behaviour and soil plasticity near the foundation.

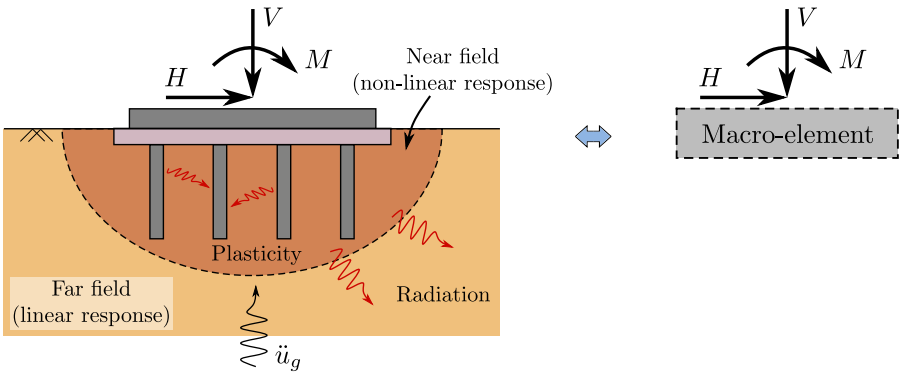

Fig. 3.3. Macro element concept: near field and far field

In reality, the stiffness of the foundation is much greater than that of the soil deposit, allowing a rigid movement for the entire foundation. Under this assumption, the non-linear constitutive laws can be defined in terms of generalised forces (forces and moments) and displacements (translations and rotations). The constitutive laws employed in the macro-element are usually formulated within the framework of classical theories of elasto-plasticity, either with or without a hardening law. Hypoplastic constitutive laws are also considered as an alternative option in several proposed macro-elements (Pedretti, 1998).

However, there are still limitations in the practical application of macro-element models. The flexibility of the foundation cannot be taken into account. The definition of the boundaries for these sub-domains lacks clarity, and it is challenging to precisely determine the evolving geometry of the near field over time (di Prisco and Pisanò, 2011). The calibration of the nonlinear constitutive laws used in these models typically necessitates experimental data or numerical simulations. Additionally, the soil inertia is usually neglected in the macro-element model without a direct simulation. However, this effect can be taken into account using a constitutive law involving the inertial effects in the underlying soil.

Macro-elements are initially employed to simulate the behaviour of joints in structural elements, such as beam-column joints or the beam-plate joints (Ganga Rao and Farran, 1986; Petrolito and Golley, 1989; Arbabi and Li, 1990). In the geotechnical domain, the early works on macro-elements primarily focus on shallow foundations (Nova and Montrasio, 1991). Over time, this concept has been extended to pile foundations and other types of foundations. Although there have been some applications of macro-elements for foundations on rigid inclusions, their utilisation in such cases remains relatively limited.

The macro-elements for foundations can be categorised differently. From the modelling scale, some macro-elements aim to simulate the global behaviour of foundations while in some macro-element approaches, a combination of several macro-elements for different parts of foundations is needed to simulate the global behaviour of the foundation. The macro-element can also be classified based on its non-linear framework, whether it is founded on elasto-plastic theory or hypoplastic theory.

In this section, the macro-element is introduced according to the type of foundation: shallow foundations, pile foundations, and inclusion-reinforced foundations.

Macro-element for shallow foundations

The initial application of macro-elements for shallow foundations is pioneered by Nova and Montrasio (1991). This work focuses on investigating the static bearing capacity of a rigid shallow foundation on sand subjected 2D monotonic eccentric static load. In this macro-element model, non-linearity is incorporated based on classical plasticity theory,

where the yield surface is enveloped by a failure surface. The evolution of the yield surface is governed by a non-associated flow rule and an isotropic hardening law.

The macro-element model developed by Martin (1994) is designed to predict the load-displacement response of shallow foundations for offshore structures situated on cohesive soil. To address the 2D problem, the combined load yield surface suggested by test data is described in the (V, H, M) space, where V represents vertical load, H represents horizontal load, and M represents bending moment. Non-linearity in this model is incorporated using plasticity theory with a suitable flow rule.

Houlsby and Cassidy (2002) proposed a hardening plasticity model with an appropriate flow rule to simulate the behaviour of rigid circular shallow foundations on loose sand. This model incorporates the resultant forces (V, H, M) and the corresponding displacements (u_z, u_h, θ) of the foundation, allowing for the prediction of responses under various load or displacement combinations. Cassidy *et al.* (2002) made modifications to the existing model proposed by Houlsby and Cassidy (2002), calibrating it using a series of tests and verifying its suitability through retrospective simulation of experimental data. However, these models are limited to solving 2D problems only.

Cassidy *et al.* (2004) investigated six degrees of freedom macro-element formulation based on plasticity theory with a hardening law. This formulation considers load-displacement behaviour in horizontal, vertical, rotational and torsional directions. The developed formulation can be integrated into 3D structural calculation programs and is applicable to both sandy and clay soils. It should be noted that these proposed macro-element models have been developed based on monotonic tests and may not be suitable for simulating cyclic behaviour.

The concept of macro-element is further extended through a small-scale footing test conducted by Wuttke *et al.* (2013). This development is built upon the previous formulation of Nova and Montrasio (1991). The novel macro-element model incorporates a parabolic failure surface, as depicted in Figure 3.4, and a yield surface with a similar shape based on the theory of elasto-plasticity. Numerical tests utilising this enhanced macro-element model on unsaturated sand demonstrate a good agreement with experimental results. However, it should be noted that the application of the proposed macro-element formulation is currently limited due to the calibration of model parameters being conducted solely based on experimental studies involving a single type of unsaturated soil. Further research and validation are necessary to explore its applicability to a broader range of soil types.

To address stability concerns related to historical towers, Marchi (2008) proposed a novel two-dimensional (2D) formulation for modelling the foundation and predicting the load-displacement behaviour of the structures. In this work, the hardening law is derived from a vertical stiffness curve obtained through oedometer tests. Although the specific

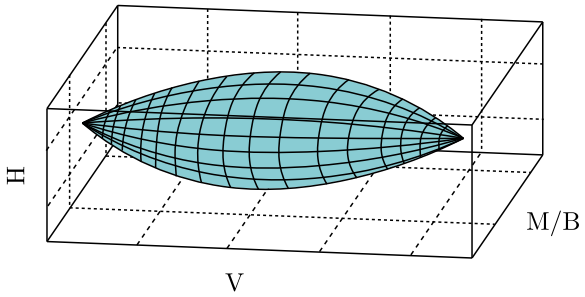

Fig. 3.4. 3D failure envelope proposed by Wuttke *et al.* (2013)

term "macro-element" is not mentioned in the work, the concept employed in this work aligns with the general idea of macro-elements.

Macro-element models offer significant computational advantages by effectively capturing soil-foundation interaction using only a few degrees of freedom. However, a common limitation shared by existing macro-element formulations is their inability to account for changes in geometry, loading, and boundary conditions. To address this limitation, Pisanò *et al.* (2016) proposed a new 2D macro-element framework to study non-linear soil-foundation interaction problems. In this innovative approach, the framework considers the influence of configuration features, such as geometry, loading and boundary conditions, on both the elastic and non-linear behaviour of shallow foundations on frictional soil. The objective of this work is to accurately model the drained load-displacement response of a shallow foundation.

With the evolution of engineering requirements, macro-element models have undergone significant development to address cyclic loading problem. In this regard, Cremer *et al.* (2001) presented a 2D cyclic SSI macro-element model for shallow foundations on cohesive soil. This model incorporated the non-linearities at the soil-foundation interface and is controlled by a yield surface and an isotropic-kinematic mixed hardening law. In order to identify the macro-element parameters, experimental tests are typically necessary. However, Cremer *et al.* (2001) also provided empirical relationships for these parameters, simplifying the parameter identification process and enabling the construction of a simple macro-element model for preliminary studies. The results obtained using the macro-element approach exhibit good agreement with those from finite element modelling.

The macro-element model for shallow foundations on sands, developed by Salciarini and Tamagnini (2009), incorporates the theory of hypoplasticity as an alternative to classical elasto-plasticity theory. The theory of hypoplasticity, initially developed in Karlsruhe and Grenoble, provides a suitable framework for describing the non-linear and irreversible behaviour of materials. This study demonstrates the applicability of hypoplasticity theory in developing a macro-element model capable of simulating the behaviour of shallow foundations under both monotonic and cyclic complex loading conditions.

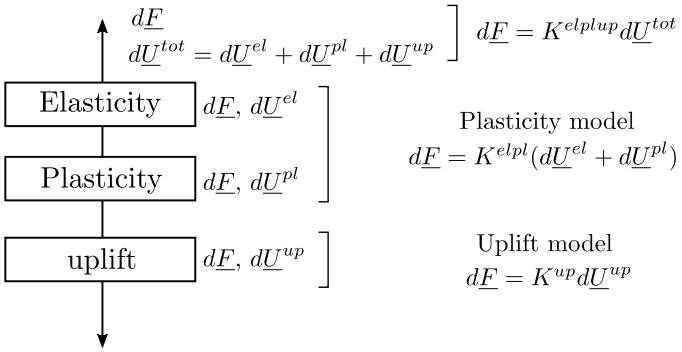

Fig. 3.5. Global macro-element model structure proposed by Cremer *et al.* (2001)

Kafle and Wuttke (2013) extended the application of macro-element models to predict the settlement of foundations on unsaturated soil. A series of displacement-controlled tests are conducted with three different soil conditions: dry, saturated and unsaturated with a suction of 2.1 kPa. In the proposed 2D macro-element formulation, a suction-dependent parameter is incorporated. The macro-element model employs a failure surface with a plastic potential inspired by the work of Wuttke *et al.* (2013). This proposed macro-element model demonstrates the capacity to simulate the accumulation of plastic settlement in foundations on multi-phase granular soil with varying suctions under cyclic loading.

In the study conducted by Khebizi *et al.* (2018), a novel macro-element is developed to provide a simplified modelling approach for soil-foundation systems, as depicted in Figure 3.6. This macro-element combines the concepts of the macro-element and the Winkler model, enabling it to simulate the load-displacement behaviour of the system while considering soil plasticity and interface non-linearity, including uplift. To validate the macro-element formulation, five previously published studies are utilised. The results obtained from the macro-element approach are compared with those obtained from other numerical modelling, under both monotonic and cyclic quasi-static loading conditions. The comparison reveals a favourable agreement, demonstrating that the macro-element approach effectively captures the non-linear behaviour of the soil-foundation system. However, it should be noted that the proposed model is limited to addressing 2D problems and may not be suitable for resolving 3D complexities.

The application of macro-element models is extended to address seismic problems as well. Under seismic conditions, particularly crucial is to consider the response of the foundation both to eccentric and inclined loads, associated with the inertial horizontal forces in the superstructure.

Cremer *et al.* (2002) extended the 2D macro-element model, originally developed for cyclic loading, to include seismic loading. The failure criterion, loading surface, hardening law, and plastic potential remain the same as in their previous work (Cremer *et al.*, 2001). To demonstrate the simplicity and efficiency of dynamic analysis using the macro-

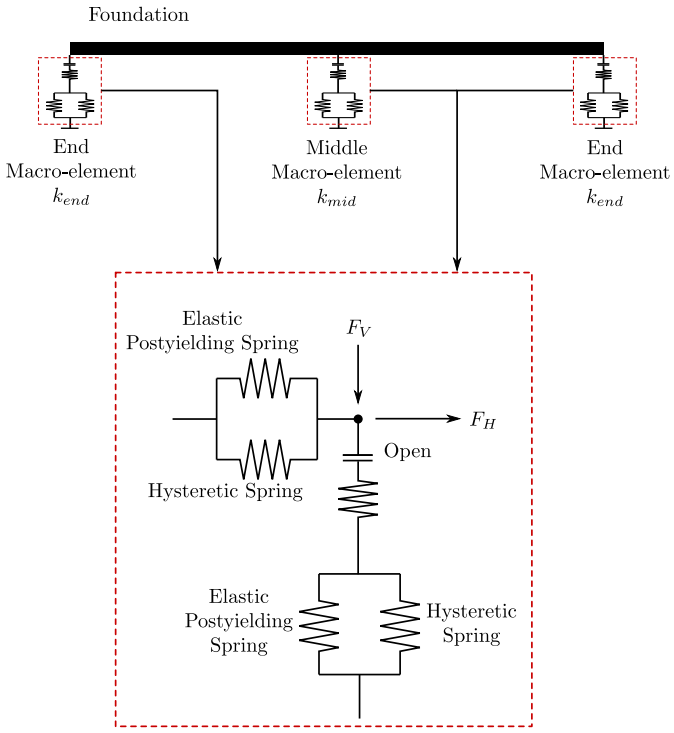

Fig. 3.6. Numerical model of the foundation with three macro-elements (Khebizi *et al.*, 2018)

element approach, as well as its capacity for extensive parameter studies, a bridge pier is selected as an application example. The application shows the effectiveness of the macro-element approach in handling dynamic analyses and its ability to perform comprehensive parameter studies.

In the doctoral dissertation of Chatzigogos (2007), a macro-element is developed to accurately simulate the behaviour of a circular foundation on cohesive soil, specifically considering its uplift behaviour under seismic loading. The bearing capacity of the circular foundation is studied using the kinematic approach of the yield design theory and validated through centrifuge tests. The macro-element consists of two main components: a linear behaviour part and a non-linear part. The linear behaviour of the foundation can be represented by dynamic impedances, which capture its response under dynamic loading conditions. The non-linear part comprises a hypoplastic soil behaviour (non-reversible) and a fully reversible uplift behaviour. The hypoplastic soil behaviour is described using a bounding surface model with an associated law, which can accurately represent the non-linear and irreversible response of the soil. The uplift behaviour is non-dissipative and is described using a non-linear elastic model. An engineering application demonstrates the practical use of the macro-element tool in the design phase of the structures, particularly when considering the nonlinear SSI.

The macro-element developed by Grange (2008) focuses on evaluating the seismic behaviour of shallow foundations, including rectangular, circular and strip foundations. It incorporated the consideration of soil plasticity and uplift behaviour within the framework

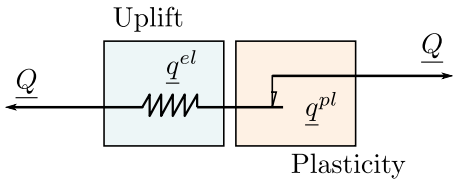

Fig. 3.7. Macro-element model structure proposed by Chatzigogos (2007)

of classical plasticity theory. The 3D SSI macro-element is described in detail, including the consideration of the plasticity and uplift, adaptation to a 3D model. The algorithm and process to resolve the non-linear numerical problem are also given. Good performance of the macro-element approach is verified by the comparison with experimental results of the foundation under monotonic loading, cyclic and dynamic loading.

Abboud (2017) developed a 3D macro-element specifically designed to analyse the behaviour of shallow foundations subjected to seismic loading. The formulation of the macro-element is based on the elasto-plastic approach using the classical plasticity theory. The macro-element incorporates three potential failure mechanisms that can occur in shallow foundations: sliding, loss of bearing capacity, and uplift behaviour. It also accounts for the effects of foundation embedding on elastic stiffness, bearing capacity, and sliding resistance. To consider the effects of loading velocity, appropriate hardening parameters are included in the macro-element formulation. The developed macro-element is implemented in the finite element software CESAR LCPC, and three different modelling strategies are proposed, as illustrated in Figure 3.8. These strategies provide alternative ways to represent the behaviour of the shallow foundation macro-element. The performance of the macro-element is assessed by subjecting it to different loading paths, and a comparison is made among the three modelling strategies. Furthermore, extensive parametric studies are conducted to define seismic damage indicators, allowing for a comprehensive analysis.

A 3D macro-element for shallow foundation was proposed by Shen (2019) to analyse non-linear SSI problems under dynamic and seismic actions. The macro-element is formulated within the framework of elasto-plasticity theory, considering a hardening law. The elastic behaviour of the foundation is described by the dynamic impedances of a shallow foundation, which can be derived from the empirical formulations or calculated dynamic impedance functions. The non-linear behaviour of the macro-element includes uplift, sliding, and loss of bearing capacity. The uplift of a shallow foundation is described using a non-linear elastic behaviour, while a Mohr-Coulomb sliding criterion is employed to simulate sliding behaviour. The formulations inspired by Eurocode 7 and 8 are chosen to simulate the loss of bearing capacity of shallow foundations. The macro-element also accounts for the effects of neighbouring buildings. Applications of this macro-element include studying a bridge pier and a seismic-isolated building to assess the advantages of this approach. The macro-element has already been successfully utilised in some industrial and nuclear structures to verify their global seismic bearing capacity.

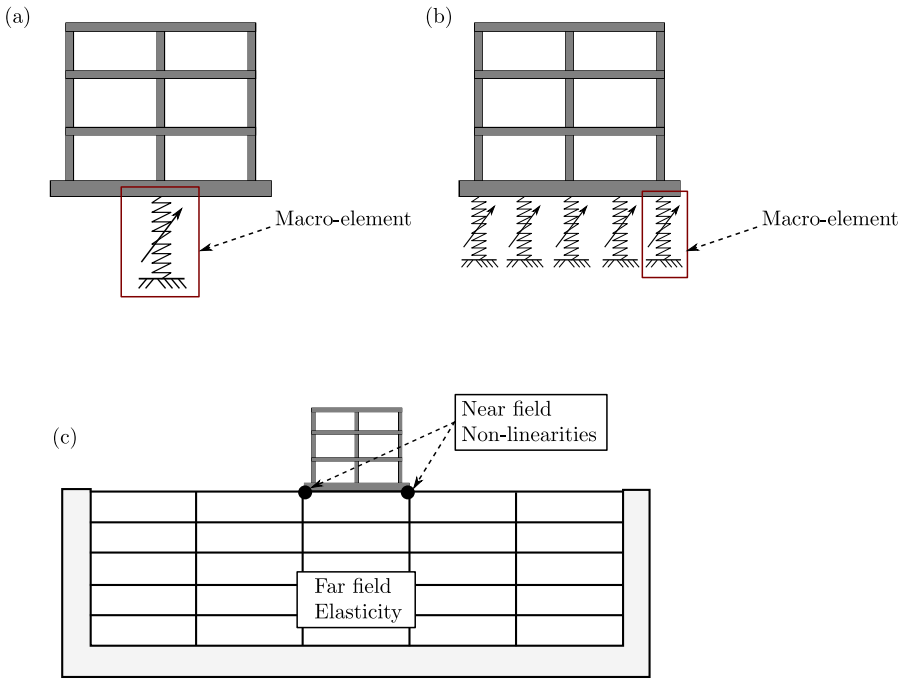

Fig. 3.8. Three modelling strategies with macro-element: (a) single macro-element model, (b) distributed macro-element model, and (c) hybrid macro-element model (Abboud, 2017)

A summary of the recent research on the dynamic SSI macro-element for shallow foundations can be found in Table 3.1.

Macro-element for pile foundations

The development of macro-element models for shallow foundations has indeed shown significant success and efficiency in engineering applications. However, the extension of this concept to pile foundations is a relatively recent advance. Similar to macro-element models for shallow foundations, the macro-element models for pile foundations typically incorporate both elastic and plastic responses within the framework of classical elasto-plastic theory or hypoplasticity theory. Macro-element models for pile foundations offer a simplified yet effective approach to analysing the dynamic or seismic behaviour of pile foundations.

Correia *et al.* (2012) introduced a 2D macro-element for single piles and applied it to analyse the seismic response of a single pile-supported bridge pier. The model consists of several components allowing to capture different aspects of pile behaviour: initial elastic impedances, the small-strain elastic response of the pile, and a gap evolution model to describe gaps that may develop between the pile and surrounding soil. Additionally, a failure mechanism is included to account for the large-strain behaviour of the surrounding soil.

Tab. 3.1. Summary of dynamic SSI macro-element for shallow foundations

Reference	Configuration	Sliding	Loss of bearing capacity	Uplift
Cremer *et al.* (2001)	Strip footing on cohesive soil	Not considered	Based on the work of Salençon and Pecker (1995b) (elasto-plasticity with hardening)	Based on FEM model (elasto-plasticity with hardening)
Grange (2008)	Circular or rectangular footing on cohesive soil	Not considered	Based on the work of Cremer *et al.* (2001) (elasto-plasticity with hardening)	Based on the work of Cremer *et al.* (2001) (elasto-plasticity with hardening)
Chatzigogos *et al.* (2009)	Circular footing on cohesive soil	Not considered	Simplified ellipsoid surface (hypo-plasticity)	Approximation relationship from numerical results (non-linear elasticity)
Abboud (2017)	Circular or rectangular footing	Coulomb friction (visco-plasticity with hardening)	Eurocode 7 (visco-plasticity with hardening)	Effective surface of foundation verification (visco-plasticity with hardening)
Shen (2019)	Circular or rectangular footing	Coulomb friction (elasto-plasticity)	Eurocode 7 and 8 (elasto-plasticity)	Reduction of stiffness on rotation proposed by Brûlé and Cuira (2018) (non-linear elasticity)

To smoothly translate between small-strain and large-strain behaviour, a bounding surface plasticity model is employed. The initial elastic impedances can be determined using analytical formulas. The behaviour of the gap is described by an elastic non-linear model using a tangent flexibility matrix that combines the initial elastic stiffness matrix with the variable stiffness matrix related to the gap depth. The failure surface and mechanism for the pile under lateral load are derived using a kinematic approach of the yield design theory. The shape of the failure surface follows a super-ellipse form. In this macro-element model for the laterally loaded pile, the axial behaviour is not studied. The proposed macro-element model is validated by comparing the results with those obtained from FEM simulations. Incremental dynamic analyses are also performed to assess the capacity of the macro-element to reproduce the response of the foundation at different loading intensity levels. The results demonstrate that the pile foundation macro-element provides stable and cost-efficient analysis capabilities.

Li (2014) proposed a 2D macro-element model based on hypo-plasticity framework for a single pile and pile group foundations in sand under seismic loading. The macro-element model considers a failure surface, which is described by analytical equations for both single-pile and two-pile group foundations. The mathematical formulation of the failure surface is calibrated using the results obtained from numerical swipe tests and radial displacement tests conducted within FEM analyses. An associated plastic flow rule is adopted in the constitutive behaviour of the macro-element, which is a commonly used approach in macro-element modelling. The loading surface is assumed to expand in

an isotropic manner as the stress path develops. The effect of pile group behaviour is incorporated by introducing a factor which represents the pile group effect. To validate the proposed macro-element model, experimental centrifuge results are employed. The comparison between the macro-element predictions and the experimental results serves as a validation of the macro-element model's accuracy and reliability.

Li *et al.* (2016) presented two calibration strategies for the pile macro-element model. The first strategy involves calibration based on 3D finite element simulations and experimental results, which is considered the ideal strategy but can be expensive. Alternatively, the authors proposed an empirical correlations calibration approach that is more cost-effective. The validation tests demonstrate that the macro-element calibrated using the simplified empirical procedures exhibits satisfactory performance. Furthermore, the study extends the applicability of the pile macro-element from homogeneous soil profiles to layered soil profiles. Building upon the previous work, Li *et al.* (2018) explored the behaviour of single batter piles in sand using the pile macro-element model. Various aspects of the behaviour, such as pull-out capacity, bearing capacity, lateral resistance, and rotational resistance, are studied using a 3D finite element model. The failure surface used in the macro-element model, as developed in Li *et al.* (2016), is modified to account for the inclination and loading directions associated with single batter piles.

In the study conducted by Pérez-Herreros (2020), the central focus is to develop a macro-element model specifically designed for analysing the behaviour of pile groups under various loading conditions. Dynamic centrifuge tests are conducted using a multilayered soil profile. The tests explore various configurations of pile groups subjected to seismic excitation. Additionally, the author also performed a numerical investigation using non-linear finite element analysis, and the results are compared with respect to the findings from the centrifuge experiments.

A three-level modular macro-element concept is proposed, as depicted in Figure 3.9. This concept aims to incorporate the static behaviour of individual piles, static group effects, and dynamic effects, including frequency effects and radiation damping. The formulation of the static single pile macro-element is based on the theory of hypo-plasticity, while the static interaction representing the group effects is simulated using analytical formulas. Additionally, a modified lumped parameter model is introduced in the macro-element to replicate the dynamic behaviour of the pile group. By comparing the results obtained from the macro-element model with those obtained from non-linear finite element analysis, the author demonstrated that the macro-element is capable of accurately capturing the response of the pile group under both static and seismic loading.

A summary of the recent research on the dynamic SSI macro-element for pile foundations can be found in Table 3.2.

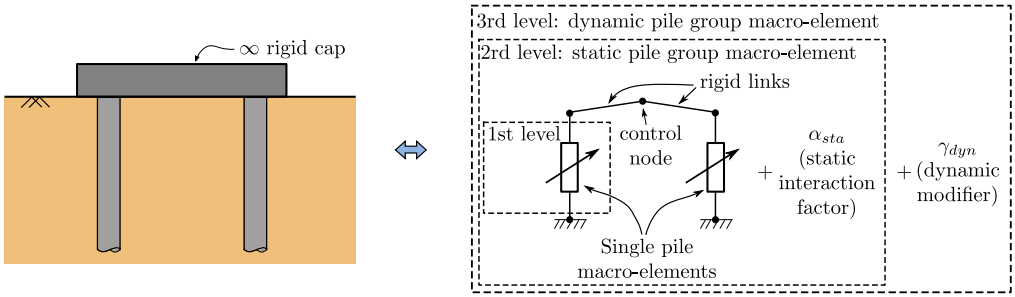

Fig. 3.9. Modular macro-element concept for a pile group (Pérez-Herreros, 2020)

Tab. 3.2. Summary of dynamic SSI macro-element for pile foundations

Reference	Configuration	Description
Correia *et al.* (2012)	Single pile	Composed of initial elastic impedances, small strain elastic response, gap evolution model and failure mechanism of surrounding soil
Li (2014) and Li *et al.* (2016, 2018)	Vertical and inclined Single pile and two-pile group	Failure surface obtained by numerical swipe test, adaptation for layered soil profiles and pile inclination
Pérez-Herreros (2020)	Vertical single pile and pile group	Proposition of three-level modular macro-element concept incorporating the static behaviour of individual piles, static group effects, and dynamic effects

Macro-element for foundation reinforced by rigid inclusions

The Rio-Antirrio bridge, already presented in Section 1.1.3, is the earliest application where the macro-element concept is used for foundations reinforced by rigid inclusions under seismic load.

In this application, the Performance Based Design criteria are employed to provide a more realistic approach that reflects the physics of the non-linear interactions, including geometrical and material non-linearities. Regarding this concept, a macro-element approach based on a rheological model combining a finite number of springs and Coulomb sliders is used in the calculation, as depicted in Figure 3.10.

The parameters of the model are derived from the static finite element analysis results. The macro-element model is validated by the results from the centrifuge tests, presented in Section 2.3, and from cyclic finite element analyses (Pecker, 2004).

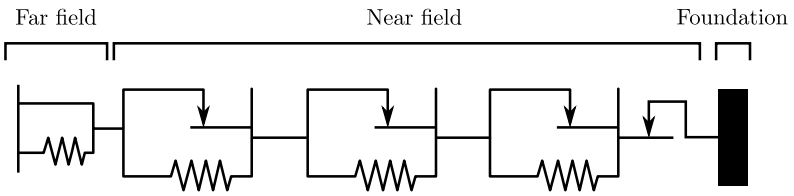

Fig. 3.10. Rheological model for soil-foundation system (Pecker, 2004)

3.3 Focused analysis approach for soil reinforcement

In the previous section, strategies for investigating the global dynamic behaviour of the structure-foundation-soil system were explored. However, it is equally important to introduce some analysis approach focusing on the behaviour of the reinforced system. These approaches include the homogenisation method, yield design theory, and more.

The yield design theory, which has been previously employed to address the bearing capacity problem of foundations, has the potential to analyse the bearing capacity of foundations when rigid inclusions are present. Drawing inspiration from pile foundation analysis, a Winkler-type model can also simulate the behaviour of rigid inclusions. The homogenisation method enables the study of the overall behaviour of reinforced soil, providing valuable insights into its stiffness and strength characteristics. A practical engineering approach, based on the same homogenisation concept, employs a fictive monolith and is commonly used in design offices due to its simplicity.

Each of these approaches offers a unique perspective on the behaviour of reinforced foundations at different scales, as shown in Table 3.3. In practice, it can be chosen based on the specific objectives of the analysis.

Tab. 3.3. Focused analysis approaches with different research scale

Scale	Approach	Research target
Global system	Yield design theory	Limit resistance of foundations and no displacement information
Foundation element	Winkler-type model, simplified approaches with fictive monolith	Displacement and force of rigid inclusion elements
Continuous medium	Multi-phase model	Strain and stress of homogenised reinforced soil

3.3.1 Yield design theory

The yield design theory, known as *théorie de calcul à la rupture* in French, was introduced by Salençon (1983). This theory was developed within the framework of the original "equilibrium/resistance" approach (Salençon, 2013). It provides a comprehensive methodology for designing structures based on the concept of ultimate limit state design. In more recent times, this concept has been adopted by several construction codes, including Eurocodes.

The yield design theory enables a direct investigation of limit loads in a more intuitive manner by starting with their initial characterisation. The limit loads are independent of the initial state of self-stress, elastic characteristics of the material and the loading path (Salençon, 2002). This theory relies exclusively on three system information, namely geometrical data, the loading mode of the system, and the resistance of the constituent material. However, to definitively determine the system's stability, additional knowledge regarding other aspects of the system is necessary, such as the constitutive law and loading history (Salençon, 1983).

The general theory was initially developed for the 3D continuum model and subsequently extended to both the 1D and 2D continuum models to address various problems. This theory offers a systematic approach to assess the resistance of the structures and foundations while considering the effects of seismic forces. The yield design theory solves dynamic problems as pseudo-static problems. The soil inertia can be considered as a pseudo-static body force. However, the wave propagation and frequency effect cannot be modelled in this approach.

This theory has been successfully applied to study the seismic stability of nailed soil (Schlosser and Unterreiner, 1990; de Buhan *et al.*, 1992; de Buhan, 2004) and foundations reinforced by rigid inclusions (Pecker *et al.*, 1998; Salencon and Pecker, 1999; Pecker, 2023b).

Potentially safe load domain

In the yield design theory, the potentially safe load domain denoted K, is an important notion. This domain refers to all the loads that are considered potentially safe for the structure. The term "potentially" signifies that there is no guarantee that the extreme load determined by the yield design theory has been reached (de Buhan, 2007).

Knowing only the strength criteria of a material does not guarantee the stability of a structure under a given load. However, if the linear elastic and perfectly plastic behaviour with an associated plastic flow rule is assumed, it is possible to establish the existence and uniqueness of a solution for quasi-static elasto-plastic problems (Chatzigogos, 2007). This implies that the domain K encompasses all the loads that the structure is capable of

effectively supporting. Any loads that fall outside the domain K will not be supported by the system.

Static interior approach and kinematic exterior approach

The static interior approach aims to establish an approximate boundary for the potentially safe load domain K by inside, as depicted in Figure 3.11 (a). This approach involves constructing a stress field, represented by $\underline{\underline{\sigma}}$, that is in equilibrium with the external loads Q while ensuring that it does not exceed the resistance of the material at any point within the system. However, the challenge arises when attempting to construct stress fields that satisfy the resistance condition, which implements the interior approach complex (Salençon *et al.*, 2009). The analytical or semi-analytical implementation of the static interior approach can be quite challenging, particularly when dealing with highly heterogeneous configurations such as reinforced soils. It is often necessary to employ numerical methods, such as the finite element method, in conjunction with convex optimisation procedures, as indicated by de Buhan (2023).

The kinematic exterior approach provides an alternative approach to approximate the domain K. It is important to note that the exterior approach approximates the boundary of the domain K "from the outside", as depicted in Figure 3.11 (b). This approximation is obtained through the mathematical dualisation of the equilibrium-resistance compatibility condition. The external approach is based on the principle of virtual powers. The maximum resisting power P_{rm} can be determined for a given virtual velocity field with knowledge of the strength of the materials. If the external virtual power P_e of the external loads with the given virtual field exceeds the maximum resisting power P_{rm}, it indicates that the system cannot withstand the assumed external load. An approximation of the domain K can be obtained by testing several virtual velocity fields. The kinematic exterior approach can be easily implemented, either analytically using conventional failure surfaces, or numerically through a finite element discretisation of the explored velocity fields (de Buhan, 2023).

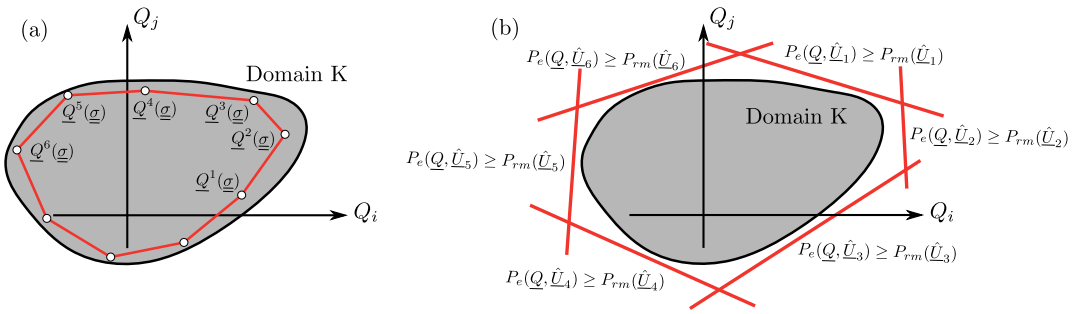

Fig. 3.11. Yield design approach: (a) static interior approach and (b) kinematic exterior approach

3.3.2 Winkler-type model

Winkler-type models offer a practical approach for analysing SSI, particularly in cases involving rigid inclusion soil improvement. These models adopt a "Beams on Nonlinear Winkler Foundation" representation of the foundation, where the interactions between the inclusion and the soil are captured using a series of linear or non-linear soil springs, as depicted in Figure 3.12. The simplicity of Winkler-type models makes them widely utilised in geotechnical engineering.

Within the soil-inclusion systems, Winkler-type approaches utilise the springs with p-y laws to represent lateral soil-pile interaction. They also incorporate springs with t-z laws and q-z laws to characterise vertical soil-inclusion shaft and end-bearing interactions, respectively. Additionally, advanced rheological laws can be incorporated into the springs in certain cases (Nogami and Kongai, 1988). An important advantage of Winkler-type models is their versatility, as they can be applied to both static and dynamic analyses.

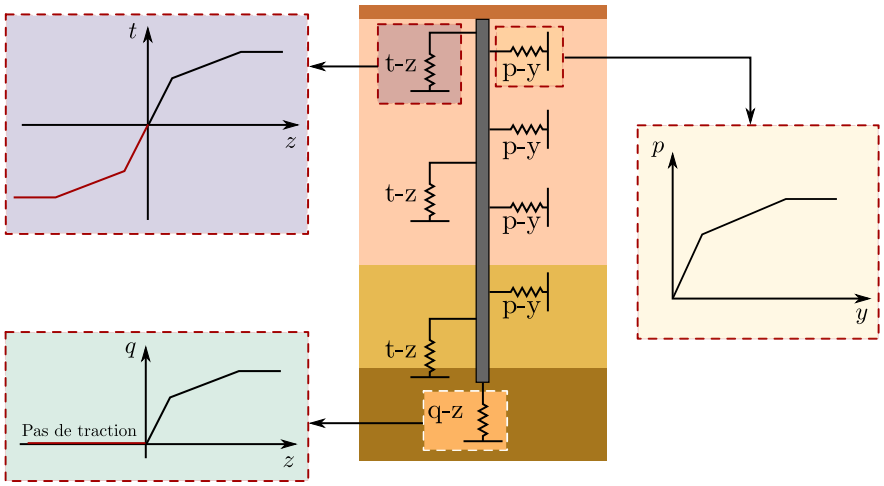

Fig. 3.12. Winkler-type model accounting for the axial and transverse interaction between the soil and the rigid inclusion

It is essential to acknowledge that Winkler-type models, which represent individual inclusions using beam segments and springs, do not inherently consider group effects. To overcome this limitation, a group effect factor can be introduced in static and dynamic analyses to account for the collective behaviour of the inclusion group.

3.3.3 Simplified approaches with fictive monolith

The ASIRI (2012) recommendations present various simplified approaches for the design of foundations on reinforced soil by rigid inclusions. The selected approaches enable engineers to evaluate force distribution between the soil and the inclusions, as well as assess settlement, and horizontal displacement in inclusion design. The MV3 model is

employed when considering purely vertical loading of the footing, while the MH3 model is used for purely horizontal loading. These models were initially introduced by Simon (2010) and have proven to be valuable design tools.

The proposed methodology comprises five sequential steps with a focus on achieving equilibrium either for the reinforced soil cylinder, known as the "monolith", with the same perimeter as the foundation, or for a single inclusion subjected to the same prescribed vertical or lateral displacement field, as depicted in Figure 3.13.

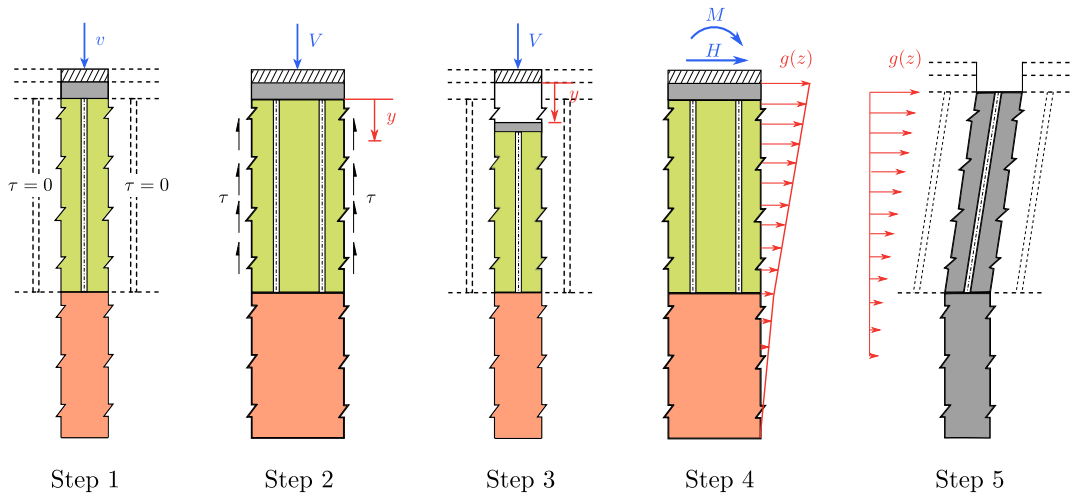

Fig. 3.13. Monolith approach MV3 and MH3 (Simon, 2010) with step 1: determination of equivalent modulus of the monolith with an elementary model, step 2: determination of vertical displacement in the monolith, step 3: application of the vertical displacement to the elementary model, step 4: application of horizontal and moment to the monolith, and step 5: application of the horizontal displacement to the elementary model

In the first step, the equivalent modulus of the monolith is determined by analysing an elementary cell under vertical loading conditions. The second step involves studying the equivalent monolith with exterior soil-soil friction as a fictive pile. This analysis aims to determine the vertical displacement field within the monolith. Moving to the third step, the vertical displacement field obtained from the previous analysis is applied to the single inclusion model. This step enables the assessment of the vertical response, including settlement and force distribution.

Continuing with the analysis of the horizontal response, the fourth and fifth steps are employed. In the fourth step, a horizontal load is applied to the monolith, treating it as a single pile. This load induces a horizontal displacement profile within the monolith. Finally, in the fifth step, the obtained displacement profile is applied to the single inclusion model. This step allows for the assessment of the horizontal response, including the horizontal displacement and the interior forces within the inclusion.

These steps can be addressed using various numerical modelling, including the typical Winkler-type model or other numerical techniques such as the finite element method. The

more details can be found in the work of Simon (2010), Cuira and Simon (2013), and Alzate *et al.* (2022).

3.3.4 Multi-phase model

The theory of the multi-phase model is based on the homogenisation approach (de Buhan, 2005). This approach entails viewing the composite reinforced soil as a homogeneous medium with anisotropy resulting from the orientation of the implemented inclusions. The multi-phase model characterised the global behaviour of inclusion-reinforced soil at a macroscopic scale as the homogenisation approach. Different from the homogenisation approach, it achieves this by separately homogenising the soil and the inclusions. The model combines multiple media, referred to as "phase", each representing either the soil or a family of inclusions in a specific direction. The interaction between different phases is established through the interaction efforts (Hassen, 2006). The multi-phase model offers the advantage of the homogenisation approach in terms of computational efficiency while explicitly considering the effects of shear and flexion stiffness of inclusions, addressing the limitation of the homogenisation approach.

A soil reinforced with a single family of vertical inclusions can be characterised using a two-phase model based on the concept of the multi-phase model. This model involves two distinct phases: the "matrix phase" representing the soil and the "reinforcement phase" representing the inclusions. In the reinforcement phase, the beam-type characteristics are described using three degrees of freedom for translation ξ^r and an additional three degrees of freedom for rotations ω^r, forming a micropolar continuum (de Buhan *et al.*, 1998). These distinctions are illustrated in Figure 3.14. The interaction forces between the two phases are determined by the constitutive relation between the interaction stiffness and the difference in deformation between the two phases. When the interaction is not considered, this term is zero.

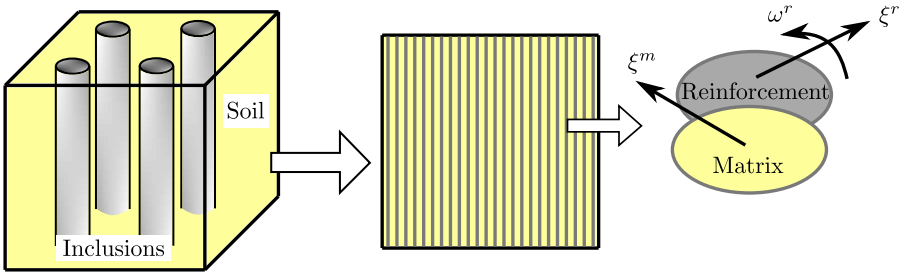

Fig. 3.14. A two-phase model for a soil reinforced by vertical inclusions (Hassen, 2006)

The multi-phase model has been utilised in various studies (de Buhan, 2005; Hassen, 2006; Son, 2009; Guéguin, 2014) to address different reinforced soil problems.

The homogenisation method was employed by Guéguin (2014) to assess the overall behaviour of reinforced soil structures, considering both stiffness properties and strength

properties. The study introduces upper-bound and lower-bound expressions to evaluate the longitudinal shear modulus of soil reinforced with circular cylindrical inclusions, as described in Equations 3.1 and 3.2. Additionally, the research evaluates the reinforcement effect for different modules, as depicted in Figure 3.15.

$$G_V^{upper} = G_s\left(1 + \frac{2\eta(G_r - G_s)}{G_r + G_s - (4\eta/\pi)(G_r - G_s)}\right) \tag{3.1}$$

$$G_V^{lower} = G_s\left(1 - \frac{2\eta(G_r - G_s)}{G_r + G_s + (4\eta/\pi)(G_r - G_s)}\right)^{-1} \tag{3.2}$$

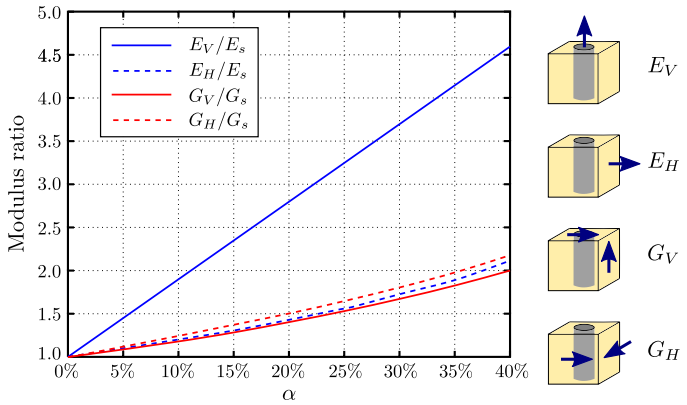

Fig. 3.15. Modulus ratios for column reinforcement (Guéguin, 2014)

Nguyen (2015) made significant progress by extending the multi-phase model to tackle the dynamic problems. The model successfully represents the reinforced soil masses under the assumption of elastic linearity, considering multiple phases to account for the presence of inclusion reinforcement. The extended model incorporates the longitudinal interaction between the soil and inclusions, as well as the bending and shear effects of the inclusions. It is demonstrated that the multi-phase model simplifies numerical implementation, substantially reduces computation time, and minimises computer memory usage compared to the direct approach. The model's accuracy and reliability are confirmed through comparisons with extensive parametric studies conducted with the hybrid finite element-boundary element analysis.

Nevertheless, in common practice, homogenisation and multi-phase models are not frequently employed.

3.4 Computer-based numerical technique

Various numerical resolution methods are available, each tailored and sometimes specialised for addressing diverse challenges such as pseudo-static response, transient response, stability domain calculation, and more. The choice of modelling technique

depends on the specific problem at hand, with certain methods being more advantageous for particular conditions. Gaining a clear understanding of these distinctions is essential for selecting the most suitable method to achieve the intended objectives. This section aims to briefly explain the different numerical techniques.

3.4.1 Finite element and finite difference analysis

The advancements in computing power and commercial calculation software have greatly facilitated the use of sophisticated numerical analyses in engineering, including geotechnical engineering problems. The finite element method or the finite difference method is widely employed in geotechnical engineering analysis software packages such as PLAXIS (Bentley, 2022b), ABAQUS (Dassault Systemes, 2023), and FLAC (Itasca Consulting Group, 2023), which are based on these numerical techniques.

The utilisation of these numerical methods enables comprehensive modelling within the direct approach framework. The main benefit of employing these numerical methods lies in their capacity to depict the complex behaviour of soils and structural elements under different loading conditions. Through these numerical techniques, the response of both structures and soils can be simulated more realistically by solving a system of equations derived from the discrete domain.

Nevertheless, it is important to note that employing these numerical methods presents certain challenges, as discussed in Section 3.2.1. One notable challenge is the computational cost involved in conducting these analyses. Performing large-scale numerical modelling necessitates significant computational resources and time. Additionally, the accuracy and appropriateness of input data, material models, and boundary conditions are critical factors in the reliability of the numerical models. In some particular modelling, the mesh quality can also play an important role. Careful post-treatment and validation of the numerical results are always indispensable.

3.4.2 Finite element limit analysis

Finite Element Limit Analysis (FELA) is a modelling technique that has garnered increasing attention in recent years (Sloan, 2013). This technique has the potential to overcome many of the shortcomings of both the finite element method and limit analysis approaches. FELA enables rapid computation of rigorous upper and lower bound plasticity solutions, significantly faster than traditional finite element modelling techniques.

Different from the traditional limit analysis, which involves determining a statically admissible stress field and a kinematically admissible velocity field, FELA offers a numerical alternative approach for obtaining lower and upper bound limit solutions without the

need to define the form of the stress and velocity fields. One of the advantages of FELA is its ability and flexibility to handle complex systems with non-homogeneous soil conditions and complex geometry, as it does not require any prior assumptions. However, FELA, as a pseudo-static analysis, considers the problem within the context of pseudo-static loading, neglecting wave propagation in the model.

To further enhance the accuracy and efficiency of the FELA solution and minimise numerical errors and computational costs, an adaptive mesh refinement (AMR) technique can be used to dynamically adjust the mesh by increasing the number of elements in regions that require more precision and reducing the mesh density in not essential areas.

The software OPTUM G2 (Optum Computational Engineering, 2021) is a robust and powerful tool designed for solving 2D static or pseudo-static geotechnical stability problems using the FELA approach.

A wide range of available soil constitutive laws have been implemented in the software which allows for the modelling of beam elements, pile elements, and interface elements. OPTUM G2 incorporates the AMR technique to improve the solution quality and accuracy.

3.4.3 Hybrid finite element method - boundary integral equation analysis

In cases where the problem lies within the elastic or equivalent elastic domain (shear deformation smaller than 0.1 %), the superposition theorem can be applied by dividing the problem into a series of simpler sub-problems. Each sub-problem can be solved independently, and their results are combined in the final step of the analysis to obtain the complete solution.

The sub-structuring approach addressing to dynamic SSI problem can be classified into four categories based on how the interaction at the soil-structure interface is treated. These categories include rigid boundary, flexible boundary, flexible volume method and substructure subtraction method (Ostadan and Deng, 2011), as depicted in Figure 3.16.

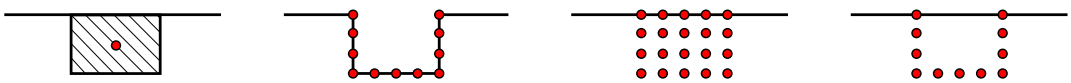

(a) Rigid boundary (b) Flexible boundary (c) Flexible volume (d) Subtraction

Fig. 3.16. Different sub-structuring methods

In the flexible volume method, it is assumed that the free-field site and the excavated soil volume interact both at the boundary of the excavated soil volume as well as within its

volume (Lysmer *et al.*, 1981). One example of calculation software using this resolution technique is SASSI (System for Analysis of Soil-Structure Interaction). SASSI utilises the flexible volume method of the sub-structuring approach to address a wide range of 2D and 3D dynamic SSI problems. This method allows for an accurate treatment of wave propagation in the soil and accounts for the dynamic interaction between structural elements and soil.

In a typical model based on the sub-structuring method in SASSI, the total soil-structure system is partitioned into three sub-structures, as illustrated in Figure 3.17.

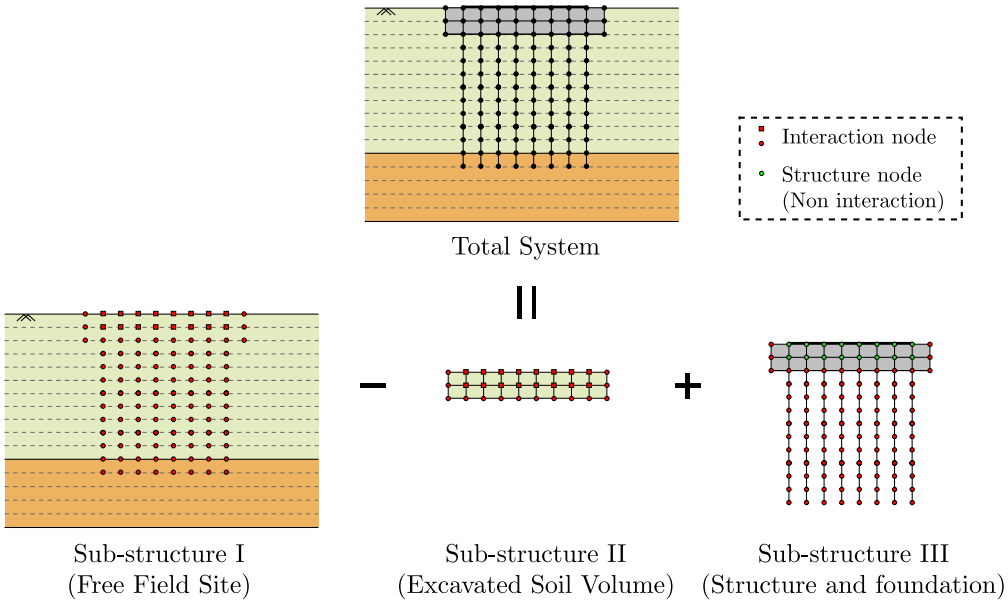

Fig. 3.17. Sub-structuring in the flexible volume method

The first sub-structure, known as the free field site, consists of semi-infinite visco-elastic horizontal layers on semi-infinite visco-elastic half-space, where Green's function is employed to calculate an impedance matrix for the degrees-of-freedoms at the so-called interaction nodes (Lysmer *et al.*, 1981). The second and third sub-structures are modelled using the finite elements method. Consequently, the SASSI calculation program is regarded as a hybrid model, combining both the boundary integral equation (BIE) and finite element methods (FEM).

3.5 Summary

This chapter provides a summary of the numerical approaches.

An introduction of the general modelling strategies for dynamic SSI analyses has been presented, covering the direct approach, substructuring approach and hybrid macro-element model, along with their respective applications. The advantages and disadvantages of each

approach are discussed, highlighting the benefits of the macro-element models, which combine the advantages of both approaches and demonstrate promising engineering potential. A detailed bibliography focusing on the macro-element is provided. With this overview of its applications, it is worth noting that the practical engineering application of the macro-element approach is still limited. Its utilisation is primarily concerned with academic examples with few specific engineering cases.

Additionally, the chapter presented typical numerical approaches that have already been applied to investigate dynamic SSI problems in the context of rigid inclusion-reinforced foundation. The Winkler-type model, due to its simplicity, is also widely applied in engineering. The yield design theory can be considered as a good tool and already solved several problems. These promising approaches have shown great potential in their application. However, some improvement or validation is still needed to adapt them to treat the dynamic problem. The numerical techniques employed for numerical modelling are also described.

It is important to emphasise that while numerical modelling is a powerful and useful tool, careful post-treatment is always necessary to accurately interpret the numerical results.

Conclusion

This part of the dissertation delved into the dynamic behaviour of inclusion-reinforced soil in geotechnical engineering, with a specific focus on seismic loading conditions.

The literature review in this part began by introducing the concept of the rigid inclusion-reinforced foundations. The main interaction mechanisms of foundations on rigid inclusions were presented representing the advantages of this improvement technique. The disconnection between the inclusion and the foundation can mitigate the stress concentration at the heads. The presence of the gravel LTP contributes to dissipating the energy with controlled mechanisms in LTP. Furthermore, the notions related to dynamic SSI are presented and particularly analysed in the context of rigid inclusion-reinforced foundation.

The comprehensive presentation of experimental research conducted in this part shed light on the dynamic SSI behaviour of inclusion reinforced soil, considering both with and without the presence of a superstructure. The observation obtained in the experimental research confirmed the supposed interaction mechanisms in the inclusion-reinforced foundation. Some other factors which may play a role in such foundation were also investigated, such as the thickness of the LTP, the gravel grade of the LTP and so on. This review of existing studies revealed a scarcity of research on the dynamic response of foundations supported by rigid inclusion-reinforced soil. Consequently, further investigation is deemed essential to enhance our understanding of the key phenomena influencing the linear and non-linear dynamic response of such a system.

Moreover, the literature review on the numerical modelling methodology and theory was also discussed. The general SSI modelling strategies can be employed, with a particular emphasis on the SSI macro-element approach. Macro-element modelling was proven to be an effective tool for analysing dynamic SSI problems. Some typical theories and modelling approach which are assigned specially to study the inclusion-reinforced soil have shown their potential. However, exploration is still needed to make the typical modelling more adaptive to solve the dynamic SSI problem for inclusion reinforcement.

In this part, the existing numerical and experimental research has already provided valuable insights, primarily within the research domain. However, transitioning towards research focused that emphasises engineering application is essential to bridge the gap and facilitate practical utilisation. Additionally, there is a need for more systematic studies on the kinematic and inertial interaction effects of such foundations, as addressed in the next part of this dissertation.

Part II

Linear elastic SSI study

Introduction

In the case where inclusions play a vital role in ensuring the stability and bearing capacity of the structure, it becomes imperative to ensure that this is no compromise in the functionality of inclusions during an earthquake event. It is commonly recommended that these inclusions and the surrounding soil should maintain their behaviour within the elastic domain. Consequently, it is essential to study the linear elastic behaviour of the rigid inclusion-reinforced foundation. Moreover, under the assumption of the linear elastic behaviour, Kausel's decomposition (Kausel *et al.*, 1978) can be applied. This approach enables the separate investigation of the kinematic et inertial interaction effects.

As highlighted in Chapter 1, the influence of kinematic interaction leads to modifications in ground motion owing to the contrast in rigidity between the foundation elements and the soil. This modification also encompasses soil deformation caused by wave propagation, resulting in additional stresses.

The inertial interaction is characterised by dynamic impedance functions that fluctuate based on the frequency of excitation. The inertial force stemming from the mass of the superstructure is imposed upon the foundation system, giving rise to supplementary forces acting on the foundation elements.

Therefore, this part of the dissertation focuses on investigating the dynamic SSI behaviour of the soil and foundation reinforced with inclusions within the linear elastic domain. It primarily addresses four key questions:

- How does the presence of foundation elements, including rigid inclusions and LTP, modify ground motion?
- How do the dynamic impedance functions change with frequency?
- What are the inertial forces that arise within rigid inclusions?
- What are the kinematic forces induced in rigid inclusions by wave propagation?

The first two phenomena are attributed to the kinematic interaction effect, while the last two subjects are associated with the inertial interaction effect.

Chapter 4 aims to investigate the ground motion modification attributed to kinematic interaction effects. The study first focuses on the ground motion modification of shallow foundations, pile foundations, and foundations reinforced by rigid inclusions subjected to harmonic loading. Furthermore, various configurations of foundations reinforced by

rigid inclusions are examined to establish a comprehensive rule regarding ground motion modifications induced by foundation elements. Multiple seismic excitations, consistent with regulatory spectra, are also utilised to validate the responses of distinct foundation systems.

Advancing in the exploration, Chapter 5 redirects its focal point towards dynamic impedances - an essential determinant influencing the dynamic behaviour of SSI within the system. A comprehensive comparative study ensues, aiming to illuminate both the similarities and differences inherent in diverse foundation systems, including shallow foundations, pile foundations, and inclusion-reinforced foundations. The comparison is also conducted between the different configurations of foundation on inclusion reinforced soil.

Within Chapter 6, the scope of investigation broadens to encompass inertial forces within the inclusions. A series of linear pseudo-static numerical models, inspired by real projects and employing a direct modelling approach, is undertaken. These models are employed to thoroughly explore the inertial interaction effects of foundations on rigid inclusions. In addition, design charts are included to enhance comprehension of these effects, facilitating their integration into the preliminary design phase of projects.

Chapter 7 delves comprehensively into analysing kinematic forces generated by wave propagation. Seismic excitation is applied to the foundation reinforced by rigid inclusions, and the resultant bending moment within these inclusions is assessed. The study encompasses diverse soil profiles to study the influence of soil variations on bending moment. Within this analysis, the bending moment profile derived from the pseudo-static approach is compared against the outcome of the dynamic analysis approach with complete modelling. The comparison is executed to validate the practicality of the pseudo-static approach. Furthermore, the group effect is explored by comparing the bending moment profiles of differently positioned inclusions.

4 Ground motion modification by rigid inclusion reinforcement

4.1 Ground motion modified by foundation elements

The presence of foundation elements introduces a rigidity contrast in the soil and modifies the wave propagation. Consequently, the signals reaching the base of the superstructure differ from those in cases where no foundation elements are present. This phenomenon, resulting from the kinematic interaction effect, has been extensively explored for both shallow and pile foundations (Gazetas, 1984; Kaynia and Novak, 1992; Gazetas *et al.*, 1993; de Sanctis *et al.*, 2015).

To quantitatively assess this modification in ground motion, Gazetas (1984) employed a displacement kinematic interaction factor for pile foundations under upward SH-waves. Building upon this foundational concept, a comparable displacement kinematic interaction factor I_u can be introduced to quantify this modification.

$$I_u = \frac{u_F}{u_0} \tag{4.1}$$

where u_F represents the horizontal displacement at the ground surface of a foundation, while u_0 signifies the free field surface displacement, as illustrated in Figure 4.1.

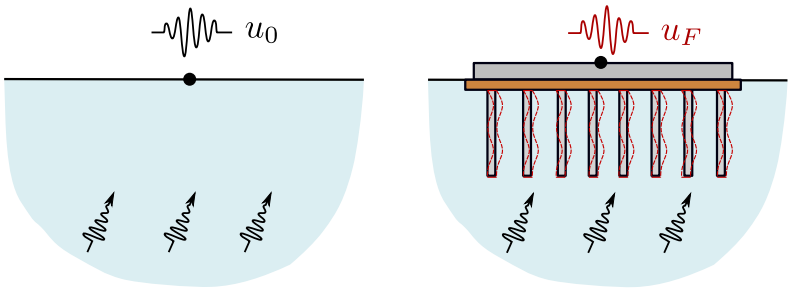

Fig. 4.1. Ground motion for a free field and for a foundation reinforced by rigid inclusions

Ground motion modification does not occur in the case of a shallow foundation without embedment under upward SH-wave excitation. Consequently, for a non-embedded shallow foundation, the displacement kinematic interaction factor retains a value of unity. Conversely, in the case of a pile foundation, the alteration of ground motion due to the kinematic effect exhibits a substantial reliance on parameters such as the frequency of

excitation, the stiffness ratio between the soil and pile, the slenderness of the pile, and other parameters.

Drawing inspiration from these prior investigations conducted on pile foundations, this chapter delves into the study of ground motion modification under upward SH-waves within the specific context of foundations reinforced by rigid inclusions. The parametric study in this chapter is conducted as follows:

- Comparative analysis under harmonic excitation for various foundation types.
- Investigation of the impact of different characteristics in reinforced foundations.
- Comparative study under seismic excitation for various foundation types.

4.2 Response of different foundation systems under harmonic excitation

4.2.1 Studied configurations

The reference configuration used in this study is illustrated in Figure 4.2. It encompasses a 10 m × 10 m rigid shallow foundation positioned on a 0.5 m-thick LTP, extending beyond the edges of the shallow foundation by 0.5 m. Detailed soil profile parameters are presented in Table 4.1.

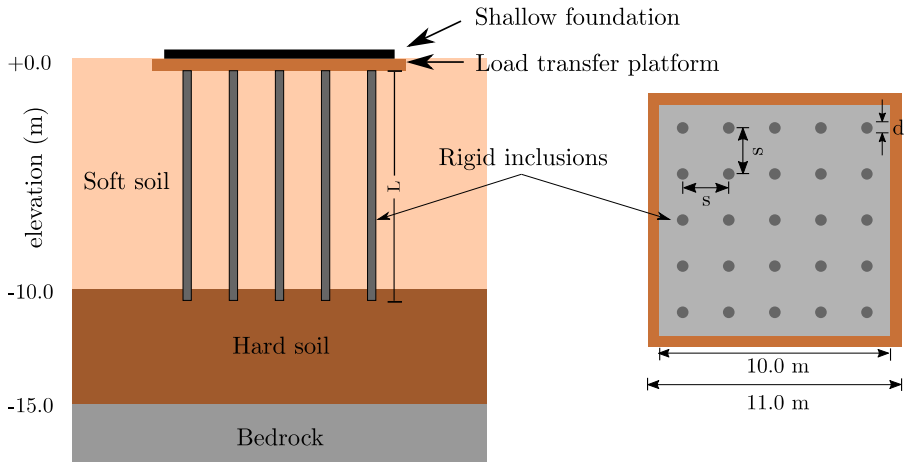

Fig. 4.2. Reference configuration of rigid inclusion-reinforced foundation used in the study of ground motion modification

The rigid inclusions, with a length of 10 m, are embedded 0.5 m into the hard soil layer. In the reference configuration, the inclusions have a diameter of 0.42 m, a dimension commonly used in France. A centre-to-centre spacing of 2 m is applied.

Tab. 4.1. Mechanical properties of soil and foundation

	Soft soil	Hard soil	Bedrock	LTP	Rigid inclusions
Shear modulus G (MPa)	45	320	2 500	125	12 500
Young's modulus E (MPa)	130.5	928	7 250	362.5	30 000
Shear wave velocity V_s (m/s)	150	400	1 000	250	2 236
Poisson's ratio ν (-)	0.45	0.45	0.45	0.35	0.2
Mass density ρ (t/m^3)	2.0	2.0	2.5	2.0	2.5
Material damping ratio ξ (-)	0.05	0.05	0.05	0.05	0

In the context of a pile foundation, the concept of transfer length l_0 is significant for quantifying the relative stiffness between the pile and the soil. If the total length of a pile exceeds three times the transfer length l_0, it can be considered flexible in terms of its transverse response. Given the characteristics of rigid inclusions, their transfer lengths can be estimated using Equation 4.2. It is worth noting that in the studied configurations, all these rigid inclusions are considered flexible in terms of their transverse response.

$$l_0 = \sqrt[4]{\frac{4E_pI_p}{E_s}} \tag{4.2}$$

where E_p represents the Young's modulus of pile, I_p signifies the quadratic moment of section area of rigid inclusions, and E_s stands for the linear lateral reaction modulus. The value of E_s under seismic loading can be approximated using the soil shear modulus, as described by Equation 4.3 proposed by Gazetas *et al.* (1993).

$$E_s = 2.4(1+\nu)G \tag{4.3}$$

This section presents a comparison of ground modification across various foundation systems. The assessed foundation configurations are depicted in Figure 4.3. The primary characteristics of these configurations are outlined in Table 4.2.

Tab. 4.2. Main characteristics of studied configurations

Case	Number of inclusions (-)	Length of inclusions (m)	Spacing (m)	Diameter of inclusions (m)
(a) Free field	-	-	-	-
(b) Shallow foundation	-	-	-	-
(c) Shallow foundation with LTP	-	-	-	-
(d) Pile foundation	25	10	2	0.42
(e) Pile foundation with LTP	25	10	2	0.42
(f) Foundation on rigid inclusions	25	10	2	0.42

*piles in case of pile foundation and rigid inclusions in case of inclusion-reinforced foundation

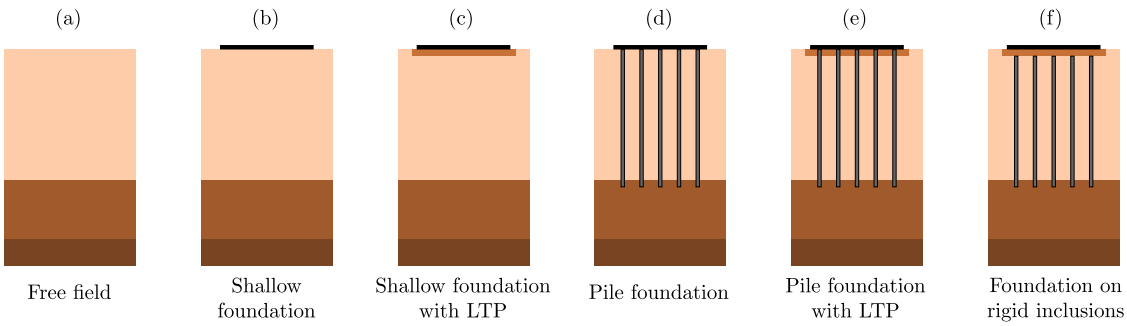

Fig. 4.3. Layout of different foundation systems

4.2.2 Model description

As previously mentioned, the objective of this chapter is to investigate the alteration of ground motion resulting from the kinematic interaction effect. The investigation employs a hybrid BIE - FEM model, which is constructed within the framework of SASSI2010 program (Ostadan and Deng, 2011). This hybrid approach, presented in Section 3.4.3, provides a comprehensive approach to address the problem in the frequency domain. It facilitates the accurate consideration of wave propagation within the soil and appropriately accounts for the dynamic interaction between inclusions and soil.

A visualisation of the numerical modelling for a foundation reinforced with rigid inclusions is presented in Figure 4.4(a). The illustration highlights the foundation, the rigid inclusions, and the granular LTP. In this model, the soil is represented by horizontal layers with visco-elastic behaviour atop a half-space, simulated through interaction nodes, as depicted in Figure 4.4(b).

The foundation is simulated by a weightless three-dimensional rigid beam grid, as exemplified in Figure 4.4(c). The explicit modelling of the LTP is demonstrated in Figure 4.4(d). Inclusions are modelled using beam elements, disconnected from the shallow foundation, as illustrated in Figure 4.4(e). Utilising beam elements for modelling rigid inclusions can significantly increase calculation efficiency without compromising the results. Mánica Malcom *et al.* (2016) have demonstrated that the beam element can reproduce the same axial and bending stiffness and can adequately interact with the surrounding soil.

The LTP is explicitly represented through 8-node hexahedral volume elements. To ensure accurate propagation of dynamic waves across the relevant frequency range, a sufficiently fine mesh is employed, ensuring that the largest dimension remains less than 1/8 of the shortest wavelength. The model is subjected to upward SH-wave excitation without inclination.

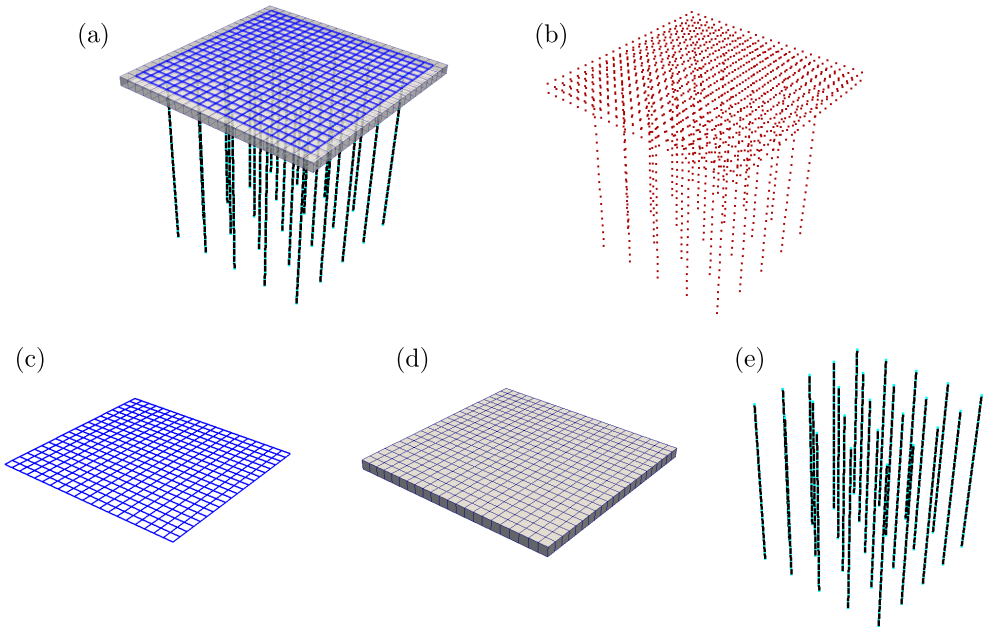

Fig. 4.4. Modelling of rigid inclusion reinforced foundation in SASSI: (a) global layout of model, (b) interaction nodes, (c) shallow foundation, (d) LTP, (e) rigid inclusions

4.2.3 Response under harmonic excitation

A harmonic excitation is first applied to the foundation systems. Figure 4.5 shows the kinematic interaction factor concerning a foundation reinforced by rigid inclusions, in addition to two different shallow foundation configurations. These two shallow foundation configurations are proposed to examine the impact of rigid inclusions and the LTP on ground motion modification.

The variation of the kinematic interaction factor is depicted with the dimensionless frequency a_0, as defined in Equation 4.4.

$$a_0 = \frac{\pi f B}{V_s} = \frac{\omega B}{2V_s} \tag{4.4}$$

where B stands for the foundation width, f represents the loading frequency, ω represents the circular frequency, and V_s indicates shear wave velocity.

As anticipated, the kinematic interaction factor I_u for the shallow foundation remains equal to unity within the selected frequency range. Furthermore, the addition of an LTP in the shallow foundation leads to a minor reduction in the kinematic interaction factor I_u, primarily noticeable for dimensionless frequency a_0 exceeding 4. However, in contrast, a more pronounced variation is observed for the rigid inclusion-reinforced foundation, characterised by a mitigation of approximately 10 % at a frequency of 17.5 Hz, due to the presence of rigid inclusions.

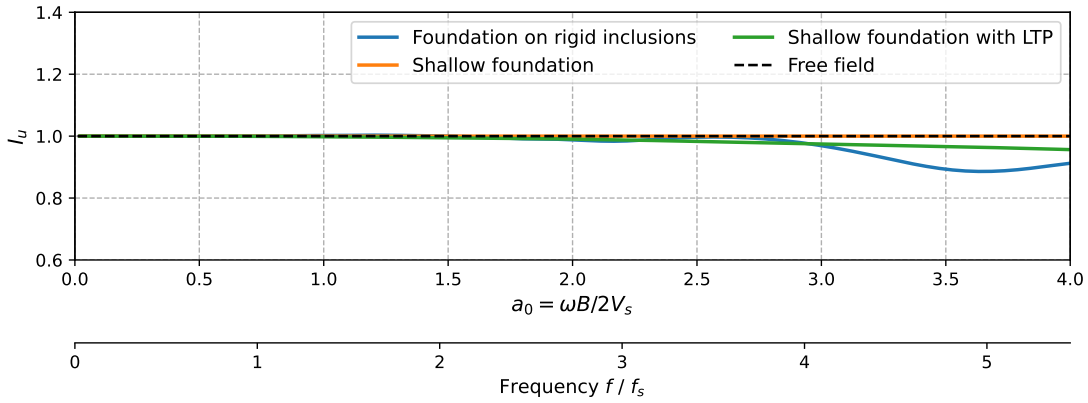

Fig. 4.5. Evolution of kinematic interaction factor for a rigid inclusion-reinforced foundation and comparison to other shallow foundation systems

The calculated kinematic interaction factor I_u, applied to the foundation reinforced by rigid inclusion as well as two pile foundation configurations, showcases a frequency-dependent feature, as depicted in Figure 4.6. The objective of this comparison is to study the impact of the connection between the piles and the raft foundation on the ground motion. All three analyses exhibit a similar trend. Significantly, the surface displacement is more adversely affected in the context of pile foundations. This phenomenon can be attributed to the specific connection between the piles and the raft foundation.

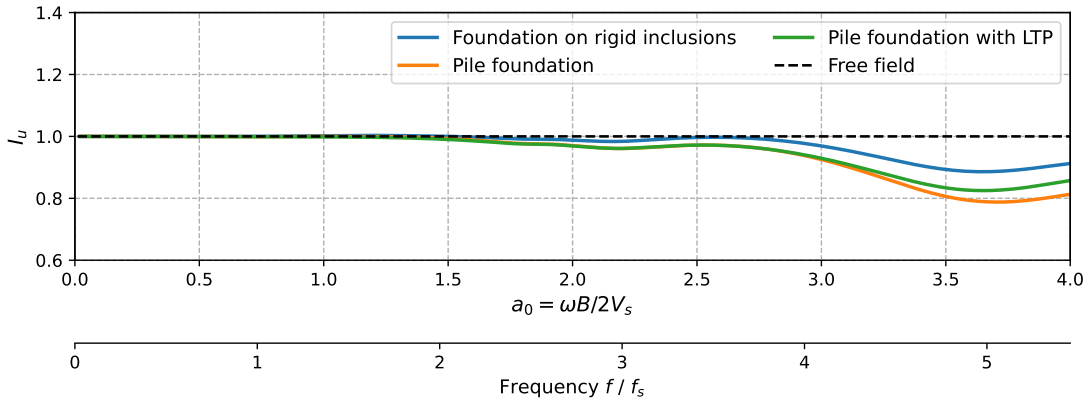

Fig. 4.6. Evolution of kinematic interaction factor for a rigid inclusion-reinforced foundation and comparison to other deep foundation systems

4.3 Influence of different characteristics of soil improvement under harmonic excitation

4.3.1 Studied configurations

A parametric investigation is conducted, building upon the reference configuration illustrated in Figure 4.2. The study involves the manipulation of parameters such as the stiffness of the soft soil, the diameter of inclusions, and their centre-to-centre distance.

Key attributes of the configurations used in this study are outlined in Table 4.3. The main characteristics of different groups are listed as follows:

- Group A: reference configuration (α = 3.46 %);
- Group B: shear wave velocity V_s, 100 m/s for B01 and 200 m/s for B02;
- Group C: coverage area ratio α, α = 2.01 % for C01, α = 5.31 % for C02 and α = 7.54 % for C03 ;
- Group D: centre-to-centre spacing, 1.5 m for D01 and 2.5 m for D02.

It should be noted that the change of the centre-to-centre spacing leads to an increase in the number of inclusions in Case D01.

The parameter α, referred to as the "coverage area ratio", quantifies the surface area of its cross-section to that of the reinforcement grid, as described in Equation 4.5. This parameter is an essential factor for reinforcement efficiency.

$$\alpha = \frac{\pi d^2}{4s^2} \tag{4.5}$$

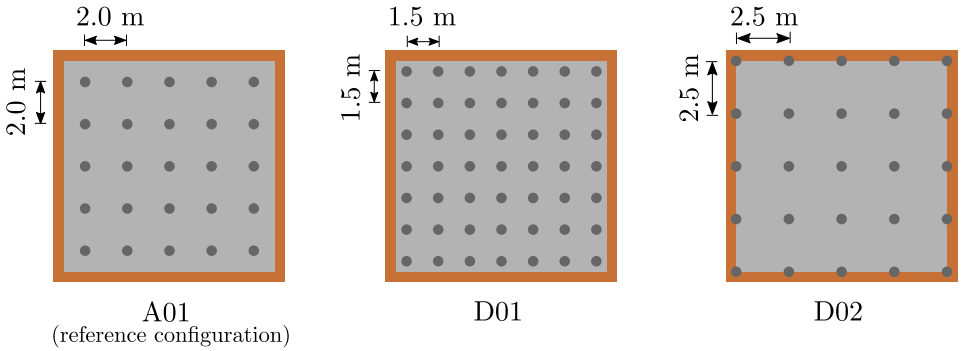

Fig. 4.7. Layouts of the rigid inclusions with different spacings

The displacement kinematic interaction factor I_u, as presented in Equation 4.1, is also used here to study the influence of different characteristics of rigid inclusion ground improvement.

Tab. 4.3. Main characteristics of studied configurations

Group	Case	Fundamental frequency f_s (Hz)	L/d	E_p/E_s	s/d	α (%)	V_s of soft soil
A	01	3.50	23.8	230	4.76	3.46	150
B	01	2.42	23.8	517	4.76	3.46	100
	02	4.43	"	129	4.76	"	200
C	01	3.50	31.3	230	6.25	2.01	150
	02	"	19.2	"	3.85	5.31	"
	03	"	16.1	"	3.23	7.54	"
D	01	3.50	23.8	230	3.57	6.15	150
	02	"	"	"	5.95	2.22	"

4.3.2 Influence of soil stiffness

Group B is designed to explore the influence of soil stiffness on the kinematic interaction effect. Kinematic interaction factors I_u of different cases are illustrated in Figure 4.8. The reduction in kinematic interaction factor I_u is notable when the dimensionless frequency a_0 exceeds 2.

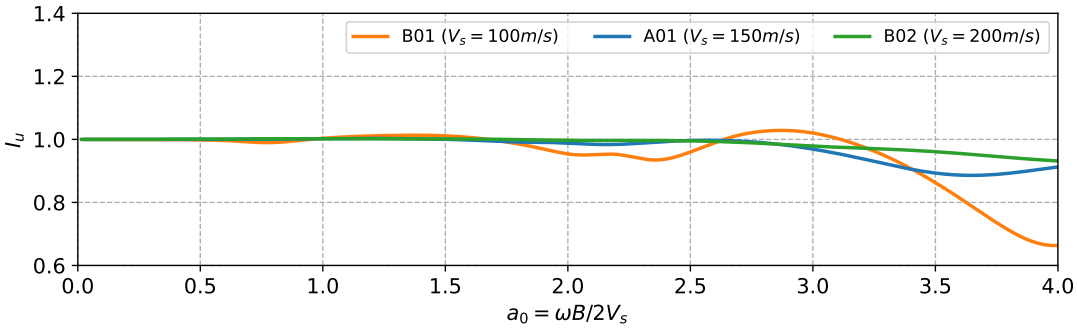

Fig. 4.8. Evolution of kinematic interaction factor for rigid inclusion-reinforced foundations with different soft soil stiffness

In Case B01, where the shear wave propagation velocity V_s of the soft soil is 100 m/s, the variation of the kinematic interaction factor I_u is more pronounced than in the other two cases. When the shear wave propagation velocity of the soft soil is increased to 200 m/s, the reduction becomes less prominent.

4.3.3 Influence of coverage area ratio

Figure 4.9 showcases the impact of coverage area ratio α on the modification of ground motion. The reduction in ground motion is not evident for dimensionless frequencies a_0 below 3. Notably, larger diameters, representing a large coverage area ratio α, exert a more pronounced influence on ground motion.

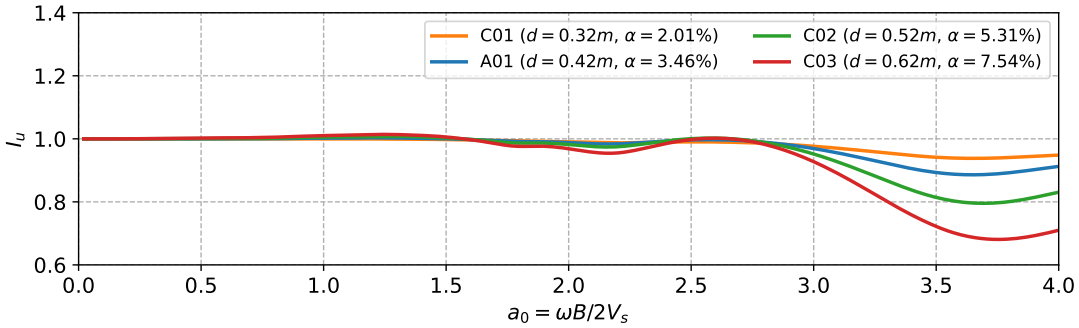

Fig. 4.9. Evolution of kinematic interaction factor for rigid inclusion-reinforced foundations with coverage area ratios of inclusions

In Case C03, where the coverage area ratio α is 7.54 %, the ground motion attenuation reaches 25 %. However, in contrast, for Case C01 with a coverage area ratio α of 2.01 %, the ground motion reduction is up to 5 %.

4.3.4 Global effects of different soil improvement configurations

Similar filtering effects as observed in pile groups are evident. These comprehensive parametric studies reaffirm that ground motion modifications are seldom observed at low frequencies. The impact becomes relatively pronounced solely at higher frequencies. By definition, the kinematic interaction is notably influenced by the rigidity contrast between the soil and foundation elements. In scenarios featuring softer soil and a larger coverage area ratio, the effects of kinematic interaction become more pronounced.

After conducting these extensive case studies, it is important to find a general pattern that can explain how ground motion changes based on configuration parameters such as soil stiffness and coverage area ratio. To achieve this, the kinematic interaction factor I_u is depicted against a dimensionless frequency F, inspired by the approach proposed by Gazetas (1984) for pile groups:

$$F = \frac{f}{f_s}\left(\frac{L}{d}\right)^{-0.35}\left(\frac{E_p}{E_s}\right)^{0.5}\left(\frac{s}{d}\right)^{0.2} \tag{4.6}$$

Where f represents the excitation frequency, f_s is the natural frequency of the soil column, $E_p\,/\,E_s$ stands for the ratio of inclusion elastic modulus to soil elastic modulus, $L\,/\,d$ signifies the ratio of the length of inclusions to their diameter, representing the slenderness of inclusions, $s\,/\,d$ is the ratio of the centre-to-centre distance between inclusions to the diameter of inclusions.

The outcomes are presented in Figure 4.10, which includes a trend curve to illustrate the main pattern. This observation confirms the impact of rigid inclusions at the high-frequency response, influencing the signal reaching the base of the structure. This phenomenon implies a potentially advantageous impact on the response of the structure, which is also in accordance with those already reported in the literature for pile groups (Kaynia, 1982).

Two distinct ranges can be roughly distinguished at $F = 25$. The first range indicates an absence of kinematic interaction effects, while the second range signifies kinematic interaction effects that are substantial. For instance, in the case of configuration C02, with an inclusion diameter d of 0.52m, and subjected to a 4 Hz excitation, no significant modification is observed. However, under a higher-frequency harmonic load of 18 Hz, a notable 20 % reduction in the signal at the base becomes apparent.

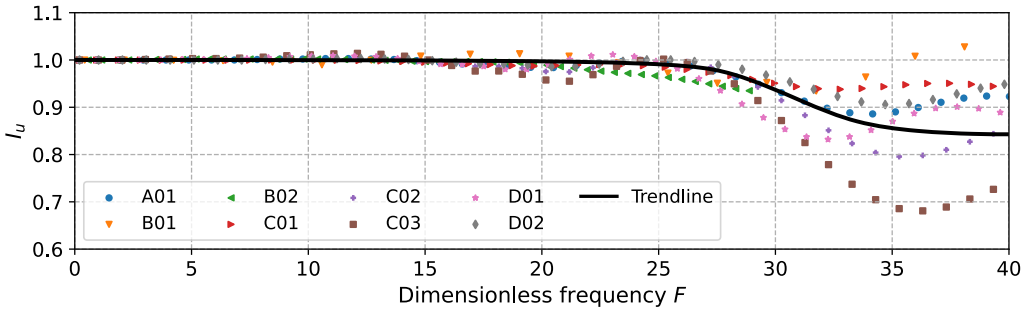

Fig. 4.10. Kinematic interaction factor as a function of the dimensionless frequency F

4.4 Response of different foundation systems under seismic excitation

4.4.1 Seismic excitation

After the investigation of the responses of the foundation under harmonic excitation, the study subsequently shifts to seismic excitation. The seismic input motion employed is derived from the elastic design response spectrum specified in Eurocode 8 (AFNOR, 2007). Five artificial accelerograms in accordance with the design spectrum have been formulated using the approach proposed by Gasparini and Vanmarcke (1976). This method establishes a correlation between the response spectrum and the spectral density function. A strong phase duration of 20 seconds is adopted.

Figure 4.11 illustrates the response spectra at 5% damping for each of the calculated accelerograms (depicted by dashed curves), the average spectrum derived from the five accelerograms (depicted by the red curve), and the target spectrum (represented

by the black curve). These five accelerograms serve as the input excitation sources, and the subsequent results showcase the averaged system response under five different accelerograms.

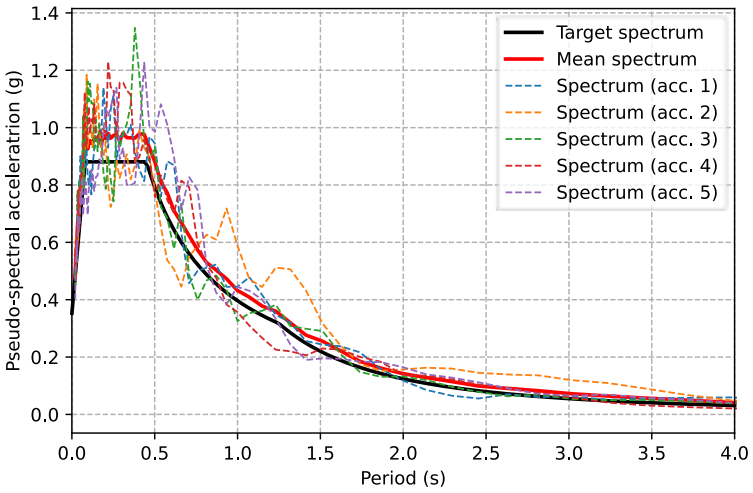

Fig. 4.11. Comparison of the average spectrum of artificial accelerograms and the target spectrum

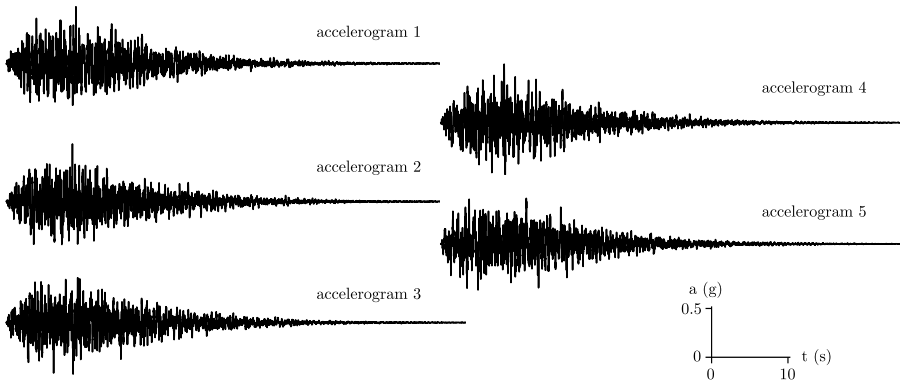

Fig. 4.12. Time history of artificial accelerograms

4.4.2 Response under seismic excitation

This section explores the modification of signal at the base of the structure arising from seismic excitation, owing to the presence of rigid inclusions. The analysis centres on comparing the kinematic responses of three foundation types: a foundation reinforced by rigid inclusions, a shallow foundation with LTP, and a pile foundation. Each configuration's kinematic response is characterised by the acceleration time history, which is subsequently transformed into pseudo-acceleration response spectra.

The pseudo-acceleration spectra for the three foundation configurations, under both accelerogram 1 and accelerogram 2, are depicted in Figure 4.13. The pseudo-acceleration

is represented as a function of frequency, normalised by the horizontal fundamental frequency of the soil column f_s, which in this case is 3.5 Hz. Upon observation, it becomes apparent that there are negligible differences at low frequencies among the three foundation configurations. At higher frequencies, the pseudo-acceleration of the shallow foundation closely resembles the free field response. Conversely, the pile foundation can filter out high-frequency components, thereby reducing the pseudo-acceleration. The inclusion-reinforced foundation also demonstrates a capacity for attenuating the system's responses. However, this reduction is comparatively less significant than that observed with the pile foundation.

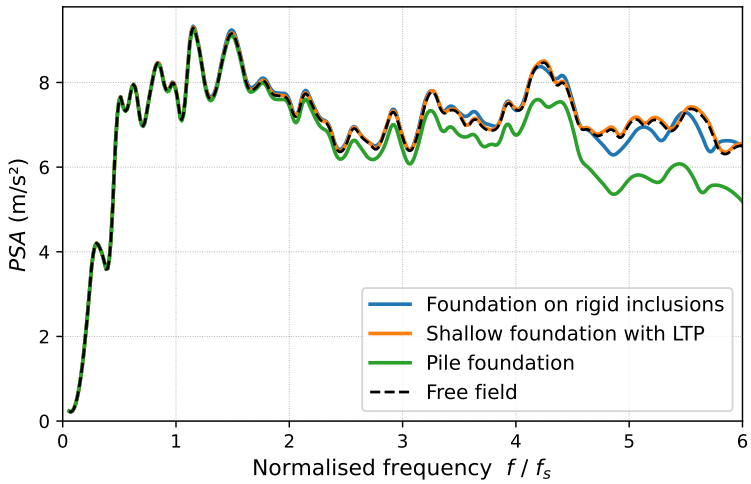

Fig. 4.13. Pseudo-acceleration PSA at the centre of the foundation with accelerogram 1

To facilitate a more precise quantification of the response in comparison to a free field, the presented response spectra are normalised based on those obtained at the surface of the soil column in the free field. This normalisation approach allows for the establishment of a pseudo-acceleration kinematic interaction factor (I_{PSA}), which can be defined according to Equation 4.7.

$$I_{PSA} = \frac{PSA_{ri}}{PSA_0} \tag{4.7}$$

where PSA_{ri} is the spectral pseudo-acceleration for the ground motion with the foundation on rigid inclusions and PSA_0 is the free field spectral pseudo-acceleration.

In Figure 4.14, the solid curves represent the average response derived from the five artificial accelerograms. These curves are enveloped by the range of maximum and minimum responses.

For a shallow foundation with LTP (blue curve), the response spectrum closely mirrors that of the free field, rendering it acceptable to disregard kinematic interaction effects. Regarding a pile foundation (green curve), the presence of piles leads to a notable attenuation of the response spectrum (up to -25% at higher frequencies), distinct from

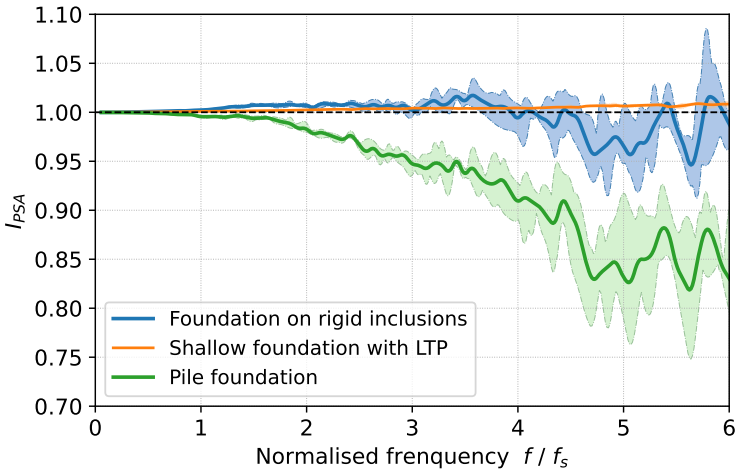

Fig. 4.14. Comparison of pseudo-acceleration kinematic interaction factors between several types of foundations

the free field response. In contrast, for a foundation reinforced by rigid inclusions (black curve), the alteration of the response spectrum is minimal (less than 10 %) and becomes evident only for SSI frequencies exceeding three times the fundamental frequency of the soil column f_s. Therefore, it can be concluded that in most scenarios, neglecting the effects of kinematic interaction on the input motion may be deemed acceptable.

4.5 Summary

This study explores the kinematic interaction effect for foundations reinforced by rigid inclusions under harmonic and seismic excitation. The numerical analyses address a significant aspect of SSI stemming from kinematic interaction: the modification of the signal at the base of the structure due to the presence of the foundation elements.

Concerning the modification of input motion at the base of the structure, kinematic interaction factors I_u are calculated. The results reveal an attenuation of high-frequency signal amplitude, attributed to the presence of inclusions and the LTP. This reduction can be as significant as 20 %.

A set of five artificial accelerograms is employed to explore the modification of ground motion. While a similar trend to that observed for pile foundations is evident, the amplitude of the ground motion modification evaluated by pseudo-acceleration kinematic interaction factor I_{PSA} is notably smaller in the case of foundations on rigid inclusions.

Furthermore, the observations outlined in the different soil improvement configuration studies emphasise that the presence of inclusions has the potential to modify the seismic motion reaching the base of a structure. This modification is particularly pronounced for

high values of the dimensionless frequency, which is associated with a high-frequency loading, a high coverage area ratio, utilisation of large diameter inclusions, or the presence of softer soil.

While engineering practice often focuses on vertically propagating SH-waves, it remains interesting to study the impact of inclined SH-waves, SV-waves and Rayleigh waves in future work.

5 Dynamic impedances for a rigid inclusion-reinforced foundation

5.1 Concept of foundation dynamic impedances

An essential step in the current approach to dynamic analysis of SSI systems under seismic or machine-induced inertial loading is the estimation of the dynamic impedance functions, using analytical or numerical methods. Incorporating the dynamic impedances of a foundation into the dynamic SSI analysis allows for the accurate modelling of SSI, enabling a comprehensive assessment of the dynamic behaviour of the soil-foundation-structure system. The chapter is dedicated to the study of dynamic impedances for foundations reinforced by rigid inclusions.

To understand the concept of the dynamic impedances of a foundation, drawing a close analogy with a single-degree-of-freedom (SDOF) damped oscillator is insightful. The harmonic response of a SDOF damped oscillator, represented as $Ue^{i\omega t}$, can be deduced by calculating the corresponding harmonic excitation, denoted as $Fe^{i\omega t}$, as shown in Equation 5.1.

$$U = \frac{F}{(k - m\omega^2) + i\omega c} \tag{5.1}$$

The expression for complex stiffness for the SDOF system is provided by Equation 5.2.

$$Z = (k - m\omega^2) + i\omega c = k\left[1 - \left(\frac{\omega}{\omega_n}\right)^2 + 2i\xi\frac{\omega}{\omega_n}\right] \tag{5.2}$$

In Equation 5.2, ω_n denotes the angular frequency of the system, and ξ signifies the damping ratio. This equation illustrates that the complex stiffness is the result of the static stiffness k and the dynamic component $\left[1 - (\frac{\omega}{\omega_n})^2 + 2i\xi\frac{\omega}{\omega_n}\right]$. The dynamic component comprises a real part $1 - \left(\frac{\omega}{\omega_n}\right)^2$, which can turn negative when subjected to high-frequency harmonic excitation, and an imaginary part $2i\xi\frac{\omega}{\omega_n}$.

The amplitude of the steady-static harmonic responses for this SDOF system can be given in Equation as follows:

$$\rho = \frac{F}{k}\left[(1-(\frac{\omega}{\omega_n})^2)^2 + (2\xi\frac{\omega}{\omega_n})^2\right]^{-1/2} \tag{5.3}$$

Naturally, the ratio of the resultant harmonic response amplitude to the static displacement which would be produced by the force F can be called the dynamic magnification factor D, as defined in Equation 5.4.

$$D = \frac{\rho}{F/k} = \left[(1-(\frac{\omega}{\omega_n})^2)^2 + (2\xi\frac{\omega}{\omega_n})^2\right]^{-1/2} \tag{5.4}$$

When dealing with a weightless foundation, the complex stiffness, so-called dynamic impedances, can also be defined as the ratio between the harmonic force (or moment) F and the resultant harmonic steady-state displacement (or rotation) U at the centre of the foundation (Gazetas, 1991a). However, due to the presence of radiation and material damping within the soil-foundation system, there is always a phase shift between the resulting displacement U and the applied force F. Similar to Equation 5.2, the dynamic impedance function Z can thus be expressed as Equation 5.5, which contains also a real component, and an imaginary component.

$$\underline{\underline{Z}} = \frac{\underline{\underline{F}}}{\underline{\underline{U}}} = \Re(\underline{\underline{Z}}(\omega)) + \Im(\underline{\underline{Z}}(\omega)) \tag{5.5}$$

with

$$\Re(\underline{\underline{Z}}(\omega)) = \underline{\underline{K}}(\omega) \tag{5.6}$$

and

$$\Im(\underline{\underline{Z}}(\omega)) = i\omega\underline{\underline{C}}(\omega) \tag{5.7}$$

The real component $\underline{\underline{K}}$, referred to as "dynamic stiffness", reflects the stiffness of the soil-foundation system. The imaginary component $\omega\underline{\underline{C}}$, is the product of the excitation circular frequency ω and the "dash-pot matrix" $\underline{\underline{C}}$, as described in Equation 5.7. The "dash-pot matrix" $\underline{\underline{C}}$ reflects the radiation and material damping generated in the system due to energy carried by waves spreading away from the foundation and energy dissipated in the soil through hysteretic action.

Additionally, the damping ratio for different degrees of freedom can be calculated using Equation 5.8.

$$\xi_i(\omega) = \frac{\omega C_i(\omega)}{2K_i(\omega)} \tag{5.8}$$

The same dynamic magnification factor D for the foundation for each direction can be also defined in Equation 5.9 as the same for the SDOF damped oscillator.

$$D_i(\omega) = \frac{U_i(\omega)}{U_i(\omega = 0)} \tag{5.9}$$

This factor is an important index describing the amplification and attenuation of the steady-state response of the foundation system varied with the frequency compared with the static response.

Numerous research studies have delved into the dynamic impedances in both shallow foundations and pile foundations. For shallow foundations, extensive work has been conducted by researchers such as Kausel (1974) and Gazetas (1984, 1991a,b). For a shallow foundation without embedment, Deleuze (1967) have contributed valuable design charts to facilitate the estimation of dynamic impedances with respect to frequencies. Similarly, investigations concerning pile foundations have been undertaken by researchers including Novak (1974), Kaynia (1982), Novak (1991), and Gazetas *et al.* (1993).

However, in the context of inclusion-reinforced foundations, there is a need for a systematic exploration of dynamic impedances. The impedance functions, compassing dynamic stiffness and damping, are influenced by a multitude of parameters, including soil characteristics, foundation dimensions, inclusion configuration encompassing quantity, diameter, and the spacing of inclusions.

5.2 Model description

The investigation of dynamic impedances for foundations predominantly occurs within the elastic or visco-elastic framework. The hybrid BIE-FEM numerical model employed for the exploration of kinematic interaction in Chapters 4 and 7 can be also used in the dynamic impedance study. In this model, the foundation is represented as a weightless three-dimensional rigid beam grid, which is a conventional assumption in the calculation of dynamic impedances (Gazetas, 1991a). Elaboration on the numerical modelling principles is furnished in Section 4.2.2, accompanied by an illustrative depiction of the adopted model, as presented in Figure 5.1.

The analysis is executed within the frequency domain, encompassing a defined frequency range. Specifically, the frequency interval chosen for the calculations spans from 0.1 to 20 Hz, utilising increments of 0.5 Hz. This frequency width is sufficiently small to adequately capture the frequency-dependent behaviour of the dynamic impedances across the chosen frequency range.

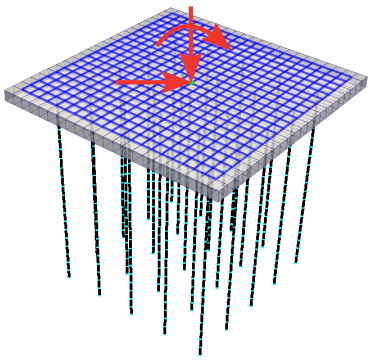

Fig. 5.1. Calculation modelling for dynamic impedance functions

The outcome of the calculation yields a 6×6 compliance matrix $\underline{\underline{S}}(\omega)$ at the centre of the foundation. This compliance matrix establishes the connection between the applied forces $\underline{F}(\omega)$ and the corresponding displacements $\underline{U}(\omega)$ at the same point on the foundation.

$$\underline{U}(\omega) = \underline{\underline{S}}(\omega)\underline{F}(\omega) \tag{5.10}$$

where:

$$\underline{\underline{S}}(\omega) = \begin{bmatrix} S_{xx}(\omega) & S_{xy}(\omega) & S_{xz}(\omega) & S_{xrx}(\omega) & S_{xry}(\omega) & S_{xrz}(\omega) \\ S_{yx}(\omega) & S_{yy}(\omega) & S_{yz}(\omega) & S_{yrx}(\omega) & S_{yry}(\omega) & S_{yrz}(\omega) \\ S_{zx}(\omega) & S_{zy}(\omega) & S_{zz}(\omega) & S_{zrx}(\omega) & S_{zry}(\omega) & S_{zrz}(\omega) \\ S_{rxx}(\omega) & S_{rxy}(\omega) & S_{rxz}(\omega) & S_{rxrx}(\omega) & S_{rxry}(\omega) & S_{rxrz}(\omega) \\ S_{ryx}(\omega) & S_{ryy}(\omega) & S_{ryz}(\omega) & S_{ryrx}(\omega) & S_{ryry}(\omega) & S_{ryrz}(\omega) \\ S_{rzx}(\omega) & S_{rzy}(\omega) & S_{rzz}(\omega) & S_{rzrx}(\omega) & S_{rzry}(\omega) & S_{rzrz}(\omega) \end{bmatrix} \tag{5.11}$$

The impedance matrix is derived by inverting the compliance matrix $\underline{\underline{S}}(\omega)$. As a result, the dynamic impedances are expressed within a 6×6 complex impedance matrix $\underline{\underline{Z}}(\omega)$ that varies with frequency ω, defined as follows:

$$\begin{aligned} \underline{\underline{Z}}(\omega) &= [\underline{\underline{S}}(\omega)]^{-1} \\ &= \begin{bmatrix} Z_{xx}(\omega) & Z_{xy}(\omega) & Z_{xz}(\omega) & Z_{xrx}(\omega) & Z_{xry}(\omega) & Z_{xrz}(\omega) \\ Z_{yx}(\omega) & Z_{yy}(\omega) & Z_{yz}(\omega) & Z_{yrx}(\omega) & Z_{yry}(\omega) & Z_{yrz}(\omega) \\ Z_{zx}(\omega) & Z_{zy}(\omega) & Z_{zz}(\omega) & Z_{zrx}(\omega) & Z_{zry}(\omega) & Z_{zrz}(\omega) \\ Z_{rxx}(\omega) & Z_{rxy}(\omega) & Z_{rxz}(\omega) & Z_{rxrx}(\omega) & Z_{rxry}(\omega) & Z_{rxrz}(\omega) \\ Z_{ryx}(\omega) & Z_{ryy}(\omega) & Z_{ryz}(\omega) & Z_{ryrx}(\omega) & Z_{ryry}(\omega) & Z_{ryrz}(\omega) \\ Z_{rzx}(\omega) & Z_{rzy}(\omega) & Z_{rzz}(\omega) & Z_{rzrx}(\omega) & Z_{rzry}(\omega) & Z_{rzrz}(\omega) \end{bmatrix} \end{aligned} \tag{5.12}$$

As discussed in Section 5.1, each term $Z_i(\omega)$ within the complex impedance matrix $\underline{\underline{Z}}(\omega)$ is associated with a stiffness parameter $K_i(\omega)$ and a damping ratio $\xi_i(\omega)$, accounting for both material and radiation damping effects. The curves for stiffness and damping ratio are determined using the following relationships:

This chapter primarily focuses on the dynamic stiffness $K_i(\omega)$ and the damping ratio $\xi_i(\omega)$. Additionally, it delves into the dynamic magnification factor D of the foundation system.

5.3 Comparison between different foundation systems

5.3.1 Studied configurations

Given the characteristics of rigid inclusion-reinforced foundation configuration, which falls somewhere between a shallow foundation and a pile foundation, one might be tempted to assume a response similar to what is observed in the case of those types of foundations. Therefore, the investigation of dynamic impedances for inclusion-reinforced foundations begins with a comparative analysis involving shallow foundations and pile foundations, aiming to assess their differences and similarities. The same reference configuration as depicted in Figure 4.2 in Chapter 4 is used with the characteristics detailed in Table 5.1.

Tab. 5.1. Mechanical properties of the soil and the foundations

	Soft soil	Hard soil	Bedrock	LTP	Rigid inclusions
Shear modulus G (MPa)	20/45/80	320	2 500	125	12 500
Shear wave velocity V_s (m/s)	100/150/200	400	1 000	250	2 236
Poisson's ratio ν (-)	0.45	0.45	0.45	0.35	0.2
Mass density ρ (t/m^3)	2.0	2.0	2.5	2.0	2.5
Material damping ratio ξ (-)	0.05	0.05	0.05	0.05	0

The principal characteristics of the configurations adopted in this study are provided in Table 5.2. Several groups of configurations are proposed. In each group, only one parameter is changed based on the reference configuration A01. The main characteristics of different groups are listed as follows:

- Group A: reference configuration (α = 3.46 %);
- Group B: shear wave velocity V_s, 100 m/s for B01 and 200 m/s for B02;
- Group C: coverage area ratio α, α = 2.01 % for C01, α = 5.31 % for C02 and α = 7.54 % for C03 ;
- Group D: centre-to-centre spacing s, 1.5 m for D01 and 2.5 m for D02.
- Group E: foundation dimension B, 3 m for E01 and 20 m for E02.

The arrangement of rigid inclusions with different centre-to-centre spacing s can be observed in Figure 4.7. Similarly, the arrangement of rigid inclusions with diverse foundation sizes can be seen in Figure 5.2

Given the symmetry of the examined configuration, the horizontal responses along the x-axis and the y-axis are identical. Likewise, the rotation responses about the horizontal axes are equivalent. Consequently, the dynamic impedances are denoted by terms such as K_H, K_V, and K_M, representing horizontal, vertical, and rotational dynamic stiffnesses, respectively, while ξ_H, ξ_V, and ξ_M correspond to the horizontal, vertical, and rotational damping ratios, as depicted in Figure 5.3.

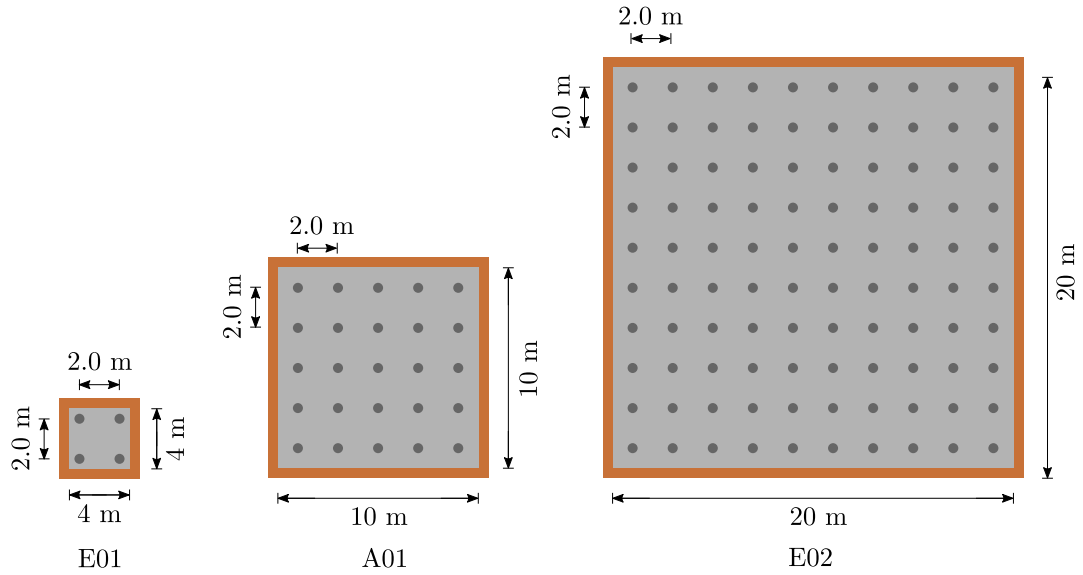

Fig. 5.2. Layout of different foundation dimensions

Tab. 5.2. Main characteristics of the studied configurations

Group	Case	$V_{s,soft\ soil}$	B/L	L/d	E_p/E_s	s/d	α (%)	f_s* (Hz)	f_c** (Hz)
A	01	150	1	23.8	230	4.76	3.46	3.50	6.89
B	01	100	1	23.8	517	4.76	3.46	2.42	4.76
	02	200	"	"	129	"	"	4.43	8.72
C	01	150	1	31.3	230	6.25	2.01	3.50	6.89
	02	150	"	19.2	"	3.85	5.31	"	"
D	01	150	1	23.8	230	3.57	6.16	3.50	6.89
	02	150	"	"	"	5.95	2.22	"	"
E	01	150	0.33	23.8	230	4.76	3.46	3.50	6.89
	02	150	2	"	"	"	"	"	"

* f_s is the horizontal fundamental frequency of the soil column

** f_c is the vertical fundamental frequency of the soil column

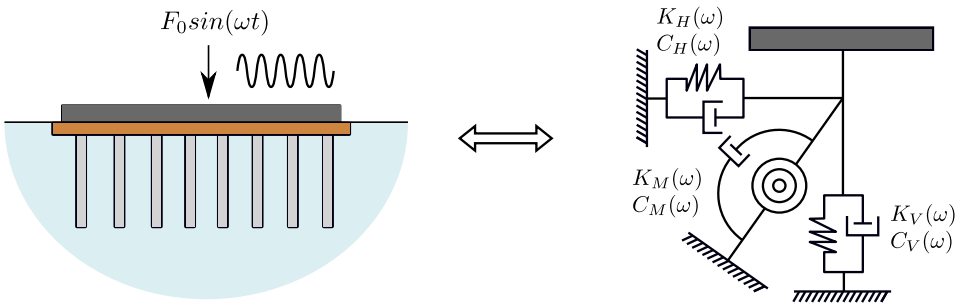

Fig. 5.3. Analogue model of a foundation on rigid inclusions under inertial interaction effects

5.3.2 Dynamic impedances of different foundation systems

In this section, the dynamic impedance functions of various foundation systems are compared. Detailed comparisons are presented between the rigid inclusion-reinforced foundation (A01) and other foundation systems are done. For a more comprehensive overview, the comparisons with other reinforced foundation configurations can be found in Appendix C.

Comparison with shallow foundations

The first study constitutes to comparison with the shallow foundations with and without LTP, as depicted in Figure 5.4.

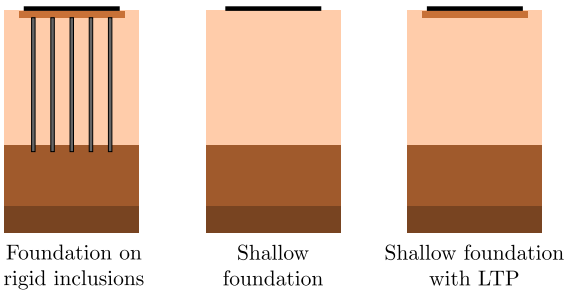

Fig. 5.4. Layout of reinforced foundation and different shallow foundations

Figure 5.5 illustrates a comparison between rigid inclusion-reinforced foundations and shallow foundations. The comparison includes two configurations of shallow foundations: one without LTP and another with LTP. To facilitate this comparison, the dynamic stiffness of these three foundation systems is normalised using the "static stiffness" ($f = 0.1$ Hz) of the shallow foundation with LTP, denoted as $K_{f=0}^{SF+m}$. The dynamic impedance functions are given as a function of the dimensionless frequency a_0.

The comparison starts with the dynamic stiffness in the horizontal direction. The dynamic stiffness of the inclusion-reinforced foundation closely resembles that of the shallow foundation with LTP in the horizontal direction, as depicted in Figure 5.5 (a). The slightly

horizontal stiffness reduction of 10 % at $a_0 = 0$ observed in the shallow foundation without LTP can be attributed to the presence of a more rigid granular LTP.

The increase in vertical stiffness due to the presence of rigid inclusions is further observed in Figure 5.5 (b). The vertical dynamic stiffness for a rigid inclusion-reinforced foundation surpasses that for both shallow foundation configurations, with or without LTP, across all the studied frequency ranges. The static stiffness of the reinforced foundation is nearly 60 % higher compared to the other two shallow foundations.

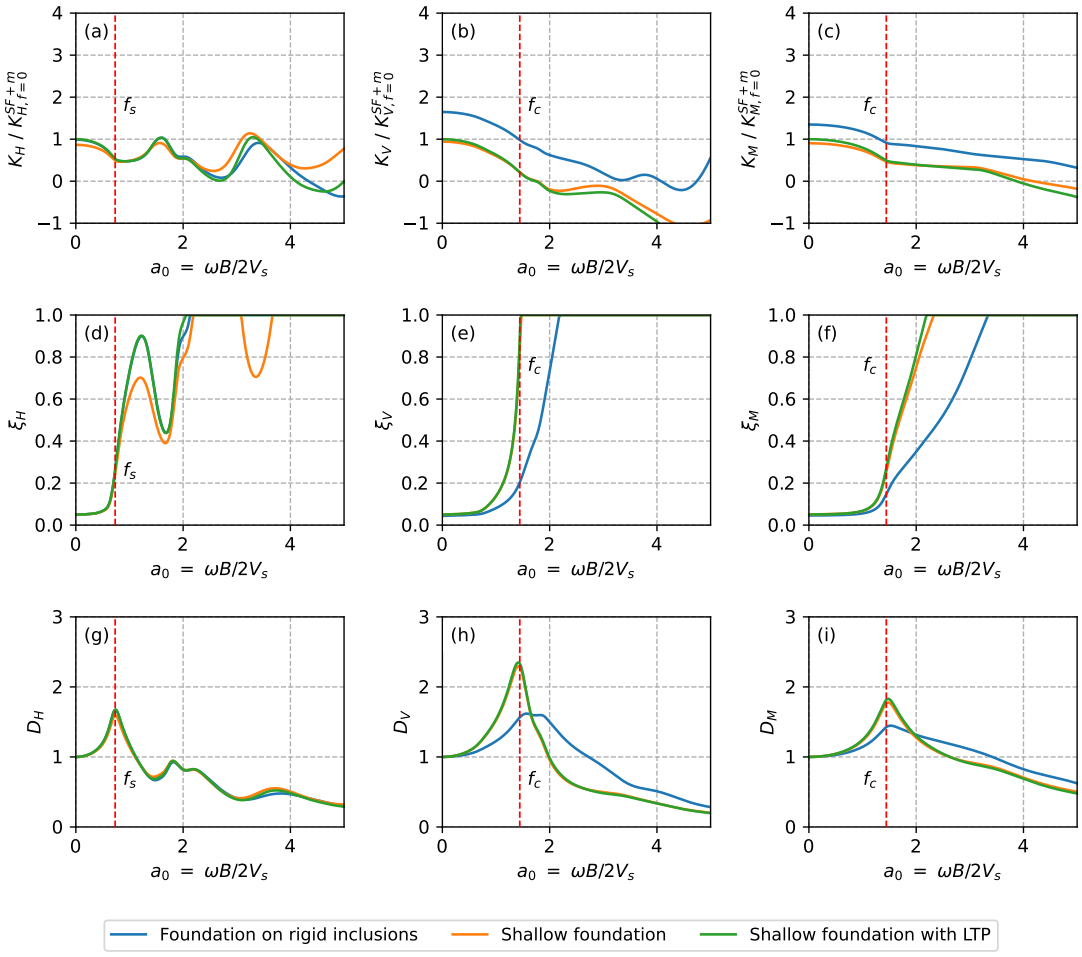

Fig. 5.5. Dynamic stiffness, damping ratio and dynamic magnification factor for reinforced foundation (A01) and shallow foundations with and without LTP

The investigation of energy dissipation centres around the analysis of damping ratios. As a reminder, an initial material damping of 5 % is assigned. In the low-frequency range, a consistent material damping ratio is observed across the three examined foundation systems. It is also noted that radiation damping is not mobilised at the low-frequency range for all studied directions. Instead, it is only excited in the high-frequency range.

The horizontal damping ratio for the three foundation systems is depicted in Figure 5.5 (d). The damping ratio curve for the foundation on rigid inclusion closely aligns with that

of the shallow foundation with LTP. This observation confirms that the presence of rigid inclusions does not impact the damping characteristic of the reinforced system in the horizontal direction.

The vertical and rotational damping ratio curves for the three analysed foundation systems are illustrated in Figures 5.5 (e) and (f), respectively. It is evident that the damping characteristics of shallow foundations with and without LTP are truly similar. Comparatively, the damping ratio of the inclusion-reinforced foundation is lower than that of the other two foundations. The fact that the inclusions work at the tips increases the vertical stiffness of the soil-foundation system. As a result, the vertical fundamental frequency of the system shifts to a higher frequency, leading to the delayed appearance of radiation damping.

Figure 5.5 (g) reveals that the inclusion-reinforced foundation and the shallow foundation with and without LTP exhibit the same variations in the horizontal direction. The frequency of maximum amplification corresponds to the horizontal frequency of the soil profile column, denoted as f_s.

In the vertical direction, a significant difference is evident in the evolution of the dynamic magnification factor between the shallow foundations and the foundation on rigid inclusions, as depicted in Figure 5.5 (h). For the two shallow foundations, the frequency of the maximum amplification coincides with the frequency of the first vertical mode of the soil column, denoted as f_c. In contrast, the frequency of maximum amplification for the foundation on rigid inclusions is approximately 1.2 f_c. Additionally, the vertical dynamic amplification for the foundation on rigid inclusions is lower than that observed for the shallow foundations.

The rotational dynamic amplification characteristics for the three studied foundation systems are presented in Figure 5.5 (i). The frequency of maximum amplification for the foundation on rigid inclusions is similar to that of the shallow foundations. However, the maximum dynamic amplification for the reinforced foundation is smaller than that of the non-reinforced shallow foundations.

Comparison with pile foundations

The first study constitutes to comparison with the shallow foundations with and without LTP, as depicted in Figure 5.6. It is important to emphasise that in the pile foundation without LTP modelling, solely the piles are connected to the soil. The foundation supported by the pile group remains detached from the soil as illustrated in Figure 5.7.

The comparison with pile foundations is depicted in Figure 5.8. The dynamic stiffness of these three foundation systems is normalised by the "static stiffness" ($f = 0$) of a pile foundation with LTP, denoted as $K^{PG}_{f=0}$.

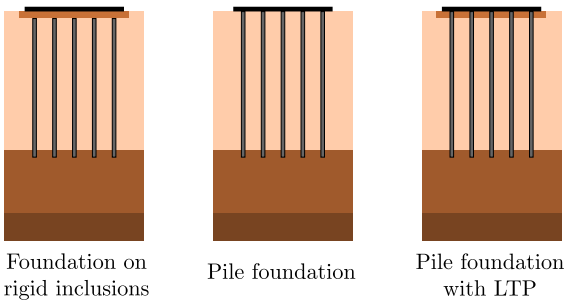

Fig. 5.6. Layout of reinforced foundation and different pile foundations

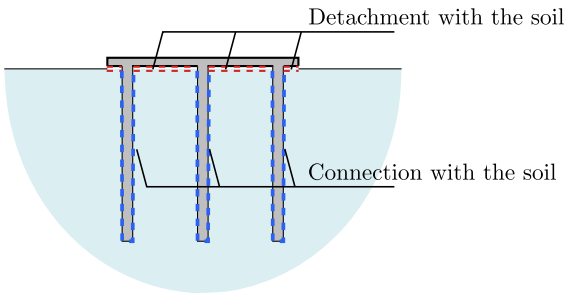

Fig. 5.7. Hypothesis of the pile foundation modelling

The comparison of horizontal dynamic stiffness is presented in Figure 5.8 (a). It can be observed that the pile group with LTP closely resembles the inclusion-reinforced foundation with LTP. Similar to the observations made in the comparison with the shallow foundation, both pile foundation and inclusion-reinforced foundation exhibit negligible influence on the dynamic stiffness of the foundation. It is important to note that this observation is reserved for the tested configurations with small pile diameters. This same conclusion is also applicable to the horizontal damping ratio, as shown in Figure 5.8 (d). Thus, it is evident that the horizontal response, encompassing both stiffness and damping, is predominantly governed by the presence of LTP.

Figures 5.8 (b) and (c) illustrate the vertical and rotational dynamic stiffnesses of the three examined foundations. Both pile groups (with or without LTP) demonstrate higher dynamic vertical stiffnesses when compared with the rigid inclusion-reinforced foundation.

Regarding the damping of foundation systems depicted in Figure 5.8 (d), (e), and (f), the damping characteristic of the foundation on rigid inclusions is similar to the pile foundation with LTP. It is also observed that for low frequencies (small a_0), the damping within the system is entirely attributed to material damping. Conversely, for higher frequencies, the damping ratio of the foundations with LTP generally exhibits greater significance compared to the pile group foundation without LTP. It is interesting to note that the damping ratio value increases rapidly and exceeds 30 % once the radiation damping starts to increase.

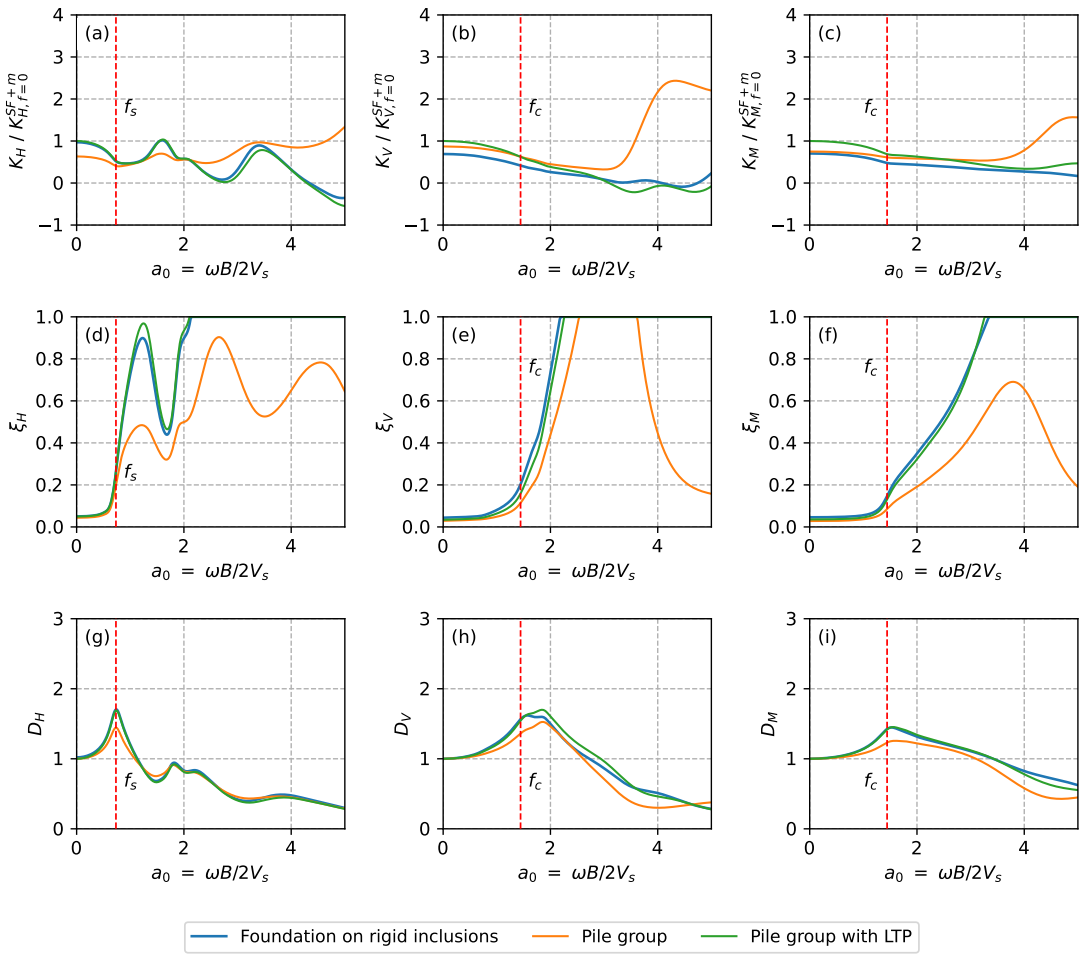

Fig. 5.8. Dynamic stiffness, damping ratio and dynamic magnification factor for reinforced foundation (A01) and pile foundations with and without LTP

From Figure 5.8 (g), (h), and (i), the dynamic magnification factors for the foundation on rigid inclusions and the pile group foundation with LTP are very similar in terms of their variation and magnitude. Both the piles and rigid inclusion can increase the vertical stiffness of the foundation. The frequencies of the maximum amplification for the three studied foundation systems are greater than the vertical frequency of the soil profile f_c, as depicted in Figure 5.8 (h).

5.4 Influence of different parameters of soil improvement

The previous comparisons have highlighted that the rigid inclusions have a negligible impact on horizontal stiffness and significant effects primarily on vertical and rotational stiffness. In the following, the interest is focused on the impact that the variation of

significant parameters describing the rigid inclusion-reinforced foundation may have on its response. Therefore, a sensitivity study is conducted to analyse the impact of:

- Coverage area ratio α;
- Length of rigid inclusions;
- Embedment of rigid inclusions in LTP.

5.4.1 Influence of coverage area ratio

To investigate the effects of varying the coverage area ratio, different diameters of the rigid inclusions vary across 0.32 m, 0.42 m, 0.52 m, and 0.62 m are employed, corresponding to the coverage area ratio α of 2.01 %, 3.46 %, 5.31 %, and 7.55 %. The results are presented in Figure 5.9, illustrating dynamic stiffness, damping ratio, and dynamic magnification factor for rigid inclusion-reinforced foundations with different coverage area ratios. The dynamic stiffness has been normalised against the "static stiffness" of the shallow foundation with LTP, denoted as $K_{f=0}^{SF+m}$.

Figure 5.9 (a) substantiates the findings outlined in the preceding section. The horizontal dynamic stiffness curves for reinforced foundations with four different diameters remain consistent. In contrast, the comparison of vertical and rotational dynamic stiffness, as depicted in Figures 5.9 (b) and (c), highlights that dynamic stiffness amplifies with the diameter of rigid inclusions.

Regarding the damping ratio, it is apparent that up to frequencies below the fundamental frequency of soil column f_s and f_c, the system predominantly exhibits material damping. This behaviour is depicted in Figure 5.9 (d) for the horizontal damping curves across different studied cases. The resemblance in horizontal damping ratios is evident. Furthermore, the trends observed in the vertical and rotational damping ratio curves are similar, as illustrated in Figures 5.9 (e) and (f). The development of radiation damping occurs at a later stage for configurations with higher coverage area ratios.

The dynamic magnification factors D for the reinforced foundation with different diameters of the rigid inclusions exhibit significant similarities in terms of their variation for the three studied directions. In the horizontal direction, the amplifications for the four studied reinforced foundations are the same for a_0 smaller than 3.5. In the vertical and rotational directions, the maximum amplification for the reinforced foundation with a smaller coverage area ratio is greater than that for the reinforced foundation with a larger coverage area ratio.

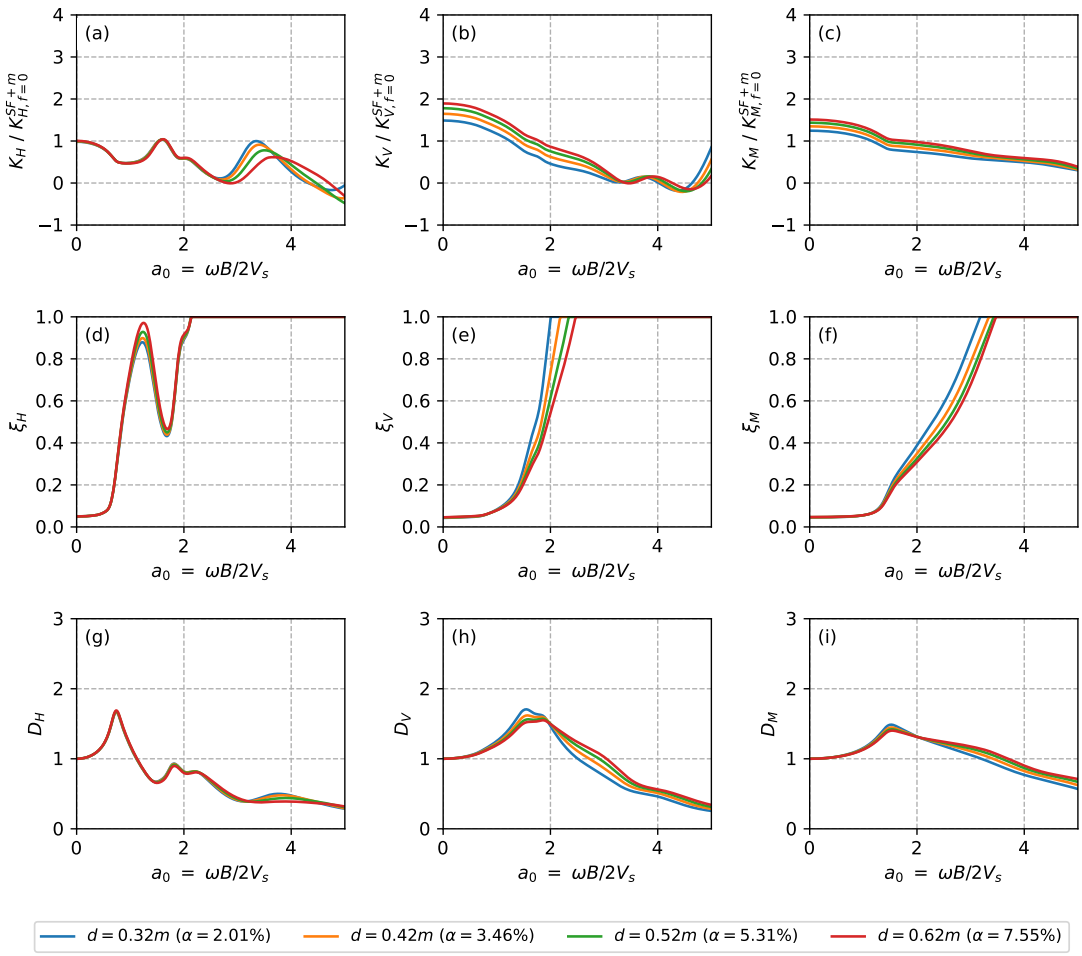

Fig. 5.9. Dynamic stiffness and damping ratio for reinforced foundations with different coverage area ratio

5.4.2 Influence of length of rigid inclusions

The rigid inclusions for soil improvement are typically end-bearing inclusions. These inclusions' tips are located at a stable load-bearing substratum, such as rock or a compact layer of soil. Unless the inclusions are properly embedded within a resistant layer of soil, the reinforcement mechanism will not function as intended.

Three different lengths of rigid inclusions have been selected, ranging from 10 m, 5 m, to 2 m. These configurations of rigid inclusions with varying lengths are illustrated in Figure 5.10.

Only the 10-m inclusions are capable of engaging with the resistance at their tips. In contrast, the shorter rigid inclusions (2 m and 5 m) in the other two cases remain unembedded in hard soil and function more like floating inclusions. The dynamic impedances corresponding to the different lengths of rigid inclusions are displayed in Figure 5.11.

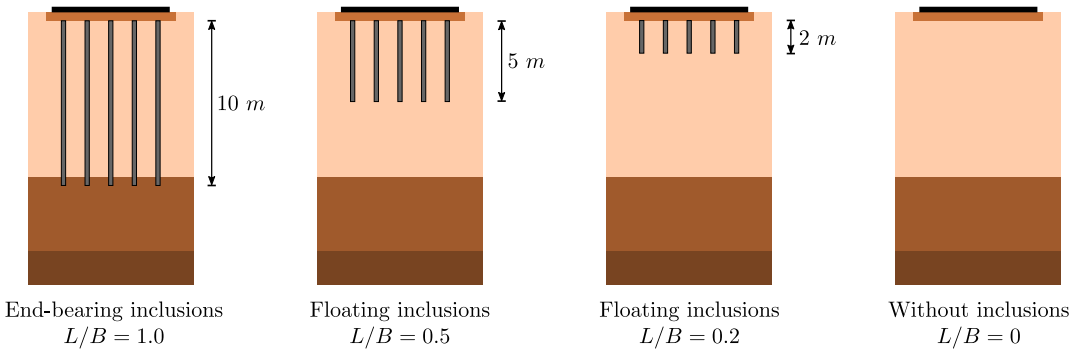

Fig. 5.10. Layouts of the rigid inclusions with different lengths

Regarding vertical and rotational stiffness, configurations with floating inclusions demonstrate similarities to the case without any inclusions (L/B=0) for dimensionless frequencies lower than 3.5. This comparison confirms that the response in the case of soil reinforced by floating rigid inclusions is governed by the stiffness of the soil surrounding the reinforced area. The dynamic response in terms of dynamic stiffness and damping ratio closely resembles that of the non-reinforced foundation with LTP.

The study also examines the dynamic magnification factors D for these foundations. It is observed that the foundation reinforced by floating inclusions exhibits similar dynamic amplification or attenuation characteristics to the shallow foundation in all directions. On the other hand, the foundation on end-bearing inclusions shows a smaller maximum amplification compared to the configurations with floating inclusions.

5.4.3 Influence of embedment of rigid inclusions in the LTP

Following recommendations from (AFPS and CFMS, 2012), the recommended configuration involves embedding rigid inclusions within LTP to ensure favourable performance in transferring horizontal forces. In this paragraph, the objective is to examine whether this embedment may influence dynamic impedances. Two cases are studied with an embedment depth of 0.2 m and of 0.5 m. A configuration without embedding is also studied for comparison purposes. These configurations are illustrated in Figure 5.12.

The dynamic impedances are displayed in Figure 5.13. The horizontal stiffness remains unaffected by the embedment depth. The vertical and rotational dynamic stiffness is slightly impacted by the embedment of rigid inclusions in LTP. In terms of damping ratio, as presented in Figures 5.13 (d), (e), and (f), the influence of embedment remains limited. Concerning the dynamic magnification factor D, there is no difference between the configurations with the embedment of the rigid inclusions in the LTP and the configuration with no embedment.

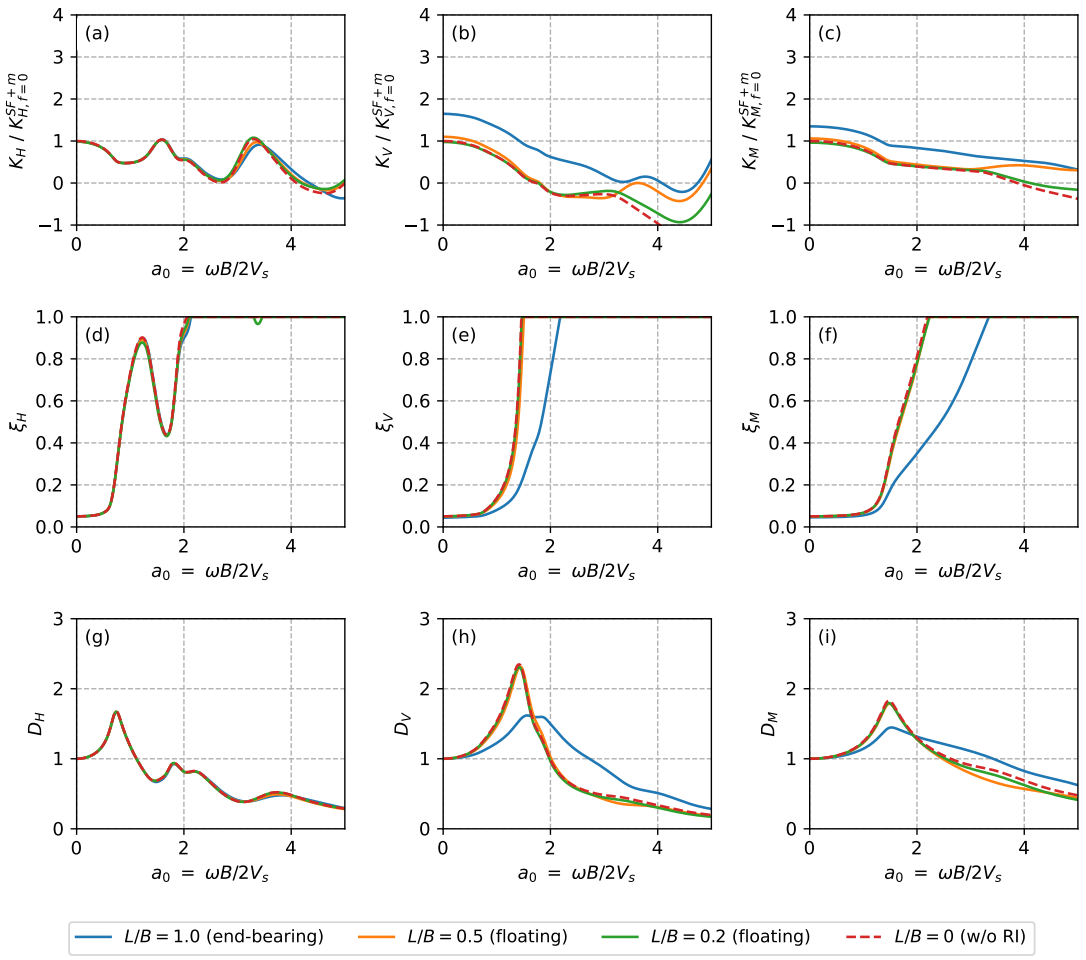

Fig. 5.11. Dynamic stiffness and damping ratio for reinforced foundations with different lengths of rigid inclusions

5.5 Evaluation of dynamic impedances with equivalent profiles

In the context of ground reinforcement by rigid inclusions, it is necessary to establish an equivalent or representative soil profile. This profile integrates the properties of the actual soil and the reinforcement into a simplified, homogeneous model that can be analysed more easily, proving advantageous as it omits explicit modelling of inclusions and LTP, thereby resulting in reduced computational resources and time.

The arrangement of inclusions introduces mechanical anisotropy within the reinforced soil, necessitating separate analyses for horizontal, vertical, and rotational behaviours. Therefore, this section aims to establish an equivalent profile for estimating dynamic impedances in both horizontal and vertical, as well as rotational directions.

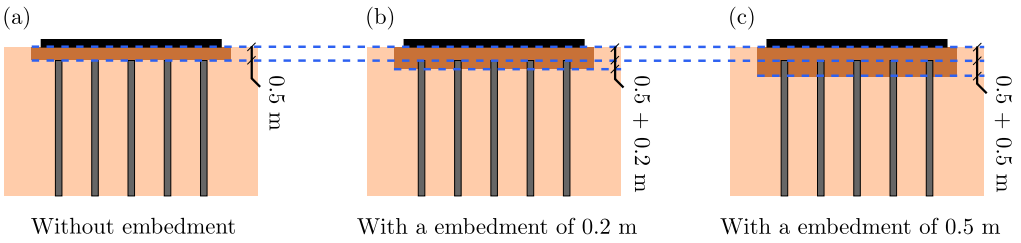

Fig. 5.12. Embedment of rigid inclusions in LTP: (a) without embedment, (b) with an embedment as 0.2 m, (c) with an embedment as 0.5 m

5.5.1 Equivalent profile for horizontal response

Based on the observations from the previous sections, within the range of common coverage area ratios, inclusions exert minimal influence on the shear stiffness of the reinforced soil. As a result, it is reasonable to estimate horizontal dynamic impedances by neglecting the contribution of inclusions.

The horizontal stiffness of a foundation system with rigid inclusions, denoted as K_H^{RI}, is then compared with the stiffness obtained for the same configuration without rigid inclusions, denoted as K_H^{SF+m}. Both foundation systems are illustrated in Figure 5.14.

The findings are presented in the form of stiffness ratios between K_H^{RI} and K_H^{SF+m}, as illustrated in Figure 5.15 with two types of frequency normalisation to cover as many cases as possible. The ratios for various configurations closely approximate unity. For frequencies below 2.5 times the fundamental horizontal frequency of soil column f_s, the difference in stiffness between the foundation with rigid inclusions and the one without rigid inclusions remains under 10 %. It can be observed that in cases where a_0 is smaller than 1, there is no difference in stiffness between the foundation with rigid inclusions and the one without rigid inclusions.

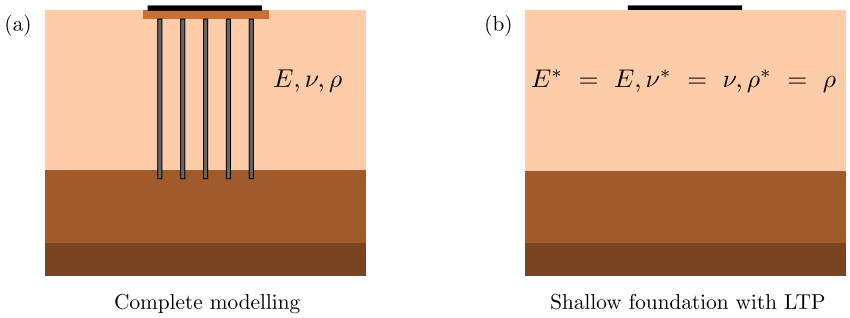

Fig. 5.14. Equivalent profile for horizontal behaviour: (a) complete modelling, (b) shallow foundation with LTP

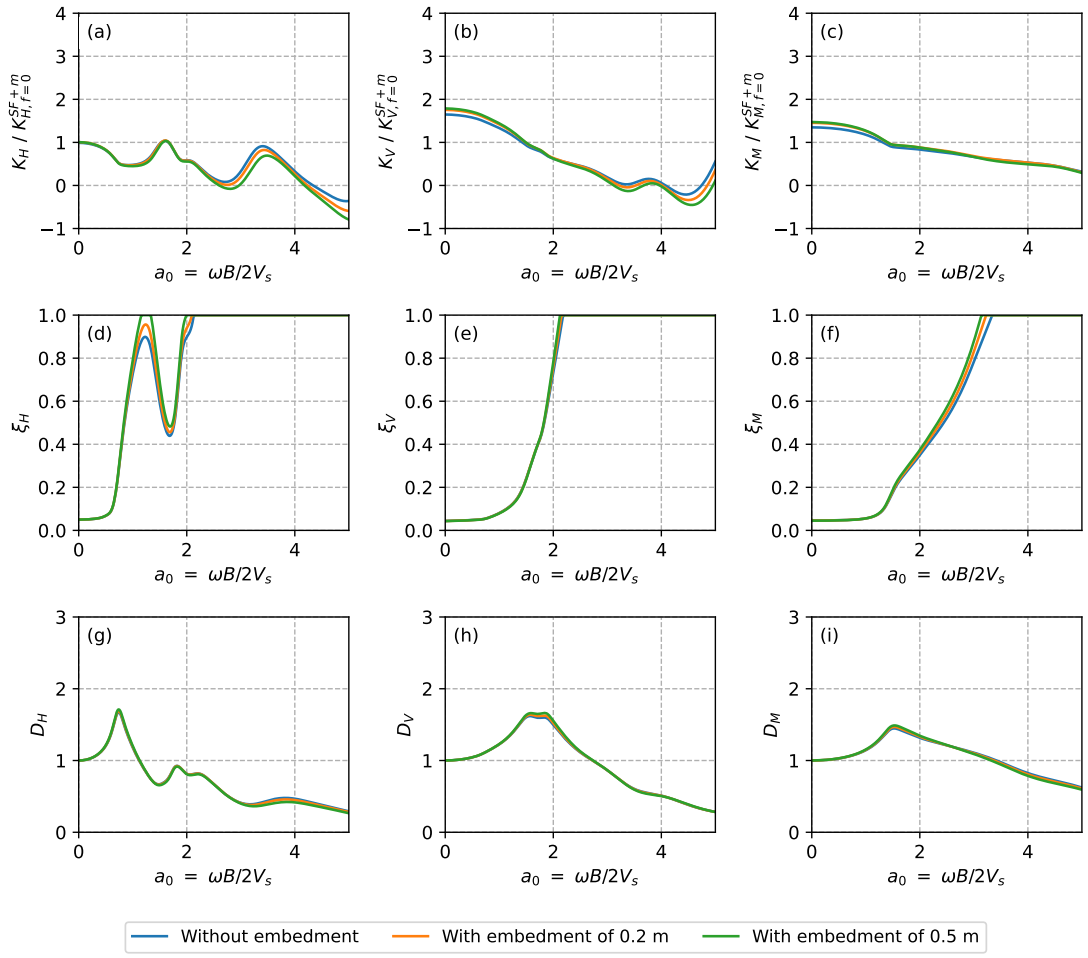

Fig. 5.13. Dynamic stiffness and damping ratio for reinforced foundations with the different embedments of the rigid inclusions into the LTP

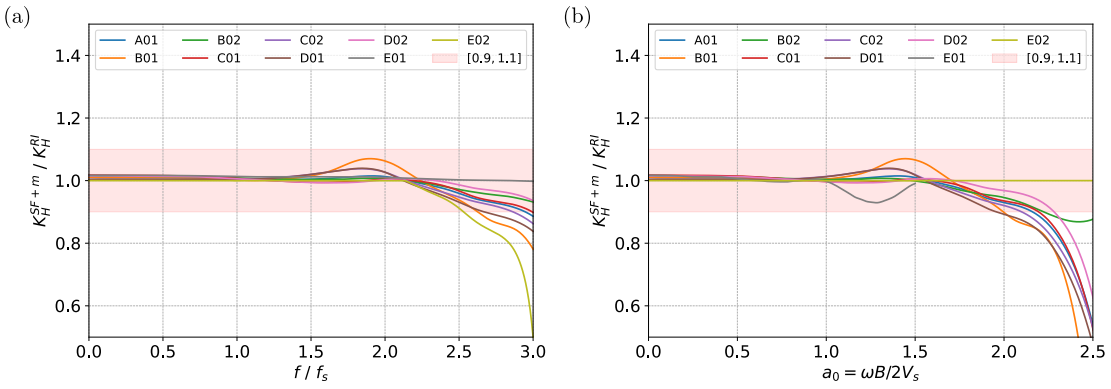

Fig. 5.15. Ratio between horizontal stiffness of complete model and equivalent profile

The comparison between C_H^{RI} and C_H^{SF+m} of the two systems highlights that the damping of the inclusion-reinforced foundation can be reasonably approximated using a shallow foundation modelling, with an error margin below 10 %, as depicted in Figure 5.16.

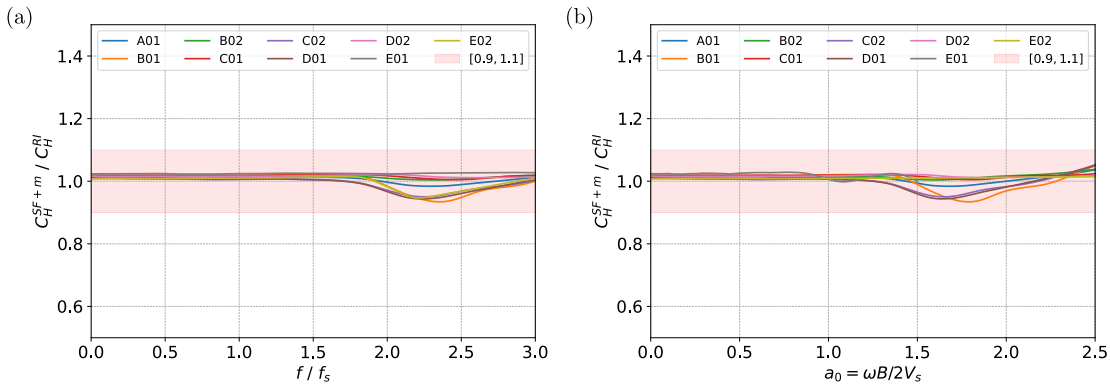

Fig. 5.16. Ratio between horizontal damping of complete model and equivalent profile

5.5.2 Equivalent profile for vertical and rotational responses

In the reinforcement system, rigid inclusions are employed to reduce the settlement, which implies an increase in vertical stiffness. Consequently, the presence of rigid inclusions should be considered in the equivalent profile.

Like the equivalent profile proposed for the horizontal direction, an equivalent profile can be defined for the vertical direction. The vertical equivalent profile is characterised by an equivalent elastic modulus E^*, a Poisson's ratio ν^*, and a mass density ρ^*, as depicted in Figure 5.17 (b).

In studies related to the inclusion reinforcement under static conditions (Cuira and Simon, 2009, 2013; Alzate and Cuira, 2022), the equivalent elastic modulus E^* can be determined using an elementary cell model, as illustrated in Figure 5.18. Equation 5.13 is used to determine this equivalent elastic modulus E^*.

$$E_{eq} = \frac{\Delta\sigma}{\Delta s/H} \tag{5.13}$$

where $\Delta\sigma$ represents the stress applied to the elementary cell, Δs is the settlement between the base of the foundation and the base of the inclusions, and H corresponds to the total height of the homogenised soil.

Similarly, for dynamic conditions, the equivalent elastic modulus E^* can be also obtained using the same model with the dynamic properties of the soil and inclusions. For the configurations outlined in Table 5.2, the parameters of the homogenised equivalent profile are listed in Table 5.3.

The dynamic impedances are computed using a shallow foundation model implemented on the equivalent profile illustrated in Figure 5.17 (b) and then compared with the dynamic impedances calculated with the complete model illustrated in Figure 5.17 (a).

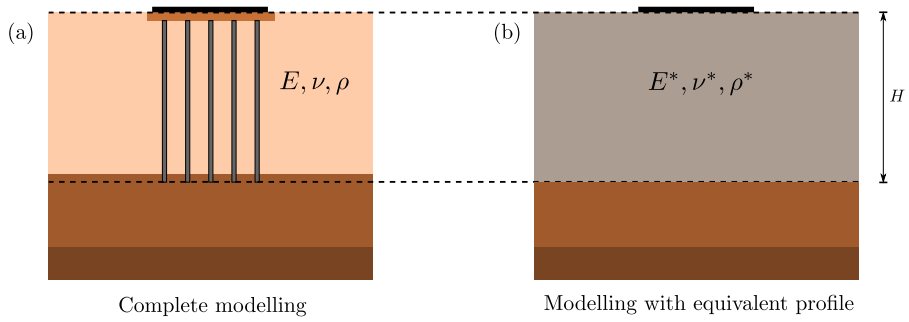

Fig. 5.17. Equivalent profile for vertical and rotational behaviour

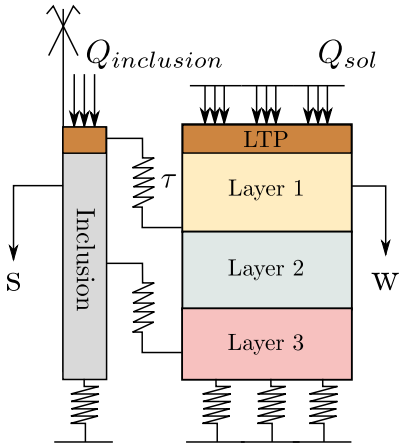

Fig. 5.18. Two-phase soil-inclusion elementary cell model

The ratio between the vertical dynamic stiffness of the two models, K_V^{homo} / K_V^{RI}, as a function of frequency normalised by f_c, is illustrated in Figure 5.19. The depicted ratio generally falls within the range of 0.8 to 1.2 for the frequencies below f_c. This comparison underscores that the vertical dynamic stiffness of an inclusion-reinforced foundation can be reasonably approximated using a shallow foundation model on an equivalent profile for frequencies smaller than the fundamental frequency of soil column f_c, with notable accuracy.

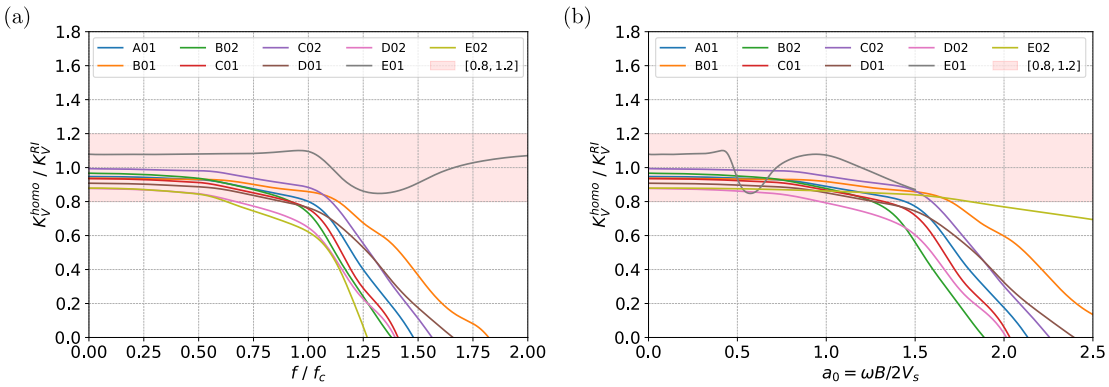

Fig. 5.19. Ratio between vertical stiffness of complete modelling and equivalent profile modelling

Tab. 5.3. Mechanical properties of equivalent profiles for different cases

Group	Case	$V_{s,soft\ soil}$ (m/s)	E^* (MPa)	ν^* (-)	ρ^* (t/m^3)	V_s^* (m/s)
A	01	150	230.7	0.45	2.0	199.4
B	01	100	149.6	0.45	2.0	160.6
	02	200	331.1	0.45	2.0	239.0
C	01	150	202.1	0.45	2.0	186.6
	02	150	263.6	0.45	2.0	213.2
D	01	150	300.6	0.45	2.0	227.6
	02	150	197.7	0.45	2.0	184.6
E	01	150	230.7	0.45	2.0	199.4
	02	150	230.7	0.45	2.0	199.4

Similarly, the ratio between the damping calculated by the two systems, C_V^{homo} / C_V^{RI}, is calculated and presented in Figure 5.20. The divergence in damping between the two models generally remains within a margin of 20 %.

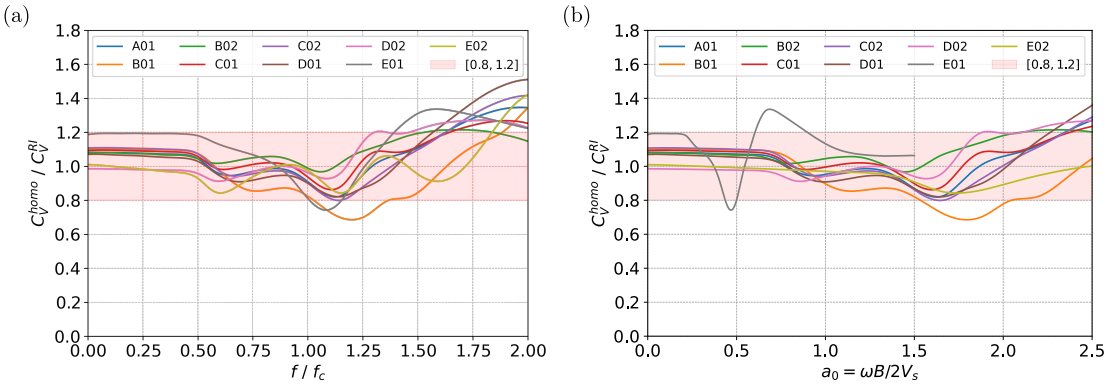

Fig. 5.20. Ratio between vertical damping of complete modelling and equivalent profile modelling

An identical investigation is conducted for the rotational dynamic stiffness K_M and rotational damping C_M. The rotational stiffness and damping comparisons between the complete modelling and the homogenised equivalent modelling are presented in Figures 5.21 and 5.22.

As depicted in Figure 5.21 (a), the ratio of rotational stiffness consistently falls within the range of 0.8 to 1.2 for frequencies below f_c. This outcome underscores that the estimation of rotational stiffness using a homogenised equivalent profile remains acceptable and accurate within the frequency range smaller than f_c.

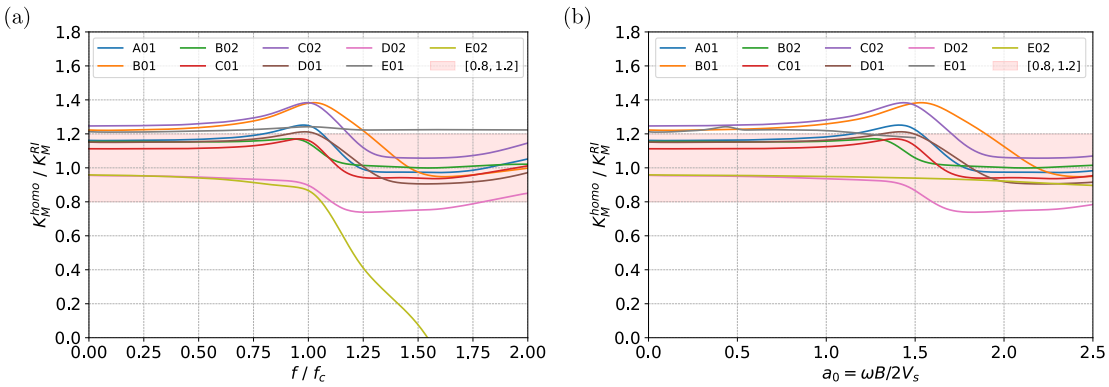

Fig. 5.21. Ratio between rotational stiffness of complete modelling and equivalent profile modelling

The exploration of rotational damping is also undertaken. The ratio of rotational damping is showcased in Figure 5.22. It becomes apparent that the equivalent profile modelling predominantly overestimates the rotational damping by up to 40 %. When estimating the damping of a rigid inclusion-reinforced foundation using a shallow foundation on the equivalent profile, it is important to consider a correction for the rotational damping ratio.

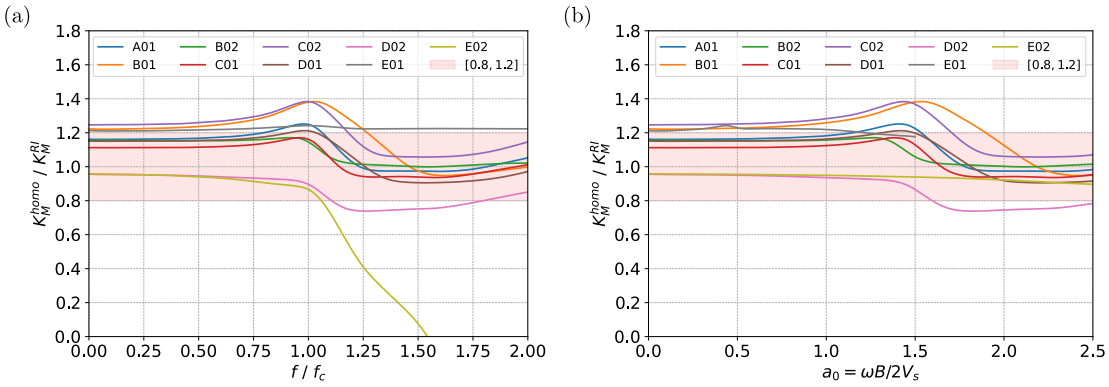

Fig. 5.22. Ratio between rotational damping of complete modelling and equivalent profile modelling

5.6 Coupling terms of dynamic impedances

In most cases, coupling effects can be disregarded when dealing with shallow foundations. The non-diagonal values, which pertain to the coupling between translation, rocking, and torsional motions, are neglected and omitted in the structural analysis. In the case of reinforcement by rigid inclusions, which share a similarity with the pile foundation system, it is important to note that coupling terms could arise. To verify the coupling

effects, the comparisons of the dynamic impedance functions with and without coupling terms for the examined configurations are illustrated in Figures 5.23 and 5.24.

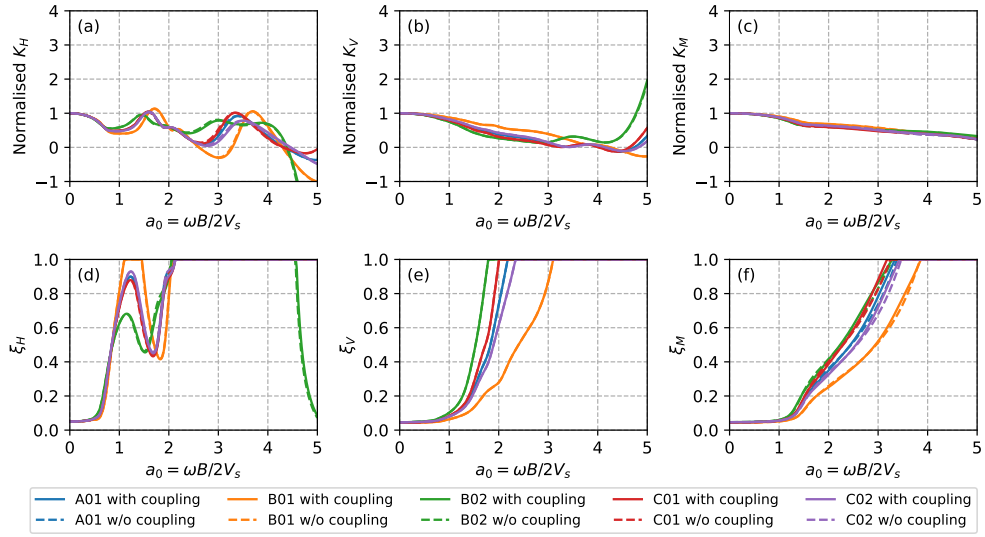

Fig. 5.23. Comparison of Dynamic stiffness and damping ratio with or without coupling terms for Configurations A01 (reference), B01 ($V_{s,soft\ soil} = 100m/s$), B02 ($V_{s,soft\ soil} = 200m/s$), C01 ($d = 0.32m$), and C02 ($d = 0.52m$)

The dynamic stiffness is normalised by the static stiffness for all studied configurations. The obtained results exhibit that the dynamic impedance functions with the coupling effect and without the coupling effect overlap each other, which means that the coupling effect is minimal. Consequently, in practical terms, it is reasonable to disregard the coupling effect when dealing with foundations reinforced by rigid inclusions.

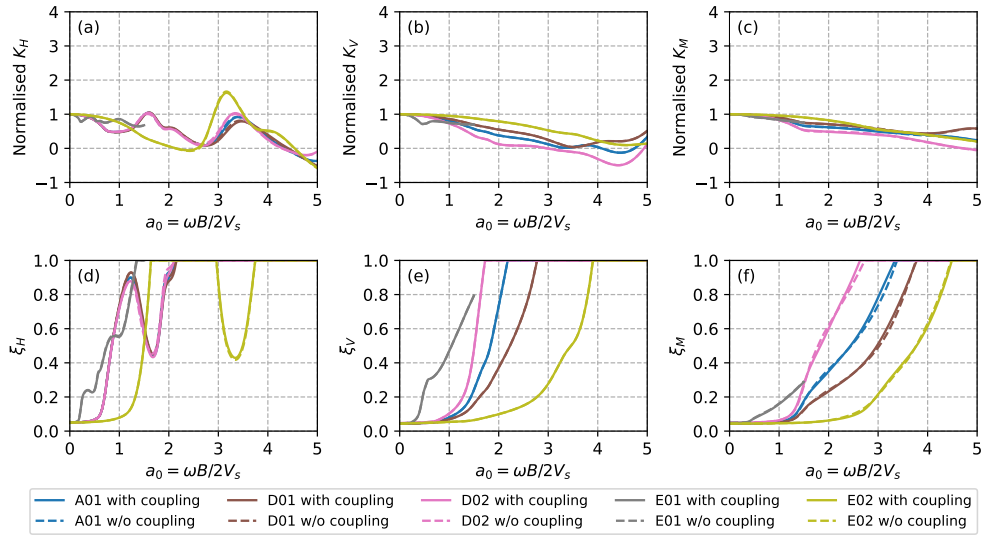

Fig. 5.24. Comparison of Dynamic stiffness and damping ratio with or without coupling terms for Configurations A01 (reference), D01 ($s = 1.5m$), D02 ($s = 2.5m$), E01 ($d = 3m$), and E02 ($B = 20m$)

5.7 Summary

The comparative analysis reveals the emergence of anisotropic behaviour in dynamic responses, which affects both dynamic stiffness and damping characteristics. Notably, the dynamic stiffness and damping behaviour in the horizontal direction for foundations on rigid inclusions closely resemble those observed in shallow foundations with LTP. It has been shown that the presence of rigid inclusion exerts negligible influence on the dynamic stiffness and damping behaviour of the foundation system in the horizontal direction.

The dynamic stiffness behaviour in both vertical and rotational modes of a foundation reinforced by rigid inclusions inherently lies between the stiffness values observed in shallow foundations and pile foundations. When compared to shallow foundations, the incorporation of rigid inclusions introduces an increase in vertical and rotational stiffness properties. On the other hand, the vertical and rotational dynamic stiffness values for pile foundations typically surpass those exhibited by foundations reinforced with rigid inclusions. This difference can be attributed to the absence of a direct structural connection between the foundation and rigid inclusions.

A comprehensive investigation has also been conducted to study how the parameters of a rigid inclusion-reinforced foundation system impact its dynamic impedances: coverage area ratio, length, and embedment of rigid inclusions in LTP. The vertical and rotational behaviour is affected by the coverage area ratio α. The reinforced foundation with a greater coverage area ratio α is much stiffer. There is a significant difference between the reinforcement by end-bearing inclusions and the floating inclusions. The vertical and rotational stiffness increase is only observed for the end-bearing inclusion configuration. These findings underline the importance of these parameters in shaping the vertical and rotational responses of the reinforced foundations.

In engineering practice, homogenised equivalent profiles are commonly employed to simplify the modelling. Such homogenised equivalent profiles negate the necessity for explicit modelling of rigid inclusions. The findings highlight that the calculation using an equivalent profile offers accurate estimations for frequencies below horizontal and vertical fundamental frequencies of soil column f_s and f_c or the dimensionless frequency smaller than a_0.

6 Inertial forces within rigid inclusions

6.1 Additional inertial forces

Apart from the static vertical loads stemming from dead loading and vertical acceleration, rigid inclusions must also bear bending moments and shear forces atop due to the horizontal inertial forces transmitted to the reinforced soil at the base of the structure, as illustrated in Figure 6.1.

The distribution of inertial loads at the base of the structure to the soft soil and the rigid inclusions is facilitated by the LTP. Consequently, the properties of LTP can have an impact on the response of this type of foundation.

Hence, there is a clear need to enhance the understanding of the force transfer mechanism and the inertial bending moment through an extensive parametric study. The objective is to generate design charts that can guide the engineering practice.

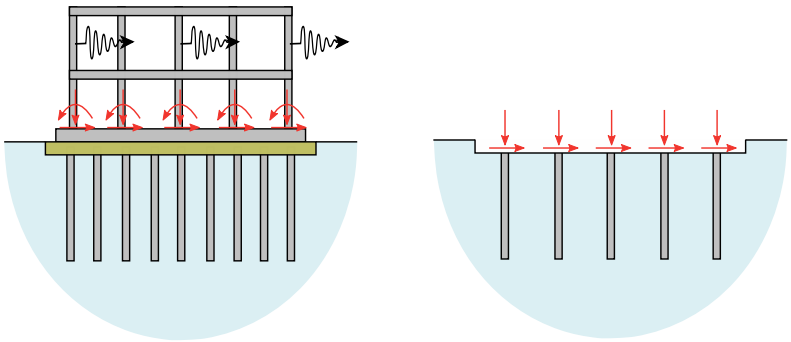

Fig. 6.1. Inertial interaction forces transferred to rigid inclusions via LTP

6.2 Forces transmitted onto the head of the inclusions

6.2.1 Force concentration at the head of the inclusions

This study examines the inertial load resulting from the mass of the superstructure in a pseudo-static mode. When a pseudo-static load is imposed on a reinforced foundation, only a portion of the load is carried by the rigid inclusions. It is of interest to investigate

the proportion of the load that is taken by the rigid inclusions versus the portion carried by the surrounding soil.

To investigate the concentration of vertical and horizontal forces at the head of the rigid inclusions, the vertical and the horizontal force concentration ratios, denoted E_V and E_H, are introduced. These ratios serve to measure the load transfer efficiency and are defined by Equations 6.1 and 6.2, respectively.

$$E_V = \frac{\sum V_{RI,i}}{V} \tag{6.1}$$

$$E_H = \frac{\sum H_{RI,i}}{H} \tag{6.2}$$

where V and H denote the vertical and horizontal pseudo-static forces applied to the foundation, while $V_{RI,i}$ and $H_{RI,i}$ represent the forces distributed at the head of the inclusions, as illustrated in Figure 6.2.

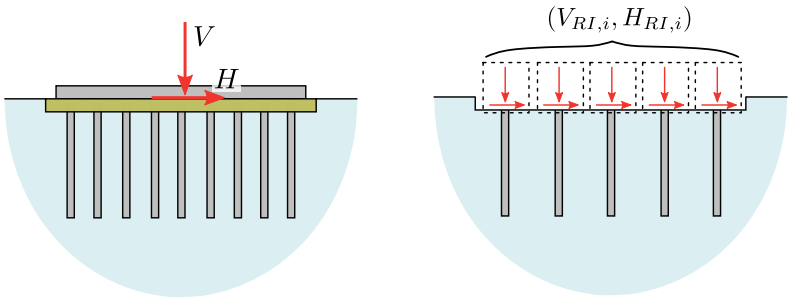

Fig. 6.2. Vertical force V and horizontal force H applied at the foundation and transmitted to the head of the inclusions

These efficiency parameters provide insights into how effectively the rigid inclusions contribute to the distribution and transfer of vertical and horizontal loads within the foundation system.

6.2.2 Studied configurations

In this study, the profile consists of a layer of soft soil with a thickness H_{soil} of 10 m and a subsequent layer of more compact soil that is 5 m thick. This profile arrangement is visually represented in Figure 6.3(a).

Two different dimensions are selected for the small square footing foundations, denoted as B, measuring 3 m and 5 m. The configuration involving the 3 m footing foundation comprises four inclusions arranged in a 2 $\times$ 2 grid pattern, as depicted in Figure 6.3(b).

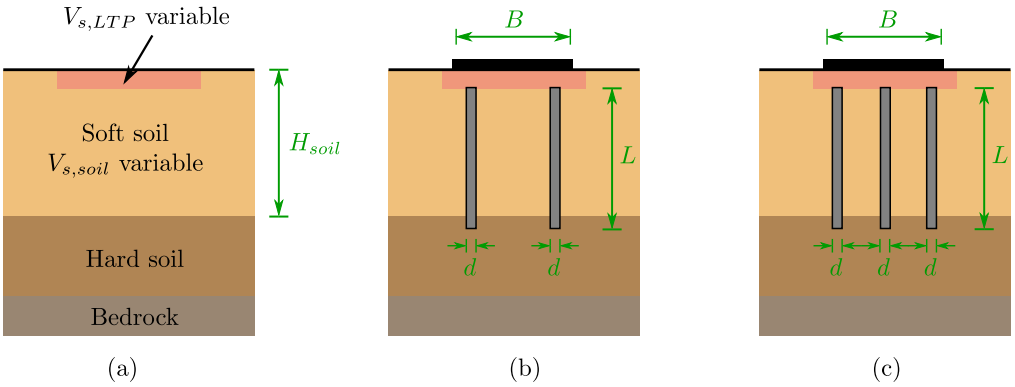

Fig. 6.3. Small footing configurations: (a) soil profile, (b) configuration with 4 (2×2) rigid inclusions and (c) configuration with 9 (3×3) rigid inclusions

The configuration featuring the 5 m footing foundation includes a total of nine inclusions arranged in a 3×3 grid pattern, as shown in Figure 6.3(c).

A large square footing is also selected, corresponding to the configuration D01 studied in Chapter 5. The square footing foundation has dimensions of 10 m. This configuration includes 49 inclusions arranged in a 7 × 7 grid pattern, as depicted in Figure 6.4.

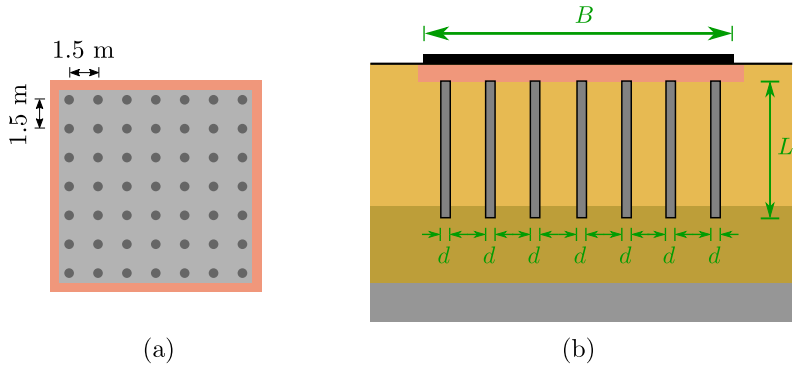

Fig. 6.4. Large footing 7 × 7 configuration: (a) plan view and (b) section view

The study investigates rigid inclusion-reinforced foundations with varying inclusion diameters of 0.32 m, 0.42 m, and 0.52 m. The LTP is characterised by the ratio of its shear wave propagation velocity V_s, LTP to that of the soft soil, denoted $V_{s,LTP}/V_{s,soil}$. The shear wave velocity of LTP varies from the velocity of the soft soil (representing the case without an LTP) to the velocity of concrete (representing a configuration with a concrete LTP). The mechanical properties employed in the model are detailed in Table 6.1.

Tab. 6.1. Mechanical properties of the soil and the foundation

	Soft soil	Hard soil	Bedrock	LTP	Inclusions
Shear modulus G (MPa)	45	320	2 500	45 to 12 500	12 500
Shear wave velocity V_s (m/s)	150	400	1 000	100 to 2 500	2 236
Poisson's ratio ν (-)	0.45	0.45	0.45	0.35	0.2
Mass density ρ (t/m^3)	2.0	2.0	2.5	2.0	2.5

6.2.3 Model description

A finite-element model of the rigid inclusion-reinforced foundation is created using PLAXIS 3D software (Bentley, 2022b). The entire footing foundation, including the inclusions, is represented in the model. The components are characterised using linear elastic behaviour. For the foundation, weightless plate elements with six nodes are employed, and a very high elastic modulus is assigned to mimic a rigid behaviour. The LTP and the soil are explicitly modelled using ten-node tetrahedral elements. Similarly, the inclusions are also modelled as volume elements. To capture the internal forces within the inclusions, such as axial force, shear force, and bending moment, a weightless fictive beam is introduced at the centre of the inclusion's volume. This fictive beam has a stiffness 1 000 times lower than that of the real cylinder concrete inclusions.

The model dimensions are set at 50 m $\times$ 50 m, ensuring that the edges are at a distance greater than 10 times the foundation dimension to prevent edge effects. A visualisation of the model is presented in Figure 6.5.

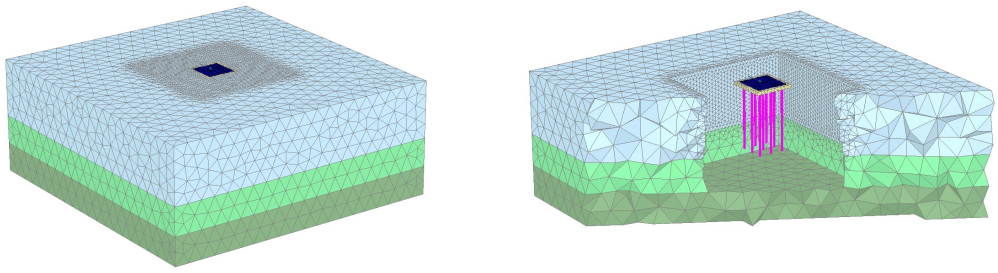

Fig. 6.5. Finite element model of a foundation on rigid inclusions

6.2.4 Vertical load transfer efficiency

The investigation begins with an analysis of a pseudo-static vertical load that is applied at the centre of the foundation. The efficiency of vertical load transfer is depicted in Figures 6.6 and 6.7, using the ratio between the vertical force concentration ratio E_V and the coverage area ratio α. These figures provide insights into the efficiency of vertical load transfer for the 2 $\times$ 2 and the 3 $\times$ 3 configurations.

The observed vertical efficiency spans from 44 % to 64 % across the studied configurations, ranging from 3 to 17 times the coverage area ratio α. The efficiency, denoted by E_V, increases as the contrast of V_s between the LTP and the soft soil becomes more pronounced. In other words, when the soil is softer in comparison to the LTP, a higher vertical force concentration is experienced. This also implies that enhancing the stiffness of the LTP can increase the efficacy of the soil improvement.

As an example, in the case of the 2×2 rigid inclusion configuration with a diameter of 0.42 m, the ratio E_V/α nearly reaches 4, resulting in a vertical efficiency E_V of approximately 24.8 % assuming that V_s for the soft soil and the LTP are equal. If the shear wave velocity $V_{s,LTP}$ increases by three times, the ratio E_V/α can reach 7.5, resulting a vertical efficiency E_V of 46.5 %.

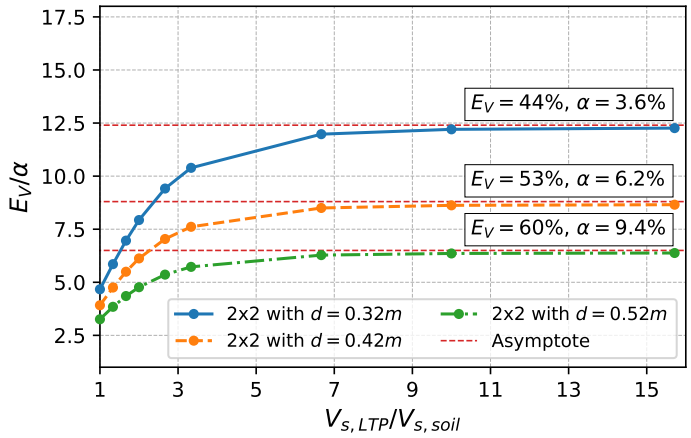

Fig. 6.6. Vertical load transfer efficiency E_V with respect to the ratio of V_s of the LTP and the soft soil for the 2 × 2 configuration with different coverage area ratios α

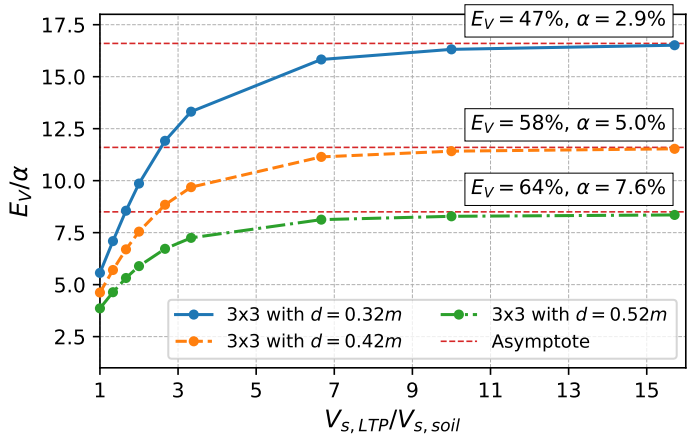

Fig. 6.7. Vertical load transfer efficiency E_V with respect to the ratio of V_s of the LTP and the soft soil for the 3 × 3 configuration with different coverage area ratios α

However, once the stiffness reaches a critical value, the efficiency plateaus and further increase becomes limited. As depicted in Figures 6.6 and 6.7, the vertical efficiency E_V stabilises around 60 % for inclusions with a diameter of 0.52 m and approximately 44 % for a diameter of 0.32 m in the context of the 2×2 inclusion configuration. The vertical transfer efficiency E_V increases with the coverage area ratio α. A similar trend is observed for the 3×3 configurations. The maximum efficiency of the reinforced foundation system is attained for ratios of $V_{s,LTP}/V_{s,soil}$ higher than 10. This implies that a further increase in the stiffness of LTP will not result in a higher vertical transfer efficiency E_V.

The same observations applicable to the small footing with few inclusions are also valid for the large footing configuration under study. The vertical load transfer efficiency for the 7 × 7 configuration is illustrated in Figure 6.8. The vertical load transfer efficiency ranges from 65 % to 77 %, covering a range from 3 to 17 times the coverage area ratio α. Comparatively, the vertical load transfer efficiency of the large square footing is slightly higher than that of the small square footing foundations.

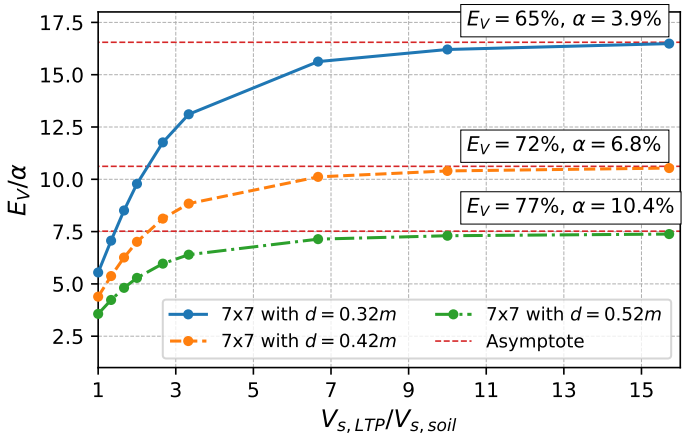

Fig. 6.8. Vertical load transfer efficiency E_V with respect to the ratio of V_s of the LTP and the soft soil for the 7 × 7 configuration with different coverage area ratios α

The study conducted in this section reveals that vertical load transfer efficiency is influenced by both the LTP-soft soil stiffness ratio and the coverage area ratio. An increase in both of these factors leads to improved vertical load transfer efficiency. However, it is important to note that increasing the LTP-soft soil stiffness ratio has a more significant impact on the vertical efficiency at low stiffness ratio. In general, beyond an LTP-soft soil stiffness ratio of 10, vertical load efficiency tends to a plateau.

6.2.5 Horizontal load transfer efficiency

The study proceeds to examine the horizontal stress concentration ratio E_H by simulating a horizontal load that could correspond for example to the inertia force of the superstructure mass applied at the centre of the foundation. The results are depicted in Figures 6.9 and 6.10, for the 2 × 2 and the 3 × 3 configurations, respectively.

Low values of the E_H / α ratio indicate that the horizontal forces are predominantly transmitted to the underlying soil. The highest value observed for E_H is approximately 20 %. The ratio E_H / α remains considerably small in comparison to the E_V / α ratio presented in Figures 6.6 and 6.7. This observation suggests that the improvement by rigid inclusions is more prominent in the vertical direction than in the horizontal direction.

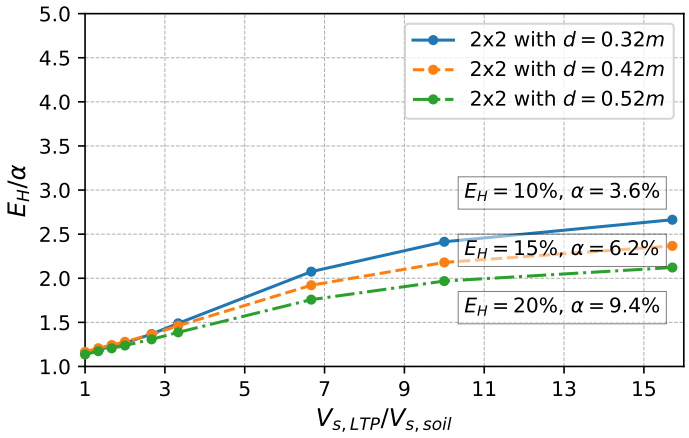

Fig. 6.9. Horizontal load transfer efficiency E_H with respect to the ratio of V_s of the LTP and the soft soil for the 2×2 configuration with different coverage area ratios α

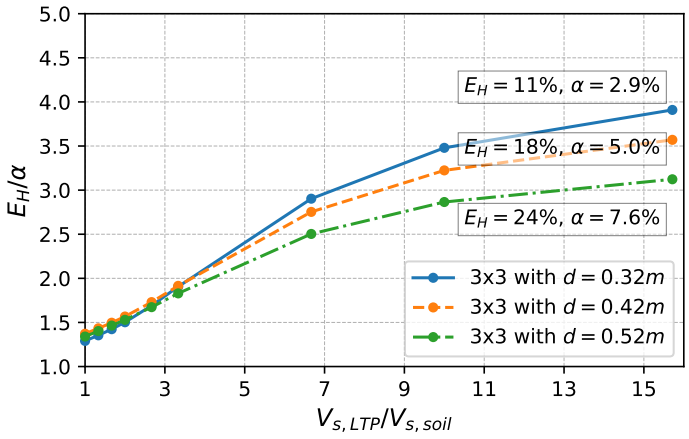

Fig. 6.10. Horizontal load transfer efficiency E_H with respect to the ratio of V_s of the LTP and the soft soil for the 3×3 configuration with different coverage area ratios α

The E_H / α ratio also increases as the stiffness contrast between the LTP and the soft soil increases. The same trend is observed in all the studied configurations.

The results from both studied configurations reveal an interesting observation: the E_H / α ratios for various diameters, reflecting different coverage area ratios α, display the same order of magnitude when the shear wave propagation velocity ratio $V_{s,LTP}/V_{s,soil}$ remains below 3.

The horizontal load transfer efficiency for the 7×7 configuration is illustrated in Figure 6.11. The conclusions drawn from the 2×2 and 3×3 configurations remain applicable to this configuration.

In summary, the horizontal load transfer efficiency rises with both the LTP-soft soil stiffness ratio and the coverage area ratio α. Unlike the vertical load transfer efficiency, there

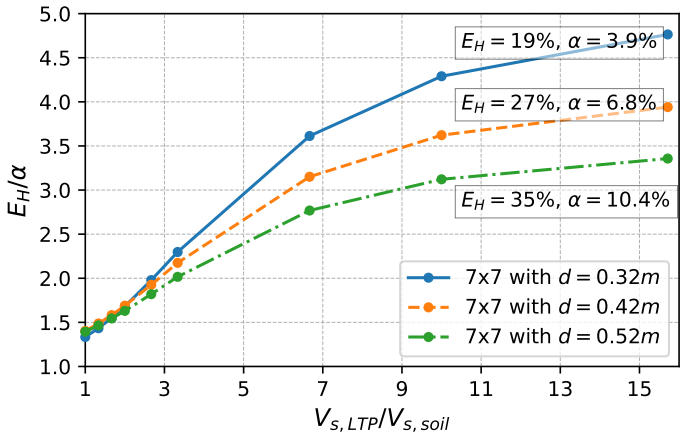

Fig. 6.11. Horizontal load transfer efficiency E_H with respect to the ratio of V_s of the LTP and the soft soil for the 7 × 7 configuration with different coverage area ratios α

is no plateau for the horizontal load transfer efficiency. The limited horizontal load transfer efficiency aligns with the observations from the dynamic impedance study in Chapter 5, indicating that the presence of rigid inclusions does not significantly enhance the horizontal dynamic stiffness.

6.2.6 Ratio between vertical and horizontal load transfer efficiencies

For a given configuration, the vertical and horizontal efficiencies can be compared in terms of the $V_{s,LTP}/V_{s,soil}$ ratio such as presented in Figures 6.12, 6.13, and 6.14.

It is evident from the results that the vertical efficiency E_V consistently surpasses the horizontal efficiency E_H, across all examined cases. The E_V / E_H ratios are systematically higher than unity. The horizontal efficiency E_H is roughly 3 to 7 times lower than the vertical transfer efficiency E_V. This finding substantiates the notion that the transfer of vertical loads through rigid inclusions is more effective than the transfer of horizontal loads.

The E_V / E_H ratio increases rapidly up to values of $V_{s,LTP}/V_{s,soil}$ around 3, after which it gradually decreases as the same ratio increases. The same pattern is observed across all tested configurations. Significantly larger differences between E_V and E_H manifest in configuration characterised by small α values (the configuration with a diameter of 0.32 m in this study). This trend is noticeable in the 2 × 2, 3 × 3, and 7 × 7 rigid inclusion configurations.

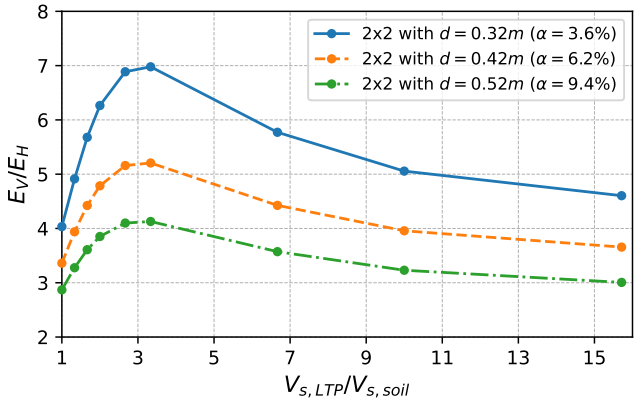

Fig. 6.12. Ratio between vertical and horizontal load transfer efficiency E_V / E_H with respect to the ratio of V_s of the LTP and the soft soil for the 2 × 2 configuration with different coverage area ratios α

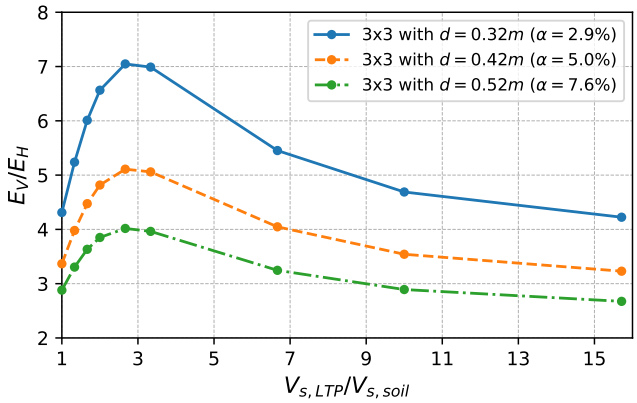

Fig. 6.13. Ratio between vertical and horizontal load transfer efficiency E_V / E_H for the 3 × 3 configuration with different coverage area ratios α

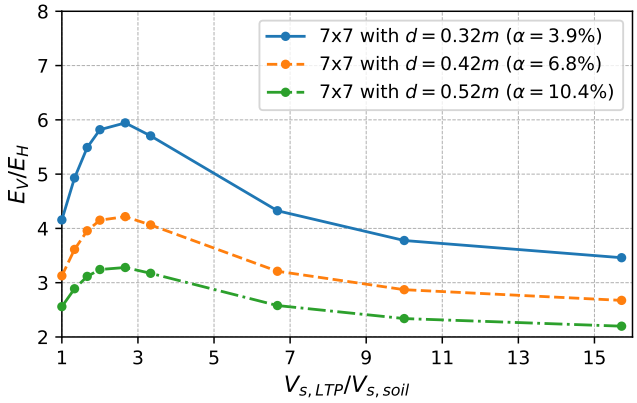

Fig. 6.14. Ratio between vertical and horizontal load transfer efficiency E_V / E_H with respect to the ratio of V_s of the LTP and the soft soil for the 7 × 7 configuration with different coverage area ratios α

The examination of the ratio between vertical and horizontal load transfer efficiencies reveals that horizontal forces are predominantly transmitted through the surrounding soil. When subjected to horizontal loading, the horizontal load transfer efficiency is 2 to 7 times lower than the vertical load transfer efficiency, and this difference is more pronounced for the configurations with higher coverage area ratios. Based on this observation, it can be concluded that the surrounding soil experiences a more inclined load when rigid inclusions are present compared to a non-reinforced foundation.

6.3 Inertial bending moment

In the previous section, the forces transmitted at the head of the inclusions are studied. However, it is important to note that forces, including bending moments, can also be generated within the rigid inclusions themselves, not only just at their heads. These inertial-induced bending moments can reach significant magnitudes. This section is dedicated to the study of the inertial-induced bending moments within the rigid inclusions.

6.3.1 Studied configurations

To investigate the bending moment experienced by inclusions within an inclusion-reinforced foundation, the study considers the same soil profile as that examined in the preceding section with a variable thickness H_{soil} for the soft soil layer, ranging between 5 m, 10 m and 15 m. This configuration is depicted in Figure 6.3 (a). Several values of the shear wave velocity V_s of the soft soil varying from 100 m/s to 300 m/s in increments of 50 m/s are used. Furthermore, the ratio of shear wave velocities between LTP and the soft soil, is fixed to be equal to 1, 1.5, and 2. The mechanical properties of the model are outlined in Table 6.2.

Two different sizes of the foundation are studied, 3 m and 5 m, including respectively 4 (2 $\times$ 2) and 9 (3 $\times$ 3) inclusions. The diameters of the rigid inclusions vary between 0.32 m, 0.42 m, and 0.52 m.

Tab. 6.2. Mechanical properties of the soil and the foundation for inertial bending moment study

	Soft soil	Hard soil	Bedrock	Inclusions
Shear modulus G (MPa)	20 / 45 / 80 / 125 / 180	320	2 500	12 500
Shear wave velocity V_s (m/s)	100 / 150 / 200 / 250 / 300	400	1 000	2 236
Poisson's ratio ν (-)	0.45	0.45	0.45	0.2
Mass density ρ (t/m^3)	2.0	2.0	2.5	2.5

6.3.2 Inertial bending moment within rigid inclusions

For a single pile, Brûlé and Cuira (2018) have proposed Equation 6.3 to assess the maximum bending moment of a hinge pile (free rotation at head) within the elastic domain in the case of a homogeneous soil, or at least for situation where the thickness of the surface layer is greater than 3 times the effective length l_0, as depicted in Figure 6.15 (a). The proposed equation takes into account three key parameters: the effective length l_0 mentioned in Equation 4.2, the applied horizontal force at the pile head H, and a constant coefficient β.

$$M_{max} = \beta H l_0 \quad \text{with} \quad \beta = 0.32 \tag{6.3}$$

This study endeavours to approximate the maximum bending moment for the rigid inclusions under a horizontal force applied at the foundation, as shown in Figure 6.15 (b). To adapt the formulation for the hinge pile, a simplified model with a single inclusion is depicted in Figure 6.15 (c). In this model, the force applied to the base of the foundation (not at the head of the inclusions) is assumed to be equal to the total horizontal force divided by the number of rigid inclusions, denoted as N_{RI}.

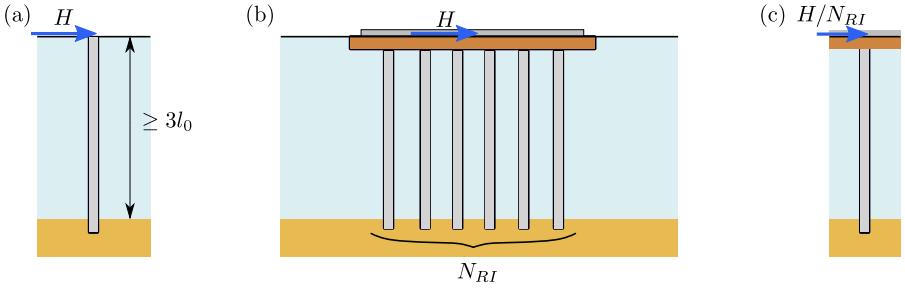

Fig. 6.15. Scheme of horizontal force applied at: (a) a single hinge pile, (b) a foundation on rigid inclusions, and (c) a single rigid inclusion

By replacing the horizontal force H in Equation 6.3 with H/N_{RI}, a similar formulation can be derived as Equation 6.4, which is employed to estimate the maximum bending moment for the rigid inclusions. In this context, a coefficient for rigid inclusions denoted as β_{RI} in Equation 6.4 is used instead of β as used in Equation 6.3.

$$M_{max} = \beta_{RI} H l_0 / N_{RI} \tag{6.4}$$

A comprehensive numerical parametric study is carried out, encompassing various configurations. The coefficient β_{RI}, which governs the maximum bending moment, is depicted graphically in Figures 6.16 and 6.17, featuring dimensionless factors derived from configuration parameters.

From the results of the studied configurations, the magnitude of the coefficient β_{RI} remains consistent, spanning the range from 0.01 to 0.07. The results demonstrate that the maximum bending moment sustained by a rigid inclusion of the rigid inclusion-reinforced foundation is significantly below that encountered by a hinge pile, with a ratio of 1/5 to 1/20.

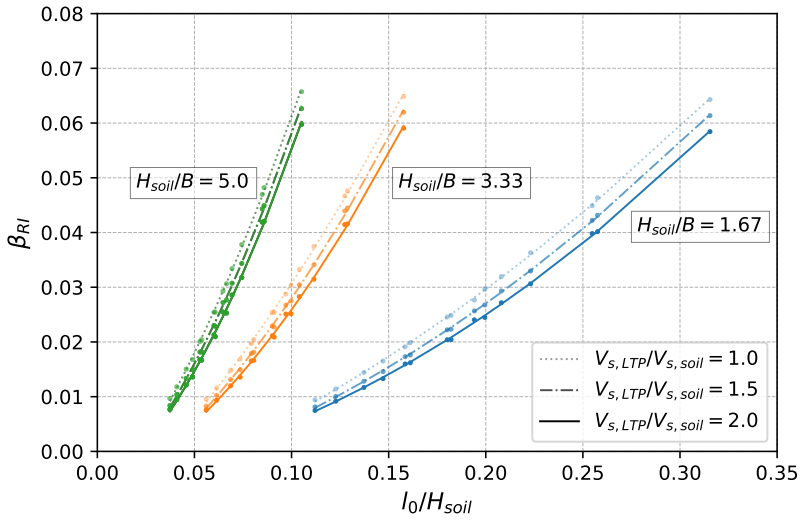

Fig. 6.16. Maximum bending moment coefficient β_{RI} in the rigid inclusions with respect to the ratio of the effective length and the thickness of the soil for the 2×2 configuration with different H_{soil}/B and $V_{s,LTP}/V_{s,soil}$ ratios

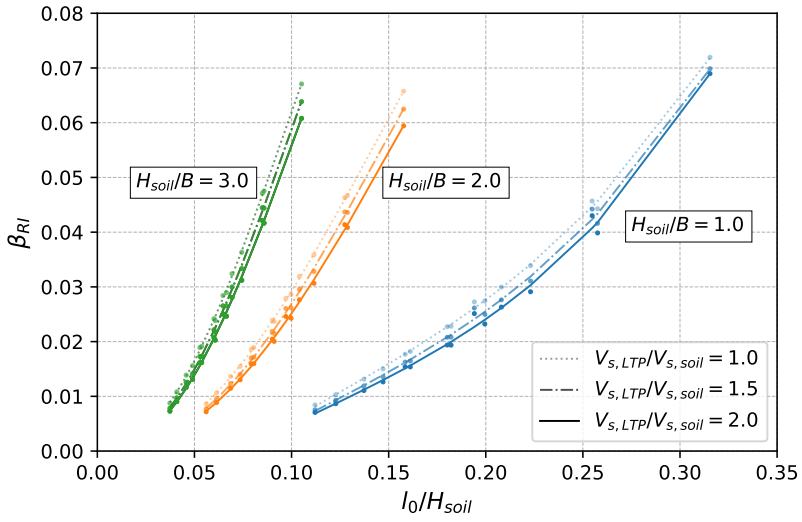

Fig. 6.17. Maximum bending moment coefficient β_{RI} in the rigid inclusions with respect to the ratio of the effective length and the thickness of the soil for the 3×3 configuration with different H_{soil}/B and $V_{s,LTP}/V_{s,soil}$ ratios

The coefficient β_{RI} increases with the ratio of effective length l_0 to the thickness H_{soil} for the same configuration with H_{soil}/B held constant. It is also noteworthy that the stiffness

contrast between the LTP and the soft soil, represented by the ratio $V_{s,LTP}/V_{s,soil}$, exerts negligible influence on the maximum bending moment.

6.4 Summary

Within this chapter, the study has been executed using a finite element model. The primary objective of the numerical investigation was to scrutinise the effects of inertial loads upon rigid inclusions in terms of load transfer efficiency and maximum bending moments.

Unlike conventional pile foundations, where the entire applied load is considered transmitted directly to the piles, the load transfer mechanism in foundations reinforced by rigid inclusions becomes inherently more intricate due to the presence of LTP. It is apparent that the load transfer mechanism, both horizontally and vertically, is influenced by the stiffness contrast between the LTP and the soft soil, evaluated through the shear wave propagation velocities $V_{s,LTP}/V_{s,soil}$. The findings highlight a noteworthy difference: the efficiency of the horizontal load transfer mechanism is lower compared to the vertical load.

The examination shifts towards the investigation of the maximum bending moment experienced by the rigid inclusions. The maximum bending moment sustained by a rigid inclusion of the rigid inclusion-reinforced foundation is significantly below that encountered by a hinge pile. These figures have the potential to serve as design charts, offering a tool for estimation of the maximum bending moment during a preliminary design phase.

In further studies, exploring the importance of different parameters on the load transfer mechanism and the maximum bending moment through a broader range of configurations via additional sensitivity analysis would be of considerable interest.

7 Kinematic bending moment within rigid inclusions

7.1 Additional kinematic forces

In addition to ground motion modification, the kinematic interaction also gives rise to additional kinematic forces, including shear forces and bending moments. These forces emerge due to the stiffness contrast between the soil and the foundation elements, as illustrated in Figure 7.1.

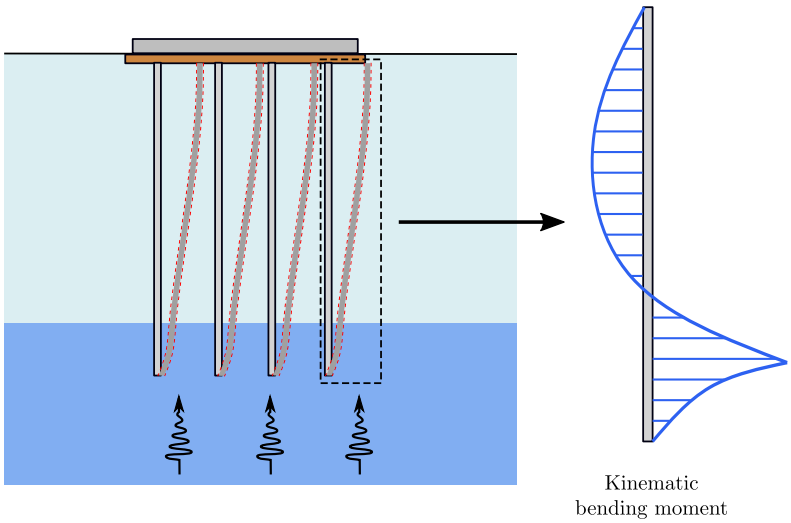

Fig. 7.1. Kinematic bending moment generated by wave propagation

In this study, the focus is on investigating the phenomenon of kinematic bending moments in rigid inclusions using a hybrid FEM-BIE modelling. Two main objectives are outlined:

- The investigation of the physical phenomenon of kinematic bending moments in rigid inclusions during earthquake excitation using dynamic calculation;
- A comparison between the complete dynamic model and the conventional pseudo-static approach to assess the validity of the latter.

The analysis is carried out on three distinct soil profile families characterised by varying soil stiffness contrasts at multiple interfaces between soil layers. These selected soil profiles are designed to closely replicate real projects.

7.2 Studied configurations

The soil improvement by rigid inclusions is commonly employed to increase the bearing capacity and to mitigate settlements under static loads. Typically, these foundation configurations are applied in situations categorised as class D or E, according to Eurocode 8 (AFNOR, 2007).

The soil profiles examined in this study aim to emulate various configurations that closely resemble those encountered in real projects. The considered profiles encompass the following configurations:

- Profile *I*: Comprises a 10 m thick layer of soft soil 1;
- Profile *II*: Built upon Profile *I*, with the initial 3 m of the soft soil layer replaced by soft soil 2, which is stiffer than soft soil 1;
- Profile *III*: Built upon Profile *I*, with an additional 2 m layer of soft soil 3 added within the soft soil layer, which is stiffer than soft soil 1.

All examined profiles involve a 5-m thick hard soil layer atop a semi-infinite dynamic substratum. The schematic illustration of the different soil profiles is provided in Figure 7.2, and the mechanical properties are summarised in Table 7.1.

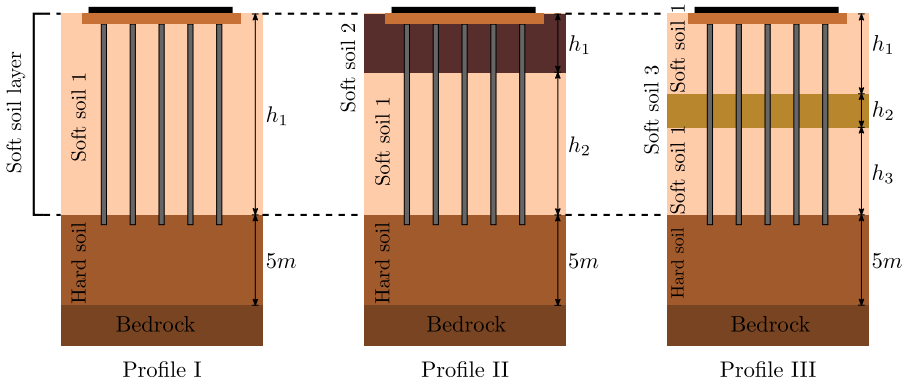

Fig. 7.2. Schemes of proposed soil profiles

Other geometric details of the proposed profiles are given in Table 7.2 along with the corresponding fundamental frequency f_s of the soil column. The shear wave velocity of the soft soil 1 varies among 100 m/s, 150 m/s and 200 m/s, respectively.

A ratio of the shear wave velocity contrast at an interface can be defined as Equation 7.1. A higher value of the ratio η indicates a greater stiffness contrast.

$$\eta = \frac{V_{s,hard}}{V_{s,soft}} \tag{7.1}$$

Tab. 7.1. Mechanical properties of soil and foundation used in the analyses

	Soft soil 1 (a/b/c)	Soft soil 2	Soft soil 3	Hard soil	Bedrock	LTP
Shear modulus G (MPa)	20/45/80	80	180	320	2 500	125
Young's modulus E (MPa)	58/130.5/232	232	522	928	7 250	362.5
Shear wave velocity V_s (m/s)	100/150 /200	200	300	400	1 000	250
Poisson's ratio ν (-)	0.45	0.45	0.45	0.45	0.45	0.35
Mass density ρ (t/m^3)	2.0	2.0	2.0	2.0	2.5	2.0
Material damping ratio ξ (-)	0.05	0.05	0.05	0.05	0.05	0.05

Tab. 7.2. Soil profile geometry and characteristic

Profile	Configuration	Shear wave velocity of soft soil 1 (m/s)	h_1 (m)	h_2 (m)	h_3 (m)	Fundamental frequency f_s (Hz)
I	*Ia*	100	10	-	-	2.42
	Ib	150	"	-	-	3.50
	Ic	200	"	-	-	4.43
II	*IIa*	100	3	7	-	2.46
	IIb	150	"	"	-	3.52
	IIc	200	"	"	-	4.43
III	*IIIa*	100	4	2	4	2.64
	IIIb	150	"	"	"	3.73
	IIIc	200	"	"	"	4.61

The foundation system is subjected to a set of five artificial accelerograms in Section 4.2.1 that align with the design spectrum, ensuring the relevance and practicality of the findings for engineering applications.

The study encompasses three soil profiles each featuring soft soil, with three distinct shear wave velocities V_s. This comprehensive parametric study encompasses a total of 45 calculations (3 soil profiles $\times$ 3 different V_s of soil soil 1 $\times$ 5 accelerograms).

7.3 Model description

In this chapter, a hybrid numerical model combining FEM-BIE is employed to investigate the kinematic bending moment within the inclusions of a reinforced foundation system.

The same numerical modelling principles outlined in Section 4.2.2 are applied here. The soil is represented through interaction nodes where Green's function is employed to calculate the dynamic impedances of the soil. The shallow foundation is modelled using a weightless rigid beam grid. The inclusions are modelled with beam elements to accurately capture their forces. The LTP is explicitly modelled with 8-node hexahedral elements. Vertically propagating SH-waves are employed as the excitation in the model. They are

defined at a point located a distance away from the modelled foundation at the ground surface level.

7.4 Kinematic bending moments calculated by dynamic approach

The physical phenomenon of kinematic bending moments in rigid inclusions during earthquake excitation is initially examined. An interesting aspect of the study is the investigation of the evolution of the kinematic bending moments at different time points, depths within the rigid inclusions, and positions of the rigid inclusions.

7.4.1 Bending moment time history

This section presents the time history of kinematic bending moments within the rigid inclusions. To keep the presentation concise, only the kinematic bending moment of the central inclusion is shown. The variations of kinematic bending moments within various soil profiles over time are illustrated in Figures 7.3, 7.4, and 7.5. For clarity, the bending moments have been normalised by the maximum bending moment value.

Figure 7.3 illustrates the distribution of bending moments at different depths during the excitation. In configuration *Ia*, where a stiffness contrast exists at the interface between soft soil and hard soil at a depth of -10 m, the temporal record of kinematic bending moments reaffirms that the most substantial bending moment occurs at the level of the interface between the soft and hard soil layers. Significant bending moments are observed within the time interval spanning from 2 seconds to 25 seconds, coinciding with significant duration. However, it is worth noting that the maximum bending moment does not coincide with either the instant of peak acceleration or the instant of maximum displacement at the surface.

The same observation found in configuration *Ia* is also applicable to configuration *IIa*, as depicted in Figure 7.4. High bending moments are located around the two interfaces, which are found at depths of -3 m and -10 m, respectively. This result confirms that the stiffness contrast at the layer interfaces is the cause of high kinematic bending moments.

In Profile *III*, there are three interfaces due to a stiff soil layer placed at the middle depth. As a result, three zones with high bending moments are observed in Figure 7.5, located at depths of -4 m, -6 m, and -10 m. Interestingly, it is also observed that the maximum response of bending moment at different interfaces does not occur simultaneously.

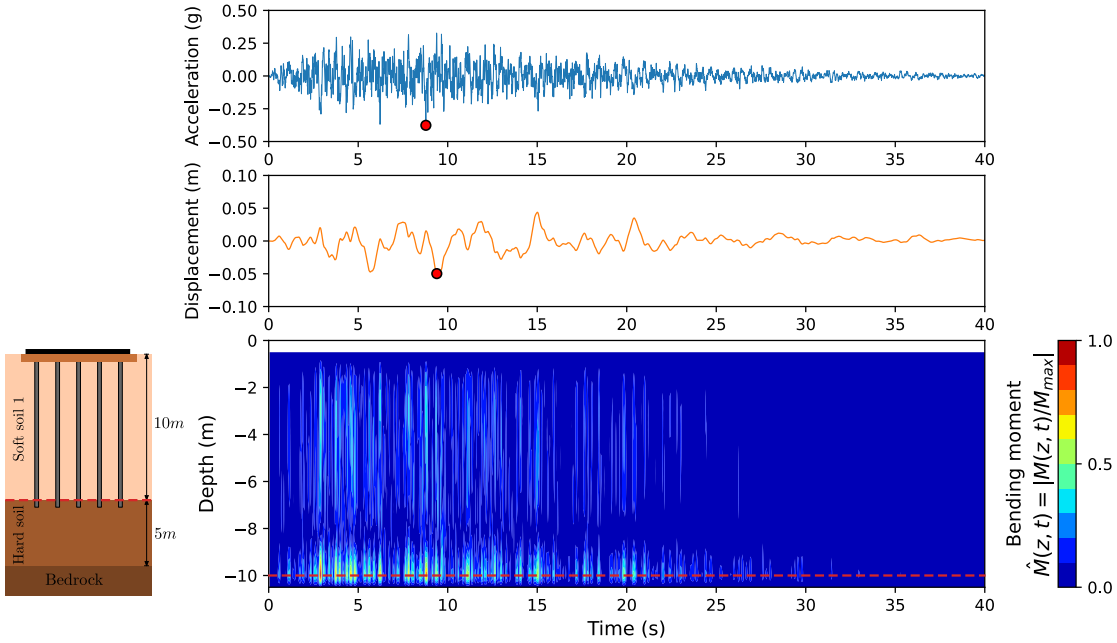

Fig. 7.3. Time evolution of kinematic bending moment for configuration *Ia* with accelerogram 3

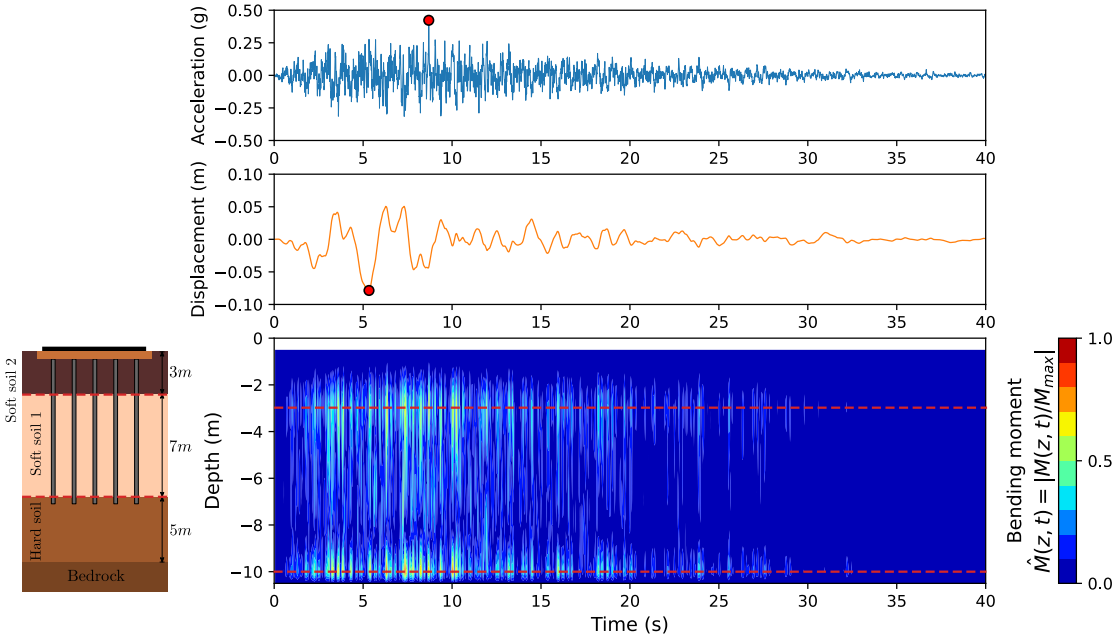

Fig. 7.4. Time evolution of kinematic bending moment for configuration *IIa* with accelerogram 2

7.4.2 Bending moment at soil layer interface

From the kinematic bending moment time history, it has been found that the maximum kinematic bending moment is consistently situated at the interfaces in each profile,

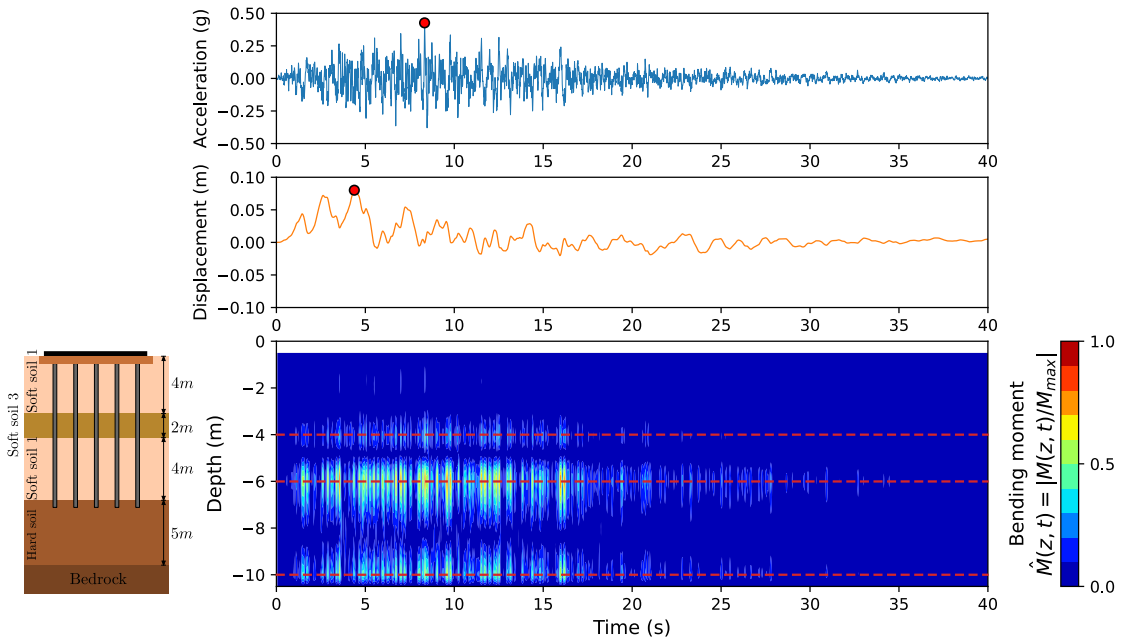

Fig. 7.5. Time evolution of the bending moment for configuration *IIIa* with accelerogram 4

resulting from the contrast in stiffness. The maximum kinematic bending moments for different configurations are studied in this section with a shear wave velocity contrast ratio η, defined in Equation 7.1.

The investigation into the amplitude of the kinematic bending moment involves varying cases using different V_s values for the soft soil, as depicted in Figures 7.6, 7.7, and 7.8.

The maximum kinematic bendings for Profile *I* at the interface are depicted in Figure 7.6. At the interface with $\eta = 2.0$, the kinematic bending moment is relatively small with a maximum bending moment of approximately 0.6-0.7 MN.m. There is no significant difference in the maximum bending moment value across different accelerograms. The most pronounced amplitude of maximum bending moment is observed with $\eta = 4.0$. The relationship between the stiffness contrast ratio and the amplitude of the maximum bending moment is evident, with the maximum bending moment increasing as the contrast of the stiffness between the stiff soil and soft soil grows.

Figure 7.7 depicts the maximum moments at two distinct interfaces of rigid inclusions within Profile *II*, varying in stiffness contrast ratio η. This observation echoes the findings in Profile *I*, wherein a higher stiffness contrast corresponds to an increased bending moment amplitude.

Profile *III* features three distinct soil interfaces. Figure 7.8 illustrates the amplitudes of kinematic bending moments at these interfaces. Notably, the same observations from Profiles *I* and *II* hold true for Profile *III* as well.

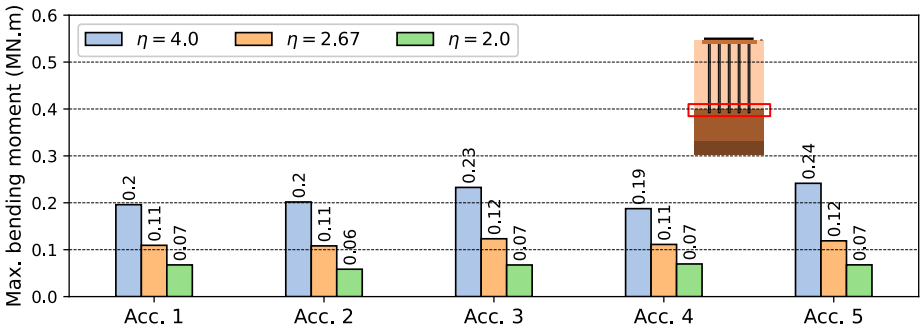

Fig. 7.6. Maximum bending moment at the different soil layer interfaces in Profile *I*

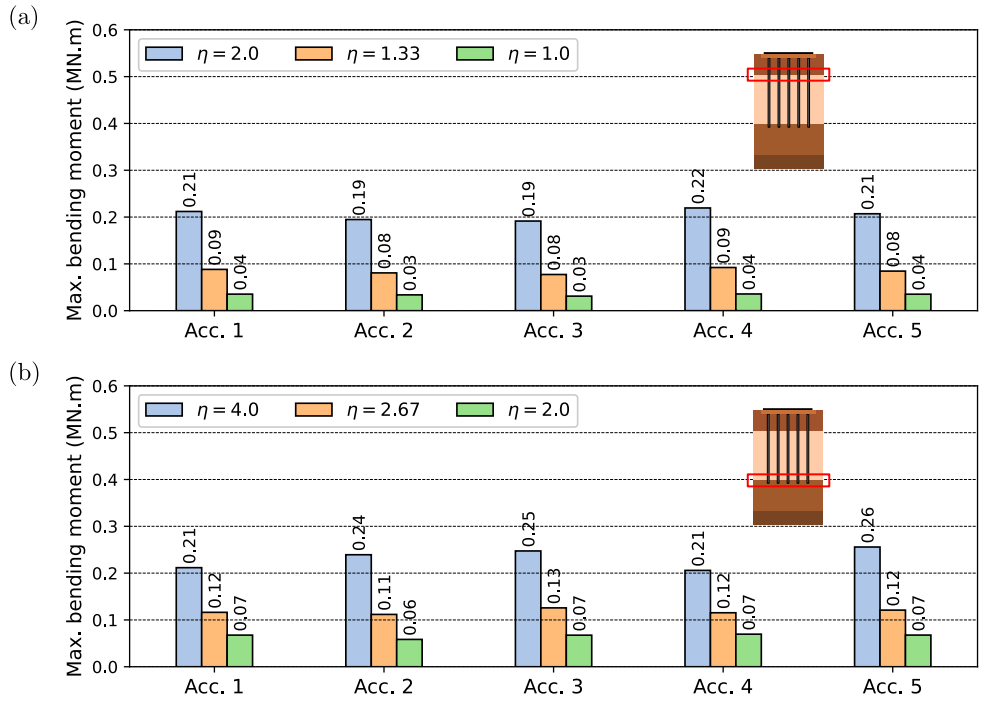

Fig. 7.7. Maximum bending moment at the different soil layer interfaces in Profile *II*: (a) upper interface and (b) lower interface

7.4.3 Bending moments of inclusions at different positions

The study investigates the evolution of kinematic bending moments during seismic excitation and examines the amplitudes and locations of the maximum bending moments. For these analyses, the central inclusion is selected. However, it raises the question of whether the central inclusion serves as a representative model for all other inclusions. Therefore, this section includes a comparison of bending moments among inclusions positioned at different locations. The comparison of kinematic bending moments of different rigid inclusions aims to investigate the significance of group effects.

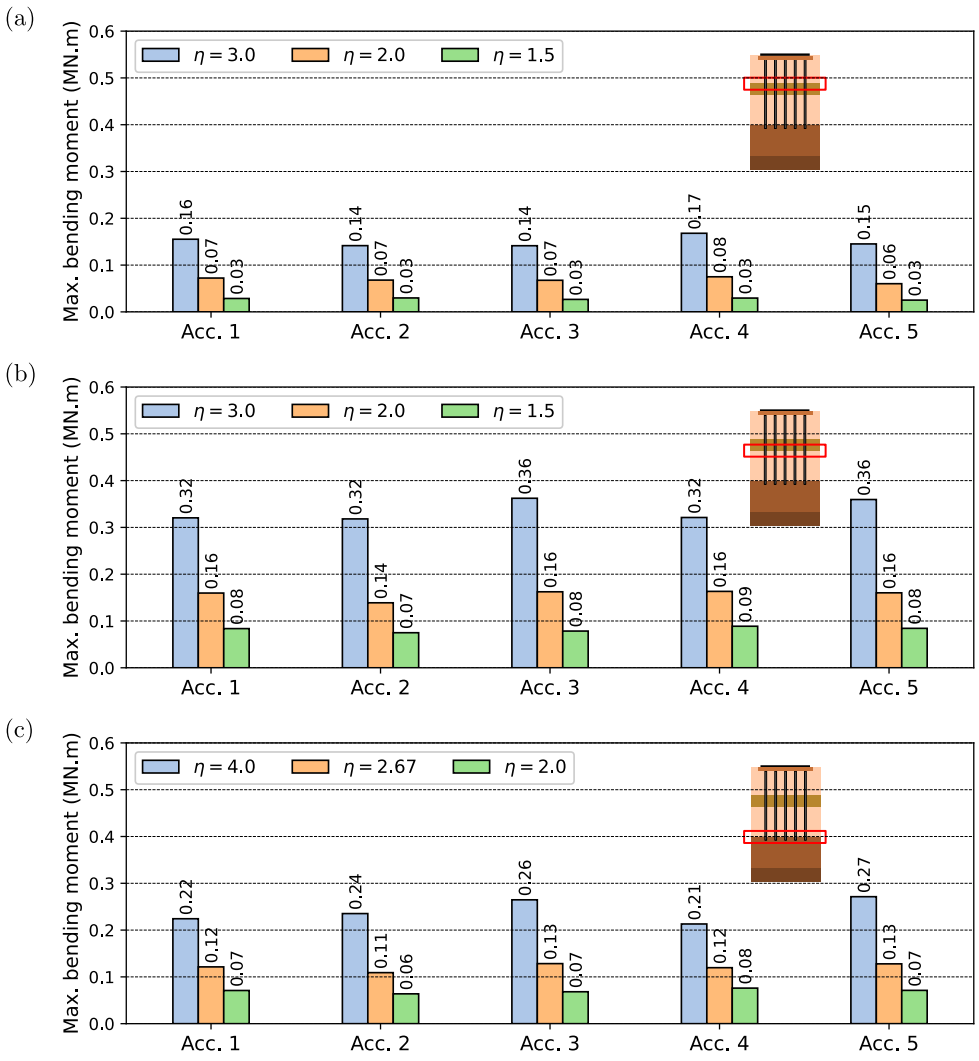

Fig. 7.8. Maximum bending moment at the different soil layer interfaces in Profile *III*: (a) upper interface, (b) middle interface, and (b) lower interface

Figure 7.9 showcases a comparison of kinematic bending moment envelopes for inclusions positioned at different locations within the three distinct soil deposits. The analysis focuses on inclusions situated at the centre, edge and corner, denoted as A, B, and C, respectively. Additionally, three varying shear wave velocities of soft soil 1 are considered. The kinematic bending moments are normalised using Equation 7.2.

$$\bar{M} = \frac{M {l_0}^2}{E_p I_p d_{max}} \tag{7.2}$$

where l_0 represents the pile's transfer length, which can be calculated using Equation 4.2, and d_{max} denotes the amplitude of displacement at the ground surface.

The investigation reveals that the dynamic responses of inclusions in terms of bending moment at various positions under seismic loading are remarkably identical. Consequently,

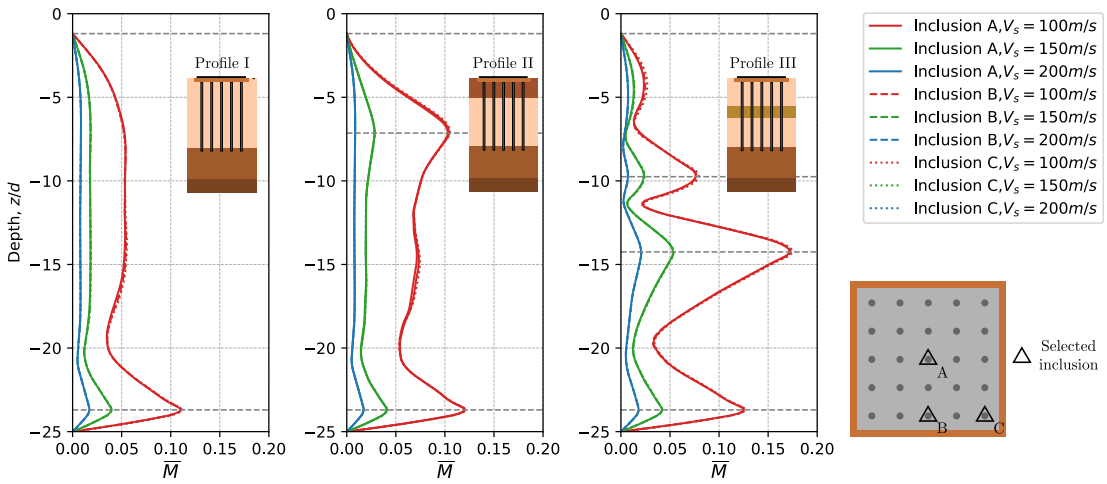

Fig. 7.9. Normalised kinematic bending moments of three profiles: comparison for inclusions at different positions

it can be inferred that the group effect has a small influence on the maximum kinematic bending moment.

The examination of kinematic forces experienced by a group of rigid inclusions can be effectively conducted by modelling only a single inclusion. It is not necessary to verify all inclusions. In the following analysis, the results of the centre inclusion are presented since it is representative enough for all inclusions.

7.5 Kinematic bending moments calculated by pseudo-static calculation

The engineering conventional examination approach of kinematic forces typically involves pseudo-static approaches based on the p-y type Winkler model, as explained in Section 3.3.2. The approach relies on various assumptions, which lack verification and validation with comprehensive models. The following comparison investigates the applicability of the conventional pseudo-static approach.

7.5.1 Pseudo-static approach based on Winkler-type model

A valuable comparison lies in assessing the kinematic bending moments within rigid inclusions through two different approaches: a pseudo-static approach involving a Winkler model (p-y type model), and a dynamic approach employing a complete model as described in Section 7.3.

The pseudo-static approach introduces the kinematic soil deformation as a free-field displacement, denoted $g(z)$, which is applied to the free end of the springs simulating inclusion-soil interaction, rather than being directly imposed on the inclusion itself (Cuira, 2012; Hoang *et al.*, 2020).

The soil displacement profile is employed in a Winkler-type model with linear elastic p-y springs, as depicted in Figure 7.10. The lateral stiffness, denoted as E_s, can be estimated using the formula presented in Equation 4.3, as proposed by Gazetas *et al.* (1993).

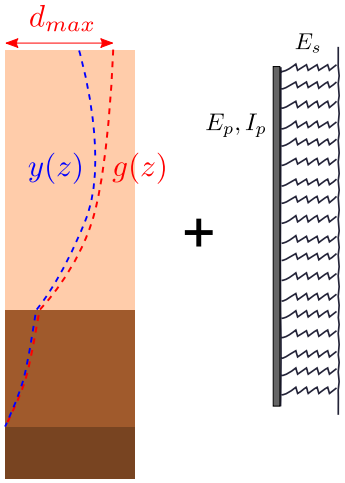

Fig. 7.10. Pseudo-static approach using p-y model

The equilibrium of the pile is described by a differential equation, as shown in Equation 7.3.

$$E_p I_p \frac{d^4 y(z)}{dz^4} + E_s[y(z) - g(z)] = 0 \tag{7.3}$$

An analogue modelling of the dynamic response of a soil column can be used to determine the displacement profiles $g(z)$. The analogue modelling is described in Appendix B. The displacement profiles $g(z)$ for the three selected soil profiles are illustrated in Figure 7.11.

7.5.2 Comparison with dynamic approach results

Bending moment diagram comparison

The kinematic bending moment diagrams for the three profile families and nine configurations are depicted in Figures 7.12, 7.13, and 7.14, respectively. The shear wave velocity V_s of soft soil 1 is also indicated in the figures for each case. The moment profiles obtained from dynamic calculations using different accelerograms are represented by dashed curves. The black curve represents the average moment profile from five dynamic

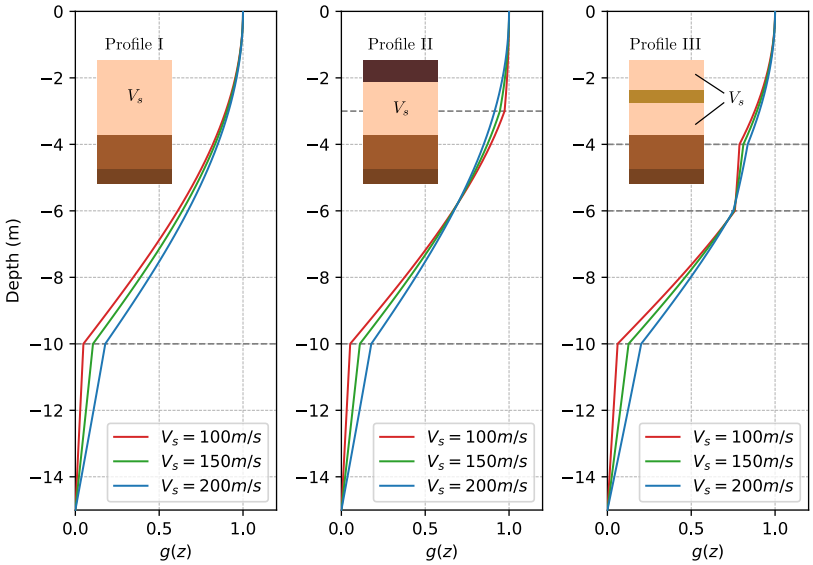

Fig. 7.11. Normalised fundamental eigenmode for three profiles

calculations. Additionally, the moment profile obtained through pseudo-static calculation is shown in red.

Figure 7.12 presents the maximum bending moment diagrams for Profile *I* obtained through dynamic calculations using five different accelerograms. In cases (b) and (c), the shear wave velocity V_s of soft soil 1 is 150 m/s and 200 m/s, respectively. In these cases, the stiffness contrast at the interface is not significant. The general trends observed in the average of the dynamic calculations and the pseudo-static solution are similar. The black curve representing the average of the dynamic calculations is generally bounded by the pseudo-static solution (red curve).

On the other hand, the comparison in case (a) shows that the result of the pseudo-static analysis is similar to the dynamic calculation at all depths. When compared with the dynamic calculation, the maximum bending moment obtained from the pseudo-static analysis is underestimated by approximately 15 %.

The results of the kinematic bending moment for Profile *II* are displayed in Figure 7.13. The local maximum bending moments are observed at the soil interfaces. Similar to Profile *I*, the maximum bending moment occurs at the soil interface (at a depth of -10 m). It is noticeable that the pseudo-static calculation generally envelops the dynamic solution in cases (b) and (c), where the shear wave velocity V_s is 150 m/s and 200 m/s, respectively. However, in case (a), where the shear velocity is 100 m/s, the kinematic bending moment diagram from dynamic calculation exhibits similarity with the results obtained through the pseudo-static approach, in terms of both the trend and the order of magnitude.

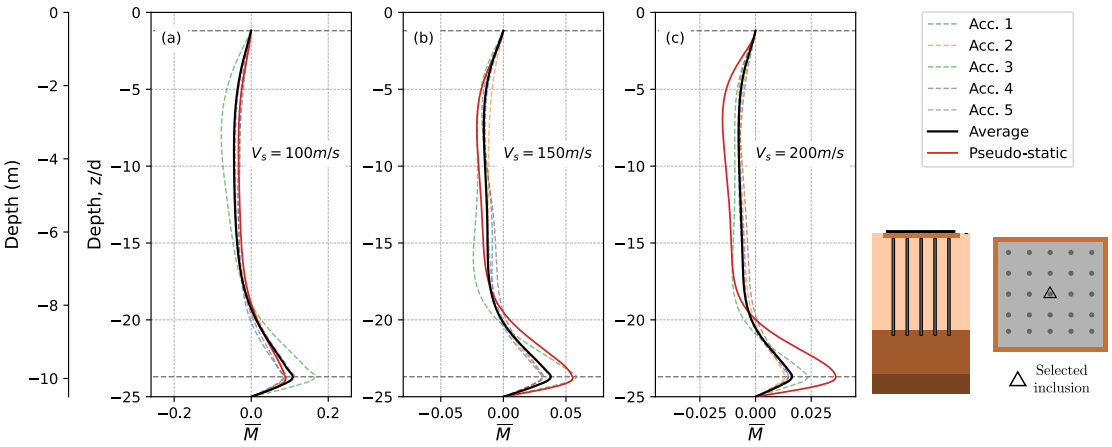

Fig. 7.12. Comparison between dynamic approach and pseudo-static approach for Profile *I* with different V_s of soft soil 1: (a) 100 m/s, (b) 150 m/s, (c) 200 m/s

The kinematic bending moment diagram is depicted in Figure 7.14. This soil profile features three soil interfaces where local maximum bending moments are observed. In contrast to Profiles *I* and *II*, the maximum amplitude of the bending moment in Profile *III* is located at the second soil interface at a depth of -6 m.

For cases (b) and (c), the results from dynamic calculation are generally enveloped by those obtained through pseudo-static analysis. For case (a), the pseudo-static approach gives a satisfactory result with a slight underestimation when compared to the average of dynamic calculation.

Based on these observations, it can be concluded that the pseudo-static approach is capable of capturing the general trend of kinematic bending moments in rigid inclusions. Both the pseudo-static and dynamic approaches confirm that the maximum bending moment occurs at the interfaces between layers. For cases with a small interface stiffness contrast, such as cases (b) and (c), the pseudo-static approach tends to overestimate the kinematic bending moment. However, in cases where a significant interface stiffness contrast is present, like case (a), the pseudo-static approach fails to provide an enveloping result.

Moment profile envelope and relative error between the approaches

The moment diagrams obtained by the conventional pseudo-static approach are examined and compared with the maximum moment diagram derived from dynamic calculations. However, it is worth noting that the moment diagram which can give the maximum moment at the interface does not necessarily reflect the maximum value at other depths. Therefore, an interesting point of comparison is to match the moment diagram from the pseudo-static approach with the envelope of the moment diagram resulting from the dynamic calculations. This comparative analysis is illustrated in Figure 7.15.

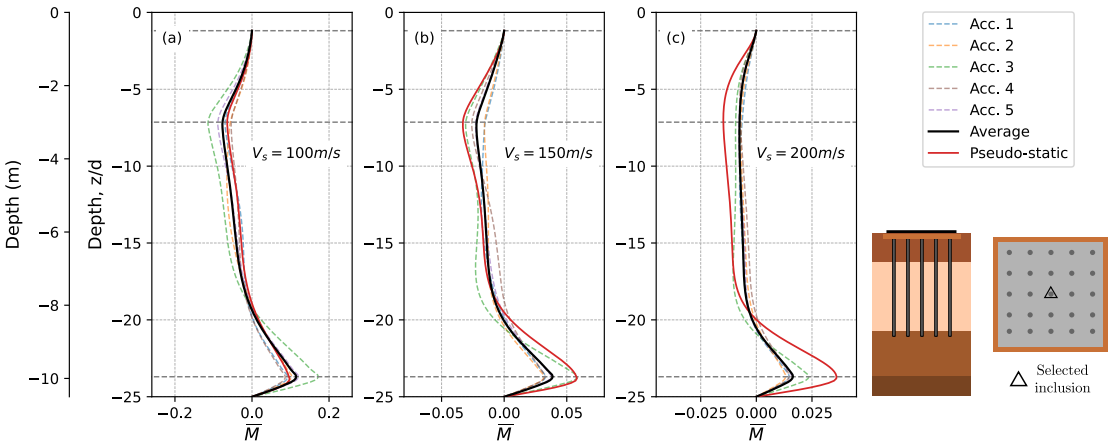

Fig. 7.13. Comparison between dynamic approach and pseudo-static approach for Profile *II* with different V_s of soft soil 1: (a) 100 m/s, (b) 150 m/s, (c) 200 m/s

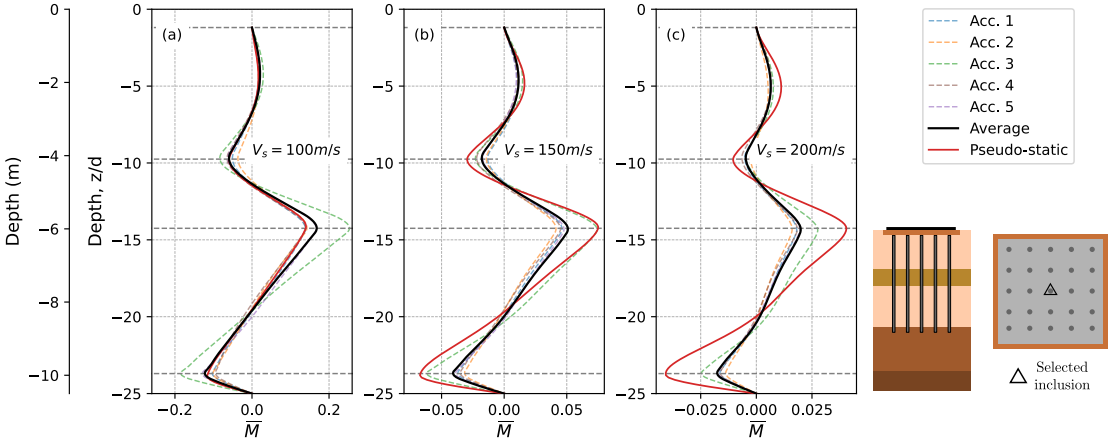

Fig. 7.14. Comparison between dynamic approach and pseudo-static approach for Profile *III* with different V_s of soft soil 1: (a) 100 m/s, (b) 150 m/s, (c) 200 m/s

Both approaches exhibit similar trends in the moment variation with depth. The comparison highlights the pseudo-static approach's capability to identify the location of the interface where the maximum kinematic bending moment occurs. In the case of small stiffness contrast profiles (V_s = 150 m/s or 200 m/s), the pseudo-static approach can provide a satisfactory envelope, except for some local underestimation.

Following the comparison of kinematic bending moment envelopes, an examination of the differences in maximum moments calculated using the two approaches at the soil layer interfaces becomes of interest. The relative error between kinematic bending moments calculated using both approaches at each interface is presented in Figure 7.16 for various values of the contrast between the hard and soft soil, evaluated by η, as defined in Equation 7.1. A positive error indicates that the kinematic bending moment calculated using the dynamic approach is greater than that from the pseudo-static approach. It is

observed that the pseudo-static approach tends to be conservative only at interfaces with a small rigidity contrast (shear wave velocity ratio smaller than 3).

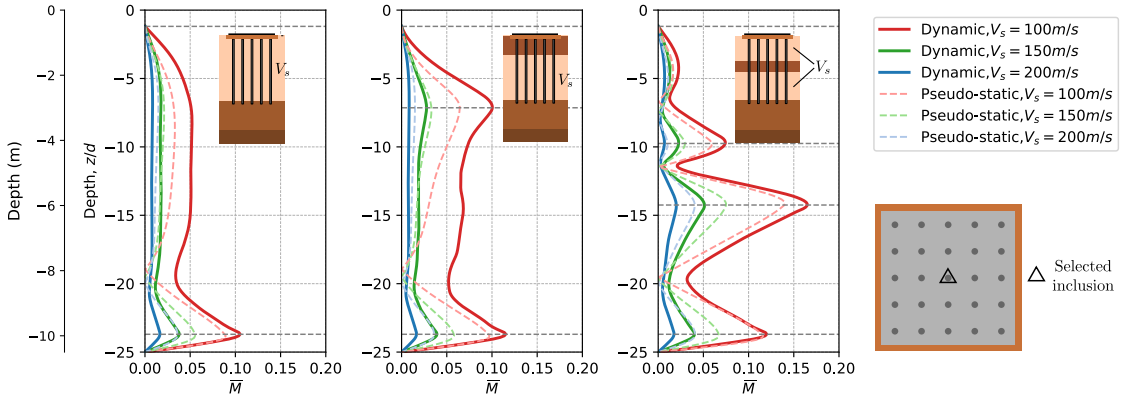

Fig. 7.15. Comparison of kinematic bending moment profiles of three soil profiles obtained with different calculation approaches

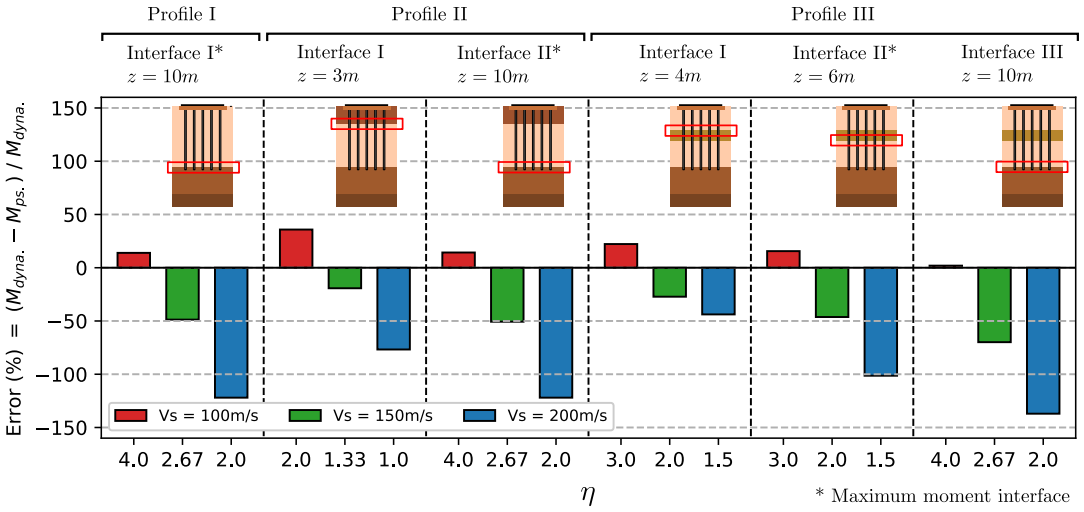

Fig. 7.16. Relative errors between the kinematic bending moments calculated using the two approaches at the soil interfaces for the three soil profiles

7.6 Summary

The passage of seismic waves through the soil surrounding the rigid inclusions results in lateral displacements and curvatures of the pile, leading to the generation of kinematic bending moments. These kinematic bending moments, which can be significant and should be carefully considered in the design of inclusions, are examined in this chapter.

Similar to the study for the piles (Nikolaou *et al.*, 2001), the maximum bending moment is situated at the interface between soil layers. Comparing the maximum bending moments at various soil layer interfaces highlights the significant influence of stiffness contrasts at

these interfaces on the amplitude of bending moments. The time history of kinematic bending moments reveals that their peak values may not align with the peak values of maximum acceleration or surface displacement. Additionally, a noteworthy observation emerges from comparing bending moment envelopes across differently positioned vertical inclusions: the same responses are found in the inclusions in different positions.

The examination of kinematic bending moment diagrams highlights that the pseudo-static approach typically captures the overall response trend. However, it tends to underestimate the maximum bending moment amplitudes at soil interfaces with significant stiffness contrasts while overestimating them in the case of minor stiffness contrasts. Considering these findings, the dynamic approach is recommended, particularly for cases featuring complex stratigraphy and substantial contrasts in soil rigidity (indicated by a shear wave velocity ratio, η exceeding 3).

Conclusion

In this part, a comprehensive investigation is undertaken to examine the fundamental dynamic SSI effects within a foundation reinforced by rigid inclusions. This study adheres to the framework of Kausel's decomposition (Kausel *et al.*, 1978). The exploration encompasses separate analyses of both kinematic and inertial interaction phenomena. Chapters 4 and 7 delve into the examination of kinematic SSI effects. Chapters 5 and 6 focus on the study of inertial SSI effects. This systematic study not only enhances the comprehension of the dynamic behaviour of foundations reinforced by rigid inclusions but also contributes to investigating the applicability of several approaches employed under pseudo-static conditions within dynamic scenarios.

In Chapter 4, an exploration of ground motion modification due to kinematic interaction effects is undertaken. Through harmonic and seismic excitation, diverse foundation types are scrutinised, including shallow foundations, pile foundations, and foundations reinforced by rigid inclusions. Different reinforced foundation configurations, encompassing soil characteristics and coverage area ratio, are also tested. Kinematic interaction factors I_u under harmonic excitation and pseudo-acceleration interaction factor I_{PSA} are used to assess the signal modification at the base of the structure, revealing a high-frequency signal attenuation, attributed to the presence of rigid inclusions.

Chapter 5 shifts its focus to dynamic impedances. A comparative study illuminates similarities and differences between inclusion-reinforced foundations and conventional foundation types, including shallow foundations and pile foundations in terms of dynamic stiffness, damping ratio, and dynamic magnification ratio. It reveals an anisotropic behaviour in foundations reinforced by rigid inclusions. In the horizontal direction, the dynamic stiffness, the damping, and the dynamic magnification ratio of foundations on rigid inclusions are akin to those of shallow foundations with LTP. Conversely, the vertical and rotational dynamic stiffness of foundations on rigid inclusions falls between the values observed in shallow foundations and pile foundations, while the damping ratio and the dynamic magnification ratio of the former align closely with pile foundations. The parametric study on the inclusion length indicates that end-bearing inclusion reinforcement increases the vertical and rotational stiffness of the foundation, whereas foundations reinforced by floating inclusions do not achieve the stiffness of the hard support layer. Additionally, the research explores a homogenised equivalent profile approach for dynamic impedance calculation. This approach enables the assessment of dynamic impedances in the low-frequency range with a certain level of precision. Lastly, the study scrutinises the coupling effects and finds no coupling effect within the studied configurations.

Chapter 6 explores inertial loading, examining load transfer efficiency and the bending moment within rigid inclusions. The findings reveal that Under horizontal loading, the stress concentration rate is 3 to 7 times lower than that observed under vertical loading. Moreover, the analysis reveals that the bending moment generated within the rigid inclusions by the applied foundation force is relatively smaller than that in a hinge pile foundation.

Chapter 7 encompasses an exploration of kinematic forces in terms of kinematic bending moment induced by seismic wave propagation. As observed in pile foundations, the maximum bending moments are situated at the interfaces between soil layers, and the magnitude of the maximum bending moment is influenced by the stiffness contrast. No group effects are not detected in the examined configurations. A comparison between pseudo-static and dynamic approaches illustrates that the pseudo-static approach can effectively capture general trends and provide a bending moment envelope, albeit underestimating the bending moment for interfaces with significant stiffness contrast.

The analyses in the part of the dissertation contribute to a deeper understanding of dynamic SSI effects of foundations reinforced by rigid inclusions, shedding light on the potential phenomena governing their behaviour in pseudo-static or dynamic conditions.

Part III

Seismic bearing capacity

Introduction

The issue of foundation bearing capacity is perpetually significant within the field of geotechnical engineering. In the literature, researchers employ both experimental and numerical methods to address this crucial matter. Among the various numerical approaches, the yield design theory, presented in Section 3.3.1, stands out as a proven and efficient tool. It has been successfully utilised to investigate the bearing capacity of non-reinforced shallow foundations and the stability of nailed slopes subjected to static and seismic loads.

Drawing inspiration from these studies, this part of the dissertation delves into the issue of assessing the bearing capacity of rigid inclusion-reinforced foundations under both static and seismic loads. The analysis is conducted using the kinematic exterior approach in the framework of the yield design theory.

The kinematic exterior approach offers a comprehensive upper-bound solution, allowing not only to determine the ultimate bearing capacity under vertical loads but also to assess the ultimate bearing capacity under diverse load conditions, taking into account the load inclination, load eccentricity, and soil inertia. By combining several ultimate bearing capacity values, the interaction diagrams can be derived, delineating all the possible load combinations applied to the foundation for which the foundation fails and for which it remains stable.

In Chapter 8, an analytical approach is established within the framework of the kinematic exterior approach to address the bearing capacity problem in inclusion-reinforced foundations. This approach involves identifying potential failure mechanisms within a rigid inclusion-reinforced foundation system. To tackle this complex challenge, the system is partitioned into sub-systems based on the identification of potential failure mechanisms. Within these sub-systems, a particularly challenging aspect is how to appropriately account for the contribution of rigid inclusions. Taking inspiration from the multicriterion approach used for nails, a novel multicriterion approach for rigid inclusions is introduced to aid in determining the forces provided by these rigid inclusions. The interaction diagram can be obtained by superimposing the results from different sub-systems.

Chapter 9 is dedicated to the numerical validation. This chapter is focused on validating the proposed analytical approach. The numerical FEM modelling analyses are used to accomplish both qualitative validation of the studied failure mechanisms and quantitative validation of the interaction curves and the ultimate vertical bearing capacity for such foundations.

Chapter 10 utilises the validated analytical approach to investigate the significant influence of load eccentricity, load inclination, and soil inertia on the bearing capacity of foundations reinforced by rigid inclusions. Furthermore, the study introduces essential reduction factors, such as i_e, i_δ, and i_g for various coverage area ratios. The effect of embedding the rigid inclusions in the LTP is also investigated.

8 Seismic bearing capacity: Theoretical framework

8.1 Kinematic exterior approach

The bearing capacity constitutes an important problem in foundation design. To describe the bearing capacity of foundations under different load conditions, interaction curves within the (V, H, M) space are employed, enabling a convenient evaluation of foundation performance under seismic conditions. These curves can be derived using various approaches, including physical experiments like swipe tests (Butterfield, 1979), and numerical simulations. Additionally, in the literature, the analyses in the framework of the yield design theory are also employed to investigate the seismic bearing capacity of foundations under both static and seismic load conditions.

Within the framework of yield design theory, the kinematic exterior approach, also known as the kinematic external approach, serves as an upper-bound analysis method, as depicted in Figure 8.1. This approach involves evaluating kinematically admissible failure mechanisms $\underline{\hat{U}}$ and verifying whether the virtual power of external loads applied to the system, denoted as P_e, is less than or equal to the maximum resisting power of the soil, denoted as P_{rm}.

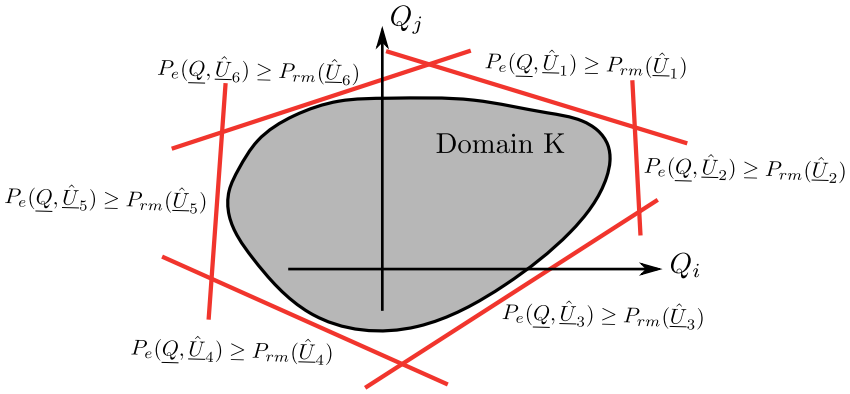

Fig. 8.1. Scheme of kinematic exterior approach

An upper-bound K encompasses within the space delineated by Inequation (8.1) (Salençon, 1983).

$$K \subset \{P_{rm}(\underline{\hat{U}}) \geq P_e(\underline{\hat{U}})\} \tag{8.1}$$

From a practical perspective, the kinematic exterior approach primarily roots in Inequation 8.1, regardless any supplementary assumptions. A thorough examination of admissible kinematic velocity fields $\|\widehat{\underline{U}}\|$ will be conducted. Employing the kinematic exterior approach to establish the stability domain K offers a well-balanced approach, considering the simplicity of the methods used, available computational resources, time constraints, and the quality of the obtained results (Salençon, 2002).

The maximum resisting power P_{rm} is equal to:

$$P_{rm} = \int_{\Omega} \pi(\widehat{\underline{\underline{d}}}) d\Omega + \int_{\Sigma} \pi(\|\widehat{\underline{U}}\|) d\Sigma \tag{8.2}$$

where $\pi(.)$ represents the density of virtual power related to the strain rate $\widehat{\underline{\underline{d}}}$ within the volume Ω and the virtual velocity $\|\widehat{\underline{U}}\|$ at the discontinuity surface Σ. These quantities are derived from strength criteria. The explicit formulation of the function $\pi(.)$ is available for various criteria applicable to both continuous materials and interfaces and can be found in the works of Salençon (1983, 2002), provided in Appendix D.

The virtual power of all external forces P_e applied to the system encompasses the power of the loads exerted on the foundation in terms of forces and moments (V, H, M), as well as the body forces $(\underline{f_x}, \underline{f_y})$ originating from soil inertia.

In the case of a foundation reinforced by rigid inclusions, the formulation of P_e remains unchanged when compared to the case without reinforcement. Nonetheless, the determination of P_{rm} must account for the contribution of reinforcement by rigid inclusions, represented by P_{RI}, as outlined in Equation 8.3.

$$K \subset \{P_{rm}(\widehat{\underline{U}}) + P_{RI}(\widehat{\underline{U}}) \geq P_e(\widehat{\underline{U}})\} \tag{8.3}$$

8.2 Seismic bearing capacity analysis by kinematic exterior approach

8.2.1 Non-reinforced foundation

Due to its capabilities, the kinematic exterior approach has been used to examine the bearing capacity of strip foundations located on uniform cohesive and frictional soils under seismic loading (Pecker and Salencon, 1991; Salençon and Pecker, 1995a,b; Paolucci and Pecker, 1997a,b; Soubra, 1999).

Problem description

The primary aim of this study is to examine the seismic bearing capacity of foundations reinforced by rigid inclusions. Nevertheless, it is insightful to start the investigation with a study focused on the non-reinforced foundations.

The problem explored in this section involves a non-reinforced strip footing. The foundation is situated on a half-space composed of cohesive soil without tensile strength, defined by a cohesion c, or a frictional soil characterised by a friction angle φ. This arrangement is depicted in Figure 8.2.

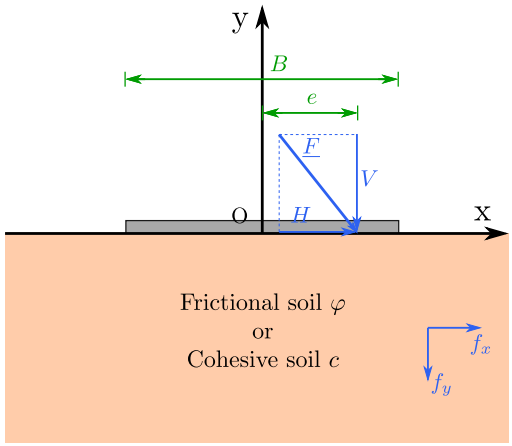

Fig. 8.2. Two-dimensional problem of the bearing capacity of a strip footing subjected to seismic loading

To simulate seismic loading on the foundation, the force couple $\underline{F}(V, H)$ is employed to represent the inertial forces transmitted through the structure. The moment $\underline{M}$ is calculated by multiplying the vertical force $\underline{V}$ by the eccentricity e. Inertial effects within the soil are also taken into account employing body forces caused by seismic and gravitational loads. These are denoted as $f_x = \rho a_x$ and $f_y = \rho(g \pm a_y)$, respectively.

It is worth noting that assuming constant inertial forces f_x is acceptable when the failure mechanism is confined to a region near the ground surface. To account for the spatial variation of acceleration within the soil, various approaches have been proposed, including the use of fundamental mode-shaped acceleration profiles. In practice, for shallow failure mechanisms, this assumption is usually valid and does not result in significant errors (Pecker and Salencon, 1991; Chatzigogos, 2007).

Foundation on cohesive soil

Salençon and Pecker (1995a) investigated the bearing capacity problem of a shallow strip foundation by assuming the soil to be purely cohesive and following Tresca's strength

criterion. This study is conducted within the framework of 2D plane strain yield design theory (Salençon, 1983, 2002).

In a related paper (Salençon and Pecker, 1995b), the authors introduced a tension cut-off condition to the soil strength criterion, specifically describing a purely cohesive medium with no tensile strength. Both the static interior approach and the kinematic exterior approach are employed. The findings of the study confirm that the bearing capacity of foundations on purely cohesive soil does not depend on the soil unit weight. The soil unit weight acts as a stabilising factor for the upper bound estimation of foundations on purely cohesive soil without tensile strength.

The rotation-translation kinematic admissible failure mechanisms $\underline{\widehat{U}}$ are illustrated in Figure 8.3. The mechanism presented in Figure 8.3 (a) shows a velocity field without uplift, characterised by a rotation at angular velocity ω of the assembly comprising the foundation $A'A$ and the soil volume IJA, about the rotation centre Ω. Within the circular sector $A'AJ$ and the triangle ALK, a purely tangential velocity field is present, and both of these blocks are deformable.

The mechanism depicted in Figure 8.3 (b) is similar to the previous one, involving a rotation at angular velocity ω of the assembly comprising the foundation $A'A$ and the soil volume IJA. This mechanism includes an uplift of the foundation from the soil along $A'I$, a purely tangential velocity field within the circular sector AJK and the triangle ALK.

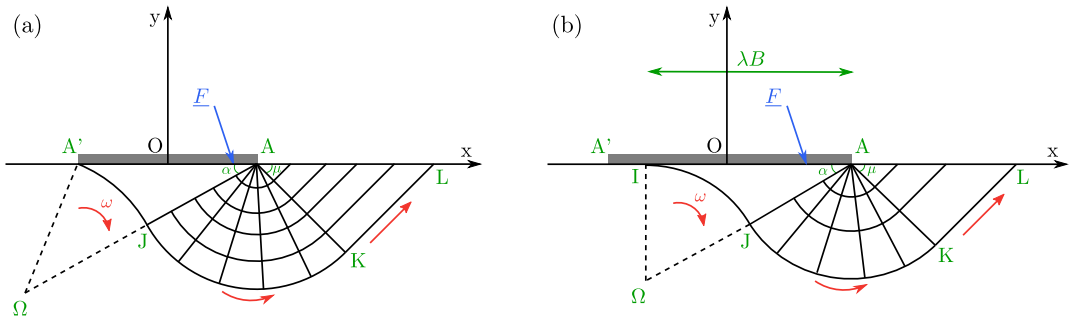

Fig. 8.3. Rotation-translation velocity fields for a rigid strip foundation on cohesive soil: (a) without uplift and (b) with uplift (Pecker and Salencon, 1991)

Several mechanisms involving only a rigid block in rotation are also proposed, as depicted in Figure 8.4. The mechanism shown in Figure 8.4 (a) involves a rotation of the foundation $A'A$ and the volume of soil aA, at angular velocity ω, forming a rigid block. This mechanism includes an uplift of the foundation along $A'a$. The rotation mechanism without uplift is similar to the one with uplift, as illustrated in Figure 8.4 (b).

An uplift velocity jump mechanism has also been tested, involving a velocity discontinuity along the interface $A'A$ as depicted in Figure 8.5. This mechanism involves sliding along the interface $A'A$ with the velocity $\underline{\widehat{U}}$ and the foundation has an uplift velocity jump at

the interface, assuming that the velocity jump takes place within the soil immediately below the interface $A'A$.

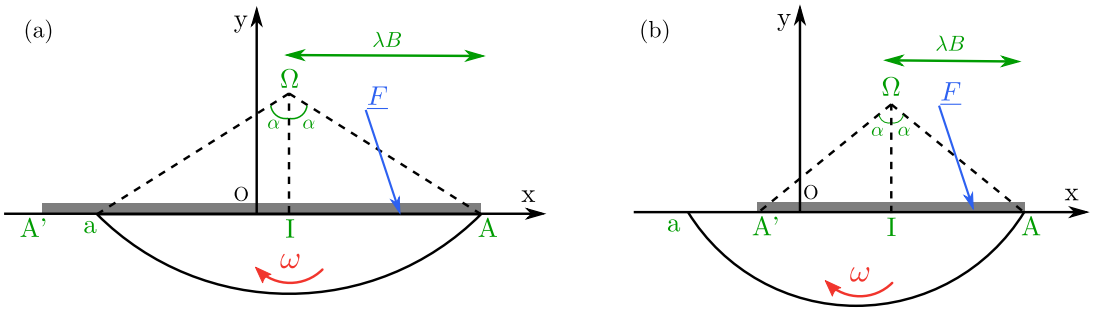

Fig. 8.4. Rotation velocity fields for a rigid strip foundation on cohesive soil: (a) with uplift and (b) without uplift (Pecker and Salencon, 1991)

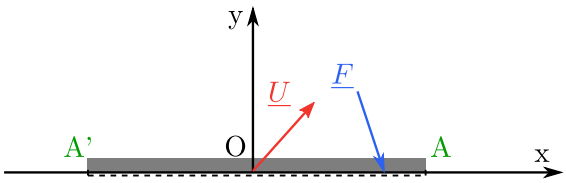

Fig. 8.5. Uplift velocity jump for a rigid strip foundation on cohesive soil (Salençon and Pecker, 1995b)

A summary of the results obtained using the kinematic exterior approach is depicted in Figure 8.7 (a), illustrating various load eccentricities e/B ranging from 0.1, 0.2, 0.3, and 0.4 and the case without eccentricity. These curves establish the optimal upper bounds for the bearing capacity, derived from distinct mechanisms, as shown in Figures 8.3, 8.4, and 8.5. The outcomes are normalised by the theoretical bearing capacity $V_{max} = (\pi + 2)B$, a value can also be acquired through the kinematic exterior approach applied in the present work. Comparing the interaction curves with varying load eccentricities reveals that the bearing capacity is sensitive to the load eccentricity.

The H-V interaction curves, considering both cases with and without soil inertia, are showcased in Figure 8.7 (b). In situations where foundations are well-designed with a safety factor exceeding 2 ($V/V_{max} \leq 0.5$) and experiencing ground motion with acceleration below $c/B\rho$, the reduction in bearing capacity resulting from the soil seismic inertia can be disregarded. Conversely, for foundations designed with a lower safety factor, the influence of soil seismic inertia becomes pronounced and leads to an important reduction in the bearing capacity.

All failure mechanisms examined by Salençon and Pecker (1995b), as depicted in Figure 8.3, 8.4, and 8.5 are investigated within the scope of this study. An algorithm is proposed in this study, allowing for a systematic exploration of all possible ranges of geometric parameters within the studied failure mechanism families. This algorithm can iterate through all possible combinations of these geometric parameters. For each combination

of geometric parameters, it computes a set of corresponding external forces $\underline{Q}$ by solving $P_{rm}(\underline{\widehat{U}}) = P_e(\underline{Q}, \underline{\widehat{U}})$. The minimum external force value represents the best estimation of the upper-bound solution, as depicted in Figure 8.6.

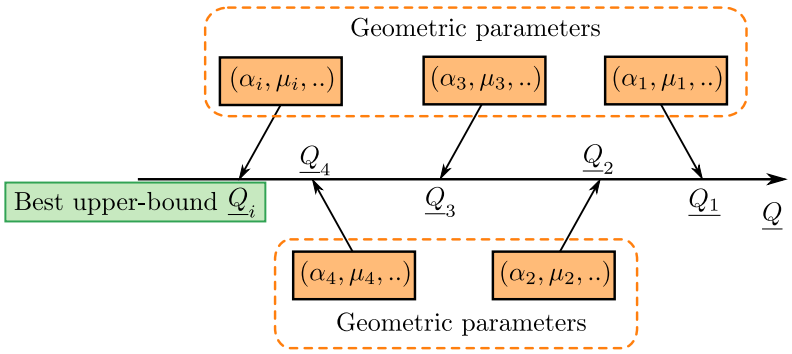

Fig. 8.6. Algorithm to find the best upper-bound solution

In the seismic stability problem of a foundation, the external force $\underline{Q}$ can encompass various components, including vertical force V, horizontal force H, rocking moment M or eccentricity e, and soil inertia f_x and f_y. In each calculation, the algorithm seeks one minimum target external force component term while keeping the other components fixed. This algorithm can be applied in both non-reinforced foundations and reinforced foundations.

The findings depicted in Figures 8.7 (a) and (b) with blue curves demonstrate a strong agreement with those described in the aforementioned references, validating the precision of the implemented algorithm.

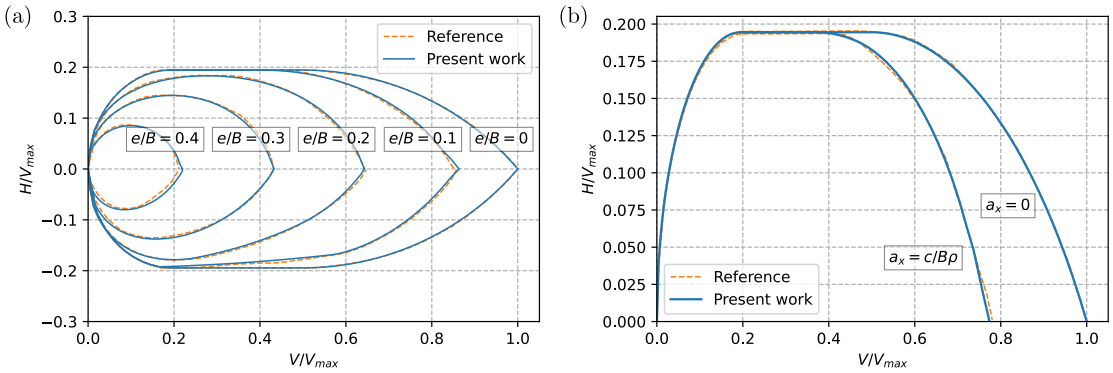

Fig. 8.7. Comparisons with the reference results for a strip foundation on cohesive soil: (a) H-V interaction curves under eccentric loading (Salençon and Pecker, 1995b) and (b) H-V interaction curves with soil inertia (Pecker, 1997)

Foundation on frictional soil

Several virtual failure velocity fields have been proposed to define the interaction diagrams for strip foundations on frictional soil in the studies by (Dormieux and Pecker, 1995; Paolucci and Pecker, 1997a).

The kinematic mechanism depicted in Figure 8.8, as outlined in the work of Dormieux and Pecker (1995), follows the Prandtl-type mechanism. The blocks AJA' and AKL are rigid triangular entities, while the block AJK is deformable and enclosed by a logarithmic spiral JK with a rotation centre at point A.

The second set of kinematic mechanisms presented in Figure 8.9 shares similarities. These mechanisms comprise a rigid block AJA' bordered by the foundation on the upper side and a logarithmic spiral JK centred at point Ω on the lower side. Additionally, they involve a deformable block AJK defined by a logarithmic spiral centred in point A, and of a deformable triangular block AKL.

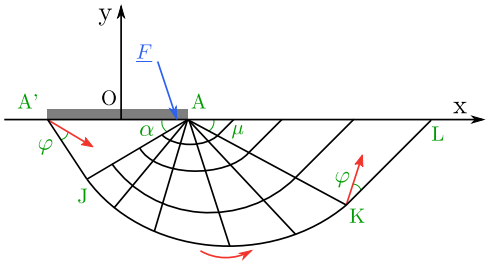

Fig. 8.8. Translation velocity fields for a rigid strip foundation on frictional soil (Paolucci and Pecker, 1997a)

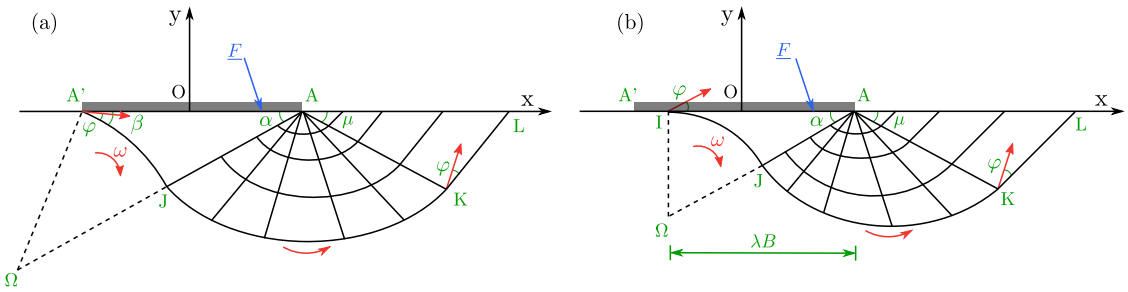

Fig. 8.9. Rotation-translation velocity fields for a rigid strip foundation on frictional soil (a) without uplift and (b) with uplift (Paolucci and Pecker, 1997a)

The investigation of the load eccentricity effect is illustrated in Figure 8.10 (a). Load eccentricity has a detrimental impact on the bearing capacity, causing a reduction in the stability domain enclosed by the interaction curve. Regarding the effects of soil inertia, the analysis indicates a relatively small reduction in bearing capacity, not exceeding 15 to 20 %, as shown in Figure 8.10 (b).

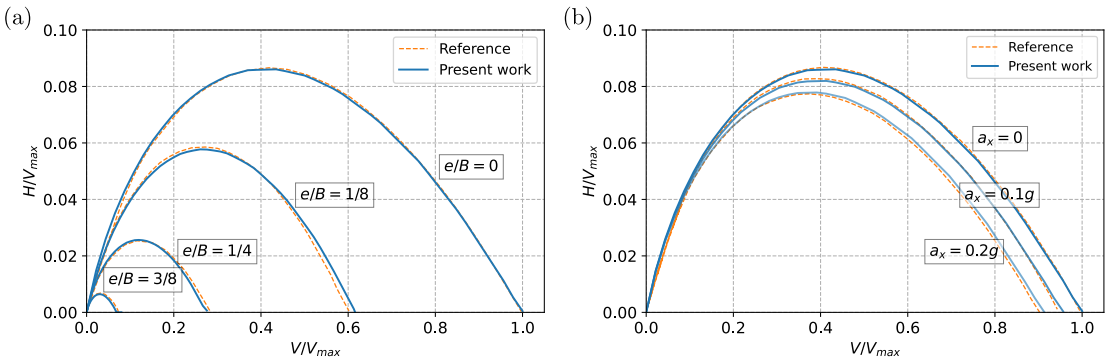

Fig. 8.10. Comparisons with the reference results for a strip foundation on frictional soil: (a) H-V interaction curves under eccentric load (Paolucci and Pecker, 1997a) and (b) H-V interaction curves with soil inertia (Paolucci and Pecker, 1997a)

8.2.2 Rigid inclusion-reinforced foundation

The seismic bearing capacity of rigid inclusion-reinforced foundations has not received sufficient attention. This is partly due to the inherent complexity introduced by the presence of three distinct components: the soft soil, the granular LTP, and the rigid inclusions. This intricate composition adds difficulty to determining the failure mechanism $\underline{\widehat{U}}$.

Pecker *et al.* (1998) evaluated the seismic bearing capacity of a shallow foundation on cohesive soil reinforced by rigid inclusions. This assessment is accomplished using a kinematic exterior approach within the framework of yield design theory. The findings are then compared with the results of five centrifuge tests carried out on a scaled model, which are associated with the Rio-Antirrio bridge project as detailed in Section 1.1.3. The associated centrifuge tests are introduced in Section 2.3.

What is particularly noteworthy in this study is the incorporation of rigid inclusions within the kinematic exterior approach. The focal point of interest lies in accounting for the presence of rigid inclusions. The resistance criterion for such inclusions is expressed by Equation 8.4, as proposed by Anthoine (1987).

$$f(n,v,m) = \left(\frac{n}{n_l}\right)^2 + \left(\frac{v}{v_l}\right)^2 + \left|\frac{m}{m_l}\right| - 1 \leq 0 \tag{8.4}$$

where n_l, v_l, and m_l represent the ultimate values of axial force n, shear force v, and bending moment m, respectively.

The maximum resisting power of a rigid inclusion, calculated using the criterion provided by Equation 8.4, is expressed as:

$$\pi = Sup\Big[n(s)\frac{d\underline{U}(s)}{ds}.\underline{e}_n + m(s)\frac{d\Omega(s)}{ds}; f(n,v,m) \leq 0\Big] \tag{8.5}$$

In Equation 8.5, the contributions of inclusion rotation, axial deformation of the inclusion, and shaft friction along the inclusion are taken into account.

A total of nine kinematic mechanisms are studied. The failure mechanisms observed in the centrifuge tests closely resemble two out of nine kinematic mechanisms considered in the calculations, resulting in the most accurate estimations of bearing capacity. These two kinematic mechanisms are illustrated in Figures 8.11 and 8.12.

The velocity field depicted in Figure 8.11 is characterised by the presence of a rigid body $A'CA$ and the foundation undergoing rotation with an angular velocity ω around point Ω. Notably, the projection of the rotation centre Ω onto the surface lies to the left of point A'. This mechanism exhibits a shear zone ACD delineated by a circle arc CD centred at point A, as well as a triangular shear zone ADE. Within the shear band enclosed by two parallel curves $A'CDE$ and $B'C'D'E'$, of thickness δ, the velocity remains continuous across the upper boundary $A'CDE$, gradually decreasing linearly to zero at the lower boundary $B'C'D'E'$. This mechanism can be perceived as a combination of a shear band and a mechanism resembling the behaviour of a non-reinforced shallow foundation, as illustrated in Figure 8.3 (a).

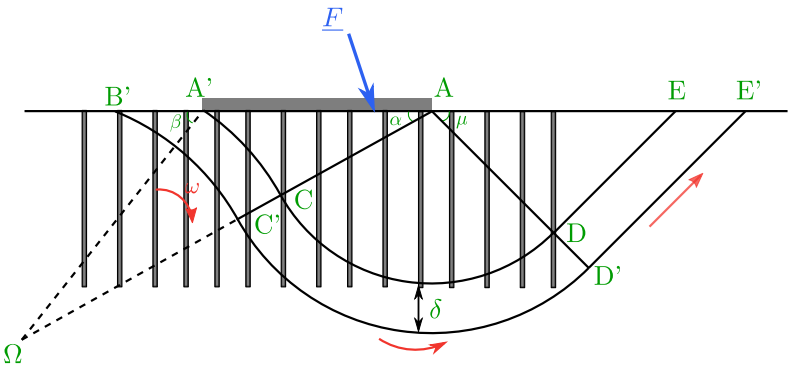

Fig. 8.11. Rotation-translation velocity fields for a strip foundation reinforced by rigid inclusion on cohesive soil without uplift (Pecker *et al.*, 1998)

Another kinematic failure mechanism illustrated in Figure 8.12 exhibits similarities to the preceding velocity field. The velocity fields associated with the blocks $A'CA$, ACD, and ADE remain consistent with those observed in the previous mechanism. However, the distinguishing factor lies in the uplift behaviour of the foundation. In this case, the resisting power accounts for the contribution from the uplift interface. To complete this mechanism, a circle arc $B'B''$ is introduced, centred at point Ω' and aligned vertically from point Ω. The volume of soil $A'B'B''$ experiences shear deformation within this mechanism. This mechanism can also be interpreted as a variation of a kinematic failure

mechanism observed in non-reinforced shallow foundations, as depicted in Figure 8.3 (b), albeit with the presence of a shear band.

It is important to note that the rigid inclusions studied in the selected failure mechanisms are not connected to the foundation. However, the LTP is not considered in the calculations using the kinematic exterior approach. Instead, a failure criterion representing the sliding failure between the LTP and the foundation is introduced and superimposed onto the results obtained through the kinematic exterior approach.

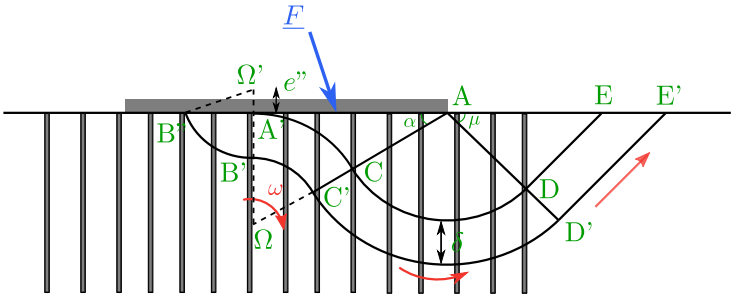

Fig. 8.12. Rotation-translation velocity fields for a strip foundation reinforced by rigid inclusion on cohesive soil with uplift (Pecker *et al.*, 1998)

The seismic bearing capacity is depicted through an interaction curve within the H-M plane, illustrated in Figure 8.13. The kinematic exterior approach curve corresponds to the interaction curve derived from the mechanism featuring uplift. It is discernible that the presence of rigid inclusions can lead to an increase in the bearing capacity. The enhancement is demonstrated by the shift of the interaction curve from the black dashed line to the red dashed line. In the presence of a granular LTP layer, a sliding failure may ensue, which is represented by the blue line in Figure 8.13.

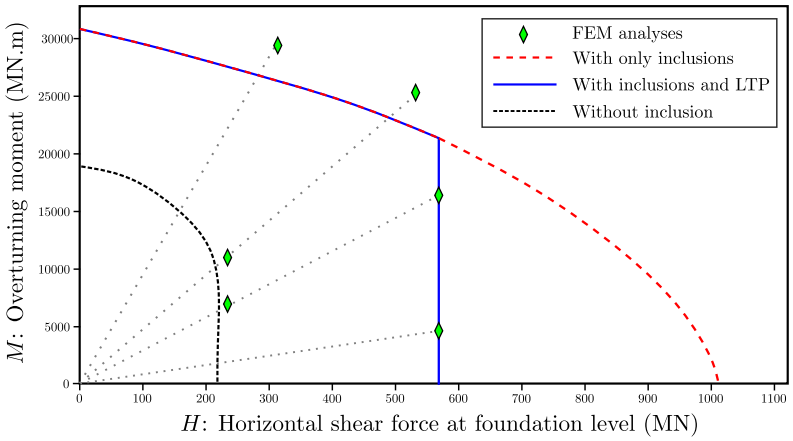

Fig. 8.13. H-M interaction curves obtained by kinematic exterior approach and compared with the results of FEM analyses (Pecker, 2023b)

8.3 Failure modes of rigid inclusions

In the existing literature, the application of ground improvement techniques involving nails or inclusions has been explored using the kinematic exterior approach in a variety of geotechnical engineering contexts.

The nailed slopes using the kinematic exterior approach are investigated by de Buhan *et al.* (1992). The study employed kinematic mechanisms based on a triangular block and a logarithmic spiral to analyse the stability of nailed slopes. Several geotechnical design software tools, including TALREN (Terrasol, 2023), PROSPER (de Sauvage and Rajot, 2018), and STARS (Anthoine, 1990), have been also developed utilising a straightforward logarithmic spiral. These software tools also offer options for controlling the contribution of nail reinforcement by employing the multicriterion based on various failure mechanisms associated with the nails. Notably, accurately assessing the force provided by the reinforcement is a critical aspect of these analyses in the context of reinforced geotechnical structures.

Building upon prior research, the present study assumes that the contribution of inclusions is incorporated by considering their forces at the intersection with the failure surface. At the intersection, the forces are decomposed into an axial force T_n, a shear force T_c and a bending moment M_c, as shown in Figure 8.14. Nevertheless, these forces are subjected to various limiting criteria :

- Material intrinsic strength;
- Vertical soil-inclusion interaction resistance;
- Lateral soil-inclusion interaction resistance: plastification of the soil;
- Lateral soil-inclusion interaction resistance: plastification of the inclusion.

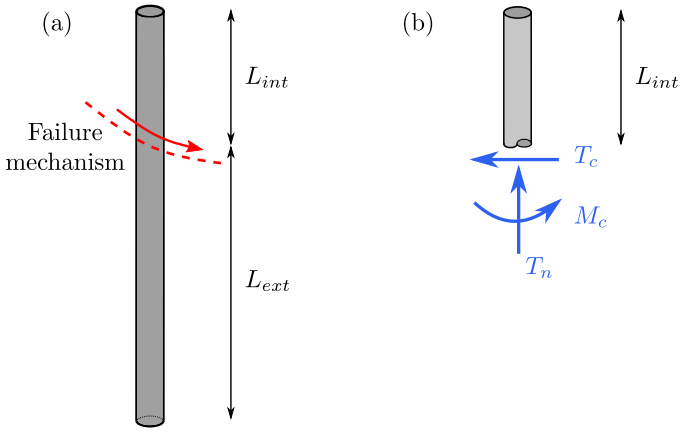

Fig. 8.14. Scheme of rigid inclusion with failure mechanism: (a) interior length L_{int} and exterior length L_{ext} and (b) inclusion forces at the intersection with failure mechanism

8.3.1 Material intrinsic strength resistance

This criterion corresponds to the failure of the inclusion due to breakage (Schlosser and Unterreiner, 1990). The combination of T_n, T_c and M_c occurring at the intersection of the inclusions and the velocity discontinuity surface can be succinctly represented by Equation (8.6), proposed by Anthoine (1987).

$$\left(\frac{T_n}{T_{n,0}}\right)^2 + \left(\frac{T_c}{T_{c,0}}\right)^2 + \left|\frac{M_c}{M_{c,0}}\right| \leq 1 \tag{8.6}$$

Where $T_{n,0}$, $T_{c,0}$, and $M_{c,0}$ represent the intrinsic strength limits of the material. The expression of this criterion forms an ellipse in the T_n-T_c plan. This same expression has also been employed in the study of nail-reinforced slopes to assess the inherent material resistance (Schlosser and Unterreiner, 1990; de Buhan *et al.*, 1992; de Buhan, 2004).

For an inclusion consisting of a cylinder with a diameter d, and a material with a maximum stress of σ_c, the value of $T_{n,0}$, $T_{c,0}$, and $M_{c,0}$ are as follows:

$$T_{n,0} = \pi d^2 \sigma_c / 4 \tag{8.7}$$

$$T_{c,0} = T_{n,0}/2 \tag{8.8}$$

$$M_{c,0} = \sigma_c d^3 / 6 \tag{8.9}$$

8.3.2 Axial soil-inclusion interaction resistance

The maximum axial force T_{nl} that rigid inclusions can provide is also governed by parameters such as skin friction, forces at the head and tip of the inclusion, and the internal "pullout" failure mechanism, as depicted in Figure 8.15. This can be described by Equation 8.10.

$$T_{nl} = min(F_0 + q_s L_{int} \pi d, F_L + q_s L_{ext} \pi d) \tag{8.10}$$

where F_0 represents the maximal force controlled by a Prandtl failure mechanism in the granular material (LTP), F_L represents the maximal force at the inclusion tip, which is typically of significant magnitude. Additionally, q_s denotes the characteristic value of the inclusion shaft friction.

The calculation of the maximal force F_0 is based on the Prandlt failure mechanism, which is applicable in situations involving large deformations within a compacted material (ASIRI, 2012), as depicted in Figure 8.16.

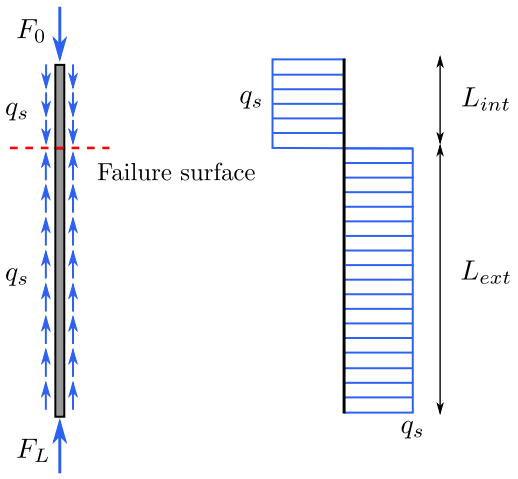

Fig. 8.15. Vertical failure mechanism of inclusion using a limit equilibrium model

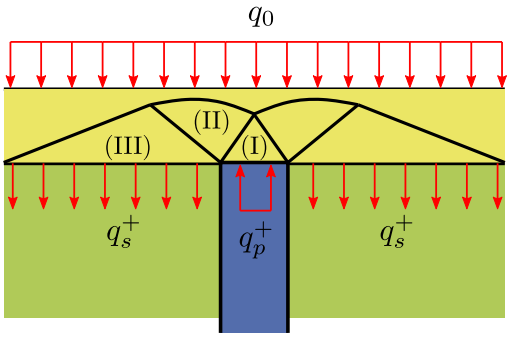

Fig. 8.16. Prandtl's failure mechanism at the head of inclusion in the load transfer platform

For vertical loading, the maximum force F_0 that can be transmitted by the LTP to the head of the inclusion is expressed as follows:

$$F_0(\delta_{RI} = 0) = \frac{\alpha N_q}{1 + \alpha(N_q - 1)} F_{cell} \tag{8.11}$$

where δ_{RI} represents the inclination of the load at the head of inclusion, α represents the coverage area ratio, N_q is the bearing factor dependent on the friction angle φ of the LTP, and F_{cell} denotes the total load on the elementary mesh being considered. The values of the factor N_q are 85.4 for $\varphi = 42°$ and 48.9 for $\varphi = 38°$. In scenarios involving an LTP of small thickness, the Prandtl's mechanism may not be viable. In such cases, a solution as proposed by Mandel and Salençon (1972) for foundations placed on a soil layer of limited thickness, situated atop of a rigid layer, can be employed to estimate the force F_0 at the heads of the inclusions.

When the loading is inclined at an angle δ concerning the vertical, the mobilisable force at the head of the inclusion F_0 can also be assumed to incline δ_{RI} with respect to the vertical direction. F_0 considering an inclination δ_{RI} can be estimated using Equation 8.12.

$$F_0(\delta_{RI}) = \left[\left(1 - \frac{2\delta_{RI}}{\pi}\right)^2 - \frac{2\delta_{RI}}{\pi}\left(2 - \frac{6\delta_{RI}}{\pi}\right)\right] F_0(\delta_{RI} = 0) \tag{8.12}$$

When considering the presence of rigid inclusions embedded at a depth D_e within the LTP, the expression for the maximal axial force T_{nl} needs to account for the section within the LTP, as illustrated in Equation 8.13.

$$T_{nl} = min(F_0 + q_s(l_{int} - D_e)\pi d + q_{s,LTP} D_e \pi d, F_L + q_s l_{ext} \pi d) \tag{8.13}$$

8.3.3 Lateral soil-inclusion interaction resistance

This criterion corresponds to the resistance of lateral soil-inclusion interaction behaviour. The pressure within the interior length L_{int} or the exterior length L_{ext} of the inclusion is restricted by the limit pressure p_l^* in the soil.

The lateral interaction of the inclusion is analysed through the limit equilibrium model, often referred to as *modèle d'équilibre limit (MEL)* in French. The comprehensive and innovative limit equilibrium models are proposed in this work and their lateral pressure distributions for various lengths of L_{int} and L_{ext} are depicted in Figures 8.17 and 8.18.

The first limit equilibrium model(MEL I) in Figure 8.17 exhibits three distinct phases based on its lateral pressure distribution. When the interior length L_{int} is less than a quarter of the total length L, an equilibrium can be achieved considering the entire length of the inclusions. However, as the interior length L_{int} exceeds a quarter of the total length L, a reduction factor denoted as β is applied to decrease the pressure acting on the interior length L_{int} to establish equilibrium along the inclusion.

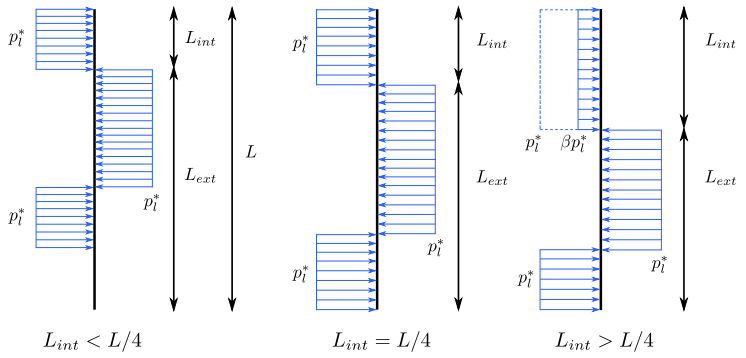

Fig. 8.17. Distribution of lateral pressure for limit equilibrium model (MEL I)

A different limit equilibrium model (MEL II) consisting of five phases is proposed. The first two phases are identical to the first limit equilibrium model. In contrast to MEL I, equilibrium is achieved with a negative pressure equal to p_l^* at the upper part of the inclusion.

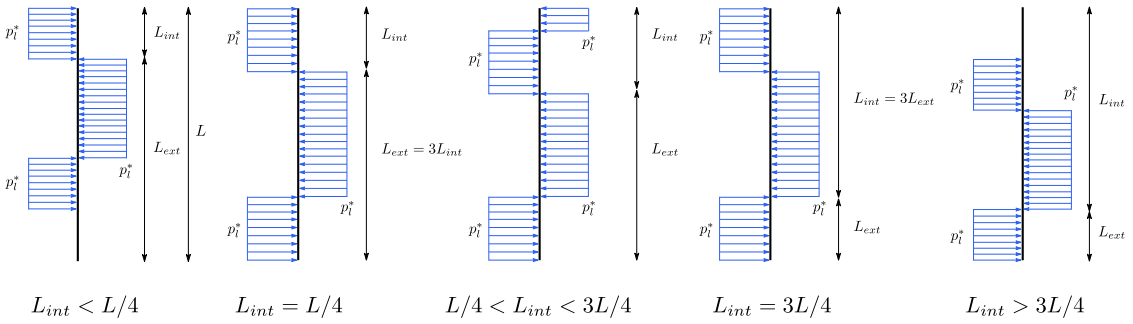

Fig. 8.18. Distribution of lateral pressure for limit equilibrium model (MEL II)

Inclusions can also experience failure at locations where the maximum bending moment exceeds the material strength. In such cases, a simplified version of the expression in Equation 8.6 is given by Equation 8.14. Figures 8.19 and 8.20 depict the normalised values of T_c, M_c, and M_{max} for varying ratios between the interior length L_{int} and the total length L of a rigid inclusion.

$$M_{max} \leq M_{c,0}[1 - (\frac{T_n}{T_{n,0}})^2] \tag{8.14}$$

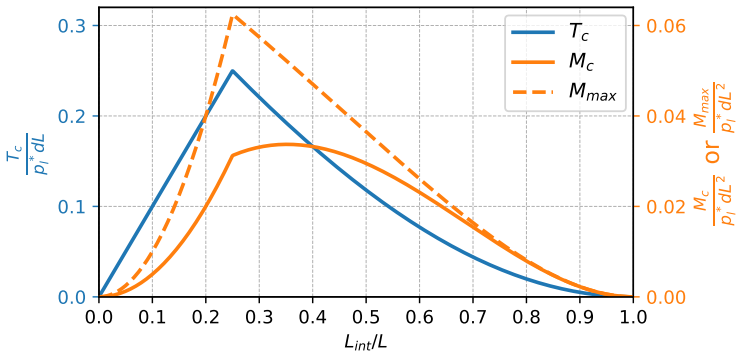

Fig. 8.19. Evaluation of T_c, M_c and M_{max} for different L_{int}/L ratios for limit equilibrium model (MEL I)

When considering the embedding of rigid inclusions in LTP with an embedment depth D_e, the limit equilibrium model is modified to account for a higher limit pressure $p_{l,LTP}^*$ in the LTP, and which surpasses the p_l^* of the soft soil. The limit equilibrium model, as depicted in Figure 8.21, also incorporates a similar reduction factor denoted as β. In this model, for a small interior length L_{int}, the reduction factor β should be employed to reduce the limit pressure in the LTP and the soft soil. This reduction is necessary to maintain equilibrium along the inclusion.

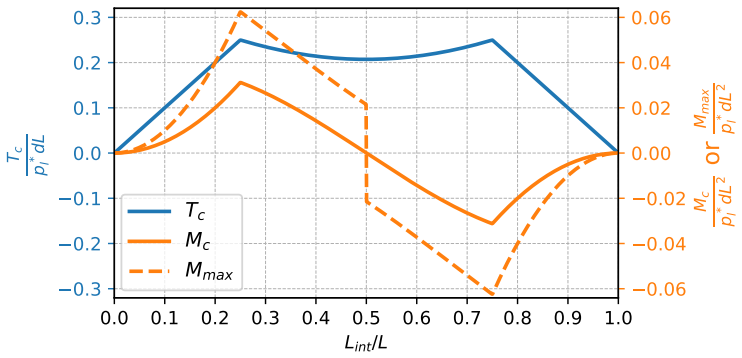

Fig. 8.20. Evaluation of T_{cl}, M_{cl} and M_{max} for different L_{int}/L ratios for limit equilibrium model (MEL II)

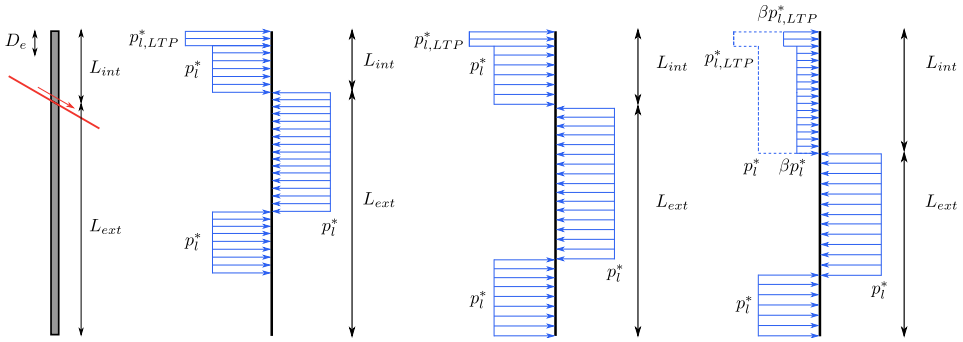

Fig. 8.21. Distribution of lateral pressure for a limit equilibrium model in the case with embedment of inclusions in LTP

Considering a configuration in which a 10 m long inclusion is embedded to a depth of 0.5 m in the LTP, with the LTP characterised by $p^*_l{}_m = 1$ MPa and the soft soil characterised by $p^*_l = 200$ kPa, and an embedment D_e of 0.5 m is used. The resulting normalised values of T_c, M_c and M_{max} for this particular case are depicted in Figure 8.22.

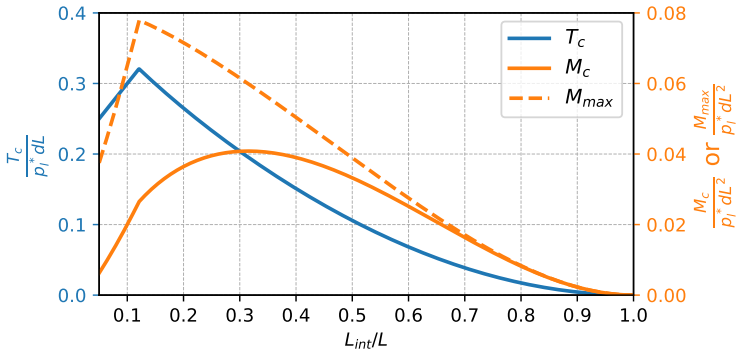

Fig. 8.22. T_c, M_c and M_{max} for different L_{int}/L ratio in the case with embedment of inclusions in LTP

8.3.4 Multicriterion for rigid inclusions failure modes

The combination of the four criteria mentioned above in the (T_n, T_c) plane defines a useful stability domain, known as the multicriterion (Schlosser and Unterreiner, 1990). This domain establishes limits on the potential forces provided by rigid inclusions and it can be visualised as an envelope formed by the four criteria. Forces within the inclusion can be located at any point within this domain, as illustrated in Figure 8.23.

When failure occurs, the forces must lie on the boundary of the useful domain, and its position is determined by the principle of maximum work (Schlosser, 1978). This principle indicates that the forces on the boundary are chosen in a way that maximises the power of inclusions within a given failure mechanism. Once the virtual velocity at the intersection of the inclusion with the failure surface is specified, the virtual power of an inclusion can be calculated.

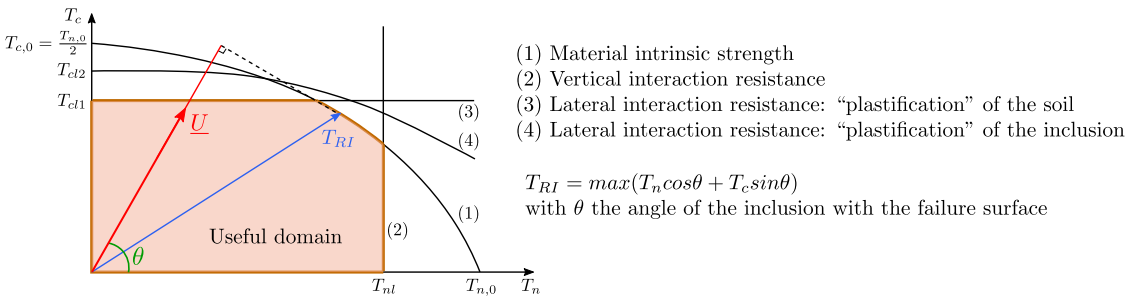

Fig. 8.23. Multicriterion combining several failure criteria in the T_n-T_c plane

8.4 Seismic bearing capacity for reinforced foundations

8.4.1 Problem description

The investigated problem in this study focuses on the seismic bearing capacity for a strip foundation reinforced by rigid inclusions. A strip foundation with width B is placed on a half-space consisting of an LTP of thickness h_{LTP} and with a friction angle φ (purely cohesionless behaviour), as well as a cohesive soft soil layer with a cohesion value c and no tensile strength. The soft soil layer is reinforced with rigid inclusions, as illustrated in Figure 8.24. The inclusions with diameter d are assumed to be regularly spaced under the foundation with a spacing s.

The seismic excitation is assumed to be applied in a pseudo-static manner. The force transmitted to the footing is denoted as $\underline{F}$, and the moment $\underline{M}$ is calculated by multiplying the vertical force $\underline{V}$ by the eccentricity e.

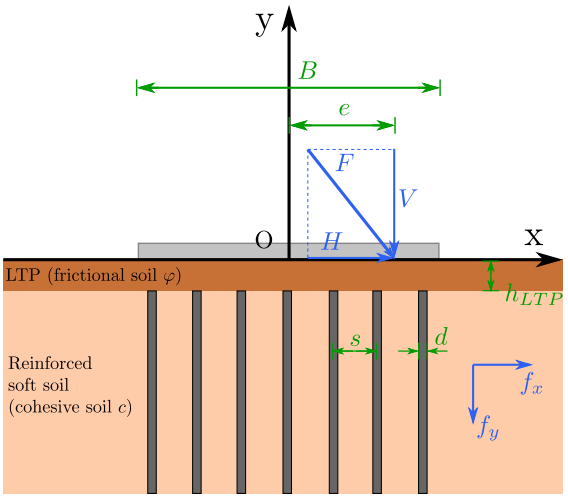

Fig. 8.24. Two-dimensional problem of the bearing capacity of a strip foundation reinforced by rigid inclusions and subjected to seismic loading

Additionally, inertial effects in the soil are considered through body forces due to seismic and gravity loading, denoted as $f_x = \rho a_x$ and $f_y = \rho(g \pm a_y)$, respectively.

8.4.2 Simplified sub-systems

In contrast to the previous cases where the foundation is directly placed on an infinite homogeneous half-space, the configuration with reinforcements involves a cohesive soil reinforced by rigid inclusions and an LTP between the foundation and the reinforced soil. Consequently, the reinforcement and the presence of an LTP layer introduce variations in the failure mechanisms for rigid inclusion-reinforced foundations compared to those for foundations without reinforcement.

To address these characteristics, three simplified sub-systems, illustrated in Figure 8.25, are proposed, corresponding to the different potential failure mechanisms. The analysis is performed, involving three distinct cases:

- **Case I**: This case considers homogeneous frictional soil, with failure primarily concentrated in the LTP, resulting in a failure depth lower than h_{LTP};
- **Case II**: This case focuses on sliding and uplift at the interface between the LTP and the reinforced soft soil;
- **Case III**: Homogeneous cohesive soil is considered, taking into account reinforcement by rigid inclusions. The failure depth in this case exceeds h_{LTP} and intersects the rigid inclusions.

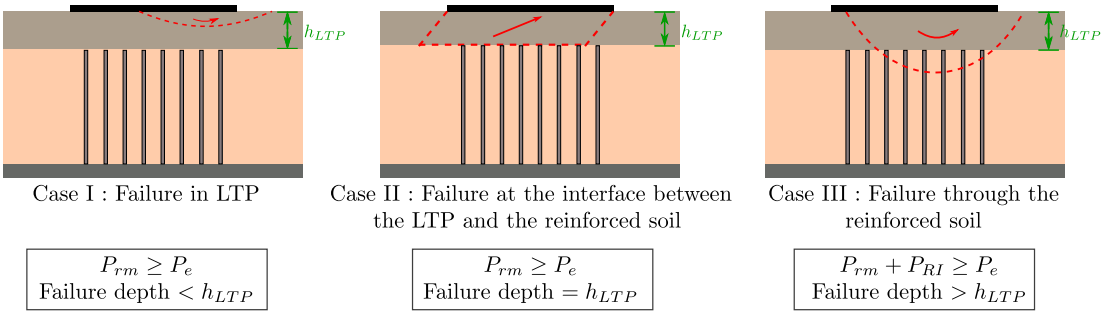

Fig. 8.25. Simplified sub-systems for a foundation reinforced by rigid inclusions

The upper-bound solutions for three cases are denoted $K^{up,I}$, $K^{up,II}$, and $K^{up,II}$. The results from these analyses are then combined to determine the stability domain K^{up} of a foundation reinforced by rigid inclusions, as described in Equation 8.15.

$$K^{up} = K^{up,I} \cap K^{up,II} \cap K^{up,II} \tag{8.15}$$

Case I is particularly relevant for understanding the failure mechanisms within the LTP, aiming to replicate similar failure modes observed in shallow foundations on frictional soil, as depicted in Figure 8.25 (a). Case III concentrates on potential failure modes occurring in the soft soil reinforced by rigid inclusions. It encompasses the same failure modes as cohesive soil, as indicated in Figure 8.25 (c).

Case II serves as a transitional mode situated between shallow failure mechanisms (Case I) and deep failure mechanisms (Case III). This mechanism draws inspiration from the work of Salençon and Pecker (1995b), as depicted in Figure 8.5. It can be roughly described as a quadrilateral block in translation, with a horizontal velocity discontinuity line passing just above the inclusion heads, thereby avoiding the mobilisation of the strength properties of the rigid inclusions. This same failure mechanism is also observed in a rigid inclusion-reinforced embankment subjected to lateral seismic loading (Hassen *et al.*, 2021). It is important to note that for configurations with rigid inclusions embedded in LTP, Case II is not applicable.

Cases I and II are relatively straightforward to analyse. Case I has already been studied in a situation with purely cohesionless soil, as described in Section 8.2.1. Case II can be simplified as the velocity jump mechanism presented in Figure 8.5. In this case, the inclusions do not significantly affect the calculation of resistance power and external force power.

The details of Case III are presented in Figure 8.26. The chosen failure mechanism for this case is inspired by the mechanisms for foundations on non-reinforced cohesive soil described in Section 8.2.1, which are tested. The selected failure mechanism family for Case III combines rotation and translation blocks with uplift behaviour and includes three geometric parameters: α, μ, and λ, as depicted in Figure 8.3 (b).

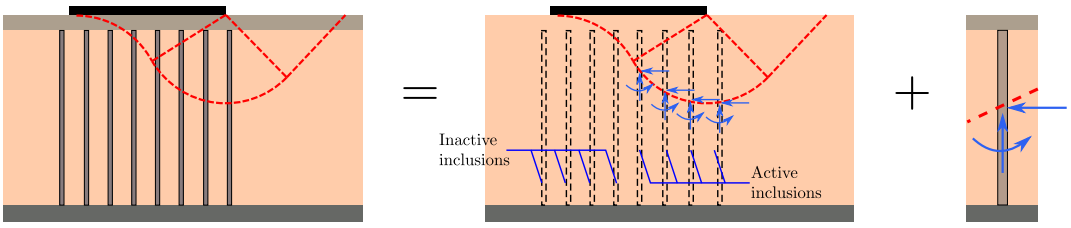

Fig. 8.26. Detailed description for Case III: (a) multi-block failure mechanism, (b) simplified configuration and (c) forces at the intersection of inclusion with failure interaction

The presence of the LTP is not considered in the calculation of the resisting power of the soil P_{rm} to simplify the analytical calculations, as shown in Figure 8.26 (b). Typically, the LTP is composed of compacted gravel material and has better resistance characteristics than the soft soil that needs reinforcement. The omission of the LTP in these calculations remains a conservative simplification. However, the LTP is taken into account in the calculation of the force at the intersection provided by the rigid inclusions, as indicated in Equations 8.10 and 8.13, consequently, in the contribution of rigid inclusions, as depicted in Figure 8.26 (c). For a system with n active inclusions, the resisting power representing the contribution of rigid inclusions can be described by Equation 8.16.

$$P_{RI}(\underline{\widehat{U}}) = \sum_{i}^{n} \left[T_{n,i}\, \widehat{U}_{n,i} + T_{c,i}\, \widehat{U}_{c,i} + M_{c,i}\, \widehat{U}_{m,i} \right] \tag{8.16}$$

where $T_{n,i}$, $T_{c,i}$, and $M_{c,i}$ represent the axial force, shear force, and bending moment provided by active inclusion i, respectively. Additionally, $\widehat{U}_{n,i}$, $\widehat{U}_{c,i}$, and $\widehat{U}_{m,i}$ represent the velocities at the intersection between the active inclusion i and the velocity discontinuity surface.

8.4.3 Superposition of three sub-systems

The problem is partitioned into three sub-systems and it is assumed that the interaction diagram can be constructed by superimposing the interaction diagrams for these three sub-systems. An illustration of this superimposition process is presented in this section.

In this example, a typical foundation configuration with rigid inclusion reinforcement is considered. It consists of a 10 m wide strip foundation, resting on a 0.5 m thick LTP layer with a friction angle of 38°. The soft soil is treated as cohesive and has an undrained shear strength c of 25 kPa ($q_s = 25$ kPa and $p_l^* = 200$ kPa). Throughout the depth of the soft soil, there are concrete rigid inclusions with a diameter of 0.4 m and a length of 10 m. These inclusions are not penetrated in the LTP. The axis-to-axis spacing is 1.5 m, resulting in a coverage area ratio of 5.6 %. The lateral interaction mechanism MEL II is used.

The interaction diagram in the V-H plane is depicted in Figure 8.27, showing the result of the superimposing of the three sub-systems presented in Figure 8.25. For small vertical forces ($V/Bc < 1$), the V-H interaction diagram is predominantly represented by Case I, corresponding to failure within the LTP layer. As the vertical force increases, a sliding mechanism between the LTP and the soft soil becomes apparent. Finally, for greater vertical forces ($V/Bc > 4$), the interaction diagram is primarily controlled by Case III, which represents a failure mechanism in the reinforced soil.

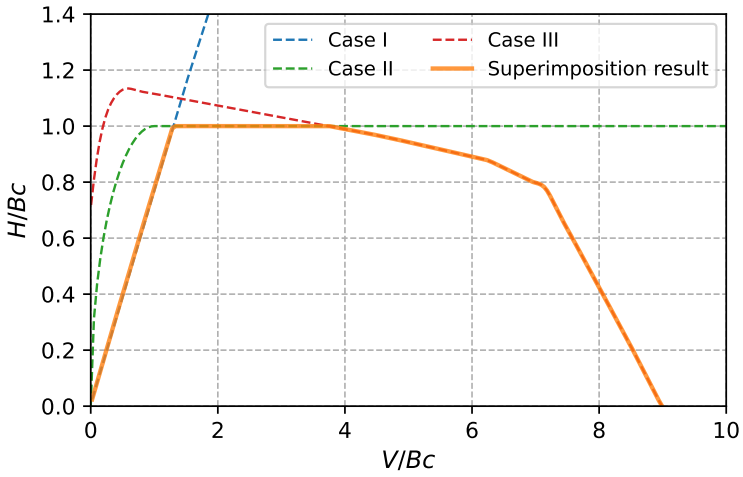

Fig. 8.27. Superimposition of the interaction curves of the simplified sub-systems in the normalised V-H plane

It is also worth considering the superimposition of the interaction curves in the V-M plane, as depicted in Figure 8.28 (a). Case II does not play a role in the V-M plane. The result of superimposition reveals that the interaction curve in the V-M plane is primarily composed of the curves corresponding to Case I and Case III. For small vertical forces ($V/Bc < 1$), the V-M interaction diagram is primarily represented by Case I, which corresponds to failure within the LTP.

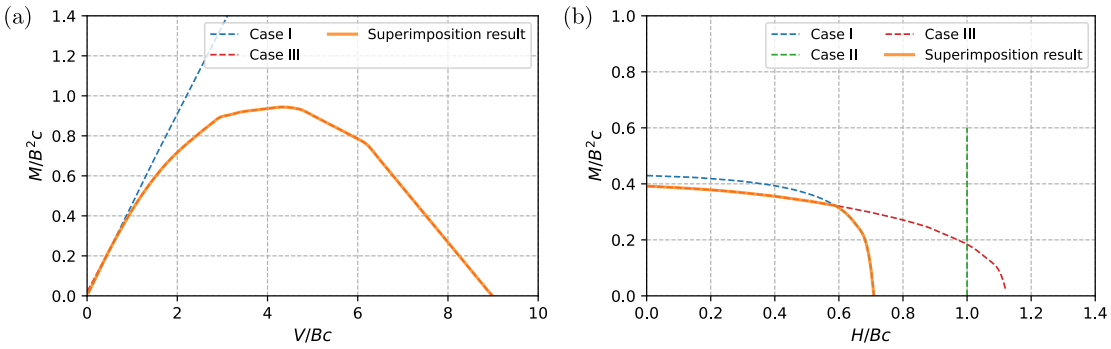

Fig. 8.28. Superimposition of the interaction curves of the simplified sub-systems: (a) in the normalised V-M plane and (b) in the normalised H-M plane for $V/V_{max} = 1/10$

Concerning the interaction diagram in the H-M plane, several interaction curves for different values of V/V_{max} are also presented. The H-M interaction diagram for $V/V_{max} = 1/10$ is displayed in Figure 8.28 (b). This curve is composed of two mechanisms: Case I and Case III.

The H-M interaction diagrams for $V/V_{max} = 1/6$ and $V/V_{max} = 1/3$ are presented in Figures 8.29 (a) and (b), respectively. In the H-M plane with $V/V_{max} = 1/6$ and $V/V_{max} = 1/3$, the frictional sliding mechanism represented by Case I does not contribute to the interaction curve. These interaction curves are composed of the interaction curve obtained from Cases II and III, representing a cohesive sliding and the failure mechanism within reinforced soil.

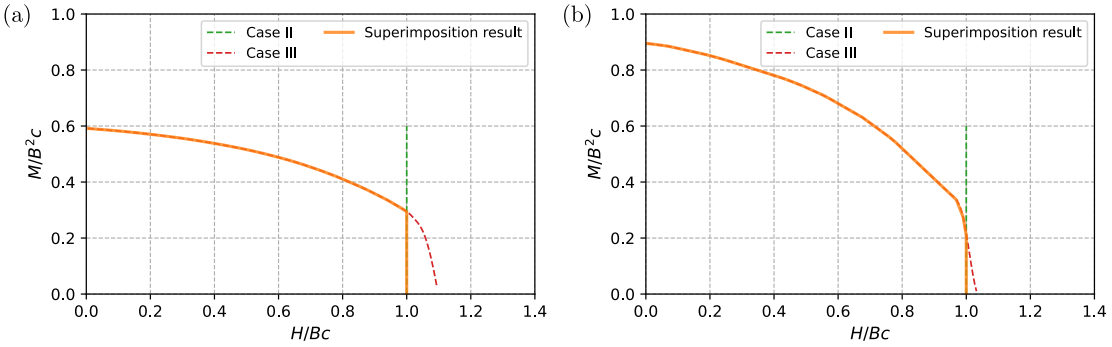

Fig. 8.29. Superimposition of the interaction curves of the simplified sub-systems in the normalised H-M plane for: (a) $V/V_{max} = 1/6$ and (b) $V/V_{max} = 1/3$

The interaction diagrams for $V/V_{max} = 1/2$ and $V/V_{max} = 2/3$ in the H-M plane are presented in Figures 8.30 (a) and (b), respectively. In these H-M planes with different V/V_{max}, it can be observed that the failure mechanism in reinforced soil (Case III) is the principle failure mechanism. This observation is confirmed by Figure 8.27 where the failure mechanism in reinforced soil is not influenced by the sliding mechanism (Cases I and II) for a high V/V_{max} ratio.

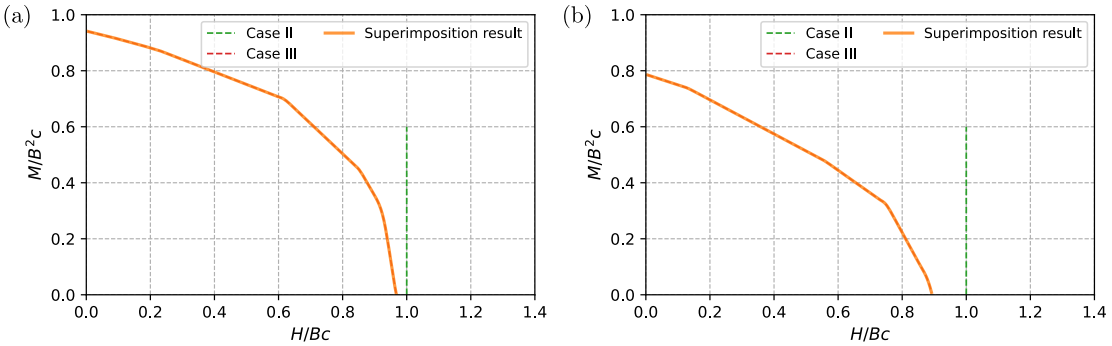

Fig. 8.30. Superimposition of the interaction curves of the three simplified sub-systems in the normalised H-M plane for: (a) $V/V_{max} = 1/2$ and (b) $V/V_{max} = 2/3$

This study is specifically applicable to 2D plane strain problems. Nevertheless, it is feasible to introduce shape coefficients, defined in Equation 8.17, analogous to those utilised in the bearing capacity calculations for square, rectangular, or circular shallow foundations (ASIRI, 2012). This extension would allow the application of the obtained results to 3D situations.

$$s_c = 1 + 0.2\frac{B}{L} \tag{8.17}$$

8.4.4 Comparison with non-reinforced foundation

In this section, the investigation of the influence of reinforcement by rigid inclusions on the bearing capacity, as described by interaction curves, is of vital interest. The interaction curves for the two systems are depicted in Figure 8.31. For the configuration with rigid inclusions, identical parameters as those presented in Section 8.4.3 are employed, as illustrated in Figure 8.31 (a). The corresponding configuration without rigid inclusions is shown in Figure 8.31 (b). The properties of LTP and soft soil remain consistent throughout the analysis.

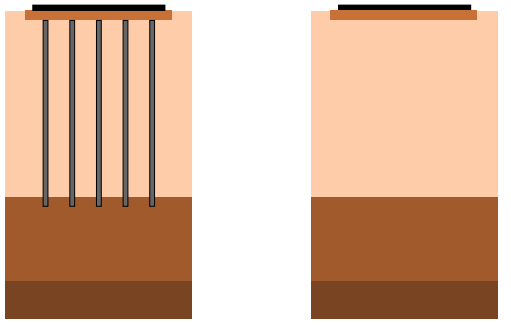

(a) With inclusions (b) Without inclusion

Fig. 8.31. Configuration of foundation: (a) with reinforcement and (b) without reinforcement

The interaction diagram is initially compared in the V-H plane, as depicted in Figure 8.32 (a). There is a substantial increase in the ultimate bearing capacity of the foundation. The bearing capacity V_{max} for the configuration with inclusions (depicted by the orange curve) approaches approximately 9 times Bc, while for the configuration without inclusions (depicted by the black dashed curve), this value is limited to 5.14 times Bc.

The interaction diagrams in the V-M plane for both configurations are also compared in Figure 8.32 (b). It is observed that the stability domain is considerably larger for the configuration with inclusions as compared to the one without inclusions. This outcome underscores the fact that the incorporation of rigid inclusions has the potential to enhance the bearing capacity of the foundations under eccentric loading conditions.

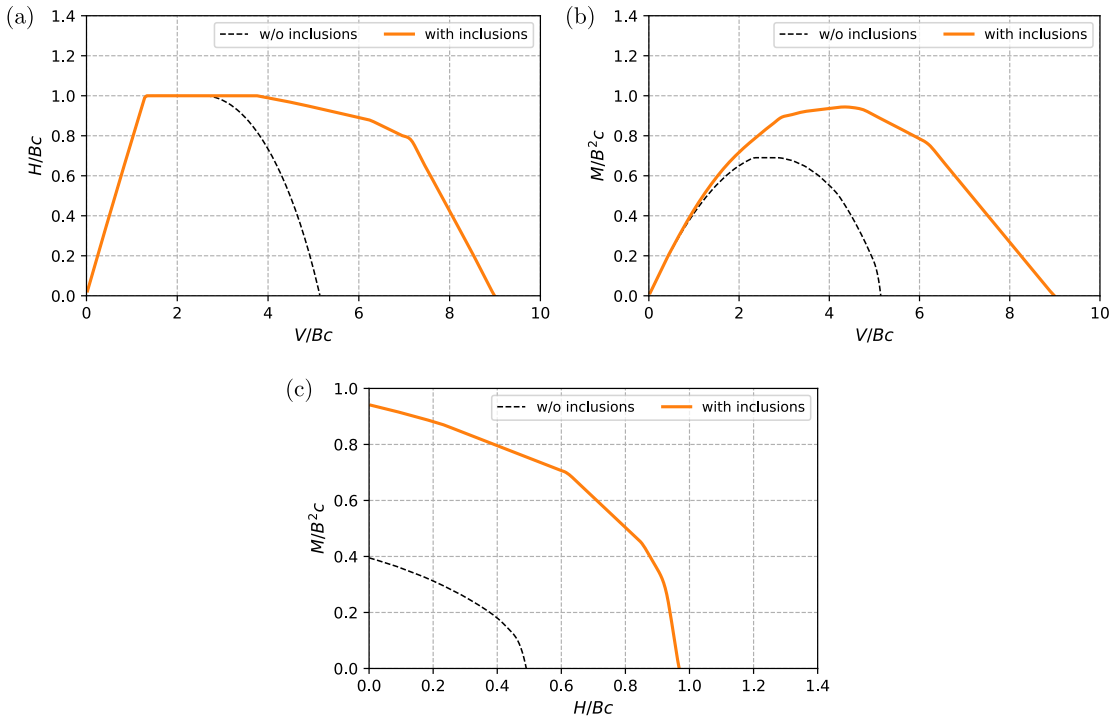

Fig. 8.32. Comparison between the interaction diagrams in (a) the normalised V-H plane, (b) the normalised V-M plane, and (c) the normalised H-M plane for the non-reinforced and reinforced foundations

The illustration of the comparison between the interaction curves for the configurations with and without inclusions in the H-M plane, with a constant value of $V = 4.5\ Bc$, can be found in Figure 8.32 (c). In the H-M plane at $V = 4.5\ Bc$, the influence of soil reinforcement by rigid inclusions is notably significant. The stability domain, as enclosed by the interaction curves, is substantially greater for the reinforced foundation in comparison to the non-reinforced foundation.

8.4.5 Contribution of vertical and horizontal forces of rigid inclusions

Following the ASIRI+ recommendation (ASIRI, 2012), it is observed that incorporating axial forces provided by rigid inclusions typically leads to a substantial improvement. Conversely, the additional advantage gained from introducing shear forces is comparatively limited. Therefore, disregarding the shear contribution does not exert a significant influence and can be considered a safe simplification. This section aims to validate this assumption.

Different interaction diagrams are calculated based on different assumptions and are presented in Figure 8.33:

- The axial forces in rigid inclusions are not considered ($T_n = 0, T_c \neq 0$);
- The shear forces in rigid inclusions are not considered ($T_n \neq 0, T_c = 0$);
- The shear and axial forces in rigid inclusions are both considered ($T_n \neq 0, T_c \neq 0$).

Figure 8.33 illustrates that the interaction curve (green curve), which considers both axial and shear forces, exhibits a larger stability domain compared to the curves obtained under the other two assumptions. Notably, the interaction curve accounting solely for shear forces (blue curve) closely resembles the curve obtained for the configuration without inclusions (represented by a black dashed curve).

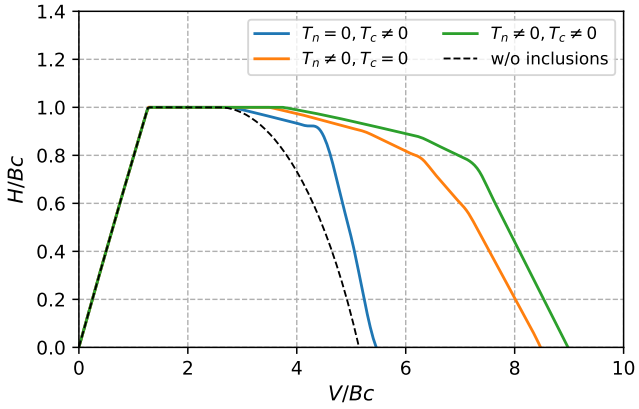

Fig. 8.33. Normalised V-H interaction curves with the contribution of different forces of rigid inclusions

This suggests that a configuration considering only shear forces in rigid inclusions performs a similar bearing capacity to that of the configuration without reinforcement by rigid inclusions. Furthermore, the configurations considering shear forces and those not considering shear forces give two similar interaction curves (green and orange curves) in Figure 8.33, implying that taking into account shear forces provides only a limited benefit.

8.5 Hypothesis verification

8.5.1 Load inclination at the head of inclusions

In Section 8.3.2, the limit force at the heads of inclusions, denoted as F_0, is influenced by the inclination of the applied load. It is worth noting that this inclination effect has not been accounted for in the results presented in the preceding sections. However, based on the inertial force analysis detailed in Chapter 6, it becomes apparent that the inclination at the heads of rigid inclusions is of less significance compared to the

overall load inclination. In essence, if the load applied to the foundation inclines δ, the inclination of the load applied at the heads of the inclusions, denoted as δ_{RI}, is consistently smaller than δ, as illustrated in Figure 8.34. To quantitatively assess this difference, an inclination ratio, denoted as κ, is proposed to capture the relationship between these angles: $tan(\delta_{RI}) = \kappa \cdot tan(\delta)$ with $\kappa \leq 1$.

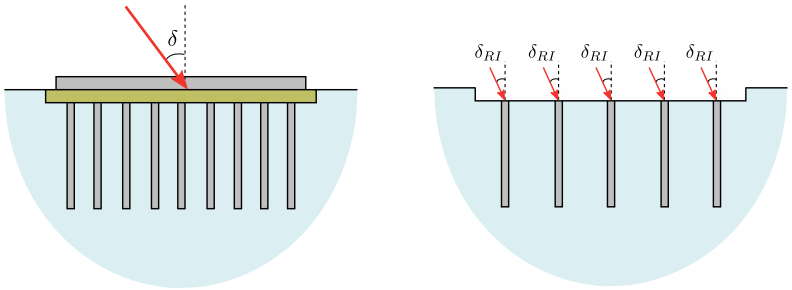

Fig. 8.34. Load inclination at the foundation and the heads of inclusions

To explore the impact of the load inclination effect on the force at the heads of inclusions F_0, the stability curves in the V-H plane are generated, considering various inclination ratios κ, as displayed in Figure 8.35. The properties of the foundation system remain consistent with those presented in Section 8.4.3.

The interaction curves exhibit similarity across various inclination ratios κ. The curves consistently demonstrate the same trend and magnitude, regardless of the different κ values employed in the calculations. These findings affirm that the inclination of the force at the heads of inclusions has minimal influence on the interaction curve and bearing capacity.

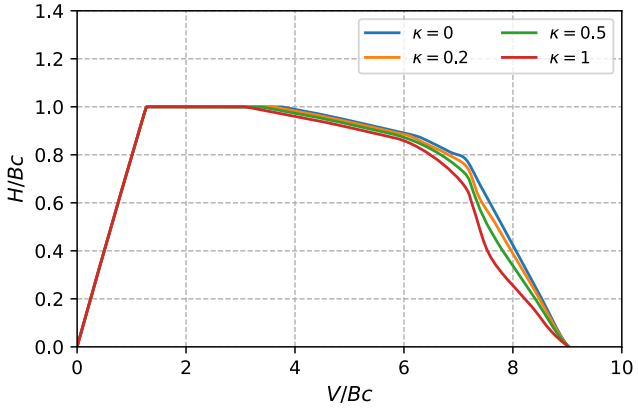

Fig. 8.35. Normalised V-H interaction curves considering various load inclination at heads of inclusions

8.5.2 Different limit equilibrium models

In Section 8.3.3, two potential limit equilibrium models for assessing the lateral interaction between soil and inclusions are introduced, denominated as MEL I (depicted in Figure 8.17) and MEL II (depicted in Figure 8.18). The examination of how distinct limit equilibrium models impact the interaction diagrams describing the bearing capacity under various load conditions is of interest. The interaction diagrams, computed using two distinct lateral limit equilibrium models, are presented in Figure 8.36.

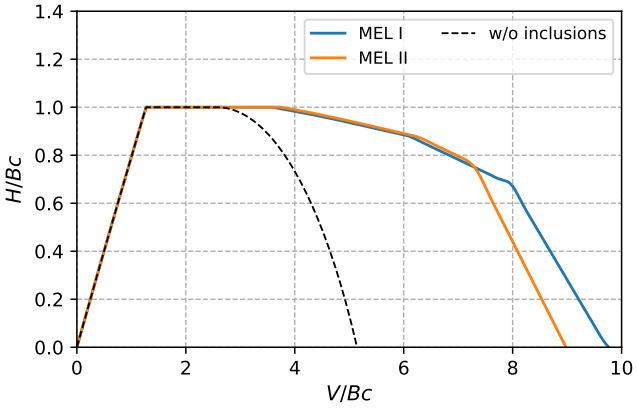

Fig. 8.36. Normalised V-H interaction curves with different lateral limit equilibrium models

It is observed that these two interaction curves are relatively close to each other and even overlap. A noticeable deviation appears for V/V_{max} ratios exceeding 7.5. The bearing capacity values under vertical load, obtained from MEL I and MEL II, are also quite similar, with MEL I proceeding 9.6 Bc and MEL II resulting in 9 Bc. These results indicate that the lateral limit equilibrium model has only a minor influence on both the bearing capacity and interaction diagram. Given that the limit equilibrium model MEL II offers a more conservative interaction curve, it is employed in this study for configurations without embedment of inclusions in the LTP.

8.6 Summary

This chapter begins with a brief overview of the existing literature on the study of the ultimate bearing capacity by the kinematic exterior approach for strip foundations on homogeneous cohesionless and cohesive soil. An examination of the failure velocity fields for strip foundations is conducted. To obtain the interaction curves corresponding to these failure velocity fields, a direct algorithm of proof by exhaustion has been employed. The algorithm and its implementation have been rigorously validated by comparing with the results presented in the cited references.

The examination of failure modes for rigid inclusions is a focal point of this chapter. Building upon the insights gained from the investigation of nailed soil, a multicriterion tailored specifically for rigid inclusions has been introduced. This multicriterion encompasses different potential mechanisms, which include intrinsic material resistance, vertical soil-inclusion interaction resistance, as well as lateral soil-structure interaction resistance. The soil-interaction resistance is explored through the utilisation of limit equilibrium models, and it is worth noting that the limit equilibrium model developed for rigid inclusions can be extended to other geotechnical structures, such as piles and retaining walls.

Recognising the complexity inherent in reinforced foundation configurations, this study initially examines a series of simplified potential failure mechanisms. The interaction diagrams that define the stability domain for this foundation type are established through the superimposition of these three distinct potential failure mechanisms. A comprehensive description of the superimposition process in various planes is provided.

Subsequently, the interaction curves obtained through the proposed methodology are compared with those generated for a non-reinforced configuration where rigid inclusions are absent. This comparison highlights the impact of reinforcement by rigid inclusions. Additionally, the contribution of both axial and shear forces provided by rigid inclusions to the stability of the foundation system is examined. The results indicate that the axial-resistant force from rigid inclusions plays a more pivotal role in stabilising the system compared to the shear-resistant force.

The study also explores various hypotheses, including factors such as the load inclination at the heads of inclusions and the use of different limit equilibrium models for lateral soil-inclusion interaction resistance. The findings suggest that these factors do not exert a significant influence on the bearing capacity.

In summary, this work establishes an innovative analytical approach for assessing the bearing capacity of foundations reinforced by rigid inclusions subjected to static and dynamic loads, employing the upper-bound kinematic approach. A novel multicriterion is proposed to better understand the forces provided by rigid inclusions and potential failure modes that can occur. These advances provide a comprehensive and versatile tool for dynamic SSI macro-element analysis and are readily applicable in engineering practice. Table 8.1 provides a comprehensive comparison of various features and hypotheses between this study and other related research endeavours.

Tab. 8.1. Application of the kinematic exterior approach to analyse reinforced soil

	Nailed slope (de Buhan *et al.*, 1992)	Design software (Terrasol, 2023)	Rio-Antirrio Bridge (Pecker *et al.*, 1998)	**This study**
Application	Nailed slope	Nailed slope	Foundation reinforced by rigid inclusions	**Foundation reinforced by rigid inclusions**
Failure mechanism	Logarithmic spirals	Logarithmic spirals	Mechanisms inspired by shallow foundations	**Mechanisms inspired by shallow foundations**
Limit equilibrium of inclusion	Single criterion	Multicriterion for nail	Single criterion	**Multicriterion for inclusion**
Stability domain	Single domain	Single domain	Superimposition of several domains	**Superimposition of several domains**

9 Seismic bearing capacity: Numerical validation

9.1 Objective of numerical validation

Chapter 8 has presented the theoretical framework for investigating the bearing capacity of rigid inclusion-reinforced foundations. Within this framework, an analytical approach is introduced for the estimation of bearing capacity and the derivation of the interaction curves for rigid inclusion-reinforced foundations.

In this chapter, a validation process is carried out using Finite Element Limit Analysis (FELA) modelling to validate the analytical approach (Optum Computational Engineering, 2021). This validation encompasses both qualitative and quantitative aspects. Qualitatively, it aims to confirm the three proposed potential mechanisms. Quantitatively, it involves a comparison of interaction curves and bearing capacities obtained through the analytical approach with those derived from the numerical calculations.

9.2 Finite element limit analysis model

In the field of geotechnical engineering, the static interior approach is not frequently employed due to the complexity involved in establishing the statically admissible stress field. However, to validate the proposed analytical approach based on the kinematic exterior approach, it is beneficial to undertake the static interior approach to pinpoint the position of the derived upper-bound solution. In this endeavour, the numerical approach: FELA model, as a kind of FEM model, can serve as a valuable validation tool. The modelling technique is detailed in Section 3.4.2. These foundations reinforced by rigid inclusions are modelled using the OPTUM FELA software (Optum Computational Engineering, 2021).

A 2D plane strain model is utilised to represent the soil-foundation system, including the LTP, the strip footing, and the rigid inclusions. Solid elements are employed for modelling both the soil and the LTP. These solid elements are triangular with the lower-bound or upper-bound element formulations, capable of providing a lower-bound or upper-bound estimation compared to the exact solution. The two-element formulations are depicted in Figure 9.1. The soft soil is simulated using the Tresca material model, which incorporates

its undrained shear strength c. The LTP is modelled using a Mohr-Coulomb material model characterised by a friction angle φ and zero cohesion.

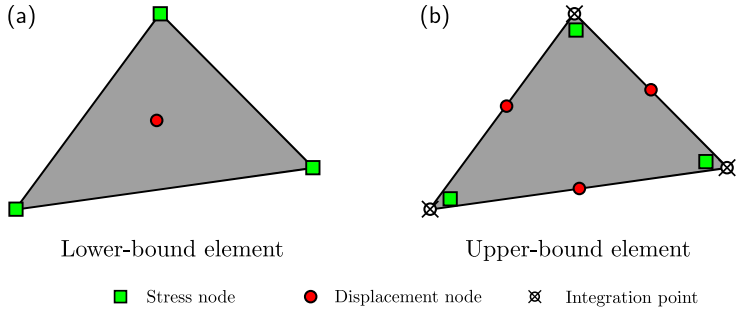

Fig. 9.1. FELA triangular: (a) lower-bound element and (b) upper-bound element

The strip foundation is assumed to be perfectly rigid and possesses infinite strength. The rigid inclusions are represented by pile rows, which are modelled using an embedded beam element in 2D plane strain analysis. To accurately simulate inclusion rows, it is necessary to define their geometric properties, including section geometries and soil-pile strength parameters such as axial strength, lateral strength, and base strength.

The geometry and mesh are depicted in Figure 9.2. It is important to highlight that the mesh displayed in Figure 9.2 (b) represents the adapted mesh following iterative calculations.

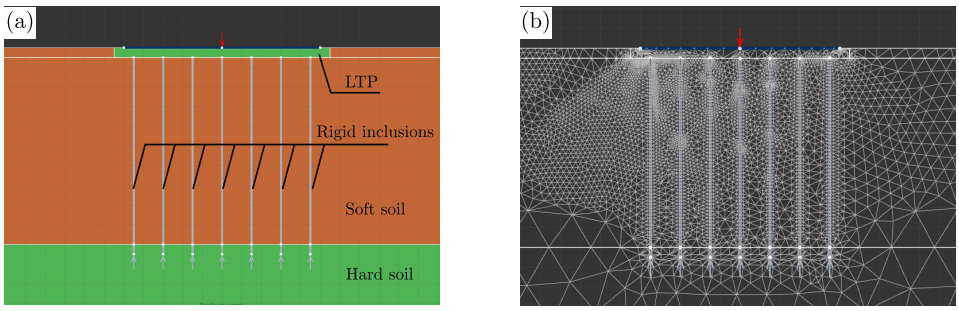

Fig. 9.2. 2D FEM model for a foundation on soil reinforced by rigid inclusions: (a) model geometry, and (b) iterated mesh

9.3 Failure mechanisms

9.3.1 Studied configurations

By utilising the failure mechanisms induced in Section 8.4.2, it becomes feasible to generate interaction diagrams in various planes through the superimposition of interaction

diagrams obtained from different sub-systems. To ensure the reliability of these failure mechanisms, validation via numerical modelling is imperative. The various load combinations are delineated in Figure 9.3. Each segment of the V-H interaction curve corresponds to a failure mechanism, as dictated by the three sub-systems. These corresponding failure mechanisms are also clearly indicated in the figure.

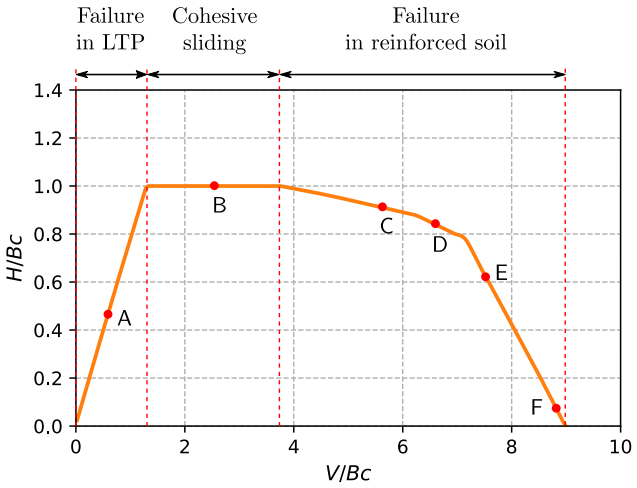

Fig. 9.3. Tested load combinations (red point) within V-H interaction plane

9.3.2 Comparison of failure mechanisms derived from two approaches

The first comparison is illustrated in Figure 9.4. The load point under investigation is located on the left part of the interaction diagram, as depicted in Figure 9.4 (a). It is noteworthy that both the analytical solution and FEM calculation have the same extreme load couple (V, H). Under the given load conditions, the kinematic failure mechanism is primarily governed by a failure mechanism within the LTP. The analytical study results in a failure mechanism, as presented in Figure 9.4 (b), while for the same load conditions, the FEM modelling exhibits a similar failure surface in Figure 9.4 (c).

An additional qualitative comparison of mechanisms is provided in Figure 9.5 to validate the mechanism representing a cohesive sliding failure occurring at the interface between the LTP and the soft soil. Figure 9.5 (b) demonstrates a sliding mechanism, and it is noteworthy that nearly identical limit force couples (V, H) are observed through both analytical and numerical approaches.

The comparison of the failure mechanism for the third tested load combination is displayed in Figure 9.6. In this particular load combination, the failure mechanism involves a failure within the reinforced soil, occurring at a much greater depth compared to the first two load combinations. Notably, this failure mechanism intersects with only one row of

inclusions. The inclusion row that intersects with the failure surface is referred to as the active inclusion and is coloured red.

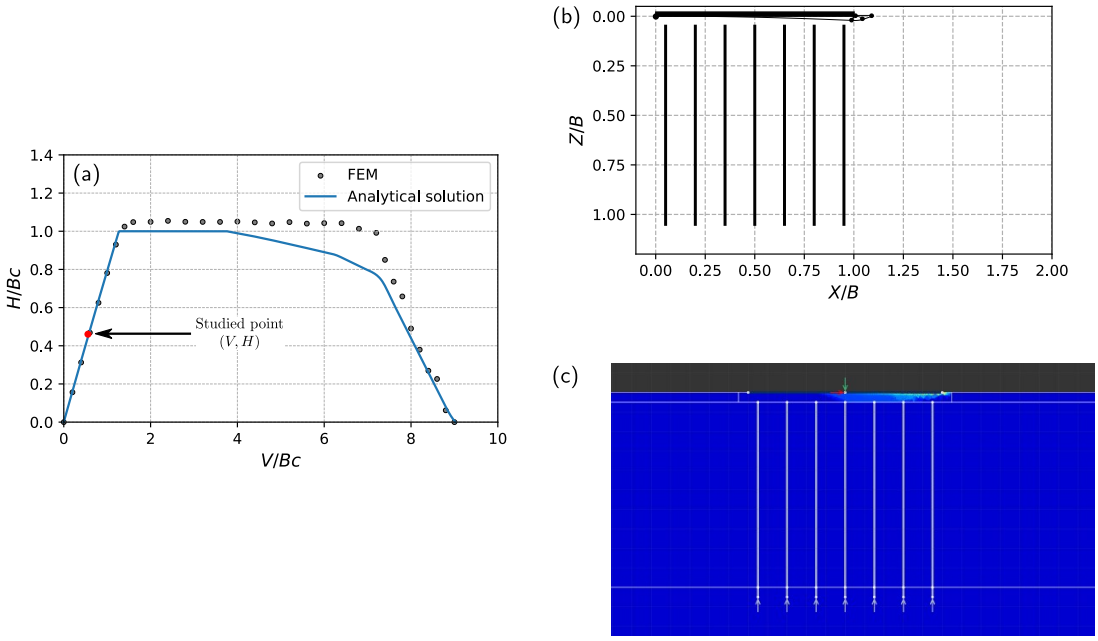

Fig. 9.4. Comparison of failure mechanisms: (a) load combination A, (b) failure mechanism obtained by analytical solution, and (c) obtained by FEM

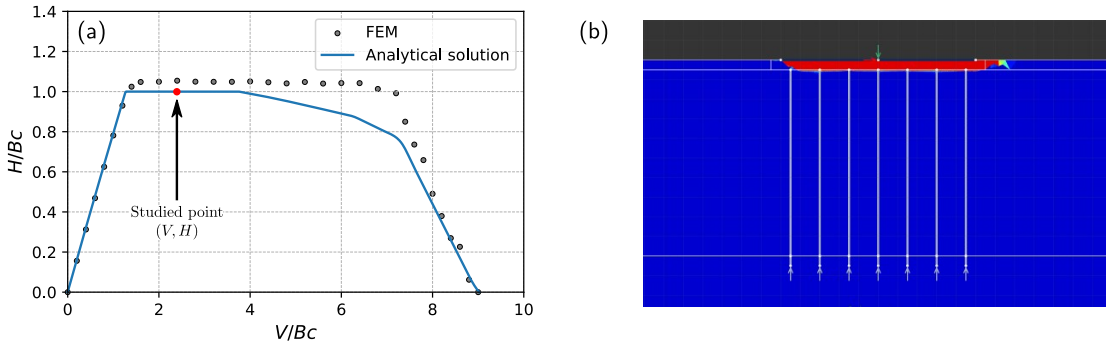

Fig. 9.5. Comparison of failure mechanisms: (a) load combination B, (b) failure mechanism obtained by analytical solution, and (c) obtained by FEM

The failure mechanism obtained through the kinematic exterior approach in this study, as depicted in Figure 9.6 (b), exhibits a resemblance to the one obtained through numerical modelling, as shown in Figure 9.6 (c).

The analytical solution has a limit horizontal force slightly smaller than the value obtained through FEM calculations. This discrepancy can be attributed to the variations in modelling between the two approaches. Notably, the analytical approach does not consider the

presence of the LTP, while in the FEM approach, the LTP contributes to an increase in the resistance for the reinforced foundation.

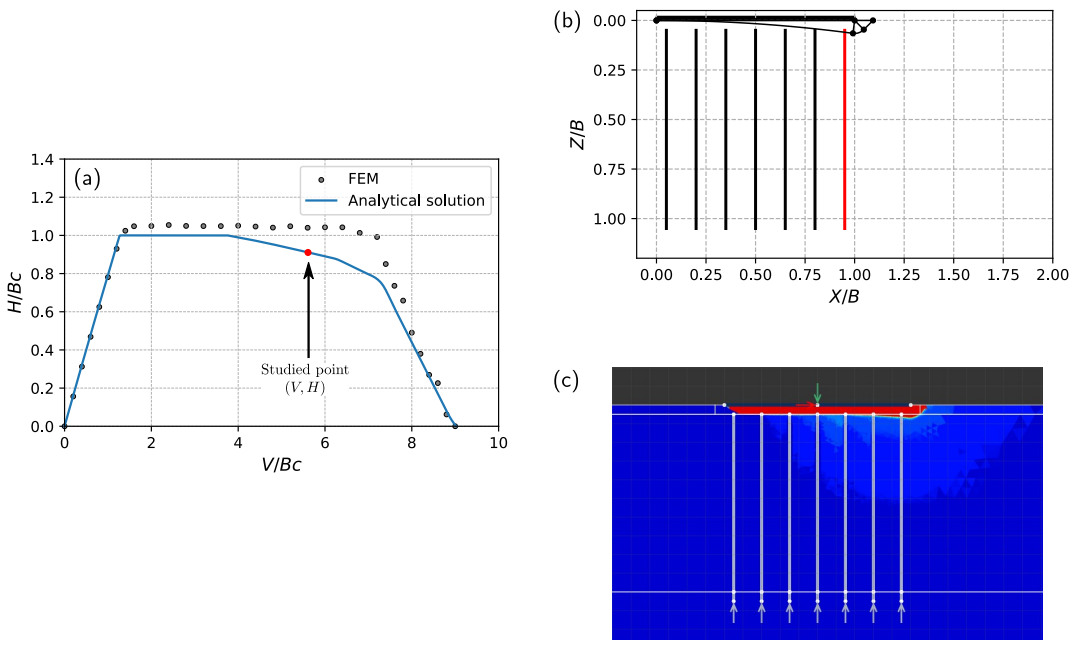

Fig. 9.6. Comparison of failure mechanisms: (a) load combination C, (b) failure mechanism obtained by analytical solution, and (c) obtained by FEM

A mechanism comparison is also conducted for the studied load combination D, situated at the interaction curve with a vertical force, of approximately 6.5 Bc. This comparison is depicted in Figure 9.7. It is evident that the failure mechanism for load combination D, as obtained through the analytical kinematic exterior approach, bears similarity to that acquired through FEM.

In both approaches, a failure mechanism that intersects with two rows of inclusions is evident. A larger vertical load results in a deeper failure mechanism, involving the participation of more rigid inclusions. It is noteworthy that the presence of rigid inclusions influences the failure mechanisms within the soil. However, in the analytical approach, which relies on certain assumptions, the contributions of the soil and the inclusions are simply superimposed. The interaction between the failure mechanism of the soil and the failure mechanism of the inclusions is not taken into consideration.

In the FEM modelling, the LTP is taken into account, which is inherently more resistant than the surrounding soft soil and thus can potentially provide some additional resistance. However, in the analytical approach, the contribution of LTP is not considered in the calculation of soil resistance. For the mechanism illustrated in 9.7 (b) and (c), it becomes apparent that a substantial portion of the soil volume involved corresponds to the LTP soil. This observation may account for the larger limit for horizontal force observed in FEM calculations.

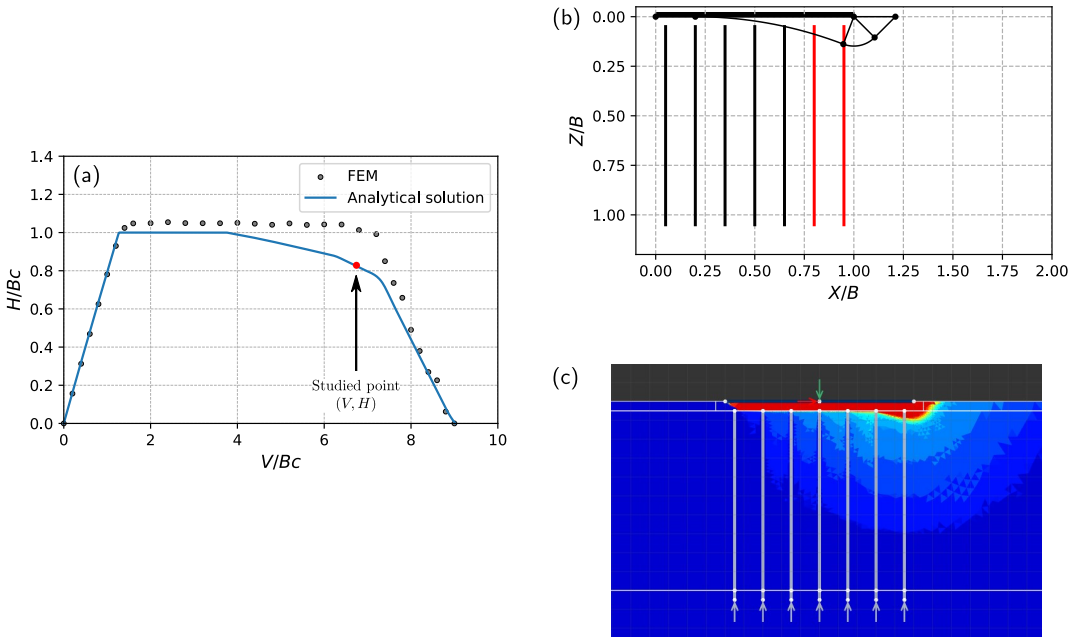

Fig. 9.7. Comparison of failure mechanisms: (a) load combination D, (b) failure mechanism obtained by analytical solution, and (c) obtained by FEM

The load combination with a larger vertical force V (load combination E) results in a deeper mechanism, and the volume of soil excited by the failure mechanism is significantly greater. In this case, only a minor difference is observed between the horizontal force limit obtained from the analytical solution and the FEM calculation.

Upon visualising the failure mechanism obtained through the kinematic exterior approach, as shown in Figure 9.8 (b), it is evident that four rows of rigid inclusions intersect with the failure mechanism. This observation is further confirmed by the failure mechanism presented in Figure 9.8 (c). The similarity between these two different approaches is apparent.

When comparing the failure mechanism of the analytical solution, which is a multi-block mechanism, with the field velocity observed in the numerical study, it is evident that the presence of the rigid inclusions does slightly influence the velocity field in the soil. Nevertheless, the overall global failure mechanisms obtained in both solutions remain similar.

Load combination F is positioned on the interaction curve with a vertical force V that approaches the bearing capacity V_{max} under vertical load. Remarkably, the extreme force couples (V, H) is nearly identical between the analytical solution and the FEM calculation.

Figure 9.9 (b) illustrates a significantly deeper failure mechanism when compared to Figure 9.8 (b). In this case, five rows of rigid inclusions, rather than four, contribute to the

stability of the reinforced foundation. The similarities between the failure mechanisms presented in Figures 9.9 (b) and 9.9 (c) serve as validation of the assumption regarding the failure mechanism.

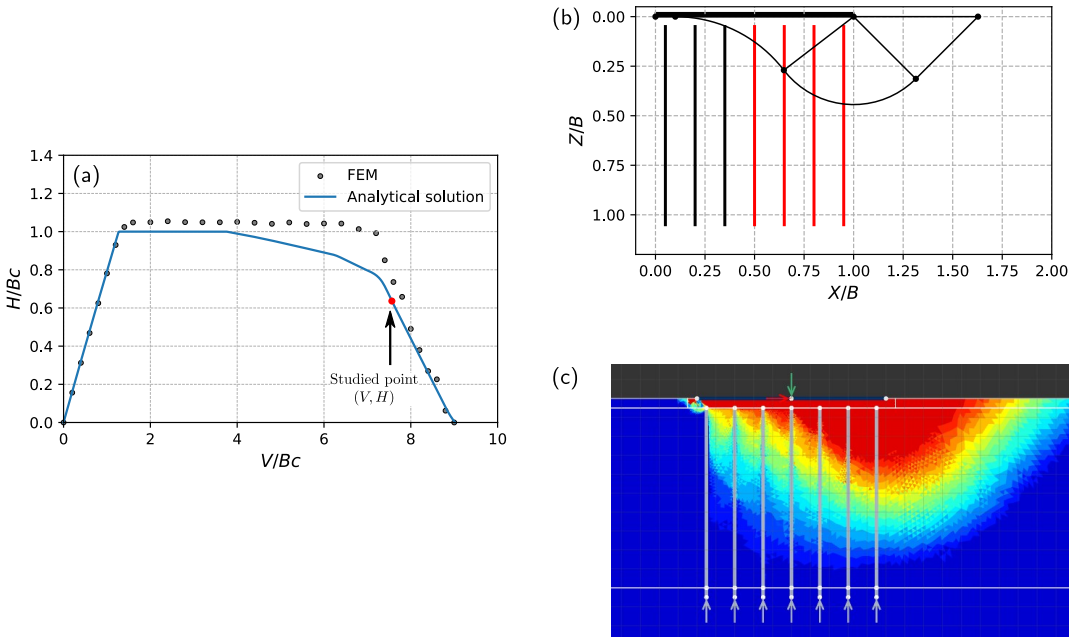

Fig. 9.8. Comparison of failure mechanisms: (a) load combination E, (b) failure mechanism obtained by analytical solution, and (c) obtained by FEM

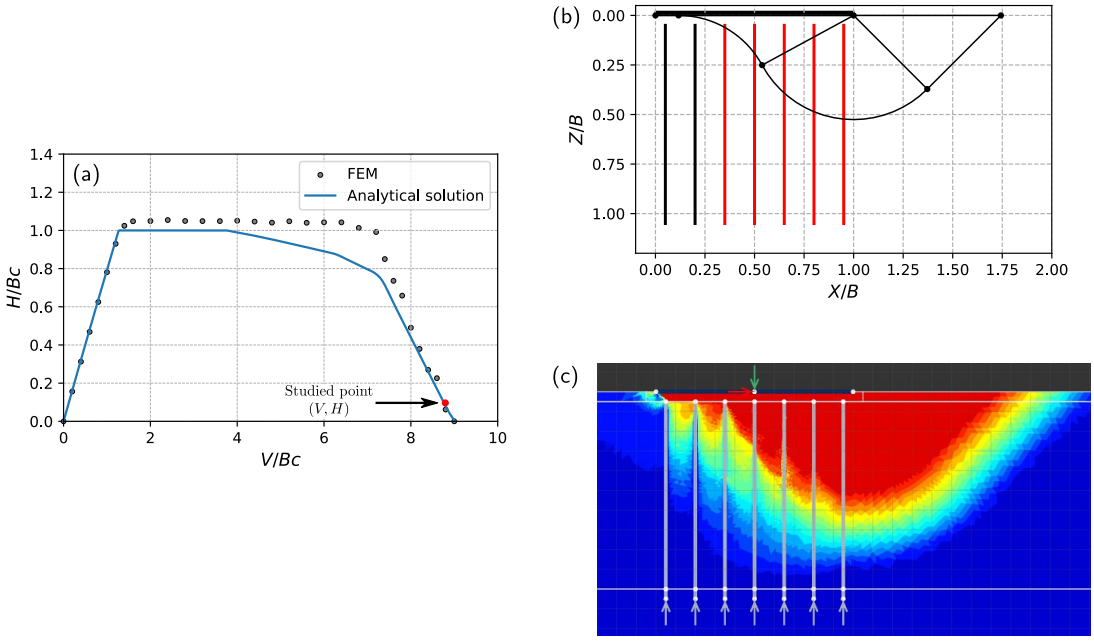

Fig. 9.9. Comparison of failure mechanisms: (a) load combination F, (b) failure mechanism obtained by analytical solution, and (c) obtained by FEM

The velocity field observed in the FEM calculation shows that the soil between the inclusions is also excited. Nevertheless, the overall global failure, represented by the red zone, bears similarity to the multi-block failure employed in the analytical solution. It should be noted that in the last two mechanisms, as depicted in Figures 9.8 and 9.9, the volume activated by the failure load is significantly larger than the volume of the LTP. In such situations, the impact of neglecting the resistance of LTP in the contribution of the soil is relatively minimal.

In summary, the comparative study of failure mechanisms with various load combinations reveals a strong agreement. Several differences in the limit loads can be attributed to the nuances in the failure mechanisms associated with the LTP and the soil volumes between inclusion rows. However, it is important to note that these results are sufficiently satisfactory for engineering applications.

9.4 Interaction diagrams

9.4.1 Studied configurations

Following a sequence of qualitative validations of the failure mechanisms, this section provides quantitative validation. It involves a comparison between the interaction diagrams obtained through the analytical approach within the framework of the kinematic exterior approach proposed in this study and those obtained through a FEM analysis.

In this validation study, a range of foundation configurations is chosen, involving variations in the dimension of the foundation B, the diameter of inclusions d, the non-drained strength of the soft soil c, and the axis-to-axis spacing of inclusions s. The loading conditions are also modified incorporating soil inertia and load eccentricity. The configurations tested are detailed in Table 9.1.

Tab. 9.1. Configurations for interaction curve validations

No.	B (m)	s (m)	d (m)	N_{RI}	Cohesion c (kPa)	Load condition
A	10	1.5	0.4	7	25	(V, H)
	10	1.5	0.4	7	25	(V, H) with $a_x = 0.1g$
	10	1.5	0.4	7	25	(V, H) with $e = 0.2B$
B	10	1.5	0.2	7	50	(V, H)
C	3	2	0.4	2	25	(V, H)

9.4.2 Comparison of interaction diagrams derived from two approaches

The first quantitative validation focuses on Case III, which represents failure within the reinforced soil. This sub-system is detailed in Figure 8.26 with detail. In this sub-system, the calculation of soil resisting contribution simplifies the LTP layer, while the LTP is considered at the heads of rigid inclusions when calculating the limit axial force T_{nl}.

To validate the calculation, two configurations utilised in FEM numerical modelling are proposed. The first configuration involves a complete model with the LTP between the foundation and the heads of rigid inclusions, as shown in Figure 8.26 (a). In this configuration, the resisting contribution is considered. The second configuration is a model without the LTP, as depicted in Figure 8.26 (b), where the soft soil is present between the rigid inclusions and the strip foundation. Theoretically, the exact solution K^{exact} (not the upper-bound solution) should fall between the solutions obtained with these two configurations, as described in Equation 9.1.

(a) (b)

Fig. 9.10. Configurations of FEM modelling: (a) with LTP modelling, (b) without LTP

$$K^{exact}_{\text{conf. (b)}} \subset K^{exact}_{\text{current work}} \subset K^{exact}_{\text{conf. (a)}} \tag{9.1}$$

The limit loads in the V-H plane for these two configurations are depicted in Figure 9.11. Lower-bound and upper-bound solutions are provided for configuration (b). Notably, the analytical solution falls between the lower-bound solution for configuration (a) and the upper-bound solution for configuration (b). This comparative diagram validates the assumption that the analytical solution should be situated between the solutions associated with these two configurations, as indicated in Equation 9.1. It is worth noting that the difference between these calculations is not significant, indicating that neglecting the LTP layer in the calculation of resisting power for the soil is acceptable.

The analytical solution based on the kinematic exterior approach can account for soil inertia by introducing a horizontal body force f_x into the calculation. The comparison is depicted in Figure 9.12. A strong agreement is evident between these two calculations.

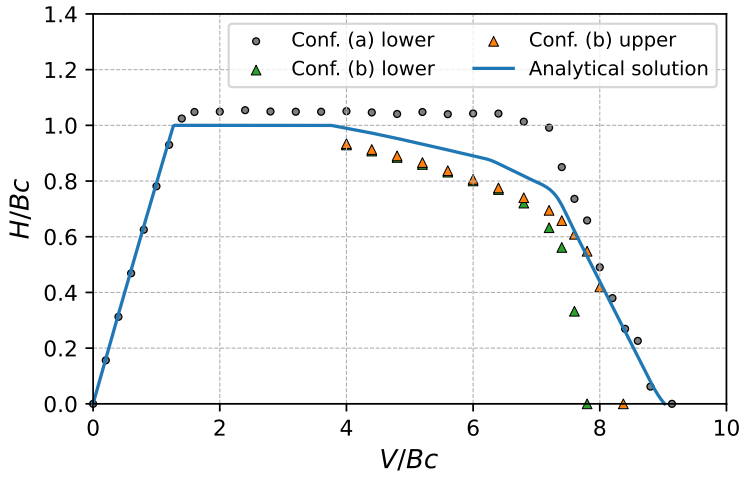

Fig. 9.11. Comparison of interaction curves in V-H plane obtained by analytical kinematic exterior approach and lower-bound and upper-bound FEM modelling

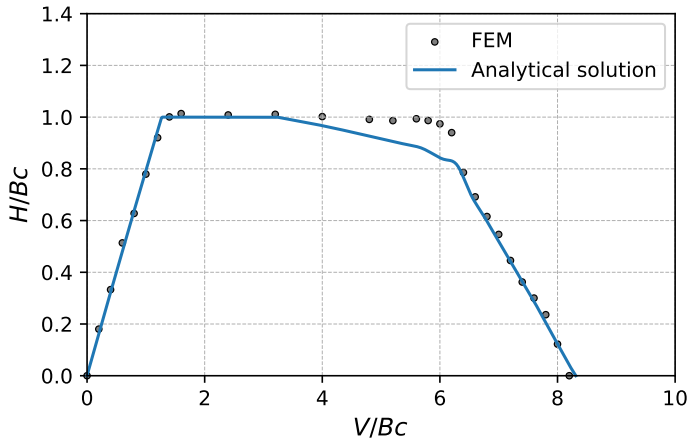

Fig. 9.12. Comparison of interaction curves in V-H plane obtained by analytical kinematic exterior approach and lower-bound FEM modelling considering soil inertia in Configuration A

With an eccentricity of $e = 0.2B$, it is evident that the analytical solution adequately captures the general trend of the interaction curve. The analytical solution also provides a good estimation of $V_{max,e=0.2}$. Although there are occasionally differences between these two solutions, these differences are within an acceptable margin smaller than 15 %.

The interaction curve of configuration B is also computed and compared with the limit force couples (V, H) obtained by FEM calculation. The cohesion of the soft soil is set as 50 kPa, and the diameter of rigid inclusions is reduced to 0.2 m. This comparative diagram is presented in Figure 9.14.

A strong agreement is evident between the two calculations. The overall trend in the results from the FEM calculation reveals three different failure mechanisms: failure within

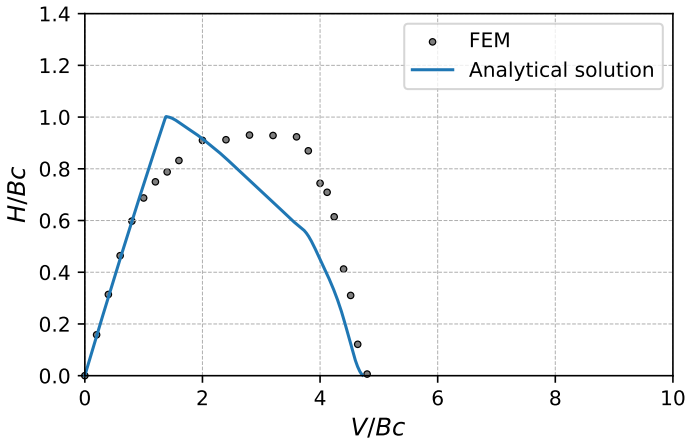

Fig. 9.13. Comparison of interaction curves in V-H plane obtained by analytical kinematic exterior approach and lower-bound FEM modelling considering load eccentricity in Configuration A

the LTP layer, cohesive sliding between the LTP and the soft soil (noted by $H/Bc = 1$), and a failure mechanism within the reinforced soft soil.

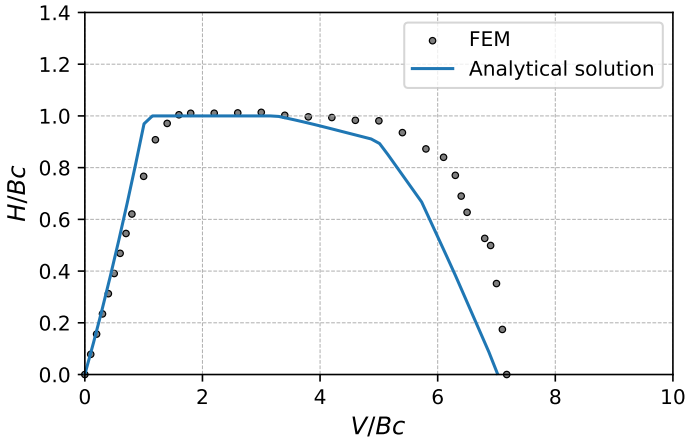

Fig. 9.14. Comparison of interaction curves in V-H plane obtained by analytical kinematic exterior approach and lower-bound FEM modelling (Configuration B: a greater soil cohesion c = 50kPa and smaller inclusion diameter of 0.2 m)

Configuration C involves a 3 m wide strip foundation with two rows of rigid inclusions. The results from both calculation approaches are compared in Figure 9.15. The FEM calculation aligns well with the analytical solution. Although the FEM calculation occasionally gives slightly higher results, the order of magnitude of the global interaction curve is well captured.

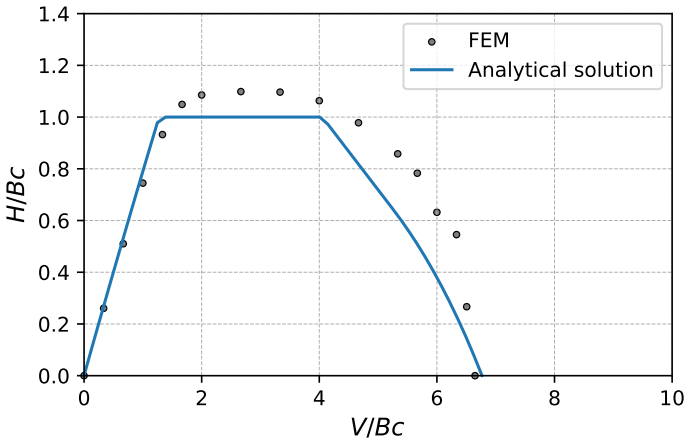

Fig. 9.15. Comparison of interaction curves in V-H plane obtained by analytical kinematic exterior approach and lower-bound FEM modelling (Configuration C: a smaller foundation of 3 m)

9.5 Ultimate vertical bearing capacity

9.5.1 Studied configurations

The previous two sections primarily concentrated on validating the failure mechanisms and interaction diagrams. In this section, the focus shifts to comparing the ultimate bearing capacity under vertical load for various configurations obtained through the analytical approach proposed in this work and those obtained through FEM. The studied configurations are detailed in Table 9.2. For each configuration, five different diameters ranging from 0.2 m to 0.6 m are tested.

Tab. 9.2. Studied configurations for ultimate bearing capacity validation

B (m)	s (m)	N_{RI}	Coverage ratio ratio range
3	1.0	3	[3.1 %, 28.3 %]
	1.5	2	[1.4 %, 12.6 %]
	2.0	2	[1.0 %, 7.1 %]
	2.5	2	[0.8 %, 7.5 %]
5	1.0	5	[3.1 %, 28.3 %]
	1.5	3	[1.3 %, 11.3 %]
	1.5	4	[1.7 %, 15.1 %]
	2.0	2	[0.6 %, 5.7 %]
	2.0	3	[0.9 %, 8.5 %]
	3.0	2	[0.4 %, 3.8 %]
10	1.5	6	[1.3 %, 11.3 %]
	1.5	7	[1.5 %, 13.2 %]
	2.0	5	[0.8 %, 7.1 %]
	2.5	4	[0.5 %, 4.5 %]
	3.0	4	[0.4 %, 3.8 %]

9.5.2 Comparison of bearing capacity derived from two approaches

Figure 9.16 presents the ultimate bearing capacity values predicted by FEM and the analytical solution for different configurations listed in Table 9.2. The analytical approach can generally capture the ultimate bearing capacity of the rigid inclusion-reinforced foundation within a margin of ± 10%.

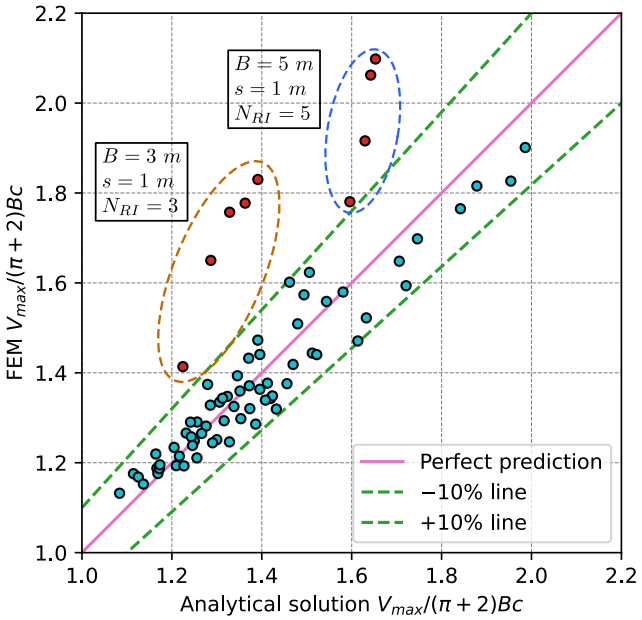

Fig. 9.16. Comparasion of the normalised ultimate bearing capacity predicted by FEM and the analytical approach

For a few configurations in which the FEM yields an over-estimation exceeding 10%, represented by red points enclosed by circles, a more in-depth examination is conducted to comprehend the source of this over-estimation.

The configuration represented by red points enclosed by the brown circle constitutes a 3 m wide strip foundation with three rows of inclusions implemented with a spacing of 1 m. The differences in the estimated bearing capacity values V_{max} range from 13.4 % to 24.4 % for the diameters of rigid inclusions of 0.2m, 0.3 m, 0.4 m, 0.5 m, and 0.6 m. The analytical solution consistently provides smaller values for V_{max} compared to the FEM calculations.

To understand the source of this difference, two failure mechanisms for the configuration with a diameter of 0.6 m are superimposed, as shown in Figure 9.17. It becomes apparent that the principal failure mechanism (red zone) obtained through FEM calculations follows

a similar pattern to the analytical multi-block failure mechanism represented by the green curves.

However, it is notable that a failure mechanism also arises between the inclusions, which cannot be simulated by the multi-block mechanism. It is evident that the soil between the inclusions experiences significant excitation, and the influence extends to a considerable depth. This mechanism could result from the interaction between the failure mechanism of the inclusions and the failure mechanism of the soil. The presence of rigid inclusions modifies the failure mechanism of the soft soil, potentially activating the soil between the rigid inclusions.

Furthermore, in the analytical solution, the contribution of the soil is calculated only with the soft soil, without accounting for the LTP. In this configuration, the failure depth is nearly twice the thickness of the LTP, indicating that disregarding the presence of the LTP is a strong assumption. This implies that the analytical approach is better suited for cases where the depth of the failure surface significantly exceeds the thickness of the LTP.

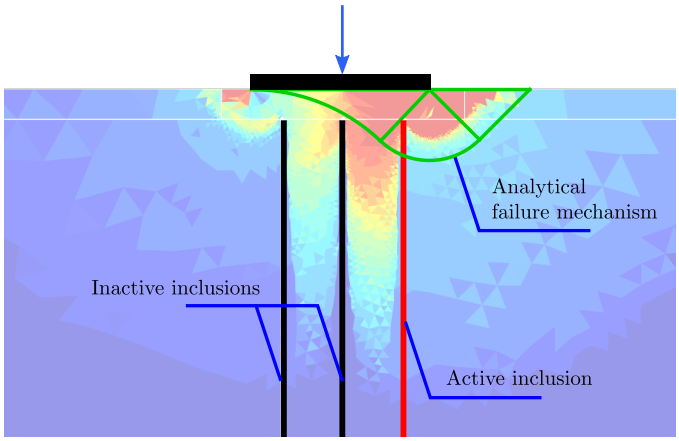

Fig. 9.17. Comparison of the failure mechanisms obtained by analytical approach and FEM for the foundation with a width of 3 m, inclusion spacing of 1 m and diameter of 0.6 m

The imperfect prediction values enclosed by the brown circle represent the configuration with a 5 m wide strip foundation reinforced by five rows of inclusions implemented with a spacing of 1 m. It is observed that the bearing capacity values V_{max} calculated by the analytical solution are consistently smaller than those obtained by FEM, with an underestimation ranging from 10.4 % to 21.2 % for the diameters of rigid inclusions of 0.3 m, 0.4 m, 0.5 m, and 0.6 m.

Figure 9.18 presents the comparison of the failure mechanisms obtained by the analytical solution and the numerical calculation for the configuration with a diameter of 0.4 m. As observed in the previous case, the principal failure mechanism can be captured by the analytical approach when comparing the red zone and the green curve. The soil between the two rows of inclusions at the right edge plays also a role.

From this comparison, it can be observed that the analytical failure depth is only twice the thickness of the LTP layer. The contribution of the LTP layer to the resisting power can be significantly pronounced. Neglecting the LTP layer naturally leads to a conservative solution. To improve the analytical approach, controlling the depth of the analytical failure mechanism and the number of intersected inclusions can be a crucial aspect to consider. In essence, this analytical approach is better suited for foundations with a small or moderate coverage area ratio α, where the failure mechanism is not confined to a shallow depth, and the soil volume involved in the failure mechanism is significantly larger than the volume of the LTP.

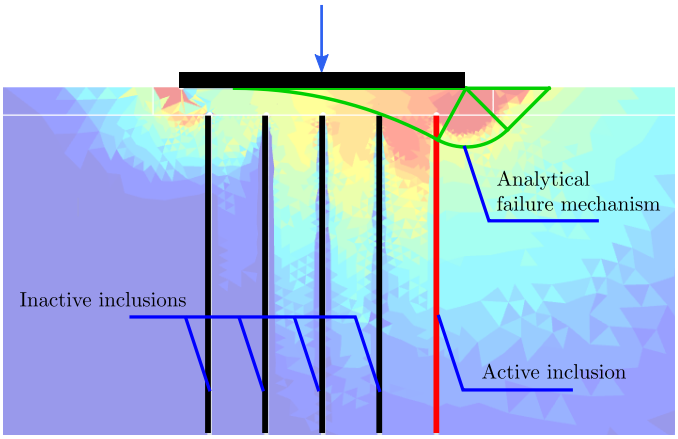

Fig. 9.18. Comparison of the failure mechanisms obtained by analytical approach and FEM for the foundation with a width of 5 m, inclusion spacing of 1 m and diameter of 0.4 m

9.6 Summary

This chapter is devoted to the validation of the analytical approach introduced in Chapter 8 for addressing the seismic bearing capacity problem in foundations reinforced by rigid inclusions. The validation encompasses three main validation studies:

- Failure mechanism validation;
- Interaction diagram comparison;
- Ultimate vertical bearing capacity comparison.

Firstly, a qualitative validation is performed by comparing the velocity field acquired through FEM calculations with the analytical solution. It is noteworthy that a high degree of similarity is observed between the failure mechanisms derived from the analytical solution and those obtained from the numerical analyses.

Following this, a quantitative validation is carried out by calculating and comparing the interaction curves for various configurations and different load conditions. This is

accomplished by employing the proposed analytical approach and comparing the results with those obtained from FEM. Encouragingly, a significant alignment is evident between the proposed approach and the numerical modelling, allowing validation for the proposed analytical approach.

Lastly, a comparative study is conducted to evaluate the ultimate bearing capacity of various reinforced foundation configurations using both numerical and analytical approaches. Considering the inherent uncertainties in soil parameters, this level of precision is deemed acceptable for engineering applications. Compared to the incertitude of the soil parameters, this precision can be acceptable for engineering utilisation. Notably, from this extensive numerical investigation, it becomes evident that the analytical approach tends to provide a conservative solution, primarily because it does not account for the presence of the LTP in the soil contribution.

10 Seismic bearing capacity: Impact factors

10.1 Bearing capacity verification criterion

Having established the validity of the analytical solution, this study proceeds also to examine the reduction factors that impact the bearing capacity of rigid inclusion-reinforced foundations. These reduction factors are associated with load eccentricity, load inclination, and soil inertia effects. Additionally, the study delves into indicating potential avenues for future development and enhancement of the proposed analytical approach.

The conventional verification framework involves comparing the vertical force V with the limit value V_{max}, following the criterion:

$$V - V_{max} \leq 0 \tag{10.1}$$

To consider seismic effects, the limit value V_{max} is adjusted by applying certain reduction factors. The verification criterion is then expressed as Inequation 10.2.

$$V - V_{max}\, i_e\, i_\delta\, i_g \leq 0 \tag{10.2}$$

where i_e represents the load eccentricity reduction factor, i_δ is the load inclination reduction factor, and i_g accounts for the soil inertia reduction factor.

10.2 Studied configurations

These three reduction factors will be examined in the following sections using the same 10 m wide strip foundation with seven rows of inclusions, as depicted in Figure 10.1. Three diameters of inclusions, 0.2m, 0.4m, and 0.55 m, correspond to coverage area ratios α of 1.4 %, 5.6 %, and 10.6 %. To assess the impact of reinforcement, a non-reinforced configuration will also be analysed. It is important to note that the non-reinforced configuration also includes a frictional LTP layer.

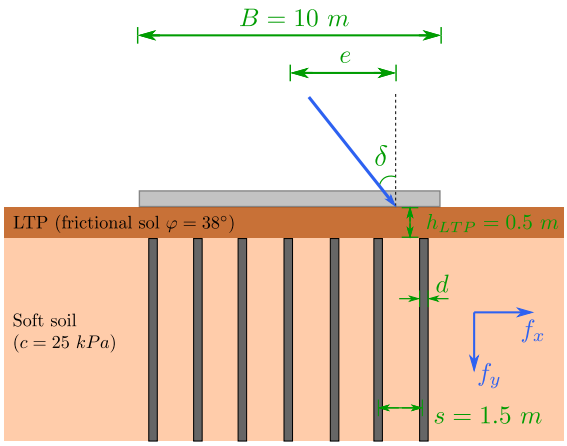

Fig. 10.1. Reinforced foundation configuration to study the factors influencing the bearing capacity of reinforced foundation

10.3 Load eccentricity effect

10.3.1 Interaction diagram under different load eccentricities

The effect of load eccentricity is first examined through the study of V-H interaction diagrams. Figure 10.2 presents these diagrams for various load eccentricities ($e = M/V$) associated with three different diameter configurations. The results reveal that an increase in load eccentricity leads to a decrease in both the ultimate bearing capacity and the maximum horizontal forces.

Figure 10.2 (a) illustrates the interaction curves for different load eccentricities e/B with a small coverage area ratio of 1.4 %. It is evident that the bearing capacity under non-eccentric vertical load, with a small coverage area ratio α, is approximately 7 Bc. However, when a load eccentricity of $e = 0.3B$ is introduced, the bearing capacity decreases significantly, reaching only one-third of the bearing capacity under a non-eccentric vertical load. Similar trends are also observed in Figures 10.2 (b) and 10.2 (c).

Figure 10.3 displays the bearing capacities for various configurations and different load eccentricities. The figure also includes the same interpretation for the configuration without rigid inclusions. A consistent trend is observed across all studied cases. As the load eccentricity increases, the bearing capacity decreases. It is evident that the presence of rigid inclusion reinforcement significantly enhances the bearing capacity of the foundation under eccentric load. For the foundation with reinforcement of α = 10.6 %, its bearing capacity under load with eccentricity of 0.2 B is as same as the bearing capacity for the foundation without reinforcement.

Among the various reinforced configurations examined, it is noteworthy that the bearing capacity is consistently higher for configurations with a larger coverage area ratio α than

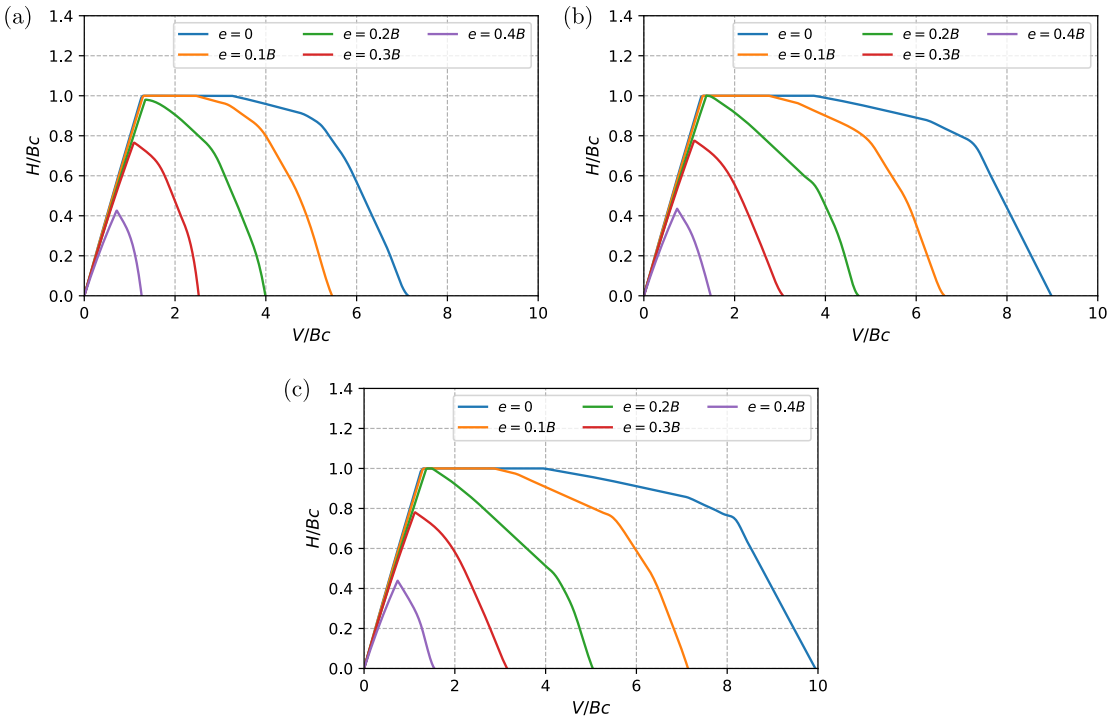

Fig. 10.2. Normalised V-H interaction curves for different load eccentricities: (a) configuration with α=1.4%, (b) configuration with α=5.6%, and (c) configuration with α=10.6%

for those with a smaller coverage area ratio α when the load eccentricity is less than $0.3B$. However, under vertical loads with significant eccentricity (exceeding $0.4B$), the coverage area ratio ceases to exert a substantial influence, and the impact of reinforcement becomes less pronounced.

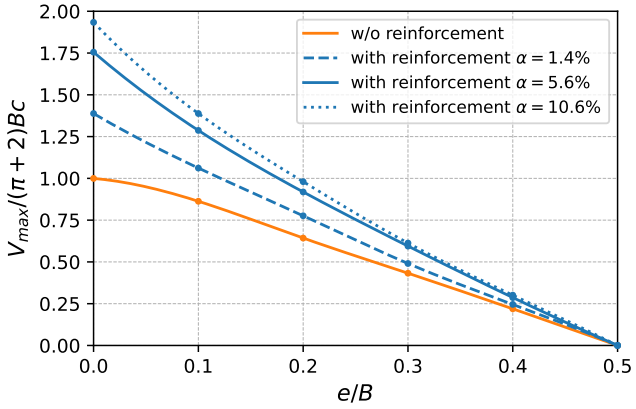

Fig. 10.3. Bearing capacity for reinforced foundations with different coverage area ratios to load eccentricities

10.3.2 Load eccentricity reduction factor

For all studied configurations, the bearing capacities under different eccentric loads are normalised by the bearing capacity under non-eccentric conditions, denoted as $V_{max,e=0}$. This ratio, represented as i_e, serves as a reduction factor affecting the foundation bearing capacity due to load eccentricity, as defined in Equation 10.3. Furthermore, the results are depicted in Figure 10.4 and compared with the eccentricity reduction factor $i_e = 1 - 2e/B$ proposed by Meyerhof (1953).

$$i_e = \frac{V_{max,e}}{V_{max,e=0}} \tag{10.3}$$

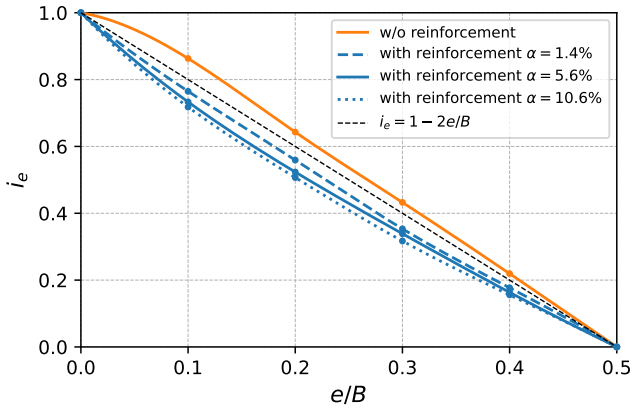

Fig. 10.4. Eccentricity reduction factor i_e for reinforced foundations with different coverage area ratios to load eccentricities

The proposed $i_e = 1-2e/B$ for the non-reinforced foundation is notably more conservative than the value obtained through upper-bound limit analyses. However, the impact of load eccentricity is more significant for foundations reinforced by rigid inclusions than for non-reinforced ones. Applying the same load eccentricity reduction factor i_e for non-reinforced foundations to the case of reinforced foundations may conduct non-conservative results. For example, at an eccentricity of $e/B = 0.2$, the strip foundation can still retain 64 % of its ultimate bearing capacity, whereas the rigid inclusion-reinforced foundation with a coverage area ratio of 5.6 % can only support 53 % of its ultimate bearing capacity.

The comparison among three reinforced configurations reveals that the configuration with a high coverage area ratio α is more susceptible to the load eccentricity effect compared to the configuration with a low coverage area ratio α. However, the variation in the i_e values for different coverage area ratios α varying from 1.4 % to 10.6 % is not significant. The three blue curves (solid, dotted, and dashed) representing reinforced foundations closely overlap.

10.4 Load inclination effect

10.4.1 Ultimate bearing capacity under different load inclinations

The bearing capacity of a non-reinforced strip foundation experiences a decay when subjected to combined inclined loading effects. However, the impact of load inclination on rigid inclusion-reinforced foundations remains unclear. As a result, this section is dedicated to studying the load inclination effect is studied in this section.

The interaction curves in the V-H plane, as illustrated in Figure 10.5, offer a direct means of assessing the impact of load inclination. It can be found that for load inclinations δ less than 16°, the interaction curves for reinforced foundations with varying coverage area ratios exhibit differences. However, for inclinations δ exceeding 16°, the interaction curves for reinforced foundations with different coverage area ratios become identical. This implies that for loads with significant inclinations, increasing the coverage area ratio does not lead to an increase in the ultimate bearing capacity. When the inclinations δ exceed 38°, equivalent to the friction angle of the LTP, the reinforced foundations lose the bearing capacity.

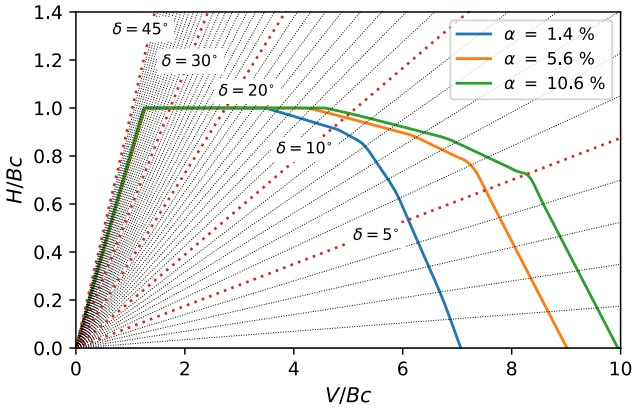

Fig. 10.5. Normalised interaction curves in V-H plane for reinforced foundation: (a) configuration with α=1.4%, (b) configuration with α=5.6%, and (c) configuration with α=10.6%

Figure 10.6 displays an evaluation of the bearing capacity under inclined loading for various studied configurations. The results are presented as a function of the load inclination δ normalised by the friction angle φ of the LTP. Additionally, the bearing capacity is normalised by the theoretical bearing capacity for non-reinforced foundations, referred to as $(\pi + 2)Bc$. This ratio evaluates the effect of soil improvement compared to the same configuration without reinforcement.

The effect of reinforcement on bearing capacity is particularly pronounced for load inclination angles smaller than $0.5\ \varphi$. However, for load inclinations exceeding 16° ($0.5\ \varphi$), the bearing capacity values for the studied configurations become nearly identical,

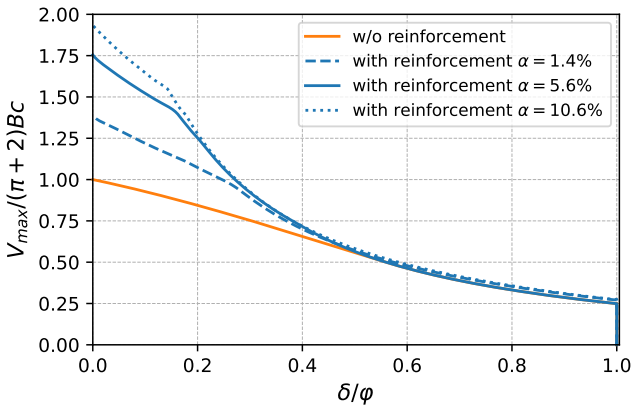

Fig. 10.6. Bearing capacity for reinforced foundations with different coverage area ratios to different load inclinations

indicating that the advantage of reinforcement by rigid inclusions diminishes for strongly inclined loads. It is also noteworthy that there is a reduction in bearing capacity when the inclination equals the friction angle φ. In the presence of a frictional LTP layer, an inclined load with an inclination equal to the friction angle φ directly leads to sliding failure. This implies that the sliding behaviour is inherently taken into account in the stability domain determined by the kinematic exterior approach.

10.4.2 Load inclination reduction factor

The load inclination reduction factor i_δ, as defined in Equation 10.4, has been calculated for the studied configurations. The reduction factor i_δ, as a function of the normalised inclination $\frac{\delta}{\varphi}$, is presented in Figure 10.7.

$$i_\delta = \frac{V_{max,\delta}}{V_{max,\delta=0}} \tag{10.4}$$

It can be observed that the load inclination reduction factor i_δ calculated for different load inclinations in the studied configurations is generally bounded by two i_δ expressions for cohesionless and cohesive soil proposed by Meyerhof (1953), as given in Equations 10.5 and 10.6 respectively.

$$i_\delta = (1 - \delta/\varphi)^2 \tag{10.5}$$

$$i_\delta = (1 - 2\delta/\pi)^2 \tag{10.6}$$

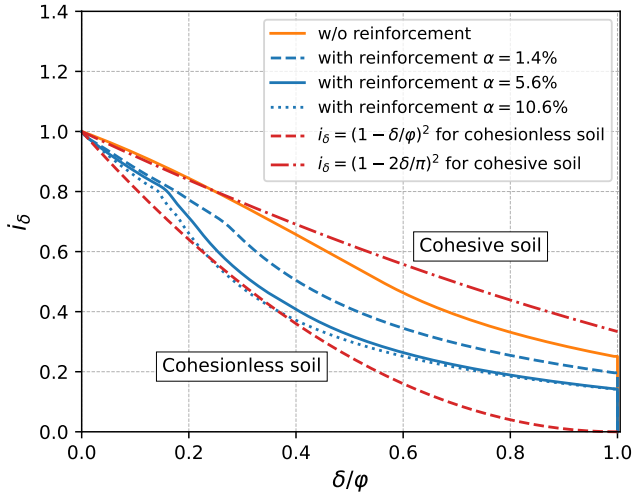

Fig. 10.7. Inclination reduction factor i_δ for reinforced foundations with different coverage area ratios to different load inclinations

From Figure 10.7, it can be observed that the load inclination reduction factor i_δ for the non-reinforced foundation is consistently higher than that for the reinforced configurations, which means that the reinforced foundations are more sensitive with the load inclination. It is interesting to note that the configuration with a coverage area ratio α of 1.4 % has a higher reduction factor i_δ value compared to the configuration with a coverage area ratio α of 10.4 %. The evaluation of the reduction factor i_δ for the configuration with a coverage area ratio of 5.6 % falls in between the other two configurations. This observation leads to the conclusion that foundations with a higher coverage area ratio α are more influenced by load inclination.

When comparing the curves representing the reinforced foundations with the conventional expressions proposed by Meyerhof (1953), it is interesting to observe that the inclination reduction factor i_δ becomes progressively closer to the expression for the cohesionless soil as the reinforcement coverage area ratio α increases.

10.5 Soil inertia effect

10.5.1 Interaction diagram under different soil inertias

The adverse impacts of soil inertia forces can at times be significant, particularly for foundations designed with a low safety factor under a static centred vertical load or those subjected to a significantly eccentric load. This observation is supported by insights gained from the 1985 Mexico earthquake (Auvinet *et al.*, 1996). Consequently, the current study is also focused on analysing the effect of soil inertia on the ultimate bearing capacity.

The configurations in this section are the same as those described in Section 10.5. The V-H interaction curves for several acceleration values in the soil ranging from 0 to $0.4g$ are displayed in Figure 10.8 for the three investigated configurations with inclusion diameters of 0.2 m, 0.4 m, and 0.55 m.

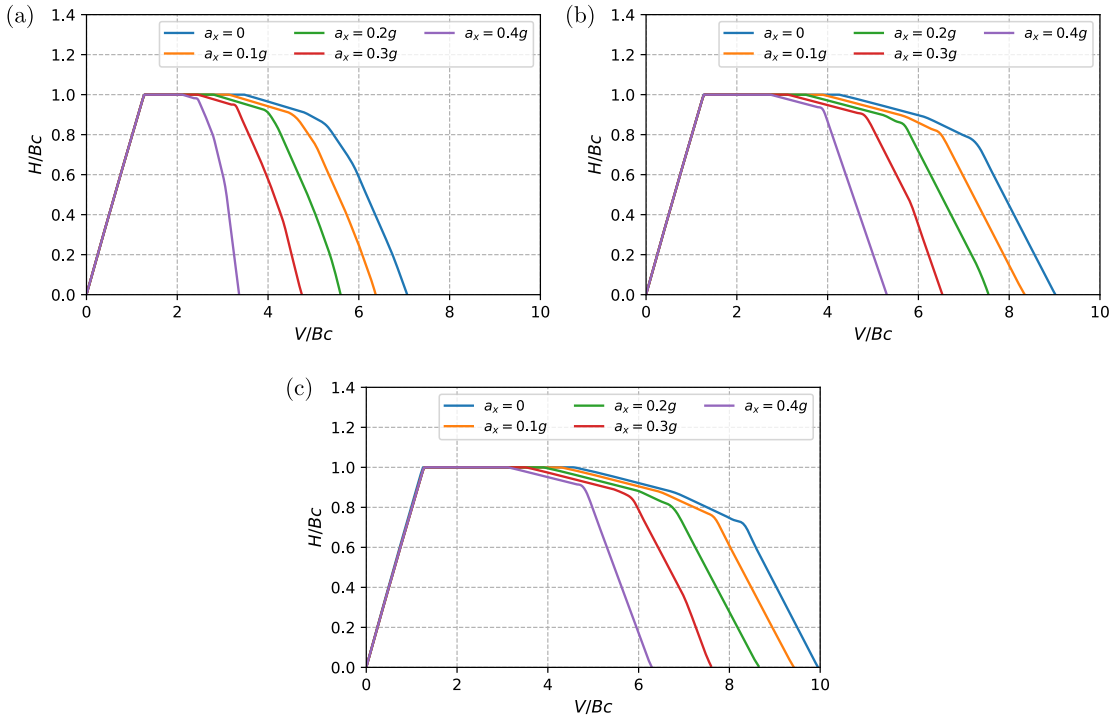

Fig. 10.8. Normalised V-H interaction curves for different soil inertias: (a) configuration with α=1.4 %, (b) configuration with α=5.6 %, and (c) configuration with α=10.6 %

It is observed that the shape of the V-H interaction curves is not affected by soil inertia effects, and only the amplitude of their right-hand side, which is controlled by the failure in reinforced soil, is influenced by the soil inertia.

The bearing capacity values for the investigated configurations to different soil inertias, described by a dimensionless soil inertia force $\bar{F}$, are depicted in Figure 10.9. This dimensionless soil inertia force $\bar{F}$ is defined in Equation 10.7.

$$\bar{F} = \rho a_x B / c \tag{10.7}$$

Comparing the non-reinforced foundation (orange curve) to the reinforced foundations (blue curves), it is evident that the rigid inclusion improvement enhances the foundation's ability to withstand the soil inertia. For instance, at a dimensionless soil inertia force of $\bar{F} = 2$ (equivalent to $a_x = 0.25$ g, $\rho = 2$ t/m^3, $B = 10$ m, and $c = 25$ kPa), the non-improved foundation experiences a 50 % reduction in its ultimate bearing capacity

due to soil inertia effect. In contrast, the reinforced configuration with the same soil inertia still retains approximately 80 % of its ultimate bearing capacity.

The normalised critical soil inertial force $\bar{F}_{cr}$ is defined as the maximum soil inertia that the foundation can withstand before losing its bearing capacity. When the normalised critical soil inertial force $\bar{F}_{cr}$ exceeds 2.3, the non-reinforced foundation becomes unable to maintain equilibrium with any external forces acting on itself. However, with the reinforcement by rigid inclusions, the normalised critical soil inertia force $\bar{F}_{cr}$ can reach nearly 4, indicating a significant enhancement in the bearing capacity of the foundation to withstand the soil inertia.

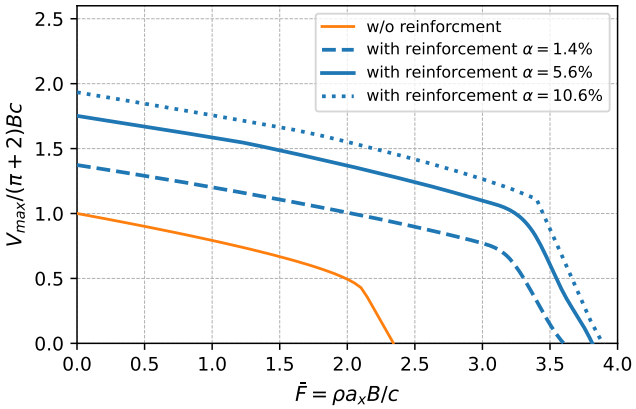

Fig. 10.9. Bearing capacity for reinforced foundations with different coverage area ratios to different soil inertias

10.5.2 Soil inertia reduction factor

Figure 10.10 examines the decrease in the ultimate bearing capacity caused by the soil inertia. This reduction can be evaluated by calculating the ratio of the bearing capacity affected by the soil inertia to the bearing capacity without the soil inertia, as defined in Equation 10.8. This ratio is represented as i_g.

$$i_g = \frac{V_{max,a_x}}{V_{max,a_x=0}} \tag{10.8}$$

As depicted in Figure 10.10, this factor diminishes as the soil inertia increases across all the studied configurations. Notably, the soil inertia reduction factor i_g for the reinforced foundations (blue curves) surpasses that of the non-reinforced foundation (orange curve). This implies that the bearing capacity for the reinforced foundations declines at a slower rate as the soil inertia intensifies. This observation underscores the reinforcement ability to enhance the resilience of the foundations under seismic excitation.

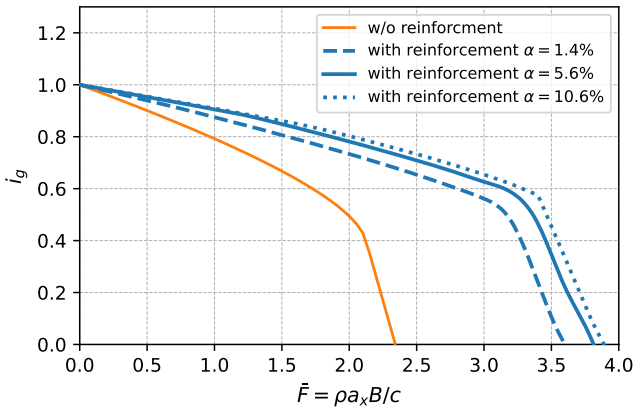

Fig. 10.10. Soil inertia reduction factor i_g for reinforced foundations with different coverage area ratios to different soil inertia

10.6 Effect of the embedment of rigid inclusions in the LTP

The embedment of rigid inclusions can indeed be a significant factor affecting the ultimate bearing capacity. In the recommendations proposed by AFPS and CFMS (2012), it is advised to embed the heads of the rigid inclusions within the LTP to ensure an effective transfer of horizontal forces under seismic loads. However, this assertion is seldom proven by existing literature studies. Therefore, the embedment of rigid inclusions in the LTP is also an important factor influencing the bearing capacity of the reinforced foundations.

This section delves into the investigation of the impact of embedment of rigid inclusions within the LTP. Two configurations, one without embedment and the other with embedment, are depicted in Figure 10.11. For the LTP, a limit pressure denoted as $p_{l,LTP}^*$, set at 1 MPa is employed. The diameter of the rigid inclusions is 0.5 m. Three levels of embedment are tested, including 0.1 m, 0.2 m, and 0.5 m. The final value of embedment corresponds to one times the diameter. All other parameters remain consistent with those defined in Section 8.4.3.

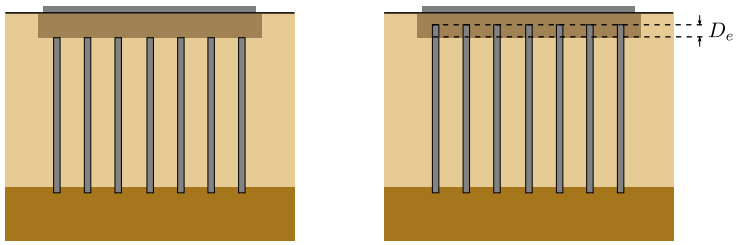

Fig. 10.11. Configuration without and with embedment of rigid inclusions in LTP

The interaction diagrams are displayed in Figure 10.12 (a). The stability domain enclosed by the interaction curve for the configuration with an embedment of one times the diameter (indicated by the blue curve) is notably larger than that for the configuration without embedment (illustrated by the black dashed curve). This observation confirms a notable enhancement effect in bearing capacity associated with the embedment of rigid inclusions in the LTP.

However, for a smaller embedment of 0.1 m (green curve), the improvement in bearing capacity is not significant enough when compared to the configuration without embedment. This observation affirms that while embedment can indeed increase the bearing capacity of inclusion-reinforced foundations, it necessitates a sufficient embedment depth D_e is necessary to ensure a more pronounced enhancement effect.

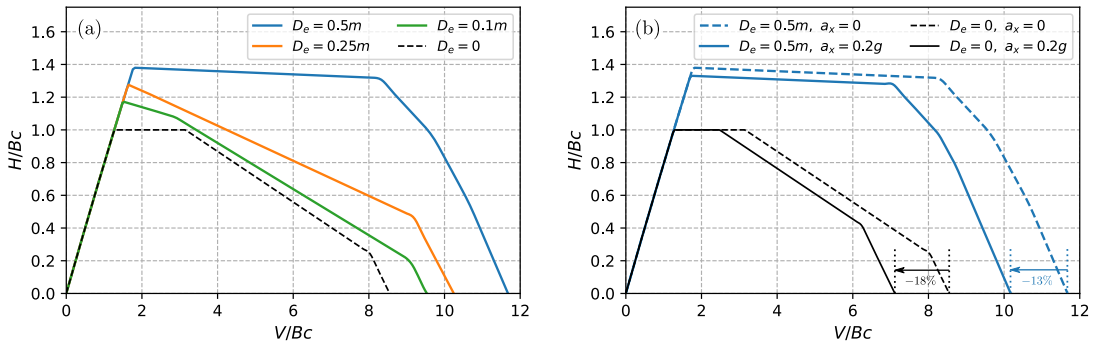

Fig. 10.12. Normalised V-H interaction curves considering different embedments of rigid inclusions in the LTP: (a) comparison between the configurations with different embedments of rigid inclusions in the LTP and (b) comparison between the configurations with and without embedment of rigid inclusions in the LTP subjected to a soil inertia of 0.2 g

Figure 10.12 (b) illustrates the interaction diagrams for the configuration without embedment of inclusions in the LTP and the configuration with embedment of inclusions in the LTP when subjected to seismic loads. In this analysis, a soil inertia of 0.2 g is applied. It is apparent that when subjected to the soil inertia from seismic excitation, the ultimate bearing capacity for the configuration with embedment decreases by 13 % while the ultimate bearing capacity for the configuration without embedment decreases by 18 %. Despite these reductions, the stability domain enclosed by the interaction curves for the configuration with embedment, even under the influence of soil inertia, remains larger than that of the configuration without embedment in the absence of soil inertia. This underscores the importance of embedding rigid inclusions in the LTP and suggests it as a recommended practice, particularly in earthquake-prone regions.

10.7 Summary

A comprehensive parametric study is conducted to explore the impact of load eccentricity, load inclination, and soil inertia on the bearing capacity of foundations reinforced by rigid inclusions.

The results obtained through this approach reveal that load eccentricity, load inclination, and soil inertia can substantially diminish the bearing capacity of the foundation. Nevertheless, the utilisation of rigid inclusion reinforcement proves to enhance the bearing capacity of the foundation under various loading conditions.

Regarding the effect of load eccentricity, the presence of rigid inclusions enhances the foundation's capacity to withstand loads with significant eccentricity. This reinforcing effect becomes more evident with a higher coverage area ratio α and diminishes as load eccentricity increases.

Concerning the influence of load inclination, it is evident that the implementation of rigid inclusions can increase the bearing capacity when subjected to inclined loads. However, the improvement effect is less pronounced for foundations subjected to highly inclined loads. The foundation can effectively withstand a maximum load inclination equal to the friction angle φ of LTP. Beyond this threshold, a sliding mechanism comes into play.

Regarding the soil inertia effect induced by seismic motion, the parametric study affirms that rigid inclusions can effectively mitigate the harmful impact of soil inertia and improve the seismic resilience of foundations. With the reinforcement by rigid inclusions, foundations can still maintain a substantial portion of their bearing capacity, even when subjected to significant soil inertia. This effect increases with the coverage area ratio α. This finding highlights the potential benefits of employing rigid inclusion-reinforced foundations in earthquake-prone regions.

These influences are also assessed using the reduction factors i_e, i_δ, and i_g, which are commonly utilised to quantify the adverse effects of load characteristics on the bearing capacity of foundations. It is noteworthy that the reinforced configuration is more susceptible to load eccentricity in comparison to the same foundation on non-reinforced soil. Consequently, there is a more significant reduction in ultimate bearing capacity due to load eccentricity than the conventional reduction factor i_e for non-reinforced foundations. A similar trend is observed with load inclination, where the load inclination factor i_δ is higher in the case without reinforcement than in the case with reinforcement. In contrast, the soil inertia reduction factor i_g is greater in the case with reinforcement compared to the case without reinforcement.

Furthermore, an investigation into the effects of embedding rigid inclusions within the LTP is also conducted. It is observed that the embedment of rigid inclusions has a significant effect in expanding the stability domain for foundations reinforced with rigid inclusions.

Conclusion

This part deals with the bearing capacity of foundations on reinforced soil by rigid inclusions both under static and seismic loads.

Chapter 8 introduces an innovative analytical method for assessing the bearing capacity of foundations within the upper-bound kinematic theory framework. A novel multicriterion incorporating several possible failure modes that control the forces generated by the rigid inclusions is developed to take into account the contribution of these reinforcements to the resistance of the foundation. This chapter also provides validation for several hypotheses, such as the impact of different limit equilibrium models and the effect of loading inclination at the heads of inclusions.

The proposed approach is subsequently subjected to both qualitative and quantitative validation by comparison with FEM modelling in Chapter 9. The validation focuses on three key aspects: the failure mechanism, the interaction diagram and the ultimate bearing capacity, and highlights the pertinence and relevance of this analytical approach.

The effects of several elements influencing the bearing capacity, such as the load eccentricity, the load inclination, and the soil inertia, are examined in Chapter 10 using the proposed approach. For various coverage area ratios, the evolution of the corresponding equivalent eccentricity reduction factor i_e the inclination reduction factor i_δ and the soil inertia influence factor i_g is examined. The observed factors are also compared with those considered to determine the bearing capacity of shallow foundations on unreinforced soil.

The work presented in these chapters establishes the basis for exploring more complex configurations in future research studies. This could include investigations into non-homogeneous soil conditions and three-dimensional failure mechanisms.

Part IV

Non-linear SSI study

Introduction

Under strong seismic excitation, the foundation can undergo non-linear behaviour, including uplift, sliding, and loss of bearing capacity. This part of the dissertation is devoted to the comprehensive examination of dynamic non-linear SSI behaviour for the inclusion-reinforced foundations, using a macro-element approach.

Chapter 11 introduces the dynamic SSI macro-element of the inclusion-reinforced foundations with its validation work. This comprehensive chapter explores the structure of the macro-element, encompassing both the non-linear elastic model and the elastic-perfectly plastic model. Moreover, it presents the numerical resolution techniques employed to solve dynamic and non-linear problems and their implementation. Additionally, this chapter includes a detailed validation study to demonstrate the correct functioning of each component, the numerical resolution and their interaction in the macro-element model.

Moving forward, Chapter 12 explores the application of the macro-element under dynamic loading conditions. The chapter encompasses two parametric studies with the macro-element, involving numerical applications to real structures represented by a lumped mass model and a continuous Timoshenko beam model. These studies consider various dynamic SSI conditions. The macro-element approach is a time-saving numerical modelling method, allowing the generation of a rich database. The primary objective of these comprehensive parametric studies is to produce insightful charts that enhance the understanding of the dynamic SSI response for structures founded on rigid inclusion-reinforced foundations based on the generated database.

11 Macro-element for a rigid inclusion-reinforced foundation: Formulation, resolution, and validation

11.1 Displacement-based seismic design using SSI macro-element approach

In light of the empirical evidence, the emphasis in the evolution of seismic design principles has shifted towards the reduction of displacements or strains during earthquakes, rather than prioritising strength. Consequently, it has become evident that seismic vulnerability should be appropriately defined in terms of deformations rather than strength (Calvi *et al.*, 2008). This shift leads to a transition from force-based seismic design to displacement-based seismic design. Additionally, as illustrated by several studies (Anastasopoulos *et al.*, 2010; Gazetas *et al.*, 2014), it is essential to emphasise that an overly designed foundation does not necessarily guarantee a safer structure.

The macro-element approach, which involves replacing the entire foundation-soil system with a single element located at the base of the superstructure, provides a straightforward method of addressing potential non-linearities within the soil-foundation system in a simplified manner. This approach can be framed within the context of displacement-based seismic design. One of its advantages is its ability to estimate residual displacement within the soil-structure system. Additionally, the modelling strategy is advantageous for its capacity to incorporate non-linearities with only minimal computational costs.

11.2 Macro-element formulation

11.2.1 Foundations with different shapes and global variables

The macro-element developed in this study aims to replicate the behaviour of reinforced foundations of various shapes in both static and seismic scenarios. It is formulated using

generalised variables, including general forces and displacements, which are defined at the centre of the foundation.

Strip foundation

The behaviour of a strip foundation can be characterised by two vectors of three components: a displacement vector $\underline{U}$ and a force vector $\underline{F}$. Equation 11.1 defines these vectors, and they are both associated with the central point of the foundation.

The vector $\underline{U}$ comprises three components: horizontal displacement u_x, vertical displacement u_z, and rotation θ_y. Similarly, the vector $\underline{F}$ consists of three components: horizontal force H_x, vertical force V, and moment M_y, as depicted in Figure 11.1. To facilitate clarity, the schematic does not include the representation of the rigid inclusions.

$$\underline{U} = \begin{bmatrix} u_x \\ u_z \\ \theta_y \end{bmatrix} \qquad \underline{F} = \begin{bmatrix} H_x \\ V \\ M_y \end{bmatrix} \tag{11.1}$$

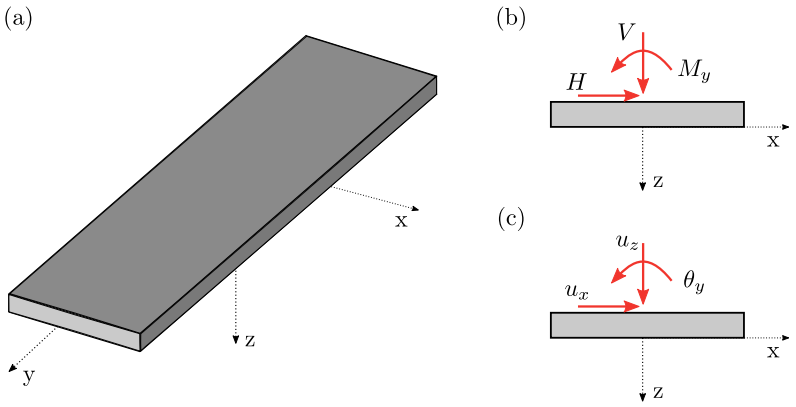

Fig. 11.1. Global variables: (a) strip foundation (b) forces and moment, and (c) displacements and rotation on the strip foundation reinforced by rigid inclusions (not shown)

Rectangular foundation

For a rectangular foundation, its behaviour can be described using two vectors of five components: a displacement vector $\underline{U}$ and a force vector $\underline{F}$, as defined in Equation 11.2.

The vector $\underline{U}$ consists of two horizontal displacements, u_x and u_y, one vertical displacement u_z, and two rotations, θ_x about the x-axis and θ_y about the y-axis. Respectively, the vector $\underline{F}$ includes two horizontal forces, H_x and H_y, one vertical force V, and two moments, M_x about the x-axis and M_y about the y-axis, as depicted in Figure 11.2. It should be noted that this study does not consider the torsion about the z-axis, similar

to the other developed macro-elements (Chatzigogos *et al.*, 2005; Grange *et al.*, 2009; Abboud, 2017).

$$\underline{U} = \begin{bmatrix} u_x \\ u_y \\ u_z \\ \theta_x \\ \theta_y \end{bmatrix} \qquad \underline{F} = \begin{bmatrix} H_x \\ H_y \\ V \\ M_x \\ M_y \end{bmatrix} \tag{11.2}$$

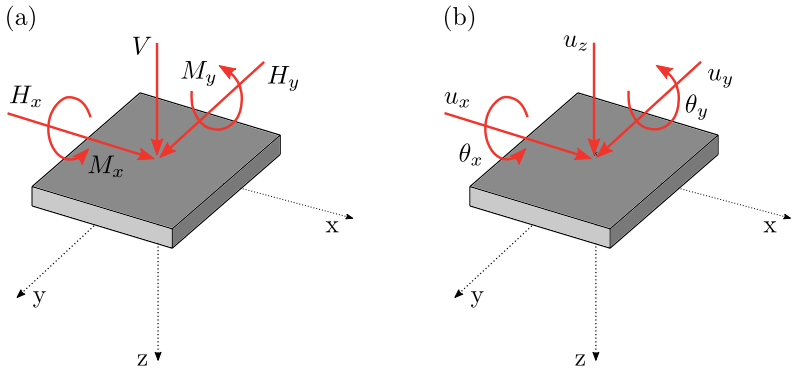

Fig. 11.2. Global variables: (a) forces and moments and (b) displacements and rotations on the rectangular foundation reinforced by rigid inclusions (not shown)

Circular foundation

Similarly to the rectangular foundation, the behaviour of the circular foundation can be characterised using a displacement vector $\underline{U}$ and a force vector $\underline{F}$, as defined in Equation 11.3.

$$\underline{U} = \begin{bmatrix} u_x \\ u_y \\ u_z \\ \theta_x \\ \theta_y \end{bmatrix} \qquad \underline{F} = \begin{bmatrix} H_x \\ H_y \\ V \\ M_x \\ M_y \end{bmatrix} \tag{11.3}$$

11.2.2 Elastic behaviour

Under low to moderate amplitude loads, a foundation reinforced by rigid inclusions demonstrates an elastic response. Recent investigations (Shen *et al.*, 2021, 2022b) and Chapter 5 have specifically focused on the dynamic impedances of shallow foundations on reinforced soils. An important finding from these studies is that the coupling terms within the dynamic impedance matrix can be considered negligible. In other words, the

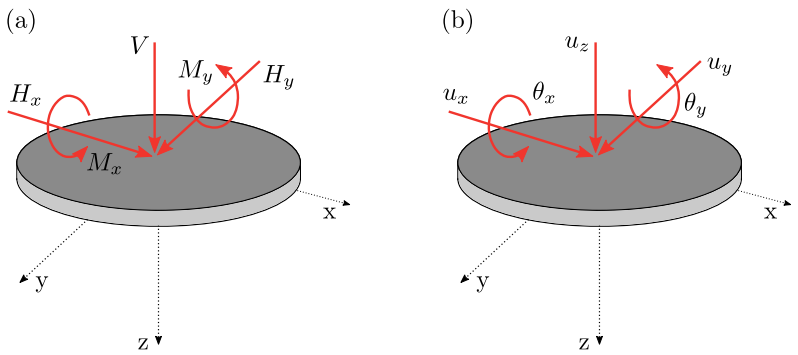

Fig. 11.3. Global variables: (a) forces and moments and (b) displacements and rotations on the circular foundation reinforced by rigid inclusions (not shown)

elastic response of these foundations can be accurately modelled using independent linear springs for each degree of freedom.

The elastic linear behaviour can be expressed through the following equation:

$$\underline{F} = \underline{\underline{K}}^e \underline{U}^e \tag{11.4}$$

In this equation, the force vector $\underline{F}$ has been previously defined, $\underline{\underline{K}}^e$ represents the elastic stiffness matrix, and $\underline{U}^e$ denotes the elastic displacement vector. For rectangular and circular foundations, the elastic stiffness matrix $\underline{\underline{K}}^e$ takes the following form:

$$\underline{\underline{K}}^e = \begin{bmatrix} K_x & & & & & \\ & K_y & & & & \\ & & K_z & & & \\ & & & K_{rx} & & \\ & & & & K_{ry} & \end{bmatrix} \tag{11.5}$$

For strip foundations, the elastic stiffness matrix $\underline{\underline{K}}^e$ can be simplified as follows:

$$\underline{\underline{K}}^e = \begin{bmatrix} K_x & & \\ & K_z & \\ & & K_{ry} \end{bmatrix} \tag{11.6}$$

Under seismic loading, various types of energy dissipation mechanisms occur as described in Section 1.2.3. In the elastic domain, it is essential to consider material and radiation damping, which can be expressed as follows:

$$\underline{F} = \underline{\underline{K}}^e \underline{U}^e + \underline{\underline{C}} \dot{\underline{U}}^e \tag{11.7}$$

The damping matrix $\underline{\underline{C}}$ can be written as follows for rectangular and circular foundations:

$$\underline{\underline{C}} = \begin{bmatrix} C_x & & & & & \\ & C_y & & & & \\ & & C_z & & & \\ & & & C_{rx} & & \\ & & & & C_{ry} & \end{bmatrix} \tag{11.8}$$

For strip foundations, the damping matrix $\underline{\underline{C}}$ can be simplified as follows:

$$\underline{\underline{C}} = \begin{bmatrix} C_x & & \\ & C_z & \\ & & C_{ry} \end{bmatrix} \tag{11.9}$$

In Chapter 5, it is evident that rigid inclusion ground improvement introduces an anisotropic behaviour under static and dynamic loading scenarios. For static loading scenarios, the determination of the stiffnesses can be achieved through static numerical modelling.

In dynamic loading scenarios, it is essential to determine both stiffness and damping terms. These terms exhibit significant frequency dependence. Calibration is performed at a frequency corresponding to the fundamental frequency of the SSI mode for each specific direction. Typically, these stiffness and damping terms are calibrated using dynamic impedance functions obtained from numerical modelling or directly from well-established analytical solutions available in the literature. Further details regarding the calibration process based on dynamic impedance functions are presented in Section 11.3.

11.2.3 Non-linear elastic behaviour

The uplift of a foundation constitutes a reversible mechanism that does not dissipate any energy. Nevertheless, this form of uplift results in an evident and rapid degradation of the rotational stiffness.

The conventional approach for studying the uplift behaviour in a rigid shallow foundation relies on assuming a trapezoidal distribution of soil reaction when no uplift occurs and a triangular distribution once the foundation uplifts, as depicted in Figure 11.4.

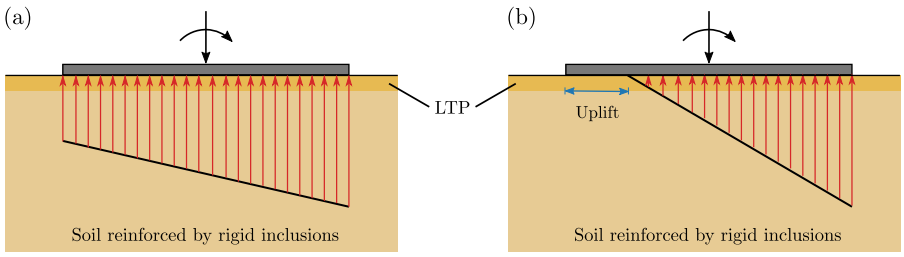

Fig. 11.4. Reinforced soil reaction under vertical force and moment: (a) trapezoidal distribution without uplift and (b) triangular distribution with uplift

For a rectangular foundation with a width of B or a circular foundation with a diameter of B, the ultimate moment M_u that causes the foundation to tip over is determined by Equation 11.10.

$$M_u = \frac{B}{2}V \tag{11.10}$$

where V represents the vertical force applied at the centre of the foundation.

In this convention, the initiation of uplift for the foundation occurs at a moment equal to $M_u/4$ for a circular foundation and $M_u/3$ for a rectangular foundation. For a rectangular foundation, a rotation of the foundation at the initiation of uplift δ_0 can be defined through Equation 11.11. This uplift is accompanied by a rapid degradation in the rotational stiffness of the foundation, whether it is circular or rectangular. The degradation curves for the rotational stiffness of both rectangular and circular foundations are depicted in Figure 11.5. The degradation of the rotational stiffness of a rectangular foundation can be described using Equation 11.12.

$$\theta_0 = \frac{M_u}{3K_0} \tag{11.11}$$

$$\frac{K}{K_0} = \frac{27}{4}\frac{M}{M_u}(1 - \frac{M}{M_u})^2 \quad \text{for} \quad \frac{M}{M_u} > \frac{1}{3} \tag{11.12}$$

where K represents the reduced rotational stiffness and K_0 is the initial rotational stiffness.

In cases involving moments about the *x*-axis and the *y*-axis, the uplift behaviour becomes more complex. To tackle this complexity, two distinct methods have been proposed for the study of this problem: the decoupled method and the coupled method.

The decoupled method is relatively straightforward. In this approach, the uplift behaviour in the two horizontal directions is treated independently. The stiffness reduction can be calculated separately for each direction, and the total detached surface can be determined by superimposing the detached surfaces of each direction. Figures 11.6 (a) and (b) depict

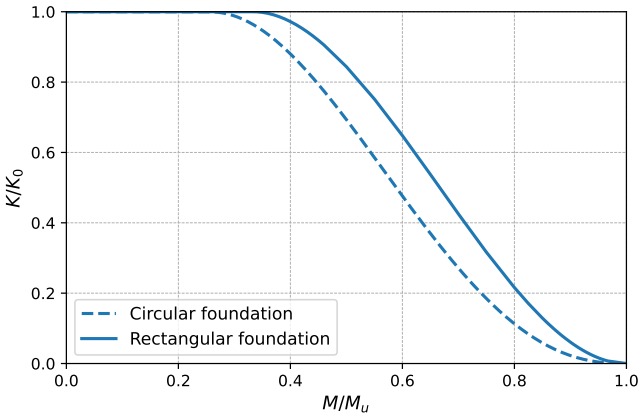

Fig. 11.5. Rotational stiffness degradation curves due to uplift

the detached surfaces under moments about the x-axis and the y-axis, respectively. The superimposed result is shown in Figure 11.6 (c). Under this assumption, the compressed surface takes on a rectangular shape. This decoupled approach simplifies the analysis by considering the two horizontal directions separately.

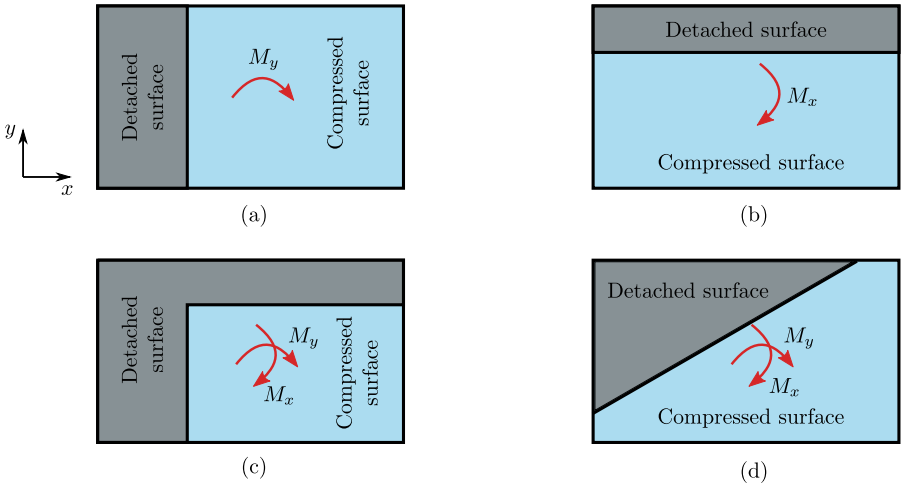

Fig. 11.6. Detached surface of the foundation: (a) under moment about the y-axis, (b) under moment about the x-axis, (c) superimposition of detached surfaces, and (d) real detached surface under moments

However, for a rectangular foundation under moments about the x-axis and the y-axis, the detached and compressed surfaces should resemble those shown in Figure 11.6 (d). To analyse this behaviour, numerical analysis becomes necessary. The foundation can be discretised into n small elements, and the global equilibrium equation can be expressed as Equation 11.13. If detachment occurs, the normal stiffness of the small element should be zero. Iterative calculations are required to determine the final detached and compressed surfaces (Alzate and Cuira, 2022).

$$\begin{cases} \sum_{i}^{n} k_i(u_0 + x_i\delta_r y + y_i\delta_r x)S_i = V \\ \sum_{i}^{n} k_i(u_0 + x_i\delta_r y + y_i\delta_r x)S_i(x_i - x_0) = M_y \\ \sum_{i}^{n} k_i(u_0 + x_i\delta_r y + y_i\delta_r x)S_i(y_i - y_0) = M_x \\ k_i = 0 \quad \text{if uplift} \end{cases} \tag{11.13}$$

In the provided equation, V, M_x and M_y denote the vertical force, moment about the *x*-axis and moment about the *y*-axis applied at the centre of the foundation. u_0 represents the rigid body movement of the foundation, $\delta_r y$ signifies the rotation of the foundation about the *y*-axis, and $\delta_r x$ represents the rotation of the foundation about the *x*-axis. S_i corresponds to the area of element i, and x_i and y_i denote the center coordinates of element i. Additionally, x_0 and y_0 stand for the centre coordinates of the foundation.

11.2.4 Plastic behaviour

The force-displacement relationship plays a pivotal role in understanding the plastic behaviour of the macro-element. These relationships are described by equations known as constitutive laws. The constitutive law for plasticity comprises several key components:

- Yield surface to determine the force state when yielding occurs;
- Flow rule to describe how the increment of plastic displacement changes when yield occurs;
- Hardening rule to explain how the yield surface evolves under plastic deformation;
- Loading-unloading conditions to specify the next move in the loading program.

In the proposed macro-element, akin to a shallow foundation, the plastic behaviour of a reinforced foundation can be characterised by two yield criteria, with each criterion representing a distinct plastic mechanism, namely sliding and loss of bearing capacity. These surfaces are delineated within the force space. For each of these surfaces, an appropriate flow rule should be established.

Within the framework of the proposed macro-element, an elastic-perfectly plastic law is employed to replicate the plastic behaviour, which offers several advantages in engineering. This law is characterised by its relative simplicity in comprehension and application. It simplifies material behaviour by assuming an instantaneous transition from the elastic domain to the plastic domain upon reaching a yield stress (force). Furthermore, it exhibits predictability, where the occurrence of plastic deformation signifies non-satisfaction with the failure criteria. It is worth noting that this study does not consider the incorporation of

a hardening rule, as determining hardening parameters can prove challenging in practical applications, and their physical interpretation may not always be apparent.

Loss of bearing capacity

- **Yield surface**

  The expression of the yield surface is derived from the yield design theory, as presented in Chapters 8 and 9. The solution to the seismic stability problem is framed within the context of 2D plane strain problems. Consequently, the resulting yield surface is inherently applicable to strip foundations reinforced by rigid inclusions.

  It is observed that the yield surface in the V-H plane lacks the smoothness required for an easily matched mathematical expression, even after experimenting with numerous numerical expressions. Therefore, three strategies are introduced to calibrate the expression of the yield surface in the V-H plane.

  – An inner expression capable of attaining the maximum value of horizontal force H_{max};

  – An outer expression designed to encompass the overall shape;

  – A generalised ellipse designed to capture the shape effectively.

  Both the inner and outer expressions draw inspiration from the formulation of the seismic stability criterion for shallow foundations as outlined in Eurocode 8 (AFNOR, 2007). To identify the optimal parameters within a specified target function form, a non-linear regression algorithm (Kitchin, 2015) is employed. The obtained criteria for the loss of bearing capacity are outlined in Equations 11.14, 11.15, and 11.16.

  – The inner expression:

$$\frac{(0.32h_x)^{1.57}}{v^{1.13}(1-v)^{1.49}} + \frac{(2.05m_y)^{2.08}}{v^{2.08}(1-v)^{2.54}} - 1 \leq 0 \tag{11.14}$$

  – The outer expression:

$$\frac{(0.22h_x)^{1.7}}{v^{1.31}(1-v)^{1.75}} + \frac{(2.05m_y)^{1.8}}{v^{1.8}(1-v)^{2.2}} - 1 \leq 0 \tag{11.15}$$

  – The general ellipse expression:

$$\frac{h_x^{1.36}}{(1-(1-2v)^6)^{1.7}} + \frac{(2.05m_y)^{1.8}}{v^{1.8}(1-v)^{2.2}} - 1 \leq 0 \tag{11.16}$$

where h_x, m_y and v represented normalised force (moment) as described in Equations 11.17.

$$v = \frac{V}{V_{max}} \qquad h_x = \frac{H_x}{H_{max}} \qquad m_y = \frac{M_y}{BV_{max}} \tag{11.17}$$

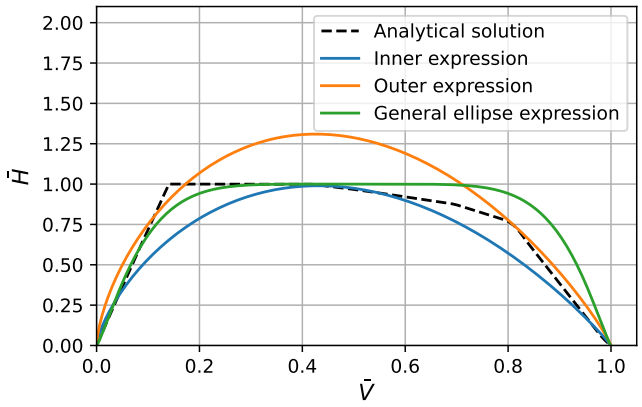

Fig. 11.7. Yield surface in the normalised V-H plane for loss of bearing capacity

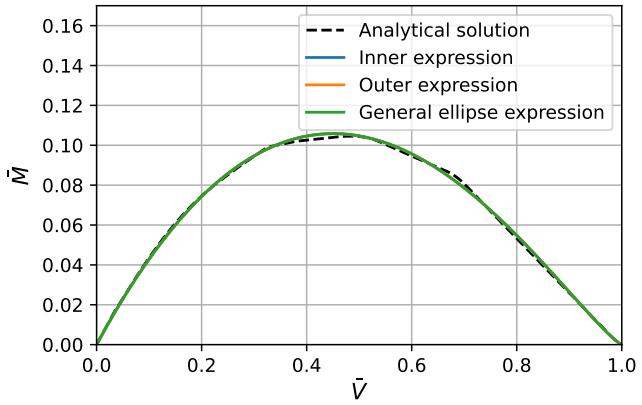

Fig. 11.8. Yield surface in the normalised V-M plane for loss of bearing capacity

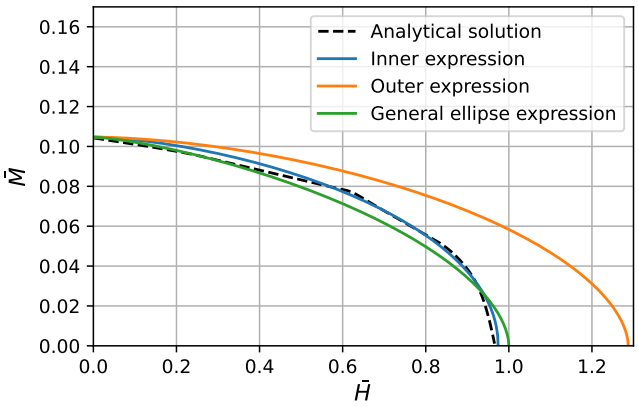

Fig. 11.9. Yield surface in the normalised H-M plane for loss of bearing capacity

To expand the applicability of the yield surfaces to circular or rectangular foundations, it is necessary to adapt the criteria for excitations in the two horizontal directions. Two additional terms need to be integrated into Equations 11.14, 11.15 and 11.16. These newly introduced terms correspond to the horizontal force H_x and the moment M_y. Consequently, 5D yield surfaces in the space (V, H_x, H_y, M_x, M_y) are obtained, and they are described by Equations 11.18, 11.19 and 11.20.

– The inner expression:

$$\frac{(0.32h_x)^{1.57}}{v^{1.13}(1-v)^{1.49}} + \frac{(0.32h_y)^{1.57}}{v^{1.13}(1-v)^{1.49}} + \frac{(2.05m_x)^{2.08}}{v^{2.08}(1-v)^{2.54}} + \frac{(2.05m_y)^{2.08}}{v^{2.08}(1-v)^{2.54}} - 1 \leq 0 \tag{11.18}$$

– The outer expression:

$$\frac{(0.22h_x)^{1.7}}{v^{1.31}(1-v)^{1.75}} + \frac{(0.22h_y)^{1.7}}{v^{1.31}(1-v)^{1.75}} + \frac{(2.05m_x)^{1.8}}{v^{1.8}(1-v)^{2.2}} + \frac{(2.05m_y)^{1.8}}{v^{1.8}(1-v)^{2.2}} - 1 \leq 0 \tag{11.19}$$

– The general ellipse expression:

$$\frac{h_x^{1.36}}{(1-(1-2v)^6)^{1.7}} + \frac{h_y^{1.36}}{(1-(1-2v)^6)^{1.7}} + \frac{(2.05m_x)^{1.8}}{v^{1.8}(1-v)^{2.2}} + \frac{(2.05m_y)^{1.8}}{v^{1.8}(1-v)^{2.2}} - 1 \leq 0 \tag{11.20}$$

where h_y and m_x are normalised force (moment) as described in Equations 11.21.

$$h_y = \frac{H_y}{H_{max}} \qquad m_y = \frac{M_y}{BV_{max}} \tag{11.21}$$

In these proposed yield surface expressions, only two parameters, namely, V_{max} and H_{max}, require identification. The bearing capacity V_{max} can be estimated using the proposed analytical approach based on yield design theory or other numerical modelling methods. The maximum horizontal force can be estimated simply using Equation 11.22.

$$H_{max} = cA \tag{11.22}$$

where c represents the cohesion of the soft soil, and A denotes the area of the reinforced foundation.

It is important to note that this expression does not account for soil inertia. However, a reduction factor i_g can be directly applied to the foundation bearing capacity V_{max}, as described in Equation 11.23. Details regarding the soil inertia reduction factor i_g are provided in Section 10.5.

$$V_{max,a_g} = V_{max} i_g \tag{11.23}$$

- **Plastic flow rule**

  An appropriate plastic flow rule is essential to characterise plasticity, and initially, an associated law is examined.

  In the context of an associated flow rule, four "trial" force vectors are illustrated in either the V-H or V-M plane, as shown in Figure 11.10. The utilisation of an associated flow rule generally assumes that the plastic displacement increment and the normal to the yield surface have the same orientation. Following this rule, the directions of plastic displacement for these four trial force vectors are indicated by the arrows in Figure 11.10.

  In the case of trial force vectors A and B, it becomes evident that the direction of the plastic vertical displacement u_z^{pl} is downward, indicating the occurrence of irreversible settlement. Conversely, for trial force vectors C and D, the direction of the plastic vertical displacement u_z^{pl} is upward, suggesting that the structure will experience an unnatural upward movement during seismic excitation.

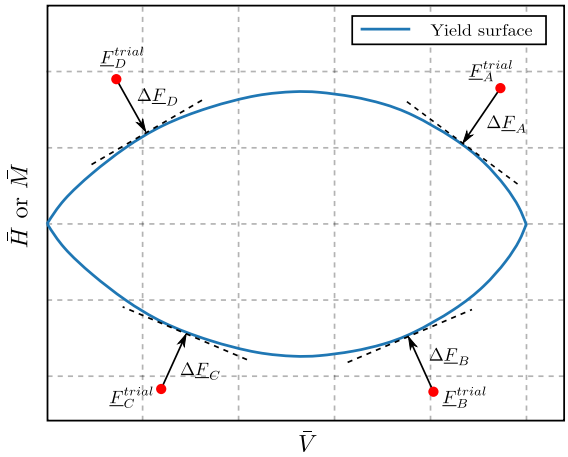

Fig. 11.10. Associated flow rule in V-H (V-M) plane

To address this concern, Cremer *et al.* (2002) introduced a non-associated plastic potential, denoted as g, which is fundamentally distinct from the yield surface. This potential describes an ellipsoid centred at the axis origin. Similarly, Grange (2008) also proposed a non-associated plastic potential, whose expression is identical to the proposed yield surface in the H-M planes but differs from the proposed yield surface in the V-H and V-M planes. This allows for the modification of the flow rule shape to control the direction of the plastic displacement u_z^{pl}. The relationship between the proposed yield surface and the plastic potential is depicted in Figure 11.11. With this proposed plastic potential, regardless of the trial force vector's position, only downward plastic vertical displacement can be generated. However, it should be noted that the proposed plastic flow rule lacks a clear physical interpretation and introduces supplementary parameters.

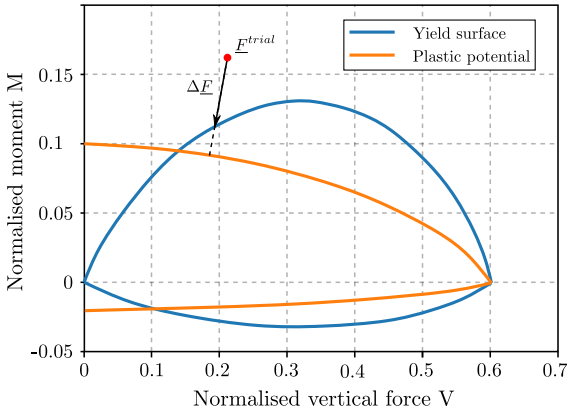

Fig. 11.11. Non-associated plastic flow rule used in the macro-element of Grange (2008)

For this reason, the non-associated law is also employed in the plastic constitutive law for loss of bearing capacity for foundations reinforced by rigid inclusions. Drawing inspiration from the work of Grange (2008), the proposed plastic potential in this study follows a similar approach. In this case, the derivation of the plastic potential

$\partial g/\partial V$ is set to 0. The direction of the plastic displacement can be visualised in Figure 11.12.

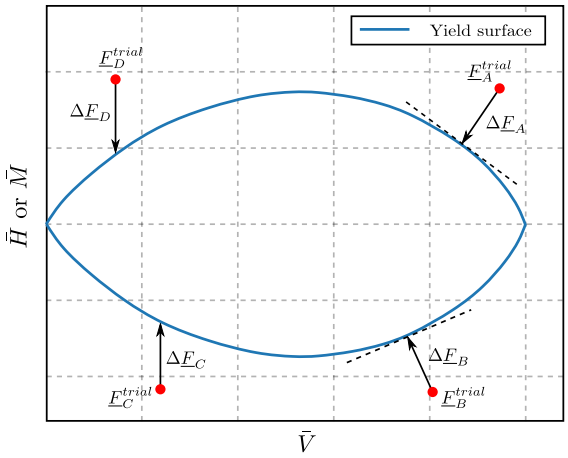

Fig. 11.12. Non-associated flow rule in V-H (V-M) plane

Compared to the associated flow rule illustrated in Figure 11.11, the directions of plastic displacement for trial force vectors A and B remain unchanged. However, for trial force vectors C and D, their directions for plastic displacement are altered and are no longer perpendicular to the yield surface. With these modified directions, no plastic vertical displacement can be generated. The modification is pertinent to the loss of bearing capacity behaviour for the reinforced foundations. Consequently, a non-associated flow rule is adopted in the proposed macro-element.

Sliding behaviour

In a foundation reinforced with rigid inclusions, the possibility of sliding failure may arise between the foundation and the LTP.

- **Yield surface**

  The expression of this yield surface is grounded in the Coulomb friction model.

  For strip foundations, the expression of the yield surface is as follows:

$$f(H_x, V) = H_x - V tan\varphi \tag{11.24}$$

  For rectangular and circular foundations, the expression of the yield surface is given by:

$$f(H_x, H_y, V) = \sqrt{H_x^2 + H_y^2} - V tan\varphi \tag{11.25}$$

- **Plastic flow rule**

  The flow rule determines the direction in which plastic displacements will occur. In a typical Coulomb friction criterion, a dilation angle ψ is introduced in the expression of the plastic potential. For strip foundations, the expression of the plastic potential is as follows:

$$g(H_x, V) = H_x - V tan\psi \tag{11.26}$$

  For rectangular and circular foundations, the expression of the plastic potential is given by:

$$g(H_x, H_y, V) = \sqrt{H_x^2 + H_y^2} - V tan\psi \tag{11.27}$$

  Equations 11.26 and 11.27 are identical to the yield surface expressions detailed in Equations 11.24 and 11.25 when the dilation angle ψ is equal to the friction angle φ. In this scenario, the flow rule is considered associated.

  For cohesionless soils, including sand and gravel, with an angle of internal frictionφ exceeding 30°, it is possible to estimate the dilation angle ψ as $\psi = \varphi - 30°$. To prevent the creation of undesirable plastic vertical displacement, setting $\psi = 0$ is advisable for the same reasons explained earlier in the context of loss of bearing capacity behaviour, to avoid unnatural upward movement.

  The findings in Section 10.4 demonstrate that the sliding mechanism is inherently considered in the loss of bearing capacity. In situations where the bearing capacity of the studied reinforced foundations is already validated, the sliding criterion can be incorporated into the macro-element.

11.3 Numerical resolution and implementation

11.3.1 Structure of macro-element

The developed macro-element comprises the following components:

- **A plasticity model**

  A plasticity model is employed to depict the irreversible behaviours of the foundation. This model replicates the inherent material non-linearity in the system and is formulated with an elastic-perfectly plastic constitutive law featuring a non-associated flow rule.

- **A nonlinear elasticity model**

  A nonlinear elasticity model, which is non-dissipative and reversible, is utilised to characterise the uplift behaviour. This model replicates the non-linearity at the soil-foundation interface and is expressed through rotational stiffness reduction.

- **A dash-pot**

  A dash-pot is employed to account for energy dissipation resulting from material properties and wave propagation. This model replicates the material damping and radiation damping within the system under dynamic loading.

The plasticity model and the nonlinear elasticity model are always connected in series. When considering static loading or an undamped system, the rheological model of the macro-element can be represented as shown in Figure 11.13.

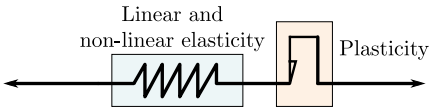

Fig. 11.13. Simplified rheological model for static or undamped macro-element

There are two possible positions for the dash-pot: it can be placed in parallel with the series of the plasticity model and the nonlinear elasticity model or in parallel with just the nonlinear elasticity model. Two potential structures for the proposed macro-element are depicted in Figure 11.14.

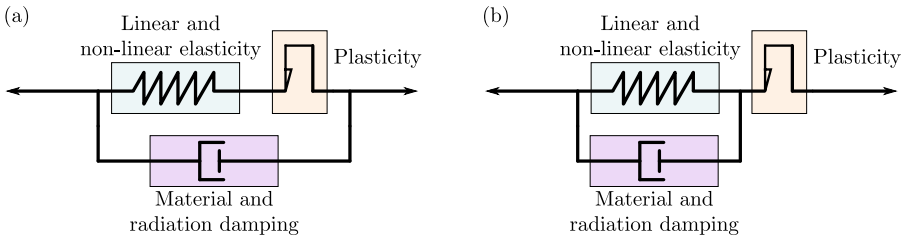

Fig. 11.14. Simplified rheological model for the macro-element subjected to dynamic loading: (a) dash-pot in parallel with the series of the plasticity model and the non-linear elasticity model and (b) dash-pot in parallel with the non-linear elasticity model

Based on the structures of the proposed macro-element, the solution is attained through time integration schemes, such as the Newmark-beta integration, in conjunction with nonlinear solution algorithms like the modified Newton-Raphson algorithm.

11.3.2 Non-linear problem resolution

Plasticity problem resolution

Traditionally, algorithms for constitutive laws formulated within the framework of classical plasticity are based on the given strains. In the macro-element, the algorithms are based on displacements. The techniques for integrating the constitutive equations can be categorised into two groups: explicit and implicit schemes (Huang and Griffiths, 2009). The implicit closest point projection method is a "return mapping" algorithm introduced by Simo and Taylor (1985) and is now widely used in the analysis of non-linear problems in geomechanics.

The return mapping algorithm involves an initial step of integrating the elastic equations with total force increments to obtain an elastic predictor $\underline{F}^{n+1,trial}$. The elastically predicted forces are then adjusted to lie on a yield surface by iteratively correcting $\Delta\underline{F}^{pl}$, leading to plastic displacement increments. This process is illustrated in Figure 11.15 (a).

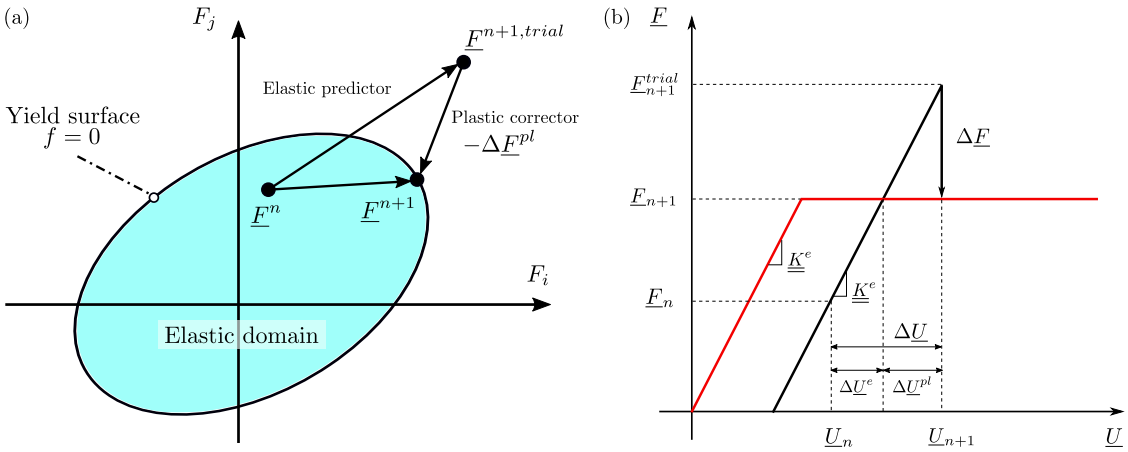

Fig. 11.15. Plasticity problem resolution: (a) Return mapping scheme for elastic-perfectly plastic model and (b) Modified Newton-Raphson algorithm in an elastic-perfectly plastic problem

A constitutive law is defined within the reference frame $(\underline{U}, \underline{F})$. For simplicity, a 1D representation is depicted in Figure 11.15 (b). The solution to the elastic-perfectly plastic problem is obtained using the modified Newton-Raphson algorithm.

The state $(\underline{U}_n, \underline{F}_n)$ represents the converged state from the previous step n and is fully known. The problem is to determine the displacement $\underline{u}_{n+1}$ and the corresponding $\underline{F}_{n+1}$. To calculate this, an auxiliary state is introduced with a "trial" exponent, which is obtained by considering a purely elastic step.

$$\begin{cases} \underline{F}^{trial}_{n+1} = \underline{\underline{K}}^e \Delta\underline{U} + \underline{F}_n \\ f^{trial}_{n+1} = f(\underline{F}^{trial}_{n+1}) \end{cases} \tag{11.28}$$

The sign of f_{n+1}^{trial} will then indicate the current regime to be considered for resolution, leading to two possibilities.

- if $f_{n+1}^{trial} < 0$, the regime is plastic, and therefore, $\underline{u}_{n+1} = \underline{u}_{n+1}^{trial}$ and $\underline{F}_{n+1} = \underline{F}_{n+1}^{trial}$.
- if $f_{n+1}^{trial} > 0$, the regime is plastic, and therefore, Equation 11.29 should be solved.

$$f(\underline{F}_{n+1}^{trial}) = 0 \tag{11.29}$$

A Taylor expansion around the trial state $(\underline{F}_{n+1}^{trial}, \underline{U}_{n+1}^{trial})$ results in Equation 11.30.

$$f(\underline{F}_{n+1}^{trial} - \Delta\underline{F}) = f(\underline{F}_{n+1}^{trial}) - \frac{\partial f}{\partial \underline{F}}\Delta\underline{F} = 0 \tag{11.30}$$

According to the flow rule, the plastic displacement can be calculated using Equation 11.31. Then, the force corrector $\Delta\underline{F}$ can be calculated by Equation 11.32.

$$\Delta\underline{U}^{pl} = \Delta\lambda\frac{\partial g}{\partial \underline{F}} \tag{11.31}$$

$$\Delta\underline{F} = \underline{\underline{K}}^{e}\Delta\underline{U}^{pl} \tag{11.32}$$

By introducing Equations 11.31 and 11.32, Equation 11.30 becomes Equation 11.33.

$$f(\underline{F}_{n+1}^{trial}) - \frac{\partial f}{\partial \underline{F}}\underline{\underline{K}}^{e}\Delta\lambda\frac{\partial g}{\partial \underline{F}} = 0 \tag{11.33}$$

The only unknown variable in Equation 11.33 is the plastic multiplier $\Delta\lambda$, which can be calculated using Equation 11.34.

$$\Delta\lambda = \frac{f(\underline{F}_{n+1}^{trial})}{\frac{\partial f}{\partial \underline{F}}\underline{\underline{K}}^{e}\frac{\partial g}{\partial \underline{F}}} \tag{11.34}$$

Once the plastic multiplier $\Delta\lambda$ is calculated, the displacement and force for the $n+1$ step can be determined, as described in Equations 11.35 and 11.36.

$$\underline{U}_{n+1}^{pl} = \underline{U}_{n}^{pl} + \Delta\underline{U}^{pl} \tag{11.35}$$

$$\underline{F}_{n+1} = \underline{\underline{K}}^{e}(\underline{U}_{n+1} - \underline{U}_{n+1}^{pl}) \tag{11.36}$$

Multiple yield surfaces

The problem with multiple yield surfaces requires a more complex formulation and numerical treatment. In the case of M activated yield surfaces, the plastic displacement increment can be considered as a sum of the contributions from each yield surface.

$$\Delta \underline{U}^{pl} = \sum_{1}^{M} \Delta \underline{U}^{pl,m} \tag{11.37}$$

This equation can be formulated using the plastic flow rule as follows:

$$\Delta \underline{U}^{pl} = \sum_{1}^{M} \Delta\lambda^{m} \frac{\partial g^{m}}{\partial \underline{F}} \tag{11.38}$$

Equation 11.33 becomes Equation 11.39. In this case, there are M equations and M unknown plastic multiplier.

$$\begin{cases} f^{1}(\underline{F}_{n+1}^{trial}) - \frac{\partial f^{1}}{\partial \underline{F}} \underline{\underline{K}}^{e} (\Delta\lambda^{1} \frac{\partial g^{1}}{\partial \underline{F}} + \Delta\lambda^{2} \frac{\partial g^{2}}{\partial \underline{F}} + \cdots + \Delta\lambda^{M} \frac{\partial g^{M}}{\partial \underline{F}}) = 0 \\ f^{2}(\underline{F}_{n+1}^{trial}) - \frac{\partial f^{2}}{\partial \underline{F}} \underline{\underline{K}}^{e} (\Delta\lambda^{1} \frac{\partial g^{1}}{\partial \underline{F}} + \Delta\lambda^{2} \frac{\partial g^{2}}{\partial \underline{F}} + \cdots + \Delta\lambda^{M} \frac{\partial g^{M}}{\partial \underline{F}}) = 0 \\ \quad \vdots \\ f^{M}(\underline{F}_{n+1}^{trial}) - \frac{\partial f^{M}}{\partial \underline{F}} \underline{\underline{K}}^{e} (\Delta\lambda^{1} \frac{\partial g^{1}}{\partial \underline{F}} + \Delta\lambda^{2} \frac{\partial g^{2}}{\partial \underline{F}} + \cdots + \Delta\lambda^{M} \frac{\partial g^{M}}{\partial \underline{F}}) = 0 \end{cases} \tag{11.39}$$

The displacement and force for the $n+1$ step can be determined, using Equations 11.35 and 11.36.

Large load step

The yield surface expression is defined for the normalised vertical force $\bar{V}$ smaller than 1. When using a large load step, there is a possibility that the elastic predictor may be located in a domain where the yield surface is not defined, as depicted in Figure 11.16.

Two situations can be identified. The first situation, where either the horizontal or moment is non-zero or the load path is not vertical, resembles the loading path starting at $\underline{F}_{A,n}$ in Figure 11.16. In this scenario, it can be observed that the elastic predictor $\underline{F}_{A,n+1}^{trial}$ falls into a domain where the yield surface is not defined, resulting in a negative plastic multiplier or a corrected force state that does not lie on the yield surface. In such cases, it is advisable to divide the load step into several smaller steps. Employing a smaller loading step from $\underline{F}_{A,n}$ to $\underline{F}_{A,n+1,i}^{trial}$ ensures that the elastic predictor remains within a domain where the yield surface is defined.

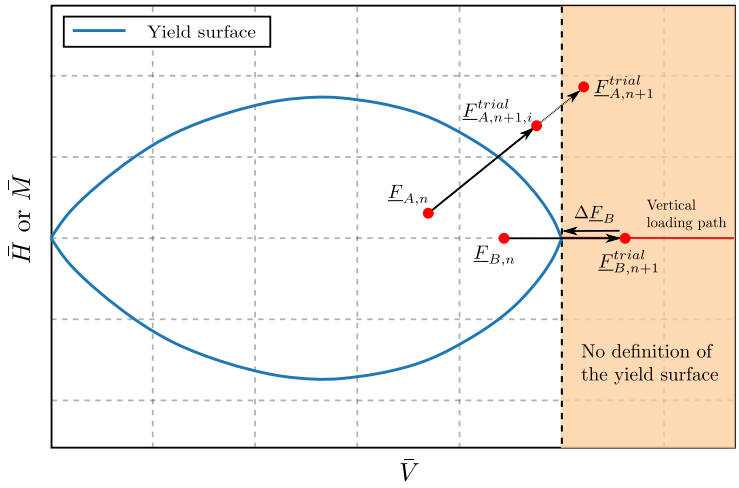

Fig. 11.16. Elastic predictor outside the yield surface's definition domain

In the second situation, where both the horizontal and moment components are not zero, and the load path is vertical, like the path from $\underline{F}_{B,n}$ to $\underline{F}^{trial}_{b,n+1}$, employing a smaller loading step cannot solve the problem. This is because the elastic predictor would directly enter a domain where the yield surface is not defined. In such cases, an imposed correction should be used. The corrected force state is adjusted to the state where $\underline{V} = 1$. The force correction $\Delta\underline{F}$ can be directly calculated without the need to calculate the plastic multiplier. The plastic displacement $\Delta\underline{U}^{pl}$ can be determined using Equation 11.40.

$$\Delta\underline{U}^{pl} = [\underline{\underline{K}}^{e}]^{-1}\Delta\underline{F} \tag{11.40}$$

The same strategy was employed in the study by El Arja (2020) for addressing the gradient discontinuity issue in the Mohr-Coulomb criterion.

Non-linear elastic problem resolution

The uplift behaviour is a non-linear elastic problem, and this study originally proposes an iterative algorithm to account for the rotational stiffness reduction with the moment. The first trial is calculated with the non-reduced rotational stiffness K_0 in each time increment, resulting in a corresponding moment $M^{trial,0}$. If $M^{trial,0}$ does not exceed $M_u/3$ for a rectangular foundation or $M_u/4$ for a circular foundation, it becomes evident that no uplift initiates, and there is no need for iterative calculation. However, if the uplift is initiated, the rotational stiffness should be reduced according to the stiffness reduction curve $K = K(M)$.

As shown in Figure 11.17, when considering the first trial moment and stiffness couple $(M^{trial,0}, K_0)$, a line connecting $(M^{trial,0}, K_0)$ and the origin point can be drawn. The intersection of this line with the stiffness degradation curve provides a new rotational

stiffness value K_1. Then, a new calculation is conducted with the updated rotational stiffness K_1. The calculation iterates until the couple $(M^{trial,j}, K_j)$ lies on the rotational stiffness degradation curve. The convergence of the calculation is assessed using an uplift criterion f_{up}, described in Equation 11.41.

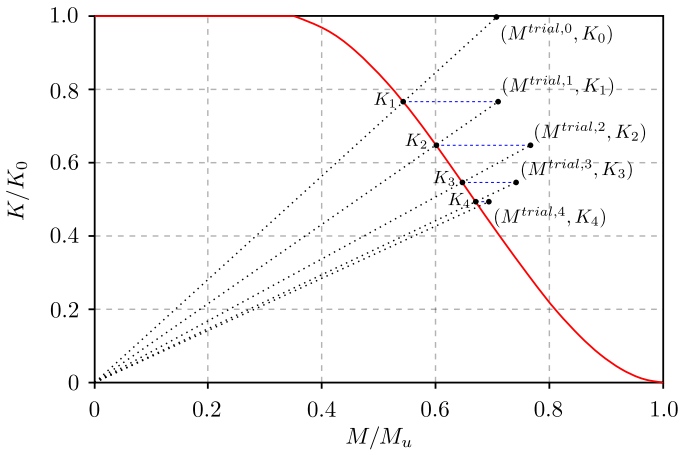

Fig. 11.17. Iterative algorithm to solve the non-linear elastic problem

$$f_{up} = \frac{M(K_{n+1}^{j+1,trial}) - M_{n+1}^{j+1,trial}}{M_{n+1}^{j+1,trial}} \tag{11.41}$$

Consideration of damping for dynamic calculations

Figure 11.14 illustrates two models with different dash-pot positions. In the first structure, where the dash-pot is in parallel with the series of the plasticity model and the non-linear elasticity model, as depicted in Figure 11.14 (a), the previously explained mathematical interpretation remains valid. This is because the force in the dash-pot does not influence the plasticity and non-linear elasticity.

However, if the dash-pot is only in parallel with the elasticity and non-linear elasticity model, as shown in Figure 11.14 (b), several adjustments should be made to the non-linear resolution algorithm.

The calculation of the elastic predictor $\underline{F}_{n+1}^{trial}$ should consider the damping terms $\underline{\underline{C}}\Delta\underline{\dot{U}}$.

$$\underline{F}_{n+1}^{trial} = \underline{\underline{K}}^e \Delta\underline{U} + \underline{\underline{C}}\Delta\underline{\dot{U}} + \underline{F}_n \tag{11.42}$$

The plastic multiplier $\Delta\lambda$ can be calculated, taking into account damping, as described in Equation 11.43.

$$\Delta\lambda = \frac{f(\underline{F}_{n+1}^{trial})}{\frac{\partial f}{\partial \underline{F}}(\underline{\underline{K}}^{e} + \underline{\underline{C}}/\Delta t)\frac{\partial g}{\partial \underline{F}}} \tag{11.43}$$

The damping term should also be considered within the non-linear elasticity model. The rotational damping can be adjusted based on the rotational stiffness, as described in Equation 11.44.

$$C = \frac{K}{K_0} C_0 \tag{11.44}$$

11.3.3 Superstructure modelling

In a dynamic SSI analysis employing the macro-element, the superstructure is usually simplified by an analogical model, as depicted in Figures 11.18 (a) and (b).

According to the dynamic characteristic of the superstructure, three types of elements can be used in the analysis to capture the key features of the superstructure. They are the Kelvin-Voight model (spring and dash-pot), the Euler-Bernoulli beam, and the Timoshenko beam combined with the lumped mass matrix or the consistent mass matrix. The formulation of the elementary stiffness and mass matrices of each element adopted in this work can be found in the literature (Zienkiewicz and Taylor, 2000; EDF, 2019; Shen *et al.*, 2022d).

Depending on the type of model chosen, the degrees of freedom for a node in a superstructure modelling are listed in Table 11.1.

Tab. 11.1. List of degrees of freedom for a node in superstructure modelling

Model	Degrees of freedom
Kelvin-Voight mode	U_x, U_y, U_z
Euler-Bernoulli beam	U_x, U_y, U_z, θ_x, θ_y
Timoshenko beam	U_x, U_y, U_z, θ_x, θ_y

The application of the macro-element is not limited to the dynamic SSI analysis with a superstructure with an analogue model. A more sophisticated 3D FEM model can be used to simulate the superstructure and combined with the macro-element approach, which is not in the framework of the thesis.

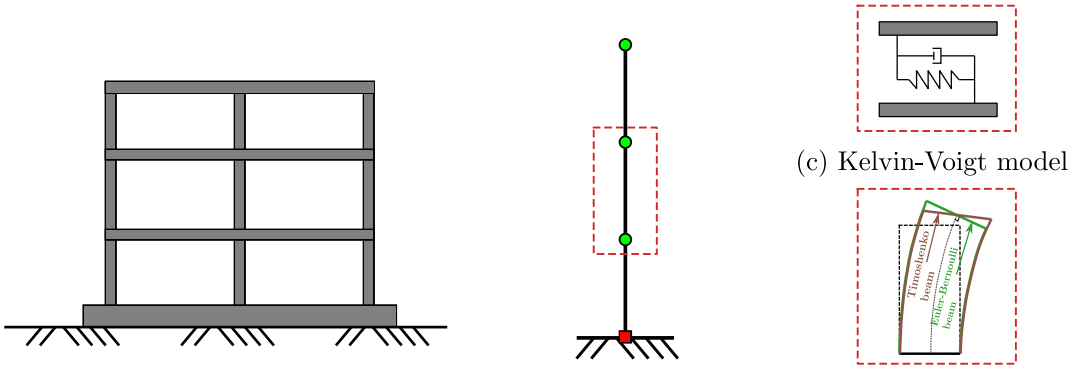

(a) 3-storey building (b) Analogical model (c) Kelvin-Voigt model (d) Beam model

Fig. 11.18. Superstructure modelling: (a) complete modelling, (b) simplified modelling, (c) spring and dash-pot model, and (d) two beam-type models

11.3.4 Dynamic equation and numerical integration

Dynamic equation of motion

To demonstrate the formulation of the dynamic equation for the system considering the SSI effect, a three-storey building is employed. This three-storey building is simplified using a lumped mass model with beams connecting the lumped masses. The macro-element is positioned at the foundation level. The configuration of the superstructure and the macro-element is depicted in Figure 11.19.

The equation of motion for the overall system can be generally expressed in matrix form as Equation 11.45.

$$\underline{\underline{M}}\,\underline{\ddot{U}} + \underline{\underline{C}}\,\underline{\dot{U}} + \underline{\underline{K}}\,\underline{U} = \underline{P} \tag{11.45}$$

where $\underline{\underline{M}}$, $\underline{\underline{C}}$, and $\underline{\underline{K}}$ represent the global mass, damping and stiffness matrices, respectively. $\underline{U}$ is the node displacement vector and $\underline{P}$ is the force vector due to externally applied dynamic or seismic loads. The Newmark dynamic integration algorithm is used to resolve the dynamic equation of motion. The details of this algorithm can be found in Section E.1 with an illustration of the global stiffness matrix assembly illustrated in Figure E.1.

Calibration of SSI springs

As discussed in Section 11.2.2, calibration is necessary to account for the frequency effect, as illustrated in Figure 11.20.

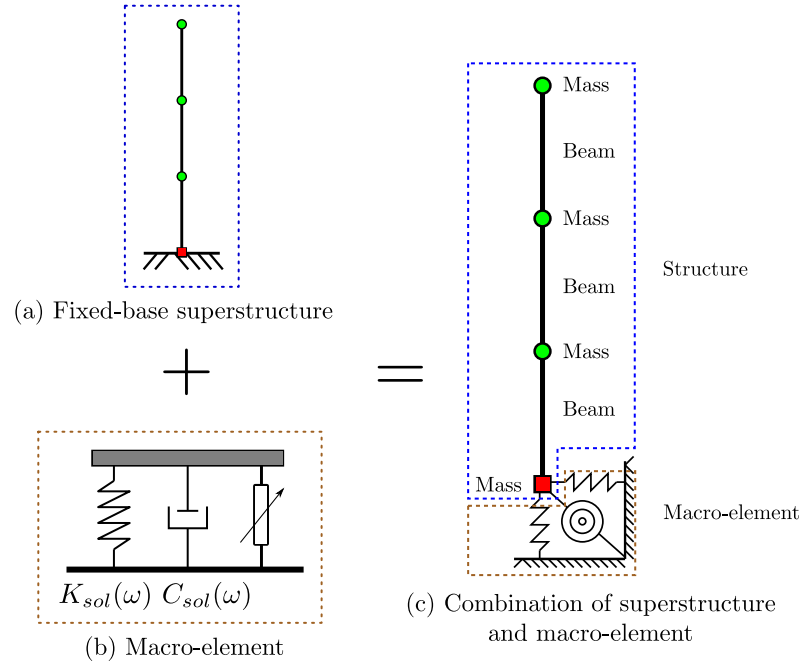

Fig. 11.19. Combination of a three-story building superstructure and a foundation SSI macro-element

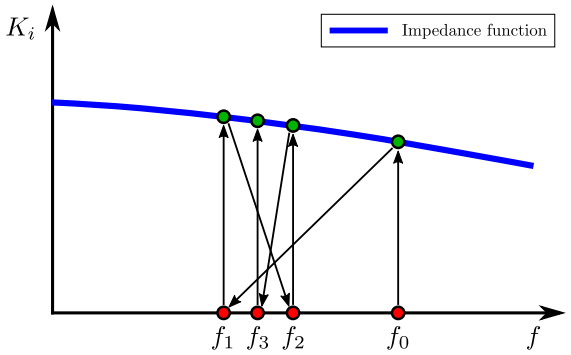

Fig. 11.20. SSI stiffness calibration based on the dynamic impedance function

The values of K_x, K_y, and K_z terms are calibrated based on the fundamental modes in translation for each direction. The rocking terms, K_{rx} and K_{ry}, are calibrated according to the fundamental modes in translation along the Y and X axes, respectively.

The iterative process can be initiated by selecting the first set of soil stiffness and damping values from the impedance functions corresponding to the structure on a fixed base. These values for stiffness and damping in each degree of freedom should be adjusted through iterative calculations to align with the principal modes of the corresponding degree of freedom. The iterative calculation should be terminated when frequencies between two iterative steps no longer exhibit significant changes. A variation of the fundamental frequency lower than 0.1 % is used as the convergence criterion. Upon the conclusion of the interactive calculation, the damping terms, including C_x, C_y, C_z, C_{rx}, and C_{ry}, can be determined from damping curves with the corresponding SSI frequencies.

11.4 Validation work

The validation study is conducted to systematically validate various components and numerical resolutions of the program. This process ensures that each element and their collective interaction are rigorously tested and confirmed to perform as intended.

Three families of validation work are organised to validate different aspects of the macro-element program, as depicted in Figure 11.21.

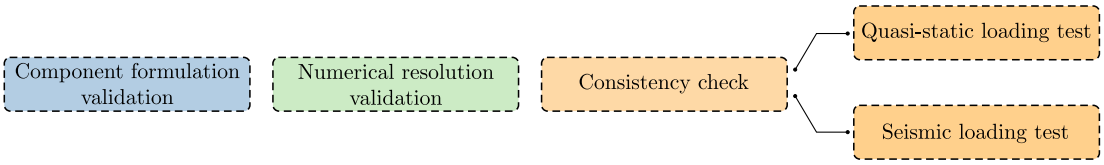

Fig. 11.21. Three families of validation work

Initially, the validation focuses on the formulation of each component, affirming the integrity of individual elements within the macro-element program. Subsequently, the validation of numerical resolution aims to ensure the precision of all applied numerical resolution algorithms. Finally, consistency checks are executed under quasi-static conditions to assess the performance coherence of the macro-element in static scenarios. Additionally, cross-comparisons under seismic conditions are carried out with a parallel program coded in VBA language, ensuring the robustness and accuracy of the macro-element.

11.4.1 Component formulation validation

The macro-element program comprises various components to simulate the SSI system. The validity of the program is controlled by these elements, as depicted in Figure 11.22.

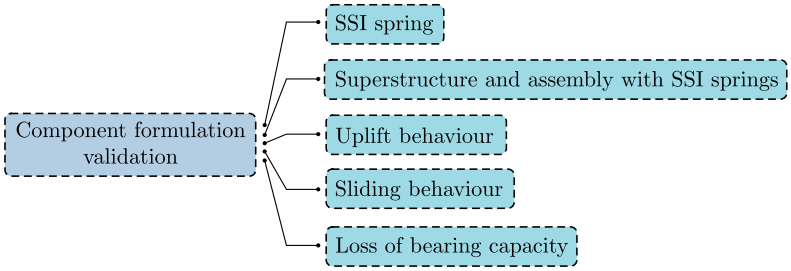

Fig. 11.22. Component formulation validation with the elements that control validity

SSI springs

In this study, the SSI springs are proposed to be calibrated based on the dynamic impedance functions. The stiffness value for each degree of freedom is incorporated into a SSI stiffness

matrix. Dynamic impedance functions can be obtained using commercial numerical software, such as PLAXIS (Bentley, 2022b), FLAC3D (Itasca Consulting Group, 2023), and SASSI (Ostadan and Deng, 2011).

The study conducted by Pereira (2020) indicates that the complete model analysis and the SSI springs calibrated based on the dynamic impedance functions yield nearly identical results.

Superstructure and assembly with SSI springs

The static response of both the Euler-Bernoulli beam element and the Timoshenko beam element implemented in the macro-element is verified through cross-comparison with Code_Aster (EDF, 2023).

Seven different tests are conducted, encompassing four static analyses and three vibration mode analyses with fixed-base superstructure models and superstructure models considering the SSI springs to validate both the superstructure and the assembly of the superstructure with the SSI springs. More information on the validation tests can be found in Section F.1.

The obtained results demonstrate the capability to accurately depict the behaviour of beam-type superstructure modelling and the assembly with SSI springs.

Uplift behaviour

The uplift behaviour for a foundation reinforced by rigid inclusions can be simulated using the rotational stiffness degradation curves presented in the work of (Brûlé and Cuira, 2018).

Sliding behaviour

The yield surface for the sliding failure mechanism is based on the Coulomb friction model, enabling the incorporation of a shear stress limit. This limit represents the maximum shear stress that the interface can sustain before the sliding occurs. The identical yield surface is employed in the studies of Abboud (2017) and Shen (2019).

Loss of bearing capacity

The yield surface for the macro-element of rigid inclusions is obtained by an analytical approach based on the yield design theory. The validation of this approach involves a series of comparisons with FELA numerical modelling, as detailed in Chapter 9.

11.4.2 Numerical resolution validation

Validation of the numerical resolution algorithms is crucial. various algorithms are employed in the macro-element to resolve the non-linear dynamic problem in the temporal domain. This validation effort is categorised into four different resolution algorithms, as illustrated in Figure 11.23.

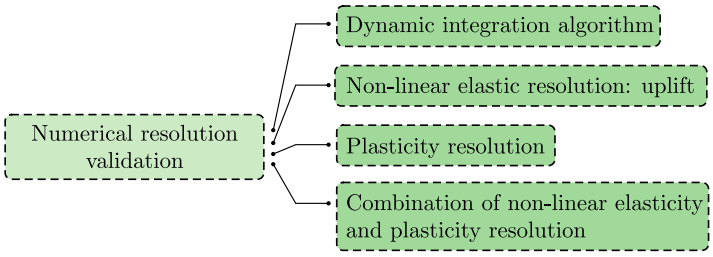

Fig. 11.23. Different numerical resolution algorithms within the numerical resolution validation

Dynamic integration algorithm

The dynamic integration algorithm is initially validated through cross-comparison with Code_Aster (EDF, 2023). These tests involve fixed-base superstructure models and superstructure models with the SSI springs subjected to a rectangular impulse. The aim is to verify the dynamic resolution algorithms incorporated into the macro-element model.

Further details of the validation tests are available in Section F.2. The results obtained from these tests affirm the validation of the implemented dynamic integration algorithm.

Non-linear elastic resolution: uplift

The performed tests are designed to validate the uplift behaviour and its resolution within the macro-element through cross-comparison with FEM software: PLAXIS 2D (Bentley, 2022a).

The studied system comprises a SDOF structure and an interface between the foundation base and the supporting soil, allowing the uplift of the foundation. The sinusoidal-type and seismic excitations are used in the validation tests.

The details of the validation tests can be found in Section F.3. For tests involving sinusoidal-type excitations, both models successfully capture the same overall response of the system, with slight differences observed within similar orders of magnitude for the macro-element model and FEM analysis. However, slight differences are noticeable, remaining within similar orders of magnitude for both numerical models. In the case of the test conducted with a seismic excitation, the responses of the macro-element approach and results of FEM analysis overlap in a very satisfactory manner.

Plasticity resolution

The validation of the plasticity resolution includes the use of a simple sliding criterion. This validation is based on the analytical solution for the sliding of a rigid block, the SLAMMER software, and PLAXIS 2D (Bentley, 2022a).

The conclusion derived from these comparisons is that the macro-element exhibits a highly satisfactory reproduction of the dynamic plastic SSI response. The obtained responses closely align with both analytical solutions and the outcomes from the referenced software. Further details on the validation tests can be found in Section F.4.

Combination of non-linear elasticity and plasticity resolution

The tests in this section are designed to confirm the integration of non-linear elastic and plasticity resolution within the macro-element. This is achieved through a comparative analysis with the "FONDA_SUPERFI" macro-element, which describes the non-linear elasto-plastic behaviour of a rectangular foundation subjected to 3D seismic excitation in Code_Aster (EDF, 2023). The examination in these tests focuses on the combined analysis of sliding and uplift behaviours.

The studied system comprises a structure modelled with an Euler-Bernoulli beam and two lumped masses. Comprehensive details of the validation tests are available in Section F.3.

Minor differences are observed in this test group, partially attributed to the utilisation of different solution algorithms and precision applied in the two analyses. Despite these occasional and marginal distinctions, both models adeptly capture the variation of the nonlinear dynamic response, with comparable magnitudes observed for key indicators.

11.4.3 Consistency checks: Quasi-static loading test

This section conducts tests on the macro-element for the foundation reinforced by rigid inclusions under quasi-static monotonic and cyclic loading, serving as a consistency check. The tests are organised as illustrated in Figure 11.24.

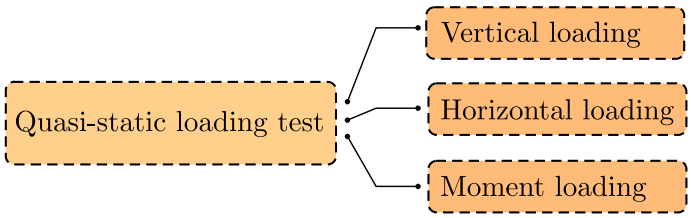

Fig. 11.24. Consistency check: Quasi-static monotonic and cyclic loading test

On one hand, the results can be examined to verify the essential characteristics of non-linear behaviours, ensuring that the macro-element reacts as predefined. On the other hand, these tests can demonstrate the fundamental features of non-linear behaviours within the foundation-soil system.

Studied configuration

In this study, a typical foundation configuration with rigid inclusion reinforcement is considered, as depicted in Figure 11.25, with several complementary parameters in the scheme used to calibrate the macro-element. The behaviour of the LTP is modelled with an elastic-perfectly plastic constitutive law using the Mohr-Coulomb criterion characterised by a friction angle $\varphi = 38\ °$. The behaviour of the soft clay is characterised by the Tresca criterion with a cohesion $c = 50$ kPa. The limit pressure p_l^* and the limit unit shaft friction q_s can be estimated as 300 kPa and 50 kPa, respectively. The configuration studied here is the same as the Group E01 configuration used in Section 5.3.2.

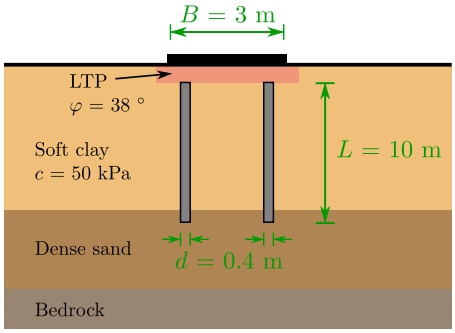

Fig. 11.25. Foundation configuration used in pseudo-static study

The elastic stiffness terms denoted as K_x, K_z, and K_{ry} employed in this research can be obtained from the previously calculated impedance functions outlined in Section 5.3.2 for Group E01. The stiffness values corresponding to a frequency of $f = 0.1$ Hz are selected. The bearing capacity of the foundation V_{max} and the maximum horizontal force H_{max} are determined by employing the kinematic exterior approach. The calibrated parameters for the macro-element in the pseudo-static test are summarised in Table 11.2.

Tab. 11.2. Calibrated parameters for the macro-element

Parameter	Value	Description
K_x	6.09×10^5 kN/m	
K_z	1.16×10^6 kN/m	Elastic stiffness
K_{ry}	2.04×10^6 kNm/rad	
V_{max}	3.64×10^3 kN	Bearing capacity
H_{max}	4.5×10^2 kN	Maximum horizontal force

Behaviour under vertical loading

The foundation is subjected to a monotonically increasing vertical displacement, and the corresponding displacement-force relationship is depicted in Figure 11.26 (a). It is observed that the model begins within the elastic domain, with the initial linear curve representing the elastic response of the system. Upon reaching the bearing capacity V_{max}, the macro-element promptly transitions into the plastic domain.

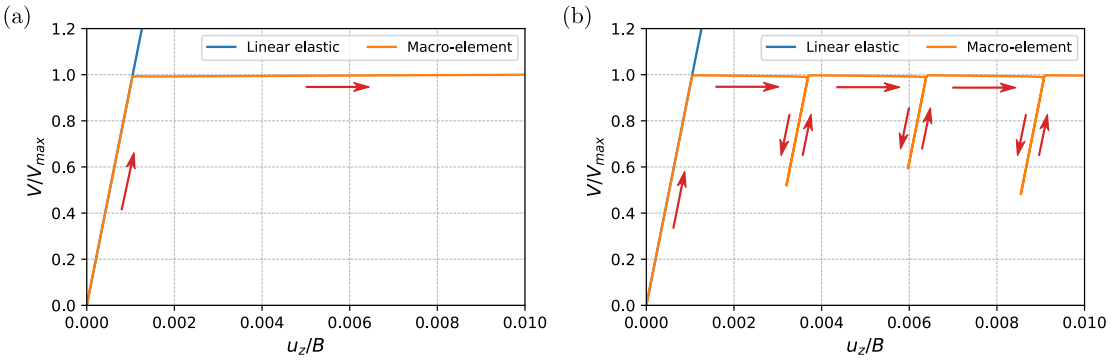

Fig. 11.26. Behaviour of macro-element under vertical loading: (a) relation between vertical displacement and vertical force under monotone vertical loading and (b) relation between vertical displacement and vertical force under cyclic vertical loading

Subsequently, a numerical loading-unloading-reloading test is conducted, as illustrated in Figure 11.26 (b). The unloading-reloading stiffness remains consistent. During each reloading cycle, the system attains the same limit platform V_{max}.

Behaviour under horizontal loading

The first pseudo-static monotonic test under horizontal loading is illustrated in Figure 11.27. The loading path is depicted in Figure 11.27 (a). The foundation is initially loaded with a vertical force to point I. Then, the foundation is horizontally loaded until the failure to the loading state II.

Owing to the elastic-perfectly plastic constitutive law featuring a non-associated flow rule, no vertical plastic displacement is generated. After entering the plastic domain, the horizontal displacement continues to increase while the horizontal force remains constant.

The second pseudo-static monotonic test under horizontal loading is depicted in Figure 11.28. Initially, the foundation is subjected to vertical loading, reaching 80 % of the ultimate vertical bearing capacity V_{max}. The load path from point I to point II exhibits an elastic loading path. Then, the foundation experiences horizontal loading. During the loading, the plasticity appears at point II and continues to point III. The corresponding loading path is presented in Figure 11.28 (a). The loading path from points II to point III

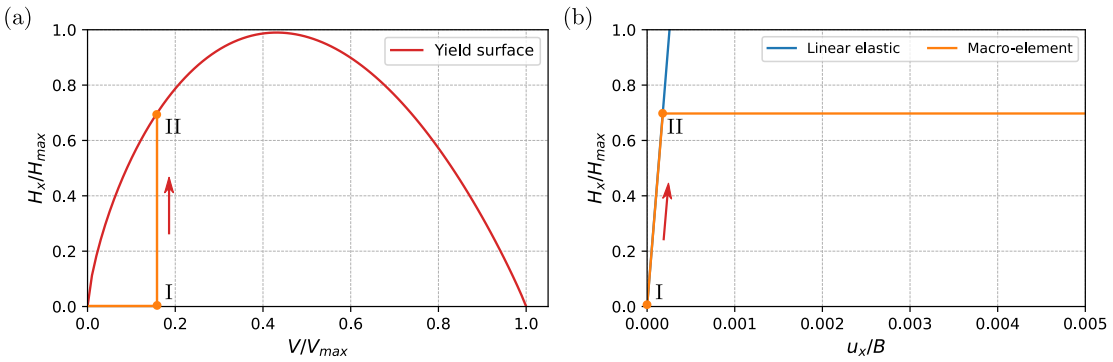

Fig. 11.27. Behaviour of the macro-element under a small constant vertical force and a constant vertical force: (a) load path and (b) relation between horizontal displacement and horizontal force

consistently aligns with the yield surface, generating plastic settlement along the loading path from point II to point III.

The relationship between the horizontal force and the horizontal displacement at the foundation is depicted in Figure 11.28 (b). From point II to point III, horizontal displacement persists under a lightly increasing horizontal force. Figure 11.28 (c) illustrates the relation between the horizontal force and vertical displacement. From point I to point II, the macro-element exhibits elastic behaviour, with no plastic deformation generated. From point II to point III, the macro-element enters a plastic state. As the plastic horizontal displacement increases, the plastic settlement is generated, as depicted in Figure 11.28 (d).

The response of the macro-element under cyclic horizontal loading is examined in Figure 11.29. The foundation is initially loaded with a vertical force to point I, followed by the application of horizontal force to attain point II. Then, the system undergoes unloading, reloading in the opposite direction to reach point III, and then reloading in the initial direction to achieve point IV, as depicted in Figure 11.29 (a).

The relation between the horizontal force and the horizontal displacement is illustrated in Figure 11.29 (b). The unloading-reloading paths II-III and III-IV exhibit the same slope as the loading path I-II. There is a clear relation between the horizontal force and the horizontal displacement during a cyclic loading and unloading process, commonly referred to as the hysteresis curve. The area enclosed by the hysteresis loop serves as a measure of the energy dissipated within the macro-element during the loading-unloading cycle.

Behaviour under moment loading

In the tests evaluating the behaviour of the macro-element under moment, the non-linear elastic response is initially examined without employing any plasticity criteria.

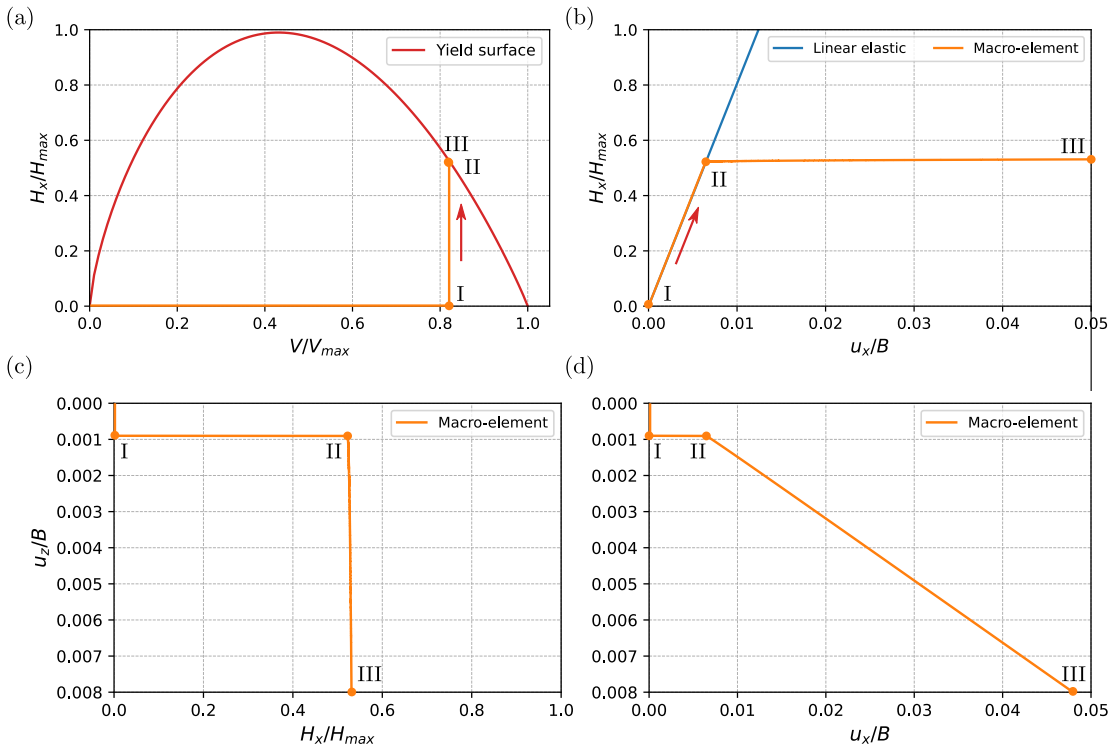

Fig. 11.28. Behaviour of the macro-element under a strong constant vertical force and a constant vertical force: (a) load path, (b) relation between horizontal displacement and horizontal force, (c) relation between horizontal force and settlement, and (d) relation between horizontal displacement and vertical displacement

The relations between the moment at the foundation and the rotation of the foundation under monotonic moment loading are presented in Figure 11.30. In this test, the foundation is subjected to a constant vertical load. Then a moment is incrementally applied at the foundation, starting from 0 and progressing through point I to reach point II.

The moment and rotation are normalised by M_u and θ_0, defined in Equations 11.10 and 11.11, respectively. Under monotonic moment loading, the uplift initiates at a rotation $\theta_y = \theta_0$ with the corresponding moment $M = M_u/3$. Before $M = M_u/3$, the load path $M-\theta$ follows the linear elastic behaviour until the point I. As the foundation experiences uplift, the $M-\theta$ load path deviates from the linear elastic trajectory, as depicted in Figure 11.30 (a). The stiffness-moment relation, depicted in Figure 11.30 (b), follows the theoretical rotational stiffness degradation curve.

Under cyclic moment loading, the foundation is loaded by a moment, followed by unloading reloading with a moment in the opposite direction, and finally unloading to zero, as depicted in Figure 11.31 (a). The load and unload paths align along the same curve, indicating no energy dissipation during this loading-unloading-reloading process.

The stiffness-moment relation, as depicted in Figure 11.31 (b), conforms to the prescribed stiffness-moment curve.

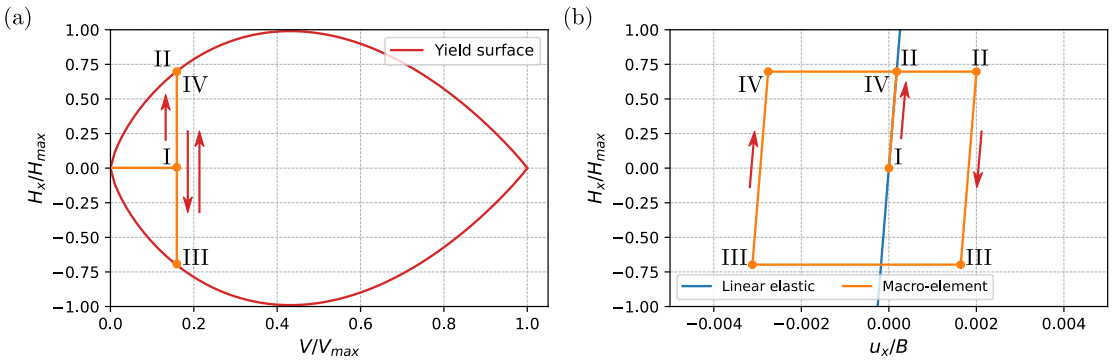

Fig. 11.29. Behaviour of macro-element under cyclic horizontal loading: (a) load path and (b) relation between horizontal displacement and horizontal force

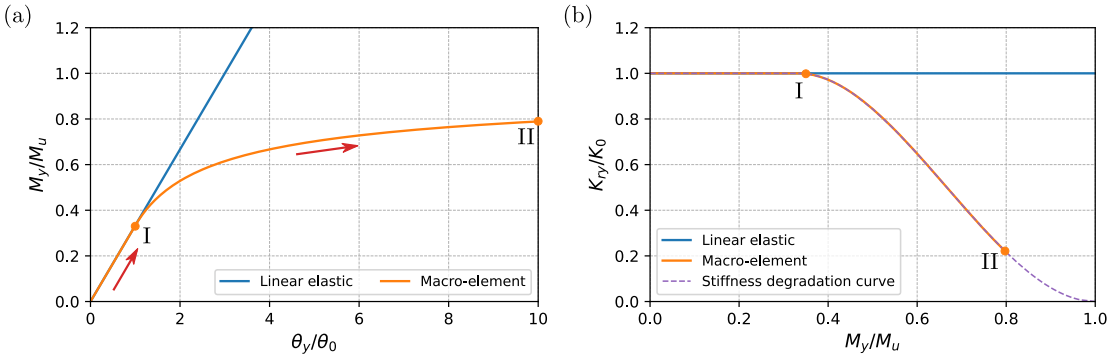

Fig. 11.30. Behaviour of macro-element under monotonic moment loading: (a) relation of rotation of the foundation and the moment and (b) rotational stiffness degradation curve

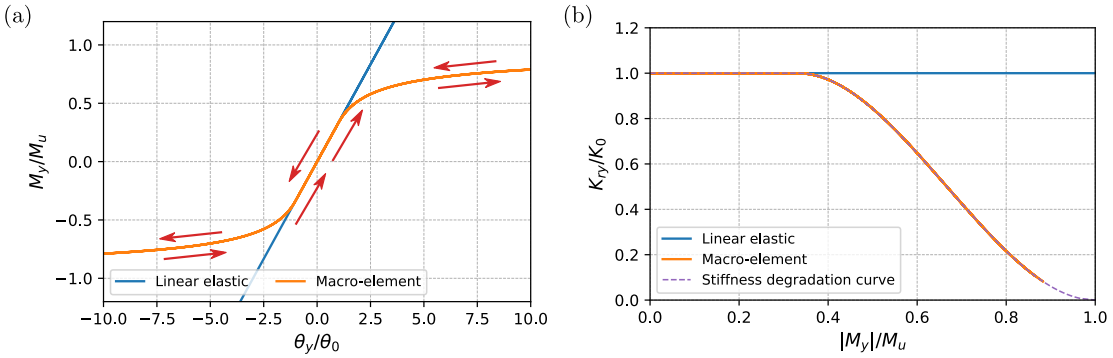

Fig. 11.31. Behaviour of macro-element under cyclic moment loading: (a) relation of rotation of the foundation and the moment and (b) rotational stiffness degradation curve

Another monotonic test is conducted to assess the combination of the uplift model and the plasticity model. The foundation is subjected to vertical loading, followed by the application of monotonic moment loading on the foundation starting from 0, passing through point I to reach point II. The load process is detailed in Figure 11.32 (a).

It is observed that the behaviour remains linear until reaching point I. Subsequently, from point I to point II, the macro-element behaviour remains within the elastic domain but exhibits non-linear elastic characteristics. Ultimately, the load state reaches point II, positioned on the yield surface, signifying the entry of the macro-element into the plastic domain.

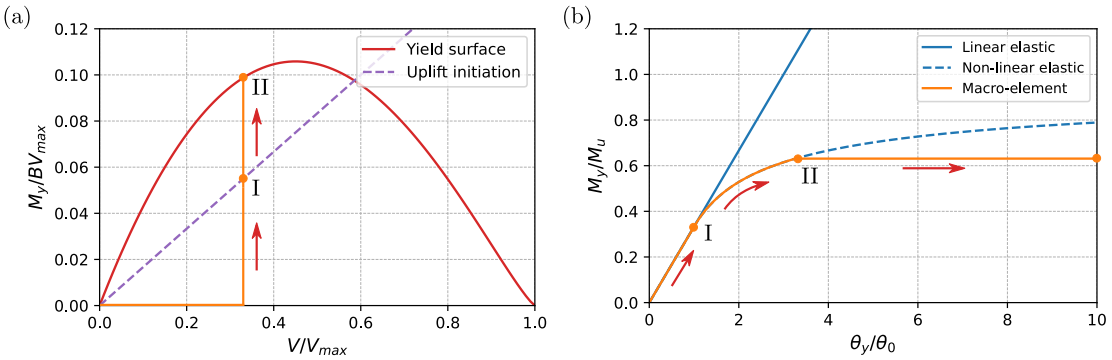

Fig. 11.32. Behaviour of macro-element under monotonic moment loading: (a) load path and (b) relation of rotation of the foundation and the moment

The relation between the rotation and the moment of the macro-element is illustrated in Figure 11.32 (b). From 0 to point I, the relation between moment and rotation is linear. From point I to point II, the load path of the macro-element deviates, following a non-linear elastic model, indicating the initiation of uplift at point I. After reaching point II, the moment remains constant while the rotation increases, which means the occurrence of the plastic behaviour.

11.4.4 Consistency checks: cross-comparison under seismic condition

Another set of consistency checks is conducted to validate the correct implementation of the resolution algorithms in the program under seismic conditions. The comparison is made against results obtained from the VBA program, which is based on the same numerical resolution algorithms. The organisation of the consistency checks is presented in Figure 11.33.

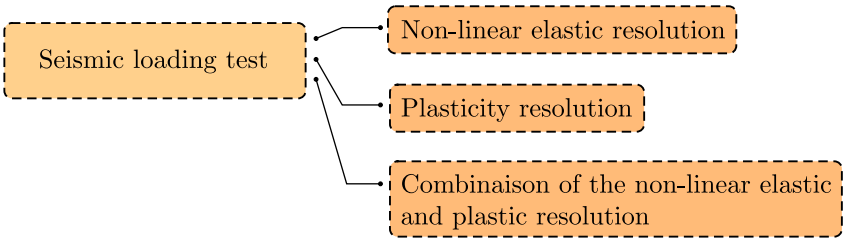

Fig. 11.33. Consistency check: cross-comparison under seismic condition

The cross-comparison under seismic conditions validates the consistency between the macro-element and the equivalent VBA program. Further details of various cross-comparison tests can be found in Section F.6.

11.5 Summary

This chapter introduces a novel SSI macro-element formulation for rigid inclusion-reinforced foundations. The proposed macro-element accounts for both the non-linear elastic and plastic behaviour of the foundation on reinforced soil.

The chapter begins by examining various reinforced foundation geometries suitable for investigation using macro-elements. The developed macro-element can address 2D problems, such as strip foundations or cases with single horizontal direction excitation, as well as 3D problems, including rectangular and circular foundations subjected to excitation in two horizontal directions. The global variables associated with foundations of different shapes are presented.

Secondly, the chapter provides a detailed analytical formulation of the macro-element. The elastic behaviour within the macro-element is described, incorporating the dynamic impedance functions. The uplift mechanism of foundations is discussed, emphasising its non-linear elastic nature. Both decoupled and coupled modelling strategies to simulate the uplift behaviour are explained. Furthermore, the analytical description of potential plastic behaviours is also introduced, including the loss of bearing capacity and sliding mechanisms. The formulations for both 2D and 3D formulations of these non-linear behaviours are presented.

The following section of the chapter focuses on the numerical implementation of the macro-element, including the rheological structures of the macro-element under both static and dynamic loading conditions. Two distinct dynamic macro-element configurations are then introduced, each featuring a different dash-pot position.

The chapter proceeds to outline the resolution of the plasticity model in the framework of the classical plasticity model using the Return Mapping Newton-Raphson method. An iterative algorithm is introduced in this study to solve the non-linear elastic problem.

To employ the macro-element for studying the behaviour of both the foundation and the supported superstructure under dynamic excitation, the dynamic equations of the system are outlined. This is demonstrated using an example of a three-storey structure. In this study, an explicit dynamic numerical integration, the Newmark-beta method, is adopted, with an unconditionally stable scheme to ensure accurate and stable results.

Numerical validation is systematically conducted to validate the macro-element program, encompassing four distinct families of validation steps.

In summary, the chapter offers an overview of the combination of non-linear problem resolution and the dynamic integration scheme, as illustrated in Section E.3.

12 Macro-element for a rigid inclusion-reinforced foundation: Practical applications

12.1 Description of applications

In this chapter, two parametric studies are conducted under seismic conditions to illustrate the practical applications of the macro-element for rigid inclusion-reinforced foundations. They are described as follows.

In the first application, the superstructure is simplified to a simple lumped mass model connected to the foundation by an Euler-Bernoulli beam. Various superstructures are tested, including different horizontal periods, varying slendernesses, different safety factors, and different soft soil shear velocities. A real earthquake record is chosen and amplified to two peak acceleration levels. Three types of boundary conditions at the base of the structure are considered and compared. The results are presented with respect to the common dynamic SSI factors.

In the second application, a study of the seismic response of a real structure is conducted. Similarly to the first application, three different boundary conditions at the base of the structure are considered. A set of real earthquake records is employed in the analysis to carry out a parametric study. Various quantities are drawn from this study to estimate the behaviour of the structure under seismic loading. The results are then analysed and the contributions of the macroelement approach are discussed.

12.2 Application to a simple lumped mass model

12.2.1 Studied configurations

Structural model

The superstructure, modelled as a simple oscillator with a discrete mass, is connected to the foundation by an Euler-Bernoulli beam characterised by EI, EA, and beam length

h_{eq}. The foundation is a 10 m $\times$ 10 m square foundation reinforced by rigid inclusions arranged in a 5 $\times$ 5 pattern with a spacing of 2 m.

The horizontal period of the superstructure, denoted as T_{str} or T_{FB}, is set to 0.5 s or 0.25 s, corresponding to the fixed-base structural frequency f_{FB} of 2 Hz or 4 Hz, respectively. The damping ratio of the structure is set at 5 %. The vertical frequency $f_{FB,V}$ of the superstructure is set at 6 Hz or 10 Hz, respectively. With the given foundation width, a series of slenderness ratios h_{eq}/B is set as 0.1, 0.3, 0.5, 0.75, 1, 1.25, and 1.5. It is assumed that h_{eq} is half of the total height of the superstructure.

The soil profile consists of a soft soil layer, where reinforcement by rigid inclusions is necessary, a hard soil layer, and a substratum. The rigid inclusions extend across the soft soil layer and are embedded in the hard soil layer with a depth of 0.5 m. The shear velocity V_s of the soft soil varies between 100 m/s, 150 m/s and 200 m/s. A gravel LTP with a thickness of 0.5 m is positioned between the foundation base and the heads of the rigid inclusions. The concrete rigid inclusions have a diameter of 0.42 m and a length of 10 m. Additional details about the foundation configurations and the soil profile can be found in Section 5.3.1 and Table 5.1.

The bearing capacity of this foundation denoted as V_{max} and the maximum horizontal force H_{max}, can be estimated by applying the analytical approach presented in Part III. The mass of the superstructure can be evaluated using Equation 12.1 with a safety factor F, varying between 6, 3, 1.5 and 1.2. The density of the structure, ρ_{str}, can be determined by the mass of the superstructure and the volume of the superstructure.

$$m = \frac{V_{max}}{F\ g} \tag{12.1}$$

With the given vertical and horizontal frequencies f_v and f_h and the mass m, the EA and EI can be evaluated using Equations 12.2 and 12.3.

$$EA = (2\pi f_{FB,V})^2 m h_{eq} \tag{12.2}$$

$$EI = \frac{1}{3}(2\pi f_{FB})^2 m h_{eq}^3 \tag{12.3}$$

Three types of boundary conditions at the base of the structure are considered, as depicted in Figure 12.1. The first corresponds to the fixed-base model (FB), where all the degrees of freedom at the base of the structure are directly fixed. In the second, a conventional linear SSI approach is employed, introducing the stiffness of the foundation-soil system in the model using an elastic stiffness matrix and damping matrix, calibrated with dynamic impedance functions. Finally, the non-linear elastic model is studied, incorporating the non-linear SSI macro-element.

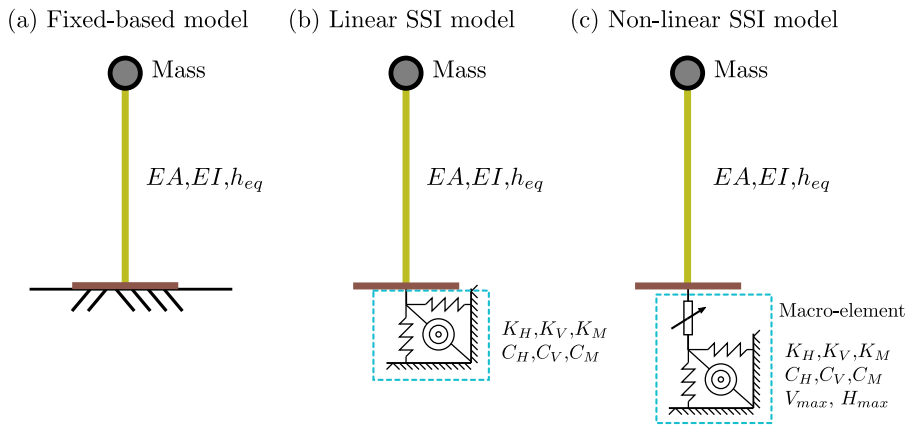

Fig. 12.1. Model accounting for different SSI condition: (a) fixed-base model, (b) linear elastic SSI model, and (c) non-linear elastic SSI model

Foundation impedance functions

The rigid inclusion reinforced foundation with the soil profile featuring three different shear wave propagation velocities has already been studied, corresponding to the cases A01, B01 and B02 in Table 5.2. The impedance functions for such foundations on rigid inclusions have been previously calculated and presented in Figures 5.8, C.1 and C.2. The dynamic stiffness and the damping ratio for these three foundation configurations are presented in Figure 12.2.

SSI calibration is required for the different superstructures, following the process outlined in Section 11.3.4. The corresponding stiffness and damping for different degrees of freedom are presented in Appendix G. The calibrated parameters for the macro-element are detailed in Table 12.1.

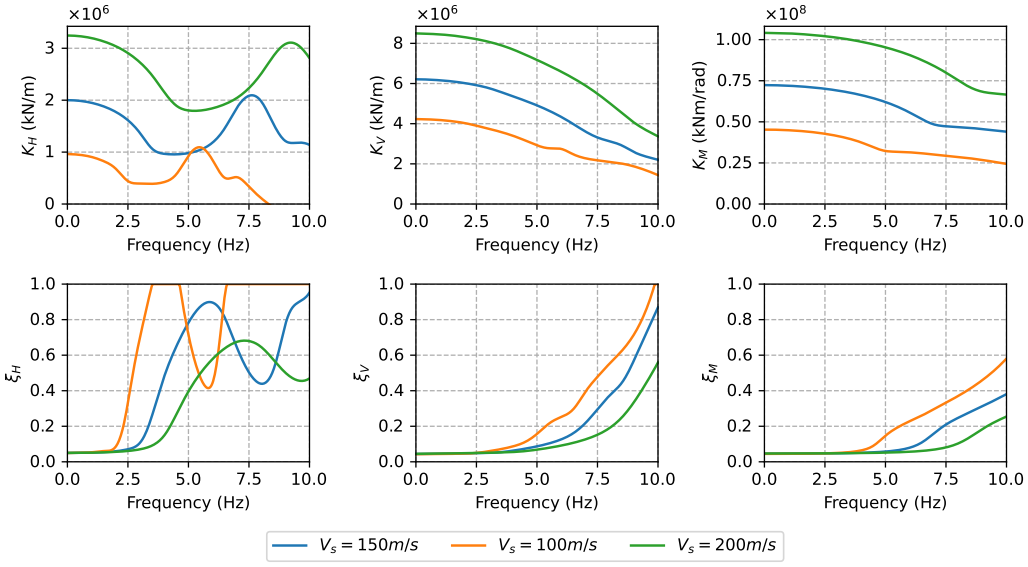

Fig. 12.2. Dynamic impedance functions for different directions at the centre of the foundation reinforced by rigid inclusions

Tab. 12.1. Calibrated parameters for the macro-element

Parameter	Value	Description
K_x K_z K_{ry}	See in Appendix G	Elastic stiffness
C_x C_z C_{ry}	See in Appendix G	Damping
V_{max}	2.35 $\times 10^4$ kN	Bearing capacity
H_{max}	5 $\times 10^3$ kN	Maximum horizontal force

Ground motion

A real seismic load is employed to investigate the response of the structure through an acceleration time history. An acceleration time history recorded during the Friuli earthquake (Italy, 1976) is depicted in Figure 12.3. The duration of the acceleration time history is approximately 22.5 seconds, and its maximum recorded acceleration is 2.5 m/s^2, equivalent to 0.25 g. The same acceleration time history scaled to 0.5 g is also used in the calculation.

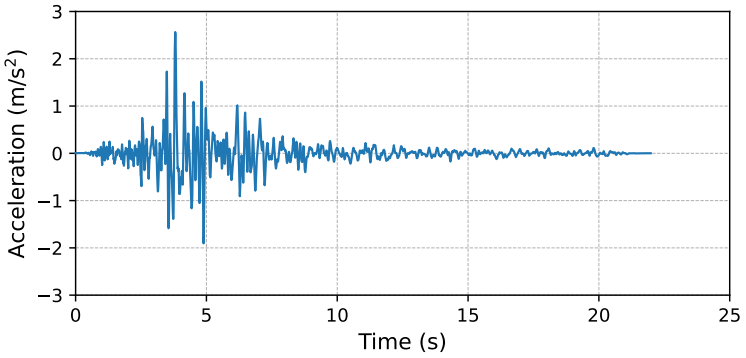

Fig. 12.3. Acceleration time history recorded during the Friuli earthquake (Italy, 1976)

12.2.2 Results: SSI impact on the dynamic responses

Dimensionless SSI parameter

The response of the SSI system primarily depends on the dimensions of the structure and the dynamic properties of both the structure and the soil. This dependence can be effectively described by the following non-dimensional parameters (Veletsos and Meek,

1974; Ghannad, 1998; Nakhaei and Ali Ghannad, 2008). Three dimensionless SSI parameters are selected in this study. They are described as follows:

- The slenderness ratio for the building: H_{eq}/B;
- The structure-soil stiffness ratio $H_{eq}/V_s T_{str}$;
- The structure-soil mass ratio: ρ_{str}/ρ_{soil}.

A structure with a high slenderness ratio has a high aspect ratio, meaning that the height of the building is significantly greater in proportion to its width. The structure-soil stiffness ratio can be defined as the relative stiffness between the structure and the soil. A stiffer structure with softer soil can result in a greater structure stiffness ratio. The structure-soil mass ratio is used to evaluate the mass density contrast between the structure and the soil. A heavy structure can have a high structure-soil mass ratio.

Period elongation

Period elongation due to SSI refers to the phenomenon where the natural period of a building or structure is lengthened. The period taking into account the SSI effect is denoted as T_{SSI}. Period elongation is studied using a period elongation ratio, which is defined as the ratio of the SSI period to the period of the fixed-base structure, denoted as T_{FB}.

The results are plotted with respect to the three previously mentioned dimensionless parameters, as depicted in Figure 12.4. Each circle represents the result from a time history analysis conducted for a case with the prescribed parameters. The line represents the evolution of the trendline of the results, and the plus or minus one-time standard deviation σ range is also indicated.

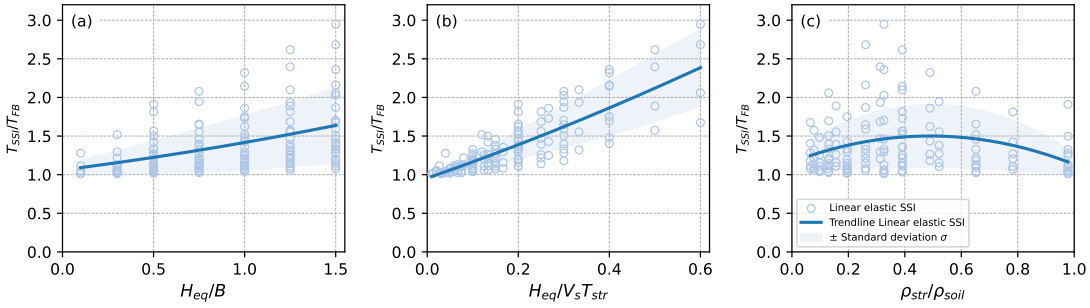

Fig. 12.4. Period elongation due to SSI effects with respect to (a) slenderness ratio, (b) structure-soil stiffness ratio, and (c) structure-soil mass ratio

The models considering the stiffness of the soil-foundation system consistently exhibit a greater period. A maximum period elongation ratio of 3 is observed, specifically for the

case with a safety factor of 1.2, h_{eq}/B of 1.5, the shear wave propagation velocity of 100 m/s, and fundamental fixed-base frequency as 4 Hz.

From Figure 12.4 (a), the trend is clear that the period elongation effect increases with the slenderness ratio. The period is lengthened for a more slender structure. For a structure with a small slenderness, the period elongation effect is less significant. The period elongation ratio also increases with the structure-soil stiffness ratio H_{eq}/V_sT_{str}, as depicted in Figure 12.4 (b). The period elongation due to the SSI effect is greater for a taller and stiffer structure founded on softer soil. However, the trendline for the period elongation increases and decreases with the structure-soil mass ratio, as depicted in Figure 12.4 (c). For the structure with a structure-soil mass ratio of around 0.3, a significant period elongation effect can reach 3.

SSI damping

Taking into account the SSI effect can also increase the damping of the system. In the linear domain, the equivalent damping ξ_{SSI} is calculated using a simplified process (Brûlé and Cuira, 2018). The equivalent dampings ξ_{SSI} are plotted as a function of the three previously mentioned dimensionless parameters, as depicted in Figure 12.5.

It is observed that the equivalent damping in all the studied cases exceeds the damping of the fixed-base structure. A maximum SSI damping ratio of up to 50 % can be attained. The SSI damping increases with the structure slenderness and the structure-soil stiffness ratio. The trend of the SSI damping is not monotonic concerning the structure-mass ratio. Similar to the observation in the period elongation, a greater SSI damping can be obtained with a structure-soil mass ratio of around 0.3.

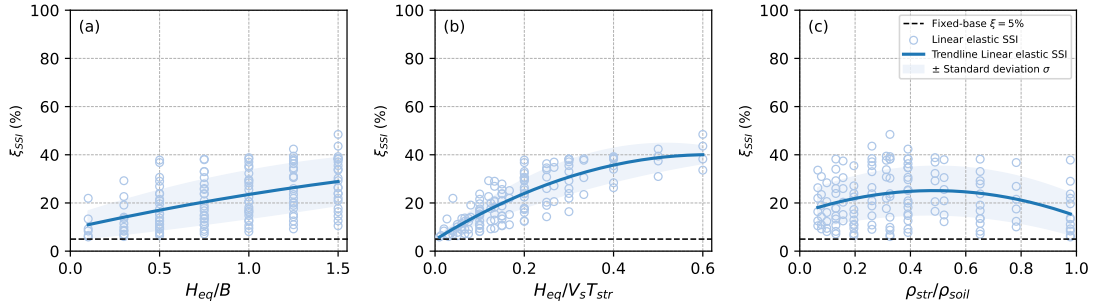

Fig. 12.5. Damping ratio of the soil-structure system with respect to (a) slenderness ratio, (b) structure-soil stiffness ratio, and (c) structure-soil mass ratio

Shear force and moment at the foundation

The shear force at the foundation is also calculated under the three boundary conditions, considering two levels of acceleration time history: 0.25 g and 0.5 g. The maximum shear

force for the configuration accounting for the SSI effect is normalised by the maximum shear force of a fixed-base model, presenting the results in the form of a shear force ratio H_{SSI}/H_{FB}. With the linear elastic SSI boundary condition, the shear force ratio H_{SSI}/H_{FB} remains unaffected by the different acceleration amplitudes. Additionally, the results for the shear force at the foundation for the linear elastic SSI boundary condition are depicted in Figure 12.6.

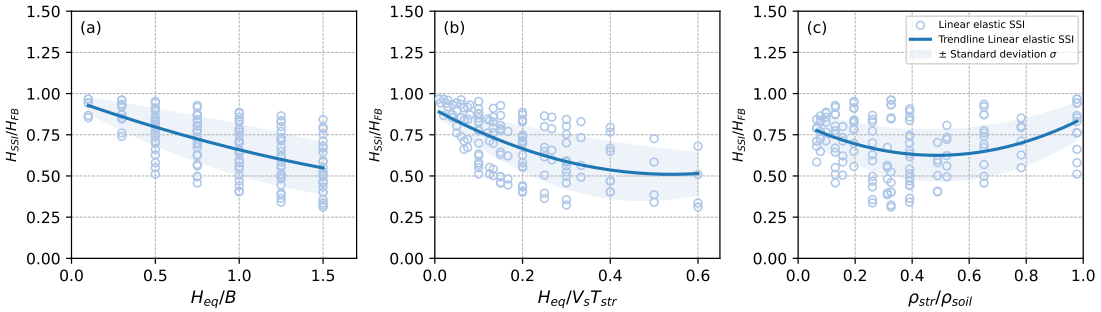

Fig. 12.6. Shear force ratio at the foundation for Linear elastic SSI boundary condition with respect to (a) slenderness ratio, (b) structure-soil stiffness ratio, and (c) structure-soil mass ratio

To facilitate comparison, only the trendlines for different configurations are presented in Figure 12.7 as other following figures. The figure reveals that the shear force ratio is consistently less than unity, indicating that considering the SSI effects generally has a favourable impact, leading to a reduction in the shear force at the foundation. When only the linear SSI effect is considered, the shear force reduction varies from 20 % to 50 % compared with a fixed-based model. However, with the consideration of the non-linear SSI effect, the shear force reduction can reach up to If the non-linear SSI effect is considered, the shear force reduction can reach up to 65 % under 0.25 g earthquake excitation and 80 % under 0.5 g earthquake excitation.

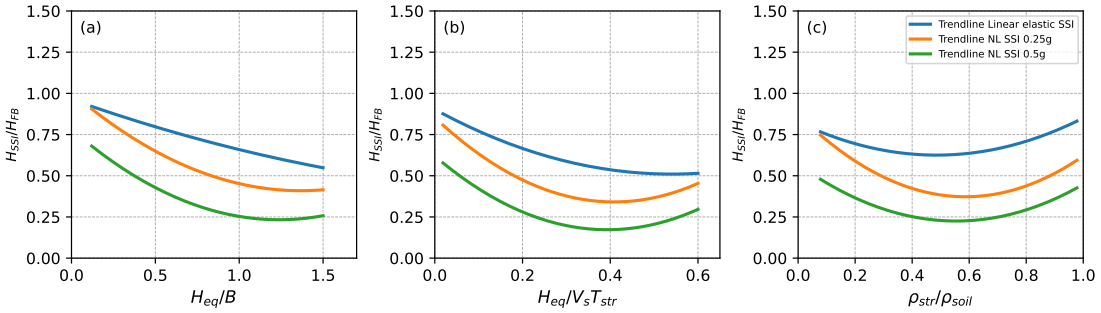

Fig. 12.7. Trendlines of shear force ratio at the foundation with respect to (a) slenderness ratio, (b) structure-soil stiffness ratio, and (c) structure-soil mass ratio

Observing Figure 12.7 (a) and (b), it can be found that the linear SSI effect is more significant, resulting in a more pronounced reduction in shear force for stiffer and more slender structures on softer soil. However, the relationship between the shear force

reduction due to the non-linear SSI effect and the SSI parameters is not monotonic. The trendlines with respect to the structure-soil mass ratio are not monotonic, suggesting the existence of an optimal structure-soil mass ratio that maximises the benefits of the non-linear SSI effect.

It can also be observed in Figure 12.7 that the non-linear SSI effect leads to a more significant reduction in shear force at the foundation compared to the linear SSI effect, albeit with the occurrence of irreversible displacement. Furthermore, the shear force reduction is more pronounced in the cases with the acceleration scaled to 0.5 g than in the cases with the acceleration scaled to 0.25 g. This implies that systems subjected to strong earthquakes derive greater benefits from the non-linear SSI effect.

The moment applied at the foundation during the earthquake excitation is also captured. The trendlines for the maximum moment ratio with and without SSI effect, denoted as M_{SSI}/M_{FB}, are presented in Figure 12.8. The same observation for the maximum shear force ratio remains valid for the maximum moment ratio.

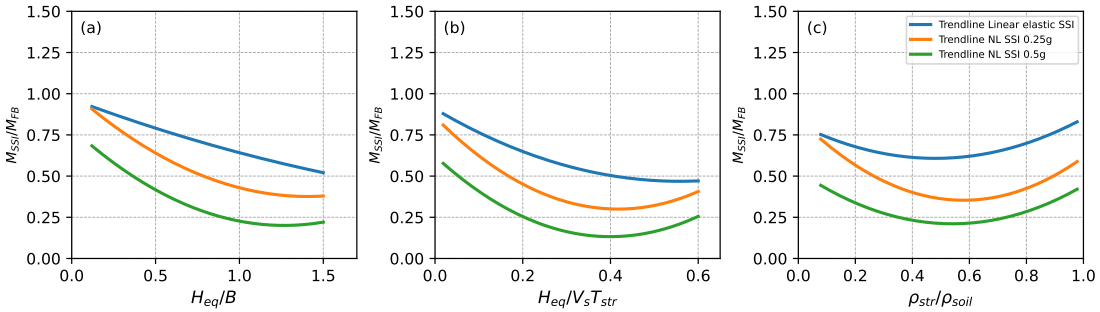

Fig. 12.8. Trendlines of moment ratio at the foundation with respect to (a) slenderness ratio, (b) structure-soil stiffness ratio, and (c) structure-soil mass ratio

Residual displacement of the foundation

In the linear domain, no irreversible displacement is generated. However, considering the non-linearities of the foundation can result in irreversible displacements. The trendlines of the residual horizontal displacement of the foundation are depicted in Figure 12.9.

The magnitude of the residual horizontal displacement is found to be smaller than 0.1 % B for the 0.5 g excitation and 0.03 % B for the 0.25 g excitation. The residual horizontal displacement increases and then decreases with the slenderness ratio and the structure-soil stiffness ratio, as depicted in Figure 12.9 (a) and (b), which corresponds the shear force reduction decreases and then increases.

The residual settlements are generated for certain cases. In this parametric study, only the configurations with safety factor $F = 1.2$ and 1.5 can generate the residual settlement.

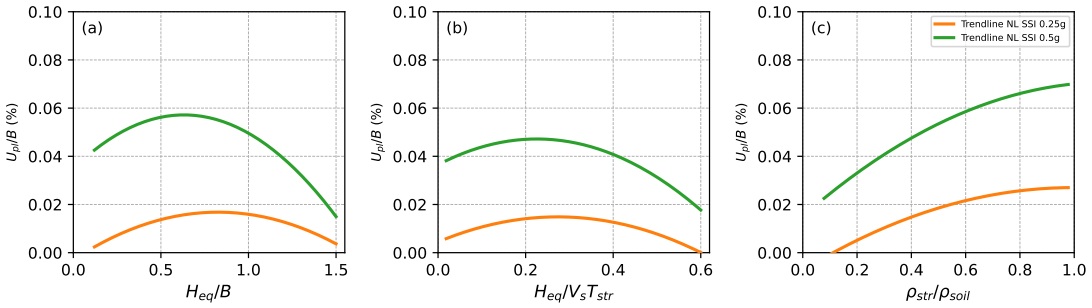

Fig. 12.9. Trendlines of residual horizontal displacement of the foundation with respect to (a) slenderness ratio, (b) structure-soil stiffness ratio, and (c) structure-soil mass ratio

There is no general monotonic trend for the residual rotation at the foundation with respect to the dimensionless SSI parameters, as depicted in Figure 12.10.

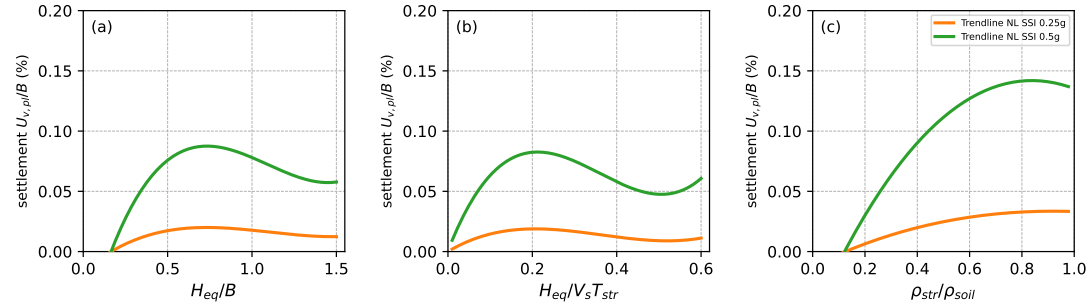

Fig. 12.10. Trendlines of residual settlement of the foundation with respect to (a) slenderness ratio, (b) structure-soil stiffness ratio, and (c) structure-soil mass ratio

The residual rotation of the foundation can result in a differential settlement. However, no general monotonic trend is observed for the residual rotation at the foundation with the dimensionless SSI parameters, as depicted in Figure 12.11. It is worth noting that the maximum residual rotation captured by the trendline does not exceed 0.1 % rad under 0.5 g earthquake excitation, which is very small.

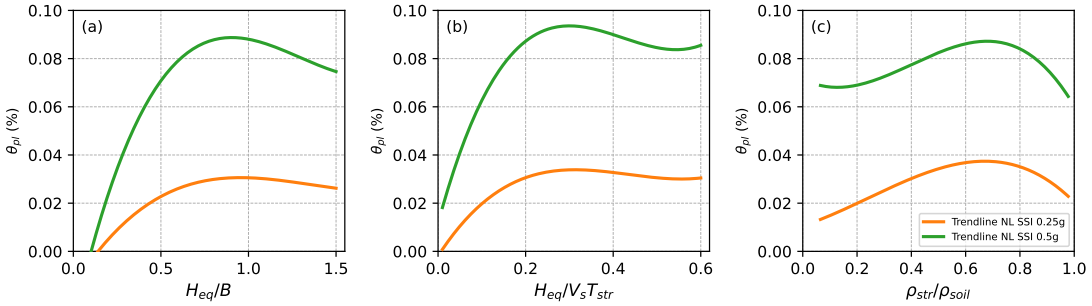

Fig. 12.11. Trendlines of residual rotation of the foundation with respect to (a) slenderness ratio, (b) structure-soil stiffness ratio, and (c) structure-soil mass ratio

12.3 Application to a 22-storey building

12.3.1 A 22-storey building

The second application focuses on a 22-storey high building inspired by Nice Prefecture, constructed in 1979 in France, as investigated in the work of Lorenzo *et al.* (2018). The prototype building, Nice Prefecture, is depicted in Figure 12.12.

The structure consists of two symmetric parts, each representing a reinforced concrete tower. These two sections are divided by a 10-centimetre joint designed to ensure the independence of dynamic responses of both sides during strong motions.

Each part comprises a reinforced concrete core wall, supporting reinforced concrete shells fixed to the core wall on each floor. The foundation of the building is reinforced by rigid inclusions.

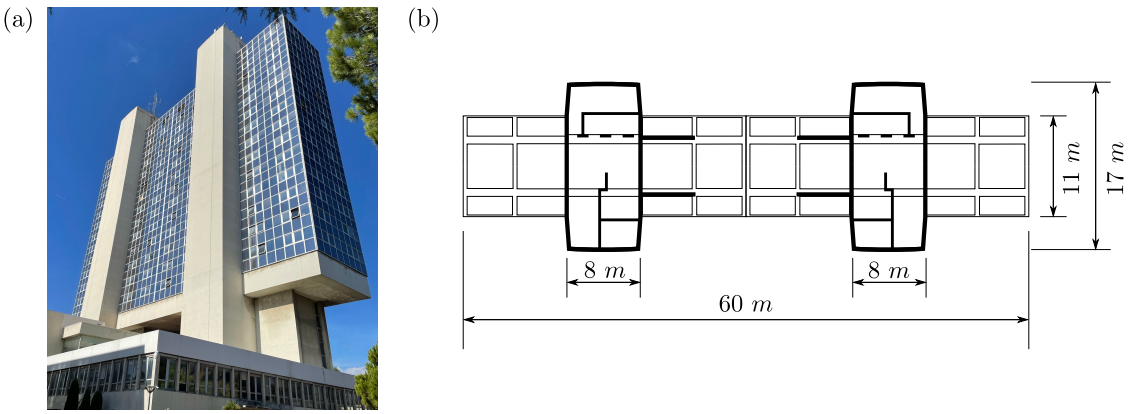

Fig. 12.12. Nice Prefecture: (a) perspective view of the building and (b) horizontal section of building structure

Structural model

The analysis conducted in this numerical application focuses on the lateral response of the building. Instead of modelling the whole structure in detail, which is numerically expensive, a simplified model of the building is used in this study. Lorenzo (2016) has identified the mechanical parameters for an equivalent homogeneous Timoshenko beam (Timoshenko, 1921). The identified geometrical and mechanical parameters are detailed in Table 12.2.

Tab. 12.2. Geometrical and mechanical parameters for the equivalent Timoshenko beam model

H (m)	b (m)	h (m)	ρ (kg/m^3)	E (GPa)	ν
66	35	38	830	1	0.48

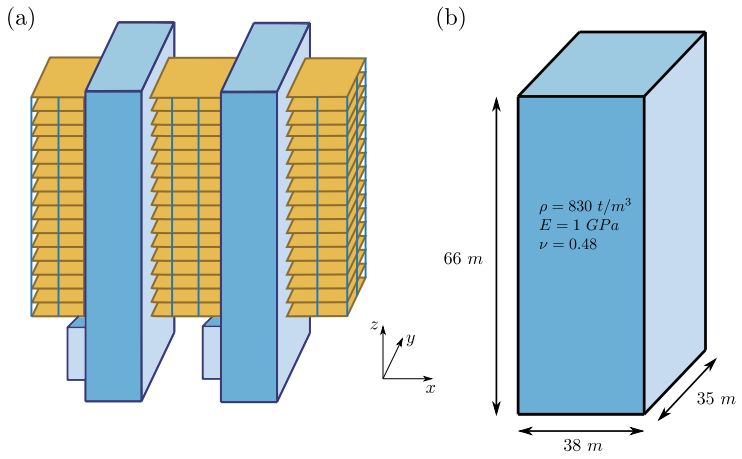

Fig. 12.13. Studied building modelling: (a) building model scheme and (b) equivalent Timoshenko beam model

The section dimensions of the equivalent homogeneous model (38 m $\times$ 35 m) significantly differ from those of the actual building (60 m $\times$ 17 m), due to a non-uniform distribution of stiffness in both horizontal directions (Lorenzo, 2016).

The modal analysis of the fixed-base simplified Timoshenko beam model is conducted. The fundamental frequencies are presented in Table 12.3.

Tab. 12.3. Natural frequencies of the building

Mode	Direction	Frequency (Hz)
1	Y	1.216
2	X	1.288
3	Z	4.162

Lorenzo (2016) has identified the nature frequency of the building by ambient vibration records. The first two nature frequencies for the X and Y directions are 1.216 Hz and 1.228 Hz, respectively. The differences between the identified frequencies and the frequencies calculated from the simplified Timoshenko beam model are less than 5 %.

Even though energy dissipation is a crucial aspect of any dynamic analysis, it is still a mishandled phenomenon. In the present study, a 5 % damping ratio is considered for the overall structure, implemented in the dynamic resolution through Raleigh damping theory (Pecker, 2023a). Similar to the investigation in Section 12.2, three types of boundary conditions at the base of the structure are considered.

Foundation

The building is supported by a 60 m × 17 m foundation reinforced by 32 × 9 concrete rigid inclusions of 0.6 m in diameter and 30 m in length[1], as depicted in Figure 12.14. The spacing of inclusions is 2 m. The rigid inclusions are embedded in a two-layered soil profile. The upper layer consists of a 30 m thick soft clay, and beneath it is a deep underlying dense sand layer. The first 0.5 m thick layer of the soft clay is replaced by a gravel LTP layer, serving as an LTP layer.

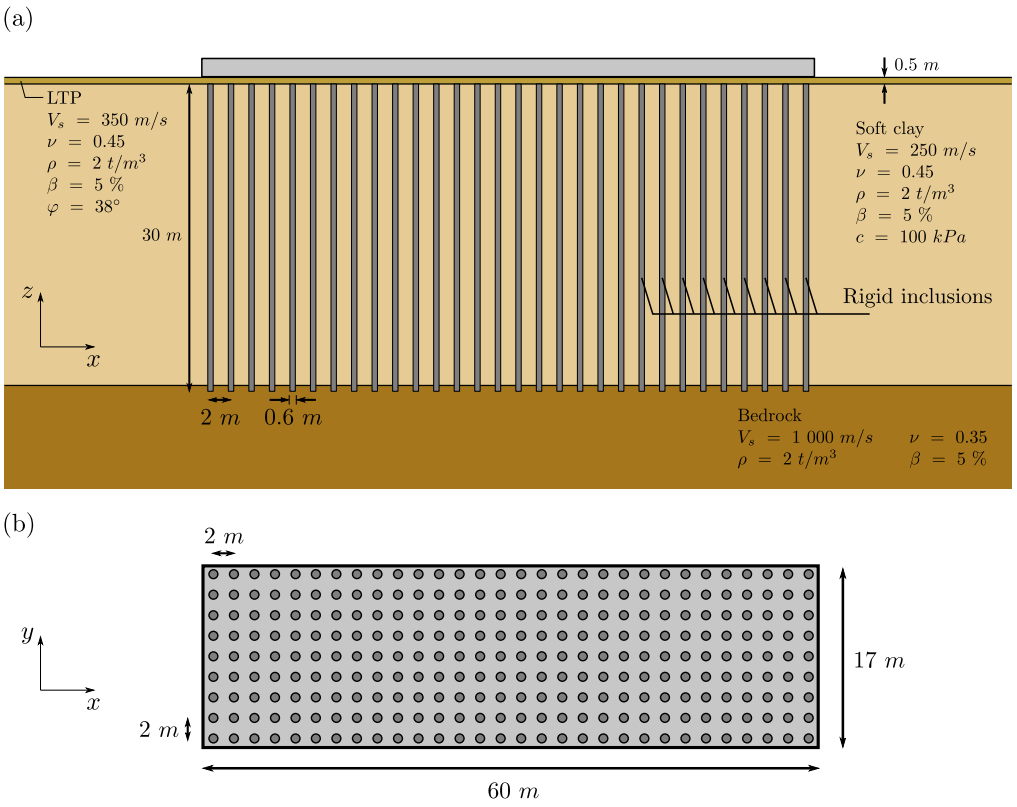

Fig. 12.14. General layout of foundation system: (a) cross-section view and (b) plan view of the foundation and the soil profile

The behaviour of LTP is modelled with an elastic-perfectly plastic constitutive law using Mohr-Coulomb criterion, with shear wave velocity V_s = 350 m/s, Poisson's ratio ν = 0.45, density ρ = 2 t/m^3, viscous damping β = 5 %, and a friction angle φ = 38 °. The behaviour of soft clay is modelled with an elastic-perfectly plastic constitutive law with a Tresca criterion, with shear wave velocity V_s = 250 m/s, Poisson's ratio ν = 0.45, density ρ = 2 t/m^3, viscous damping β = 5 %, and a cohesion c = 100 kPa. The dense sand layer is modelled as an elastic material with a shear wave velocity V_s = 1 000 m/s, Poisson's ratio ν = 0.35, density ρ = 2 t/m^3, and viscous damping β = 5 %. The rigid inclusions

[1]Due to the lack of relevant information, the configuration of the foundation and the geotechnical model are proposed by the author and may differ from the actual project.

are assumed to be elastic, characterised by Young's modulus of $E = 3 \times 10^4$ MPa, $\nu = 0.2$, and $\rho = 2.5$ t/m^3.

The dynamic impedance functions of the foundation are determined through the FEM-BIE modelling, employing the methodology described in Chapter 5. The results of dynamic impedance functions calculated for the reinforced foundation are illustrated in Figure 12.15.

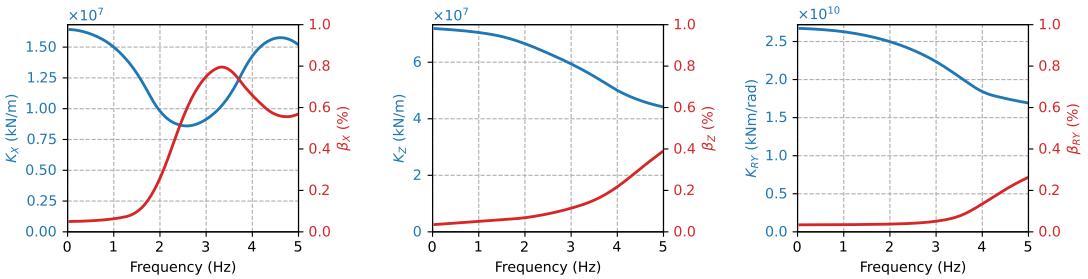

Fig. 12.15. Dynamic impedances at the centre of the reinforced foundation for the 22-storey building

Linear SSI is incorporated at the base of the Timoshenko beam model using elastic springs obtained from the dynamic impedance functions. An iterative calibration is conducted, and the natural frequencies considering the SSI are presented in Table 12.4.

Tab. 12.4. Natural frequencies of the building considering SSI

Mode	Direction	Frequency (Hz)
1	Y	1.013
2	X	1.051
3	Z	3.130

12.3.2 Calibration of macro-element parameters

In this study, a rigid inclusion-reinforced foundation is employed to simulate dynamic non-linear SSI effects at the base of the building. Before using the macro-element, it is imperative to calibrate its parameters.

The stiffness terms are already used in the nature frequency of building considering SSI. The damping terms are identified based on the corresponding SSI frequencies. The uplift behaviour and loss of bearing capacity (inner expression) are included in the non-linear SSI macro-element application. The non-linear parameters, V_{max} and H_{max}, used in the yield surface of loss of bearing capacity are also calculated through the analytical approach based on the kinematic exterior approach.

Tab. 12.5. Calibrated parameters for the macroelement for the rigid inclusion-reinforced foundation

Parameter	Value	Description
K_x	1.48×10^7 kN/m	
K_z	5.81×10^7 kN/m	Elastic stiffness
K_{ry}	2.62×10^10 kNm/rad	
C_x	1.48×10^5 kNs/m	
C_z	7.34×10^5 kNs/m	Damping
C_{ry}	2.75×10^8 kNms/rad	
V_{max}	1.78×10^6 kN	Bearing capacity
H_{max}	1.02×10^5 kN	Maximum horizontal force

12.3.3 Incremental dynamic analysis

Incremental dynamic analysis (IDA) serves as a powerful computational technique used in earthquake engineering, offering a means to evaluate the seismic performance of structures. This parametric analysis involves increasing the intensity of earthquake ground motions to evaluate how a structure responds under a range of seismic excitations (Vamvatsikos and Cornell, 2002, 2004).

The outcome of IDA is a set of IDA curves, depicting a chosen intensity measure (IM) with respect to a selected damage measure (DM) or engineering demand parameter (EDP). Each IDA curve within the set corresponds to the same structural model, providing a comprehensive view of the structure's response under varying seismic intensities.

Nowadays, the IDA is largely used in earthquake engineering, spanning various structures such as buildings and bridge piers. In the context of the dynamic SSI macro-element, this approach is utilised to examine the ductility demand imposed on the structure, as demonstrated in several studies (Pecker and Chatzigogos, 2010; Correia *et al.*, 2012; Pérez-Herreros, 2020).

In this section, a selection of earthquake records is presented and employed to conduct an IDA on a building supported by rigid inclusion-reinforced foundation macroelement. The IDA curve set obtained by this analysis is subsequently compared to those derived from the fixed-base configuration, as well as from the conventional linear SSI configuration employing only dynamic impedances.

Seismic loading

A set of 20 real earthquake records is employed in this study. They are selected for an interval of earthquake moment magnitudes, $M_W = 5$ to 7, with moderate distances R_{rup} smaller than 35 km, and for sites with $V_{s,30} \leq 200$ m/s. The non-scaled earthquake acceleration time histories are presented in Figure 12.16. General information and characteristics of the selected earthquake records are listed in Table 12.6.

As discussed in Section 1.2, the presence of the rigidity contrast between the foundation elements and the soil can affect the propagation of seismic waves and alter the incident seismic action. The numerical study in Chapter 4 confirms that the presence of inclusions has only limited potential to modify the seismic motion reaching the base of a structure. Therefore, the earthquake signals are directly applied at the base of the foundation without consideration of the ground motion modification due to the SSI kinematic effects.

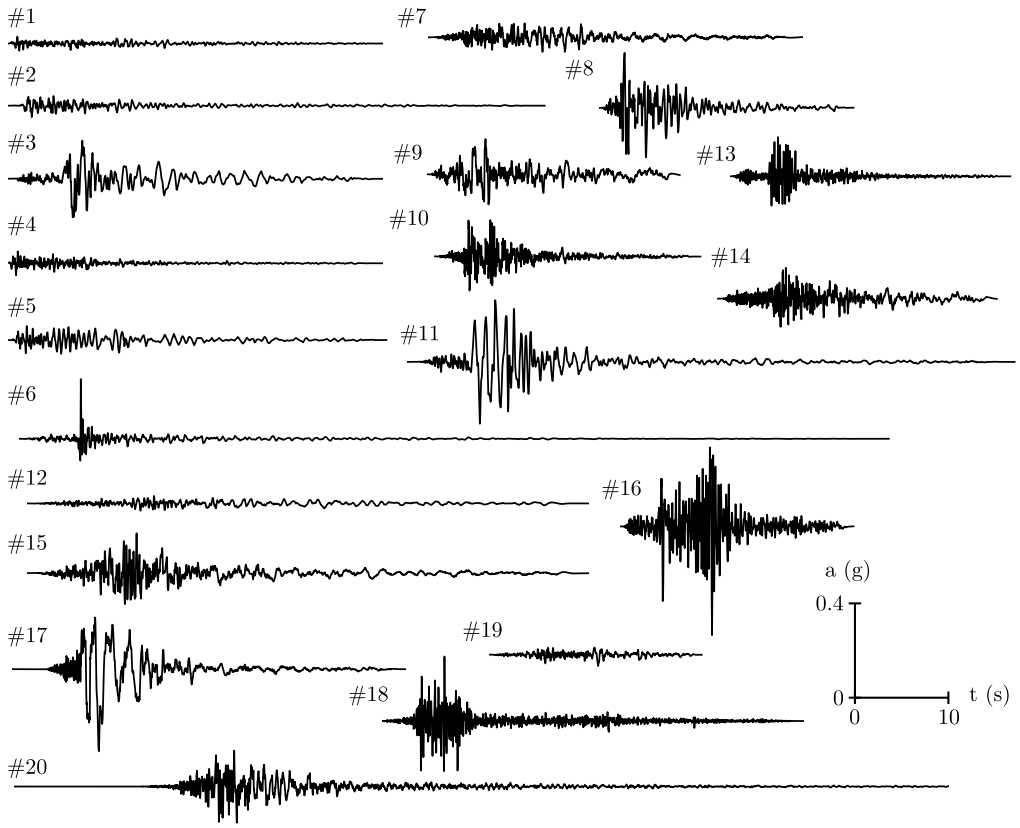

Fig. 12.16. Earthquake records used for IDA (data from the PEER Strong Motion Database (Ancheta *et al.*, 2013))

Intensity measure and damage measure

The term intensity measure (IM) is used to describe parameters that indicate the severity of the input motion while damage measures (DM) or engineering demand parameter (EDP) are used to describe parameters that characterise the response of the structure.

Different options are available for the intensity measure to be used in the IDA curves:

- The peak ground acceleration of the input motion (PGA);
- The peak ground velocity of the input motion (PGV);
- The cumulative absolute velocity (CAV);

Tab. 12.6. General information and characteristics of the earthquake records used for IDA (data from the PEER Strong Motion Database (Ancheta *et al.*, 2013))

#	Earthquake	Year	Station	ϕ^1	$V_{s,30}^2$ (m/s)	M_W^3	R_{rup}^4 (km)	PGA[5] (g)
1	Imperial Valley, USA	1951	El Centro Array #9	000	213	5.6	25.2	0.031
2	Central Calif, USA	1954	Hollister City	181	199	5.3	25.8	0.049
3	Northern Calif, USA	1954	Ferndale City Hall	044	219	6.5	27.0	0.163
4	Imperial Valley, USA	1955	El Centro Array #9	000	213	5.4	14.9	0.051
5	Hollister, USA	1961	Hollister City	181	199	5.6	19.6	0.059
6	Northern Calif, USA	1967	Ferndale City Hall	224	219	5.6	28.7	0.253
7	Friuli, Italy	1976	Codroipo	000	249	6.5	33.4	0.062
8	Coyote Lake, USA	1979	Gilroy Array	270	222	5.7	5.7	0.233
9	Victoria, Mexico	1980	Chihuahua	102	242	6.3	19.0	0.151
10	Westmorland, USA	1981	Brawley Airport	225	209	5.9	15.4	0.155
11	Coalinga, USA	1983	Parkfield - Fault Zone 14	000	246	6.4	29.5	0.262
12	Morgan Hill, USA	1984	Agnews State	240	240	6.2	24.5	0.032
13	Whittier Narrows, USA	1987	Carbon Canyon Dam	040	235	6.0	26.8	0.166
14	Superstition Hills, USA	1987	Wildlife Liquefaction Array	090	179	6.2	17.6	0.131
15	Loma Prieta, USA	1989	Agnews State	000	240	6.9	24.6	0.170
16	Northridge, USA	1994	Pacific Palisades	190	191	6.7	24.1	0.461
17	Kobe, Japan	1995	Port Island	000	198	6.9	3.3	0.348
18	Northwest, China	1997	Jiashi	000	240	5.9	24.1	0.274
19	Whittier Narrows, USA	1987	Carson - Water St	180	161	5.3	29.1	0.048
20	Tottori, Japan	2000	SMN002	002	139	6.6	16.6	0.154

[1]: Component.
[2]: Average shear wave velocity in the upper 30 m of the soil profile.
[3]: Moment magnitude.
[4]: Closest distance to fault rupture.
[5]: Peak ground acceleration.

- The spectral acceleration at the first-mode SSI period ($S_a(f_{SSI}, \xi = 5\%)$).

In this application, the peak ground acceleration of the input motion (PGA) is selected as the intensity measure of interest. For each record, a range of 10 PGA values, spanning from 0.1g to 1g, is considered.

The damage measure is a non-negative scalar value, corresponding to an observable quantity derived from the results of the corresponding non-linear dynamic analysis. In this application, several state variables are of interest, which include:

- The maximum absolute acceleration observed at the foundation and the top of the building;
- The maximum and residual displacements at the foundation;
- The maximum and residual rotation at the foundation;
- The maximum base shear force and moment experienced at the base of the building.

The SSI macro-element is a source of the non-linearities of the system. The selected damage measures therefore particularly focus on the response of the foundation, such as the maximum shear force and rocking moment. The maximum displacement (rotation) and

residual displacement (rotation) are key indicators to evaluate the seismic damage. The residual displacement (rotation) represents the final irreversible displacement (rotation) at the end of the earthquake event. Moreover, the maximum absolute acceleration at the foundation and the top of the building are also used to evaluate the amplification effect.

Results: IDA curves and SSI effect

The IDA curves for all earthquake records are presented in Figures 12.17, 12.18, 12.19, and 12.20. Each circle represents an engineering demand parameter obtained from a time history analysis conducted for a given scaled record. The lines represent the evolution of the median value of the selected engineering demand parameter for increasing values of PGA, and the 16 %-84 % fractile range is also indicated in grey. To study the SSI effect, the median value of the engineering demand parameter from fixed-base and elastic SSI configurations are also presented in the figures.

The peak absolute acceleration at the foundation and the top of the building as a function of the PGA of the input excitation is presented in Figure 12.17. It can be found that the peak absolute accelerations at the foundation level for the fixed-based configurations and the linear elastic SSI configurations are similar. The medium value of the maximum acceleration at the foundation for the linear elastic SSI configurations is a little higher than that for the fixed-base configurations, which means that the ground motion is slightly amplified with the consideration of the stiffness within the foundation-soil system.

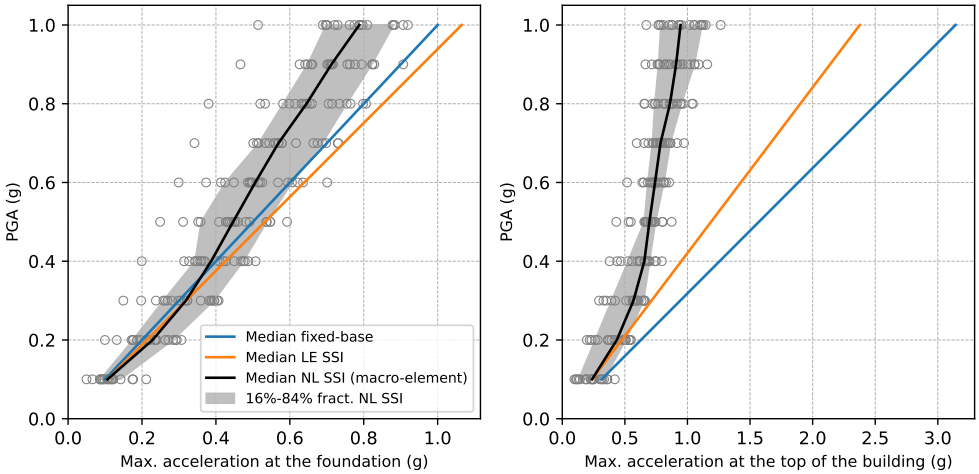

Fig. 12.17. IDA curves: peak absolute acceleration recorded at the foundation and the top of the building

The SSI plays an important role in the reduction of the maximum absolute acceleration at the top of the building. This reduction is already significant between the fixed-base configurations (blue line) and the linear SSI configurations (orange line), especially in the reduction of the maximum acceleration at the top of the foundation. However, it should

be noted that the PGA at the top of the building is largely amplified in the fixed-based configurations and the linear SSI configurations. The addition of non-linearity within the foundation-soil system, replicated by the non-linear SSI macro-element, collaborates in the reduction of the acceleration at the top of the building in a significant manner with no acceleration amplification.

The IDA curves regarding the maximum shear force and moment at the foundation are depicted in Figure 12.18. As expected, the maximum shear force and moment are smaller in the configurations with linear SSI than the fixed-base configurations. The SSI phenomenon becomes increasingly significant as the load intensity rises, underscoring the necessity of considering SSI effects in the design process. Additionally, the beneficial role of the non-linearity is observed in these comparisons. The maximum shear force and moment at the foundation of the non-linear SSI macro-element is not on the same scale as other configurations with fixed-base and linear SSI boundary conditions.

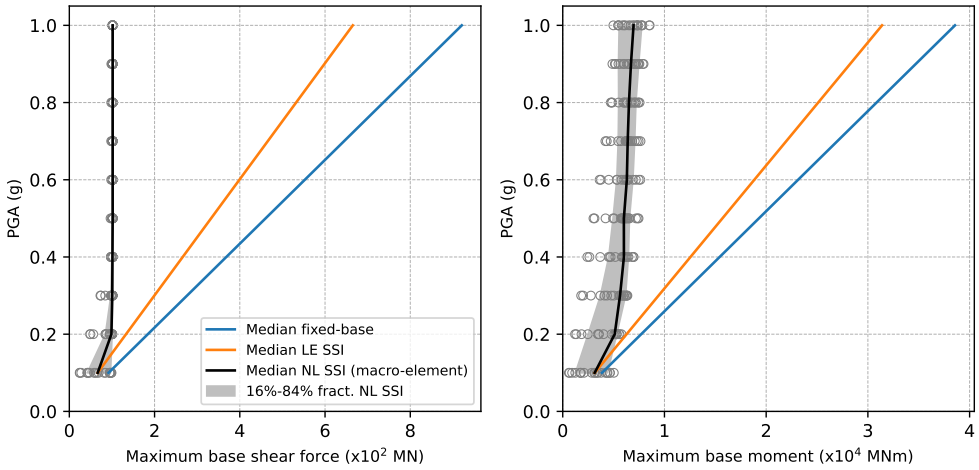

Fig. 12.18. IDA curves: maximum shear force and moment at the foundation

The outcomes, as depicted in Figure 12.19, illustrate the foundation's maximum and residual relative displacement (relative to free-field displacement). The non-linear SSI macro-element configurations produce larger horizontal displacement at the foundation, attributed to the irreversible displacement generated during the strong earthquake. Consequently, the maximum foundation horizontal displacement of the non-linear SSI macro-element configurations surpasses that of the linear SSI configurations.

Figure 12.20 illustrates the results concerning the maximum and residual rotation of the foundation. The linear SSI macro-element configurations exhibit a greater maximum rotation at the foundation compared to the non-linear SSI macro-element configurations. In the non-linear SSI macro-element model, the moment applied at the foundation is constrained by the yield surface. Consequently, the maximum rotation at the foundation in a non-linear SSI model is smaller than that in a linear SSI model even when accounting for the presence of residual rotation.

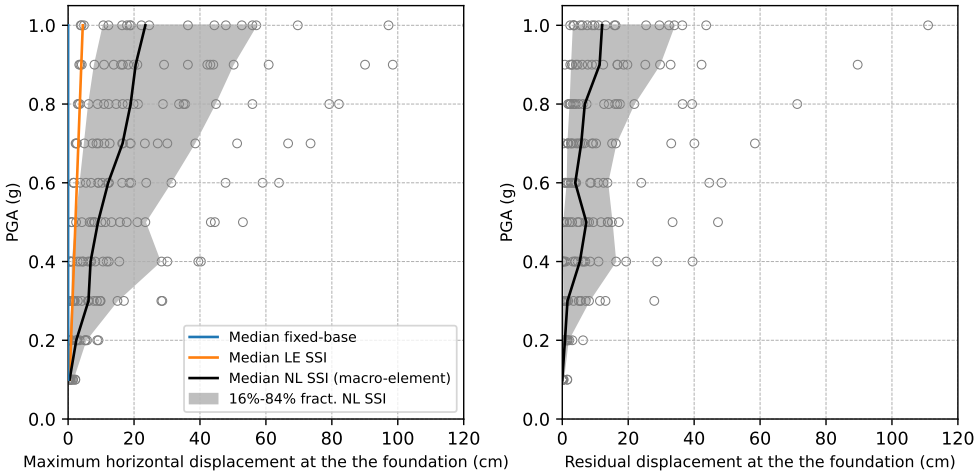

Fig. 12.19. IDA curves: maximum and residual relative displacements (relative to free-field displacement) at the foundation

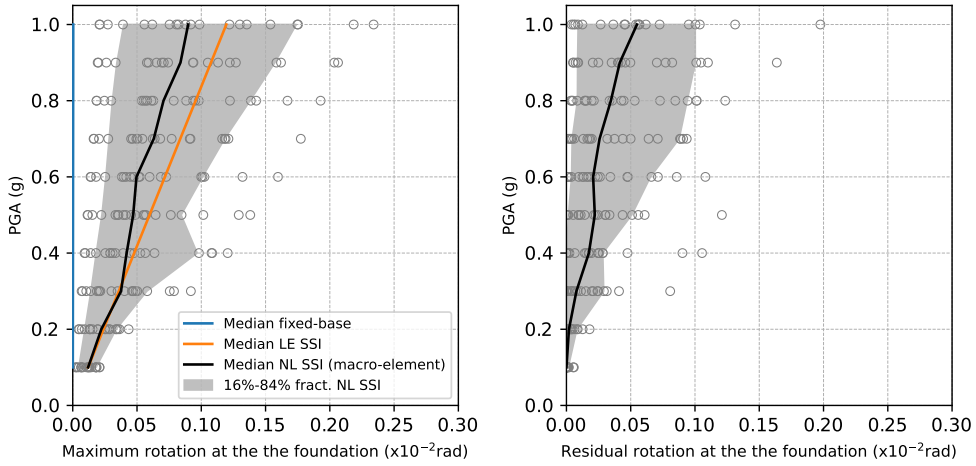

Fig. 12.20. IDA curves: maximum and residual rotation at the foundation

12.4 Summary

This chapter illustrates the application of the proposed macro-element for rigid inclusion-reinforced foundations. An important characteristic of the macro-element is that is a time-saving approach, allowing performing numerous calculations quickly. Two parametric studies involve a lumped mass model and a real structure simulated by a Timoshenko beam model.

In the first application, the structure is represented by a lumped mass model. Various superstructures are examined with variations in the natural frequency, slenderness, safety factor, and soft soil shear velocities. Three different support conditions are used, namely: fixed-based condition, linear elastic SSI condition, and non-linear SSI condition using macro-element. The results are depicted in relation to the SSI parameters to provide a

comprehensive understanding of both linear and non-linear SSI effects in such foundations. The period elongation effect and the increase in damping are observed, and these effects are significant for slender and stiffer buildings founded on soft soil.

In the second numerical application of the macro-element, a 22-storey building is investigated. The building is modelled by a homogeneous Timoshenko beam. The seismic response of the building is analysed through IDA analysis using a set of 20 different earthquake records. A comparative analysis of results is conducted for three different support conditions, emphasising the significance of considering the SSI effects in the seismic design.

From these two studies, it can be observed that incorporating SSI effects, especially introducing non-linearity through the macro-element for SSI analysis, results in a reduction in maximum base shear forces and moments.

Conclusion

This part of the dissertation is dedicated to introducing the development and the applications of SSI macro-element for rigid inclusion-reinforced foundations.

Chapter 11 outlines the development of the dynamic SSI macro-element. The proposed macro-element formulation can be applicable for solving both 2D and 3D dynamic SSI problem. This chapter provides insights into the macro-element structures under static and seismic conditions, encompassing the plasticity model and the non-linear elasticity model to simulate the sliding, the loss of bearing capacity, and the uplift behaviour of the reinforced foundations. The numerical resolutions and their implementation are thoroughly discussed in this chapter, and validation procedures are carried out to ensure the accuracy and reliability of the macro-element.

In Chapter 12, the practical applications of the macro-element are detailed. Through a statistical analysis of the results in two applications, it is observed that incorporating SSI effects and particularly introducing nonlinearity through the macro-element for soil-foundation interaction, leads to a reduction in maximum base shear forces and moments. This reduction is more pronounced when considering soil-foundation nonlinearity. The applications confirm the effectiveness of the macro-element for rigid inclusion-reinforced foundations in terms of computational time and result accuracy. It is noteworthy that the extensive number of time-history analyses could hardly be accomplished with a direct 3D FEM analysis at a reasonable cost.

Conclusion and perspectives

General conclusion

This PhD dissertation examines the dynamic soil-structure interaction phenomena of foundations reinforced by rigid inclusions under seismic loading using several complementary approaches, including different numerical models, resolution strategies and analytical analyses. The study is completed by an examination of the bearing capacity of such foundations, using the kinematic exterior approach within the framework of yield design theory. Furthermore, a novel macro-element has been developed to deal with foundations reinforced by rigid inclusions under seismic loading.

The main contributions and conclusions of this work are outlined below.

The **literature review** focuses on different dynamic soil-interaction effects and their impact on the response of the foundation, either globally or at a local level (i.e., focusing on the individual behaviour of rigid inclusions, the load transfer platform, etc.). To date, there are still few experimental studies dealing with the dynamic behaviour of foundations on reinforced soil by rigid inclusions, but existing work already makes it possible to observe interesting characteristics of this type of foundation under seismic loading. The numerical methods available today can answer most of the questions concerning dynamic SSI problems in the linear domain (i.e., kinematic interaction, group effects, etc.), but there is a need for suitable computational tools to better understand the specifics involved in the non-linear response of these foundations and to enable performance-based design analyses on a routine basis.

The key findings of the numerical and experimental studies highlighted in the literature review can be summarised as follows:

- The introduction of rigid inclusions attenuates foundation settlement during seismic excitations;
- Compared with pile foundations, rigid inclusions experience lower inertial efforts, which is mainly due to the disconnection between the raft and the piles;
- Seismic isolation effects are observed in rigid inclusion-reinforced foundations under high-intensity seismic loads. The LTP offers the possibility of developing a sliding mechanism at the interface between the foundation and the LTP, temporarily isolating the structure from the reinforced soil that supports it. This non-linear mechanism prevents part of the seismic energy arriving at the base of the structure from being transmitted, thereby reducing the load effectively applied to the structure.

The second part of this dissertation has focused on the primary dynamic SSI effects developed in foundations reinforced by rigid inclusions through an **SSI study in the linear elastic domain**. The main observations of this study can be summarised as follows:

- Compared with pile foundations, the modification of the ground motion at the base of the structure due to the kinematic interaction phenomenon is generally less significant. This effect is practically inappreciable in the low-frequency range and only becomes perceptible, albeit of relatively small amplitude (for most practical configurations), at high frequencies. From a design point of view, this generally implies a reduction in input motion compared to free-field conditions;
- The presence of the rigid inclusions has a negligible impact on the dynamic impedances of the foundation along the horizontal axes. In the vertical and rotational directions, the dynamic stiffness lies between that of shallow foundations and pile foundations;
- The vertical force transfer efficiency in a rigid inclusion-reinforced foundation system is observed to be higher than the horizontal one. The soil mainly recovers most of the horizontal forces transferred by the raft, which affects the direction of the stresses in the soil. Thus, the inclination of the loads transmitted through the soil around the reinforcements is greater than that applied to the foundation;
- Regarding kinematic bending moments in rigid inclusions, the observations are consistent with those already made for pile foundations, the maximum bending moment being located at the interfaces between different soil layers of different characteristics. Its amplitude is mainly controlled by the stiffness contrast at the interface. Differences from pile foundations can be found at the head of the rigid inclusions, which is related to the different boundary conditions at this location (no connection of the rigid inclusions to the raft). Finally, no group effects are observed when a group of rigid inclusions was submitted to kinematic loading. This is also consistent with the usual observations made for pile foundations.

The bearing capacity of the rigid inclusion-reinforced foundation is examined in Part III using the kinematic exterior approach. The **study of the foundation's seismic stability** considers the development of inertia forces in the soil as well as the inclination and the eccentricity of the loads applied by the superstructure to the foundation. The following points serve as a summary of the main contributions:

- This work extends the application of the kinematic exterior approach to rigid inclusion-reinforced foundations. The validation is achieved through comparisons with results from the literature for the non-reinforced configurations and FEM analysis for the reinforced configurations;

- To accurately estimate the contribution of the inclusions to the resistance within the framework of the kinematic exterior approach, a multicriterion for rigid inclusions is proposed, taking into account different failure modes;
- Several factors influencing the foundation's bearing capacity are explored, revealing that the bearing capacity consistently increases as the coverage area ratio does. The bearing capacity of a reinforced foundation constantly exceeds that of an unreinforced one under the same loading conditions: seismic intensity, inclination, and eccentricity;
- For reinforced foundations exhibiting a significant safety factor (i.e., more than 3) under a vertically centred static load, the impact of soil inertia may often be ignored. When the foundation's initial safety factor is already low, however, a significant loss of bearing capacity may occur as a result of the inertial forces of the soil.

A **novel macro-element for rigid inclusion-reinforced foundations under seismic loading** has been developed in Part IV, allowing to consider both linear and non-linear SSI phenomena in the study of structures founded on reinforced soil by rigid inclusions submitted to seismic loading.

The yield surface determined by yield design and the dynamic impedances of the foundation are integrated into the formulation of the macro-element. Consistency checks, third-party software, and multiple comparisons with analytical solutions verify the validity of the various parts of this macro-element.

The validated macro-element model is then employed to conduct a parametric study on a simplified structure and an Incremental Dynamic Analysis (IDA) of a 22-storey building. These applications demonstrate the macro-element approach's effectiveness and usefulness in practical design.

Perspectives

Potential future investigation could focus on the following aspects:

SSI study in the linear elastic domain

- Comparison with experimental studies

  A comparative analysis can be conducted with experimental studies like ICEDA (EDF, 2008a) to verify the validity of the numerical modelling approach and confirm the observation in the numerical study.

- Study of more complex configurations

  The study primarily focuses on foundations of relatively modest dimensions, and the investigation of larger foundations remains unexplored. Addressing this gap could fulfil specific engineering requirements, like LNG tanks or nuclear power plants.

- Improvement of the conventional pseudo-static method for the determination of the kinematic loads in deep foundations

  The work should also focus on refining the conventional pseudo-static approach used to estimate kinematic bending moments, aiming to enhance its performance and reduce the observed differences with the dynamic approach. This work would apply not only to rigid inclusions but also to pile foundations.

Seismic bearing capacity

- 3D effect for the bearing capacity

  It is also interesting to investigate the 3D effect on bearing capacity, as the current seismic bearing capacity study is conducted in a 2D plane. Further research could propose a shape factor to appropriately account for the 3D effect, employing either numerical modelling or applying a 3D virtual velocity field.

- Considering the contribution of the LTP

  The study can be improved by considering the contribution of the LTP in the failure mechanism intersecting the rigid inclusions, which is currently neglected to facilitate the use of the existing failure mechanisms developed for non-reinforced shallow foundations. This improvement could involve applying a kinematically admissible velocity field.

- Homogenised profile

  Following the inspiration of the homogenisation approach, a homogenised profile can be proposed with equivalent resistance parameters (c-φ) through an extensive analysis of various configurations. A series of charts could be established to indicate the potential correlations between equivalent resistance parameters (c-φ), the soft soil properties, and the coverage area ratio.

Macro-element approach

- Design charts

  A set of charts can be produced using this tool to offer insights into the linear and non-linear SSI response of structures founded on rigid inclusions, in terms of several dimensionless parameters.

- Cross-comparison

  A supplementary comparison study could be conducted using numerical 3D non-linear modelling, experimental results from centrifuge tests, and real seismic measurements (i.e., the Rio-Antirrio Bridge) to enrich the application of the macro-element model and gather more information.

- Frequency-dependent response

  In the present macro-element model, the far field is characterised by a set of springs and dash-pot calibrated using dynamic impedance functions. However, the current formulation does not account for the frequency-dependent response. To address this limitation, frequency-dependent effects can be integrated into the proposed macro-element model through advanced methods, such as the Laplace-Time approach.

Bibliography

Abboud, Y. (2017). “Développement d’un macroélément pour l’étude des fondations superficielles sous charge sismique”. PhD thesis. Université Paris-Est (cit. on pp. 50–52, 213, 236).

AFNOR (2007). *Design of structure for earthquake resistance - Part 5: Foundations, retaining structures and geotechnical aspect*. Paris: AFNOR (cit. on pp. 5, 82, 126, 219, 309).

AFPS and CFMS (2012). *Procédés d’amélioration et de renforcement de sols sous action sismique*. Paris: Presses des Ponts (cit. on pp. 100, 202).

Allmond, J. D. and B. L. Kutter (2014). “Design considerations for rocking foundations on unattached piles”. In: *Journal of Geotechnical and Geoenvironmental Engineering* 140.10 (cit. on pp. 32, 37, 38).

Alzate, A. M. and F. Cuira (2022). *Note of calculation of the compressed surface of an arbitrary plate*. Tech. rep. Paris, France: Terrasol (cit. on pp. 104, 217).

Alzate, A. M., N. Frattini, F. Cuira, and B. Simon (2022). “Quelques considérations pratiques autour du calcul des semelles et radiers sur inclusions rigides”. In: *Journées Nationales de Géotechnique et de Géologie de l’Ingénieur JNGG2022*. Lyon, France (cit. on p. 60).

Anastasopoulos, I., G. Gazetas, M. Loli, M. Apostolou, and N. Gerolymos (2010). “Soil failure can be used for seismic protection of structures”. In: *Bulletin of Earthquake Engineering* 8.2, pp. 309–326 (cit. on p. 211).

Ancheta, T., R. Darragh, J. Stewart, *et al.* (2013). *PEER NGA-West2 Database. PEER Report No. 2013/03*. Tech. rep. Berkeley: Pacific Earthquake Engineering Research Center (cit. on pp. 261, 262).

Anthoine, A. (1987). “Stabilité d’une fouille renforcée par clouage”. In: *4th franco-polish Conference on Application of Soil Mechanics*. Grenoble, France (cit. on pp. 154, 158).

Anthoine, A. (1990). “Une méthode pour le dimensionnement à la rupture des ouvrages en sols renforcés”. In: *Revue Française de Géotechnique* 50, pp. 5–21 (cit. on p. 157).

Arbabi, F. and F. Li (1990). “Macroelements for variable-section beams”. In: *Computers and Structures* 37.4, pp. 553–559 (cit. on p. 45).

Arıoğlu, E. (2021). “Importance of “heuristics” in suspension bridge engineering and 1915 Çanakkale bridge”. In: *Developments in International Bridge Engineering: Selected Papers from Istanbul Bridge Conference 2018*. Springer International Publishing, pp. 19–41 (cit. on p. 17).

ASIRI (2012). *Recommandations pour la conception, le calcul, l’exécution et le contrôle des ouvrages sur sols améliorés par inclusions rigides verticales*. Paris: Presses des Ponts (cit. on pp. 4, 5, 11, 14, 16, 17, 58, 158, 169, 170, 309).

Auvinet, G., A. Pecker, and J. Salençon (1996). “Seismic bearing capacity of shallow foundations in Mexico City during the 1985 Michoacan earthquake”. In: *11th World Conference on Earthquake Engineering*. Acapulco, Mexico (cit. on p. 199).

Azizkandi, A. S., M. H. Baziar, and A. F. Yeznabad (2018). “3D dynamic finite element analyses and 1 g shaking table tests on seismic performance of connected and nonconnected piled raft foundations”. In: *KSCE Journal of Civil Engineering* 22, pp. 1750–1762 (cit. on pp. 26, 37, 38).

Bentley (2022a). *PLAXIS 2D - Plane strain and axial symmetry*. Delft (cit. on pp. 237, 238).

Bentley (2022b). *PLAXIS 3D - Plane strain and axial symmetry*. Delft (cit. on pp. 62, 114, 236).

Briançon, L., V. Keller, M. Bustamante, O. Gay, E. Haza-Rozier, B. Simon, and B. Alves Dos Santos (2010). “Reinforcement of a concrete frame by rigid inclusions”. In: *Journées Nationales de Géotechnique et de Géologie de l’Ingénieur JNGG2010*. Grenoble, France, pp. 571–578 (cit. on p. 25).

Briançon, L. and J. Andromeda (2008). “Load transfer mechanisms in pile-supported earth platform under slab foundation”. In: *Second British Geotechnical Association International Conference on Foundations*. Dundee, Scotland: IHS BRE Press, pp. 1291–1302 (cit. on p. 25).

Brûlé, S. and F. Cuira (2018). *Pratique de l’interaction sol-structure sous séisme: application aux fondations et aux soutènements*. Paris: AFNOR (cit. on pp. 41, 52, 121, 236, 252, 317).

Butterfield, R. (1979). “A natural compression law for soils (an advance on e-log p’)”. In: *Géotechnique* 29.4, pp. 469–480 (cit. on p. 147).

Calvi, G. M., M. J. N. Priestley, and M. J. Kowalsky (2008). “Displacement-Based Seismic Design of Structures”. In: *3rd National Conference of Earthquake Engineering and Engineering Seismology*. Athens (cit. on p. 211).

Cassidy, M. J., B. W. Byrne, and G. T. Houlsby (2002). “Modelling the behaviour of circular footings under combined loading on loose carbonate sand”. In: *Géotechnique* 52.10, pp. 705–712 (cit. on p. 46).

Cassidy, M. J., C. M. Martin, and G. T. Houlsby (2004). “Development and application of force resultant models describing jack-up foundation behaviour”. In: *Marine Structures* 17.3-4, pp. 165–193 (cit. on p. 46).

Celebi, M. (2000). “Radiation damping observed from seismic responses of buildings”. In: *12th World Conference of Earthquake Engineering*. Auckland, New Zealand (cit. on p. 23).

Chatzigogos, C. T. (2007). “Comportement sismique des fondations superficielles : vers la prise en compte d’un critère de performance dans la conception”. PhD thesis. École Polytechnique de Paris (cit. on pp. 49, 50, 56, 149).

Chatzigogos, C. T., A. Pecker, and J. Salençon (2005). “Seismic bearing capacity of shallow foundations”. In: *11th World Conference on Earthquake Engineering*. Acapulco, Mexico (cit. on pp. 30, 213).

Chatzigogos, C. T., A. Pecker, and J. Salençon (2009). "Macroelement modeling of shallow foundations". In: *Soil Dynamics and Earthquake Engineering* 29.5, pp. 765–81 (cit. on p. 52).

Correia, A. A., A. Pecker, S. L. Kramer, and R. Pinho (2012). "Nonlinear pile-head macro-element model: SSI effects on the seismic response of a monoshaft-supported". In: *15th World Conference on Earthquake Engineering*. Lisbon (cit. on pp. 51, 54, 260).

Cremer, C., A. Pecker, and L. Davenne (2001). "Cyclic macro-element for soil-structure interaction: Material and geometrical non-linearities". In: *International Journal for Numerical and Analytical Methods in Geomechanics* 25.13, pp. 1257–1284 (cit. on pp. 47, 48, 52).

Cremer, C., A. Pecker, and L. Davenne (2002). "Modelling of nonlinear dynamic behaviour of a shallow strip foundation with macro-element". In: *Journal of Earthquake Engineering* 6.2, pp. 175–211 (cit. on pp. 48, 223).

Cuira, F. and B. Simon (2009). "Deux outils simples pour traiter des interactions complexes d'un massif renforcé par inclusions rigides". In: *17th International Conference on Soil Mechanics and Geotechnical Engineering: The Academia and Practice of Geotechnical Engineering*. Alexandria, Egypt: IOS Press, pp. 1163–1166 (cit. on p. 104).

Cuira, F. and B. Simon (2013). "Modeling edge effects at the periphery of a rigid inclusion reinforced soil volume". In: *18th International Conférence on Soil Mechanics and Geotechnical Engineering*. Paris, pp. 1955–1958 (cit. on pp. 60, 104).

Cuira, F. (2012). "Une approche simple pour l'etude du flambement d'un pieu souple dans un sol multicouche". In: *Journées Nationales de Géotechnique et de Géologie de l'Ingénieur JNGG2012*. Bordeaux, France, pp. 625–632 (cit. on p. 134).

Dassault Systemes (2023). *ABAQUS*. United States (cit. on p. 62).

De Buhan, P. (2004). "Renforcement par inclusions des sols et des roches". In: *Revue Française de Génie Civil* 8.9-10, pp. 1033–69 (cit. on pp. 56, 158).

De Buhan, P. (2005). "De l'approche par homogénéisation au développement d'un modele multiphasique: le cas des sols renforcés par inclusions linéaires". In: *Microstructure et Propriétés des Matériaux*. Paris: Presses des Ponts, pp. 29–38 (cit. on p. 60).

De Buhan, P. (2007). *Plasticité et calcul à la rupture*. Paris: Presses des Ponts (cit. on p. 56).

De Buhan, P. (2023). "Yield design-based analysis of reinforced soil structures, making use of different models of reinforced soils". In: *Revue Française de Géotechnique* 175.4 (cit. on p. 57).

De Buhan, P., L. Dormieux, and J. Salencon (1992). "An Interactive Computer Software for the Yield Design of Reinforced Soil Structures". In: *Géotechnique et informatique*. Paris: Presses des Ponts (cit. on pp. 56, 157, 158, 175).

De Buhan, P., L. Dormieux, and J. Salençon (1998). "Modélisation micropolaire de la résistance d'un milieu renforcé par inclusions". In: *Comptes Rendus de l'Académie des Sciences - Series IIB - Mechanics-Physics-Chemistry-Astronomy* 326.3, pp. 163–170 (cit. on p. 60).

Deleuze, G. (1967). “Réponse à un mouvement sismique d’un édifice posé sur un sol élastique”. In: *Annales de l’institut technique du batiment et des travaux publiques* 234, pp. 883–902 (cit. on p. 89).

De Sanctis, L., R. Di Laora, N. Caterino, G. Maddaloni, S. Aversa, A. Mandolini, and A. Occhiuzzi (2015). “Effects of the filtering action exerted by piles on the seismic response of RC frame buildings”. In: *Bulletin of Earthquake Engineering* 13.11, pp. 3259–3275 (cit. on p. 73).

De Sauvage, J. and J.-P. Rajot (2018). “Clouage des sols: conditions de long terme et amélioration du dimensionnement conventionnel”. In: *Journées Nationales de Géotechnique et de Géologie de l’Ingénieur JNGG2018*. Champs-sur-Marne, France (cit. on p. 157).

Di Prisco, C. and F. Pisanò (2011). “Seismic response of rigid shallow footings”. In: *European Journal of Environmental and Civil Engineering* 15:sup1, pp. 185–221 (cit. on p. 45).

Dormieux, L. and A. Pecker (1995). “Seismic bearing capacity of foundation on cohesionless soil”. In: *Journal of Geotechnical Engineering* 121.3, pp. 300–303 (cit. on p. 153).

EDF (2008a). *Résultats des mesures AVLS*. Tech. rep. EDF CIDEN (cit. on pp. 36, 38, 275, 314).

EDF (2008b). *Validation de la méthodologie de calcul des caractéristiques des sols équivalents et calcul dynamiques du plot d’essais*. Tech. rep. EDF CIDEN (cit. on p. 35).

EDF (2019). *“Exact” elements of beams in Aster*. Tech. rep. EDF (cit. on p. 232).

EDF (2023). *Finite element Code Aster , Analysis of Structures and Thermomechanics for Studies and Research*. Paris (cit. on pp. 236–238).

El Arja, H. (2020). “Contribution à la modélisation numérique des excavations profondes”. PhD thesis. Université Paris-Est (cit. on p. 230).

Frank, R., F. Cuira, and S. Burlon (2021). *Design of shallow and deep foundations*. London: CRC Press (cit. on p. 16).

Ganga Rao, H. V. S. and H. J. Farran (1986). “Macro-element analysis of skewed and triangular orthotropic thin plates with beam boundaries”. In: *Computers and Structures* 22.3, pp. 399–404 (cit. on p. 45).

Garnier, J. and A. Pecker (1999). “Use of centrifuge tests for the validation of innovative concepts in foundation engineering”. In: *2nd international conference on earthquake geotechnical engineering*. Lisbon, pp. 433–439 (cit. on pp. 17, 30, 31).

Gasparini, D. A. and E. H. Vanmarcke (1976). *Simulated earthquake motions compatible with prescribed response spectra*. Tech. rep. Massachusetts: Massachusetts Institute of Technology (cit. on p. 82).

Gazetas, G. (1984). “Seismic response of end-bearing single piles”. In: *International Journal of Soil Dynamics and Earthquake Engineering* 3.2, pp. 82–93 (cit. on pp. 73, 81, 89).

Gazetas, G. (1991a). “Formulas and charts for impedances of surface and embedded foundations”. In: *Journal of Geotechnical Engineering* 117.9, pp. 1363–1381 (cit. on pp. 88, 89).

Gazetas, G. (1991b). “Foundation vibrations”. In: *Foundation engineering handbook*. Springer, pp. 553–593 (cit. on pp. 22, 89).

Gazetas, G., I. Anastasopoulos, and E. Garini (2014). “Geotechnical design with apparent seismic safety factors well-bellow 1”. In: *Soil Dynamics and Earthquake Engineering* 57.2014, pp. 37–45 (cit. on p. 211).

Gazetas, G., K. Fan, and A. Kaynia (1993). “Dynamic response of pile groups with different configurations”. In: *Soil Dynamics and Earthquake Engineering* 12.4, pp. 239–257 (cit. on pp. 73, 75, 89, 134).

Ghannad, M. (1998). “A study on the effect of soil-structure interaction on the dynamic properties of structures using simplified methods”. PhD thesis. Nagoya University (cit. on p. 251).

Ghobarah, A. (2001). “Performance-based design in earthquake engineering: State of development”. In: *Engineering Structures* 23.8, pp. 878–884 (cit. on p. 3).

Giannakou, A., P. Tasiopoulou, J. Chacko, and H. Kim (2019). “Assessment of lateral spreading demands on the 1915 Çanakkale bridge tower foundation”. In: *Earthquake Geotechnical Engineering for Protection and Development of Environment and Constructions*. CRC Press, pp. 2643–2650 (cit. on pp. 17, 19).

Grange, S. (2008). “Modélisation simplifiée 3D de l’interaction sol-structure : application au génie parasismique”. PhD thesis. Institut Polytechnique de Grenoble (cit. on pp. 49, 52, 223).

Grange, S., P. Kotronis, and J. Mazars (2009). “A macro-element to simulate 3D soil-structure interaction considering plasticity and uplift”. In: *International Journal of Solids and Structures* 46.20, pp. 3651–63 (cit. on p. 213).

Guéguin, M. (2014). “Approche par une méthode d’ homogénéisation du comportement des ouvrages en sols renforcés par colonnes ou tranchées”. PhD thesis. Université Pairs-Est (cit. on pp. 60, 61).

Ha, J. G., K. W. Ko, S. B. Jo, H. J. Park, and D. S. Kim (2019). “Investigation of seismic performances of unconnected pile foundations using dynamic centrifuge tests”. In: *Bulletin of Earthquake Engineering* 17.5, pp. 2433–2458 (cit. on p. 32).

Han, X., Y. Li, J. Ji, J. Ying, W. Li, and B. Dai (2016). “Numerical simulation on the seismic absorption effect of the cushion in rigid-pile composite foundation”. In: *Earthquake Engineering and Engineering Vibration* 15.2, pp. 369–378 (cit. on pp. 15, 42).

Hassen, G. (2006). “Modélisation multiphasique pour le calcul des ouvrages renforcés par inclusion rigides”. PhD thesis. École Nationale des Ponts et Chaussées (cit. on p. 60).

Hassen, G., E. Donval, and P. de Buhan (2021). “Numerical stability analysis of reinforced soil structures using the multiphase model”. In: *Computers and Geotechnics* 133.2021, p. 104035 (cit. on p. 165).

Hoang, M. T., A. Abboud, and F. Cuira (2020). “Utilisation d’une approche en deplacement pour l’évaluation des effets parasites s’exercant sur un pieu à proximlité d’un remblais”. In: *Journées Nationales de Géotechnique et de Géologie de l’Ingénieur JNGG2020*. Lyon, France (cit. on p. 134).

Houlsby, G. T. and M. J. Cassidy (2002). “A plasticity model for the behaviour of footings on sand under combined loading”. In: *Géotechnique* 52.2, pp. 117–129 (cit. on p. 46).
Huang, J. and D. V. Griffiths (2009). “Return Mapping Algorithms and Stress Predictors for Failure Analysis in Geomechanics”. In: *Journal of Engineering Mechanics* 135.4, pp. 276–284 (cit. on p. 227).
International Seismological Centre (2023). *ISC-GEM Catalogue Overview* (cit. on p. 3).
IRSN (2012). *Pourquoi et où se produisent les séismes ?* (Cit. on p. 3).
Itasca Consulting Group (2023). *FLAC3D — Fast Lagrangian Analysis of Continua in Three-Dimensions*. Minneapolis (cit. on pp. 62, 236).
Jenck, O. (2005). “Le renforcement des sols compressibles par inclusions rigides verticales - Modélisation physique et numérique”. PhD thesis. Institut National des Sciences Appliquées de Lyon (cit. on p. 25).
Kafle, B. and F. Wuttke (2013). “Cyclic macroelement for shallow footing over unsaturated soil”. In: *Advances in Unsaturated Soils*. London: CRC Press, pp. 521–526 (cit. on p. 48).
Kashiwa, H., S. Ohmura, H. Nakagawa, and S. Nakai (2020). “Shaking Table Test of Insulated Pile Foundation for Effective Utilization of Existing Pile”. In: *17th World Conference on Earthquake Engineering*. Sendai, Japan (cit. on pp. 27, 28).
Kausel, E. (1974). “Forced vibrations of circular foundations on layered media.” PhD thesis. Massachusetts Institute of Technology (cit. on p. 89).
Kausel, E., R. V. Whitman, J. P. Morray, and F. Elsabee (1978). “The spring method for embedded foundations”. In: *Nuclear Engineering and Design* 48.2-3, pp. 377–392 (cit. on pp. 43, 71, 141).
Kaynia, A. (1982). “Dynamic behavior of pile groups”. PhD thesis. Massachusetts Institute of Technology (cit. on pp. 82, 89).
Kaynia, A. M. and M. Novak (1992). “Response of pile foundations to rayleigh waves and obliquely incident body waves”. In: *Earthquake Engineering & Structural Dynamics* 21.4, pp. 303–318 (cit. on p. 73).
Khebizi, M., H. Guenfoud, and M. Guenfoud (2018). “Numerical modelling of soil-foundation interaction by a new non-linear macro-element”. In: *Geomechanics and Engineering* 14.4, pp. 377–386 (cit. on pp. 48, 49).
Kitchin, J. (2015). *Python computations in science and engineering* (cit. on p. 219).
Ko, K. W., H. J. Park, J. G. Ha, S. Jin, Y. H. Song, M. J. Song, and D. S. Kim (2019). “Evaluation of dynamic bending moment of disconnected piled raft via centrifuge tests”. In: *Canadian Geotechnical Journal* 56.12, pp. 1917–1928 (cit. on pp. 33, 34, 37, 38).
Kroon, I. B., H. Polk, and K. Fuglsang (2021). “1915 Çanakkale Bridge – Meeting the Challenge”. In: *Developments in International Bridge Engineering*. Springer International Publishing, pp. 55–69 (cit. on pp. 17, 19, 20).
Li, Z. (2014). “Etude expérimentale et numérique de foundations profondes sous sollicitations sismiques : pieux verticaux et pieux inclinés”. PhD thesis. Ecole Centrale de Nantes (cit. on pp. 30, 52, 54).

Li, Z., P. Kotronis, S. Escoffier, and C. Tamagnini (2016). “A hypoplastic macroelement for single vertical piles in sand subject to three-dimensional loading conditions”. In: *Acta Geotechnica* 11.2, pp. 373–390 (cit. on pp. 53, 54).

Li, Z., P. Kotronis, S. Escoffier, and C. Tamagnini (2018). “A hypoplastic macroelement formulation for single batter piles in sand”. In: *International Journal for Numerical and Analytical Methods in Geomechanics* 42.12, pp. 1346–1365 (cit. on pp. 53, 54).

Liang, F., T. Li, Y. Qian, C. Wang, and Y. Jia (2021). “Investigating the seismic isolation effect of the cushioned pile raft foundation in soft clay through dynamic centrifuge tests”. In: *Soil Dynamics and Earthquake Engineering* 142.106554 (cit. on pp. 34, 38).

Lin, L., J. Zhang, Y. Li, Z. Rao, and Z. Sen (2022). “3D Finite Element Analysis of Seismic Response of Rigid Pile Composite Foundation with Microprobe Group”. In: *International Journal of Analytical Chemistry* 2022 (cit. on pp. 28, 29).

Loli, M., J. A. Knappett, M. J. Brown, I. Anastasopoulos, and G. Gazetas (2015). “Centrifuge testing of a bridge pier on a rocking isolated foundation supported on unconnected piles”. In: *6th International Conference on Earthquake Geotechnical Engineering*. Christchurch, New Zealand (cit. on pp. 32, 33, 37, 38).

López Jiménez, G. A., D. Dias, and O. Jenck (2019). “Effect of the soil–pile–structure interaction in seismic analysis: case of liquefiable soils”. In: *Acta Geotechnica* 14.5, pp. 1509–1525 (cit. on p. 42).

Lorenzo, G. W. F., M. P. S. D’Avila, A. Deschamps, E. Bertrand, E. D. Mercerat, L. Foundotos, and F. Courboulex (2018). “Numerical and empirical simulation of linear elastic seismic response of a building: The case of Nice Prefecture”. In: *Earthquake Spectra* 34.1, pp. 169–196 (cit. on p. 256).

Lorenzo, G. W. F. (2016). “From accelerometric records to the dynamic behavior of existing buildings”. PhD thesis. Université Côté d’Azur (cit. on pp. 256, 257).

Low, B. K., S. K. Tang, and V. Choa (1994). “Arching in piled embankments”. In: *Journal of geotechnical engineering* 120.11, pp. 1917–1938 (cit. on p. 25).

Lysmer, J., M. Tabatabaie, F. F. Tajirian, S. Vahdani, and F. Ostadan (1981). *SASSI: A System for Analysis of Soil Structure Interaction*. Tech. rep. University of California, Berkeley (cit. on p. 64).

Mandel, J. and J. Salençon (1972). “Force portante d’un sol sur une assise rigide (étude théorique”. In: *Géotechnique* 22.1, pp. 79–93 (cit. on p. 159).

Mánica Malcom, M. Á., E. Ovando-Shelley, and E. Botero Jaramillo (2016). “Numerical study of the seismic behavior of rigid inclusions in soft Mexico City Clay”. In: *Journal of Earthquake Engineering* 20.3, pp. 447–475 (cit. on pp. 42, 76).

Marchi, M. (2008). “Stability and strength analysis of leaning towers”. PhD thesis. University of Padova (cit. on p. 46).

Martin, C. (1994). “Physical and numerical modelling of offshore foundations under combined loads”. PhD thesis. University of Oxford, p. 306 (cit. on p. 46).

Mattsson, N., A. Menoret, C. Simon, and M. Ray (2013). “Case study of a full-scale load test of a piled raft with an interposed layer for a nuclear storage facility”. In: *Géotechnique* 63.11, pp. 965–976 (cit. on pp. 17–19).

Messioud, S., U. S. Okyay, B. Sbartai, and D. Dias (2016). “Dynamic Response of Pile Reinforced Soils and Piled Foundations”. In: *Geotechnical and Geological Engineering* 34.3, pp. 789–805 (cit. on p. 42).

Meyerhof, G. G. (1953). “The bearing capacity of foundations under eccentric and inclined loads”. In: *3rd Soil Mechanics and Foundation Engineering Conference*. Zurich, pp. 440–445 (cit. on pp. 196, 198, 199).

Nakagawa, H., H. Kashiwa, and S. Nakai (2020). “Three-Dimensional Finite Element Analysis of a Building With Insulated Pile Foundation”. In: *17th World Conference on Earthquake Engineering*. Sendai, Japan (cit. on p. 27).

Nakagawa, H., H. Kashiwa, and S. Nakai (2018). “Evaluation of Seismic Behavior of a Building With Insulated Pile Foundation”. In: *16th European Conference on Earthquake Engineering*. Thessalonique, Greece (cit. on pp. 26, 27, 38).

Nakhaei, M. and M. Ali Ghannad (2008). “The effect of soil-structure interaction on damage index of buildings”. In: *Engineering Structures* 30.6, pp. 1491–1499 (cit. on p. 251).

Nguyen, V. T. (2015). “Analyse sismique des ouvrages renforcés par inclusions rigides à l’ aide d’une modélisation multiphasique”. PhD thesis. Université Paris-Est (cit. on p. 61).

Nikolaou, S., G. Mylonakis, G. Gazetas, and T. Tazoh (2001). “Kinematic pile bending during earthquakes: Analysis and field measurements”. In: *Geotechnique* 51.5, pp. 425–440 (cit. on p. 138).

Nogami, T. and K. Kongai (1988). “Time domain flexural response of dynmaically loaded single piles”. In: *Engineering Mechanics* 114.9, pp. 1512–1525 (cit. on p. 58).

Nova, R. and L. Montrasio (1991). “Settlements of shallow foundations on sand”. In: *Géotechnique* 41.2, pp. 243–256 (cit. on pp. 5, 45, 46, 309).

Novak, M. (1974). “Dynamic stiffness and damping of piles”. In: *Canadian Geotechnical Journal* 11.4, pp. 574–598 (cit. on p. 89).

Novak, M. (1991). “Piles under dynamic loads”. In: *Second international conference on recent advances in geotechnical earthquake engineering and soil dynamics*. St. Louis, Missouri, pp. 2433–2456 (cit. on p. 89).

Okyay, U. S., D. Dias, P. Billion, D. Vandeputte, and A. Courtois (2012). “Impedance functions of slab foundations with rigid piles”. In: *Geotechnical and Geological Engineering* 30.4, pp. 1013–1024 (cit. on pp. 19, 35, 42).

Okyay, U. S. (2010). “Etude expérimentale et numérique des transferts de charge dans un massif renforcé par inclusions rigides Application à des cas de chargements statiques et dynamiques”. PhD thesis. Institut National des Sciences Appliquées de Lyon (cit. on pp. 25, 35).

Optum Computational Engineering (2021). *OPTUM G2*. Copenhagen, Denmark (cit. on pp. 63, 177).

Ostadan, F. and N. Deng (2011). *Computer Program: SASSI2010-A System for Analysis of Soil-Structure Interaction*. Tech. rep. San Francisco: Geotechnical and Hydraulic Engineering Services (cit. on pp. 63, 76, 236).

Paolucci, R. and A. Pecker (1997a). "Seismic bearing capacity of shallow strip foundations on dry soils". In: *Soils and Foundations* 37.3, pp. 95–105 (cit. on pp. 148, 153, 154).

Paolucci, R. and A. Pecker (1997b). "Soil inertia effects on the bearing capacity of rectangular foundations on cohesive soils". In: *Engineering Structures* 19.8, pp. 637–643 (cit. on p. 148).

Papanikolas, P., A. Stathopoulos-Vlamis, A. Panagis, A. Pecker, and S. Infanti (2010). "The behavior of Rion–Antirion bridge during the earthquake of "Achaia-Ilia" on June 8, 2008". In: *the 3rd international FIB conference*. Washington D.C, pp. 587–605 (cit. on p. 18).

Park, H.-J., J.-G. Ha, S.-Y. Kwon, M.-G. Lee, and D.-S. Kim (2017). "Investigation of the dynamic behaviour of a storage tank with different foundation types focusing on the soil-foundation-structure interactions using centrifuge model tests". In: *Earthquake Engineering and Structural Dynamics* 46.14, pp. 2301–2316 (cit. on pp. 32, 38).

Pecker, A. (1997). "Analytical formulae for the seismic bearing capacity of shallow strip foundations". In: *Seismic Behaviour of Ground and Geotechnical Structures*. London: CRC Press, pp. 261–68 (cit. on p. 152).

Pecker, A. (2003). "Aseismic Foundation Design Process Lessons Learned From Two Major Projects : the Vasco Da Gama and the Rion-Antirion Bridges". In: *ACI International Conference on Seismic Bridge Design and Retrofit*. La Jolla, California (cit. on p. 31).

Pecker, A. (2004). "Design and Construction of the Rion Antirion Bridge". In: *the Conference on Geotechnical Engineering for Transportation Projects*. Los Angeles (cit. on pp. 17, 19, 54, 55).

Pecker, A. (2006). "Enhanced seismic design of shallow foundations : example of the Rion Antirion Bridge". In: *4th Athenian lecture on Geotechnical Engineering*. Athens (cit. on p. 17).

Pecker, A. (2023a). *Dynamique des structures et des ouvrages*. Paris, France: Presses des Ponts (cit. on pp. 42, 257).

Pecker, A. (2023b). "Interrelationships between practice, standardisation and innovation in geotechnical earthquake engineering". In: *Bulletin of Earthquake Engineering* 21, pp. 3091–3132 (cit. on pp. 14, 15, 17, 18, 56, 156).

Pecker, A. and C. T. Chatzigogos (2010). "Non linear soil structure interaction: impact on the seismic response of structures". In: *Earthquake engineering in Europe*. Springer. Chap. Chapter 4, pp. 79–103 (cit. on p. 260).

Pecker, A. and J. Salencon (1991). *Détermination de la capacité portante des fondations superficielles sous sollicitations dynamiques*. Tech. rep. Laboratoire de mécanique des solides, École Polytechnique de Paris (cit. on pp. 148–151).

Pecker, A. and J.-P. Teyssandier (2009). “Conception parasismique du pont de Rion-Antirion”. In: *19ème Congrès Français de Mécanique*. Marseille, France (cit. on pp. 17, 18).

Pecker, A., H. Harikiopoulos, P. de Buhan, L. Dormieux, and P. Morand (1998). *Comportement sismique d’une fondation sur sol renforcé par inclusions rigides*. Tech. rep. École Nationale des Ponts et Chaussées (cit. on pp. 56, 154–156, 175).

Pedretti, S. (1998). “Nonlinear seismic soil-foundation interaction: analysis and modelling method”. PhD thesis. Politecnico di Milano (cit. on p. 45).

Pereira, L. (2020). *Méthodes avancées pour la prise en compte de l’Interaction Sol-Structure dynamique non-linéaire*. Tech. rep. Paris: École Nationale des Ponts et Chaussées (cit. on p. 236).

Pérez-Herreros, J. (2020). “Dynamic soil-structure interaction of pile foundations : experimental and numerical study”. PhD thesis. Ecole Centrale Nantes (cit. on pp. 5, 30, 41, 53, 54, 260, 309, 310).

Petrolito, J. and B. W. Golley (1989). “Macro element analysis of composite beam-slab systems”. In: *Computers and Structures* 33.1, pp. 139–148 (cit. on p. 45).

Pisanò, F., L. Flessati, and C. Di Prisco (2016). “A macroelement framework for shallow foundations including changes in configuration”. In: *Géotechnique* 66.11, pp. 910–926 (cit. on p. 47).

Rangel-Núñez, J. L., A. Gómez-Bernal, J. Aguirre-González, E. Sordo-Zabay, and E. Ibarra-Razo (2008). “Dynamic response of soft soil deposits improved with rigid inclusions”. In: *14th World Conference on Earthquake Engineering*. Beijing (cit. on p. 42).

Romo-Organista, M. P., J. H. Chen, J. Lysmer, and H. B. Seed (1980). *PLUSH: A computer program for probabilistic finite element analysis of seismic soil-structure interaction*. Tech. rep. Berkeley: University of California (cit. on p. 42).

Saadatinezhad, M., A. Lakirouhani, and S. Jabini Asli (2021). “Seismic response of non-connected piled raft foundations”. In: *International Journal of Geotechnical Engineering* 15.1, pp. 66–80 (cit. on p. 42).

Salciarini, D. and C. Tamagnini (2009). “A hypoplastic macroelement model for shallow foundations under monotonic and cyclic loads”. In: *Acta Geotechnica* 4.3, pp. 163–176 (cit. on p. 47).

Salencon, J. and A. Pecker (1999). “Ground reinforcement in seismic areas”. In: *XI Panamerican Conference on Soil Mechanics and Geotechnical Engineering*. Foz do Iguassu, Brazil (cit. on p. 56).

Salençon, J., C. T. Chatzigogos, and A. Pecker (2009). “Seismic bearing capacity of circular footings: a yield design approach”. In: *Journal of Mechanics of Materials and Structures* 4.2, pp. 427–440 (cit. on p. 57).

Salençon, J. and A. Pecker (1995a). “Ultimate bearing capacity of shallow foundations under inclined and eccentric loads. Part I: purely cohesive soil”. In: *European Journal of Mechanics - A/Solids* 14.3, pp. 349–375 (cit. on pp. 148, 149).

Salençon, J. and A. Pecker (1995b). “Ultimate bearing capacity of shallow foundations under inclined and eccentric loads. part II: purely cohesive soil without tensile strength”. In: *European Journal of Mechanics - A/Solids* 14.3, pp. 377–396 (cit. on pp. 52, 148, 150–152, 165).

Salençon, J. (1983). *Calcul à la rupture et analyse limite*. Paris: Presses des Ponts (cit. on pp. 5, 56, 147, 148, 150, 309).

Salençon, J. (2002). *De l'élasto-plasticité au calcul à la rupture*. Paris: Presses des Ponts (cit. on pp. 56, 148, 150).

Salençon, J. (2013). *Yield Design*. John Wiley & Sons (cit. on p. 56).

Schlosser, F. (1978). “Behaviour and design of soil nailing”. In: *Symposium on Recent Developments in Ground Improvement Techniques*. Bangkok, pp. 399–413 (cit. on p. 163).

Schlosser, F. and P. Unterreiner (1990). “Soil nailing in France: research and practice”. In: *Transportation Research Record* 1330, pp. 72–79 (cit. on pp. 56, 158, 163).

Seed, H. B. and I. M. Idriss (1970). *Soil moduli and damping factors for dynamic response analyses*. Tech. rep. December. Berkeley: Earthquake Engineering Research Center, University of California (cit. on p. 22).

Sekiguchi, T., S. Nakai, M. Yamamoto, K. Fukutake, and Y. Taji (2015). “Evaluation of seismic behaviour of the insulated pile foundation based on site model experiment”. In: *10th Pacific Conference on earthquake Engineering*. Sydney, Australia (cit. on pp. 36–38).

Semblat, J. F. (2011). “Modeling seismic wave propagation and amplification in 1D/2D/3D linear and nonlinear unbounded media”. In: *International Journal of Geomechanics* 11.6, pp. 440–448 (cit. on p. 42).

Shen, Y. (2019). *Prise en compte des effects non-linéaires dans la conception des fondations superficielles sous charge sismique*. Tech. rep. Paris: Ecole Nationale des Ponts et Chaussées (cit. on pp. 50, 52, 236).

Shen, Y., J. Pérez-Herreros, F. Cuira, J.-F. Semblat, and S. Burlon (2021). “Dynamic response of shallow foundations on reinforced soil with rigid inclusions”. In: *17th Conference on Earthquake Engineering*. Sendai, Japan (cit. on pp. 42, 213).

Shen, Y., J. Pérez-Herreros, F. Cuira, J.-F. Semblat, and S. Burlon (2022a). “Interaction cinématique sol-structure d'un massif renforcé par inclusions rigides sous séisme”. In: *Journées Nationales de Géotechnique et de Géologie de l'Ingénieur JNGG2022*. Lyon, France (cit. on p. 42).

Shen, Y., J. Pérez-Herreros, F. Cuira, J.-F. Semblat, and S. Burlon (2022b). “Interaction inertielle sol-structure d'un massif renforcé par inclusions rigides”. In: *Journées Nationales de Géotechnique et de Géologie de l'Ingénieur JNGG2022*. Lyon, France (cit. on pp. 42, 213).

Shen, Y., J. Pérez-Herreros, F. Cuira, J.-F. Semblat, and S. Burlon (2022c). “Kinematic interaction forces in rigid inclusions under seismic loading”. In: *3rd European Conférence on Earthquake Engineering & Seismology*. Bucharest, Roumania, pp. 172–179 (cit. on p. 42).

Shen, Y., J. Pérez-Herreros, and L. Pereira (2022d). *Manuel scientifique FONDSIS*. Tech. rep. Paris: Terrasol (cit. on p. 232).

Simo, J. C. and R. L. Taylor (1985). "Consistent tangent operators for rate-independent elastoplasticity". In: *Computer Methods in Applied Mechanics and Engineering* 48.1, pp. 101–118 (cit. on p. 227).

Simon, B. (2010). "Une methode simplifiee pour le calcul des semelles sur sol renforce par inclusions rigides". In: *Journées Nationales de Géotechnique et de Géologie de l'Ingénieur JNGG2010*. Grenoble, France, pp. 529–536 (cit. on pp. 59, 60).

Sloan, S. W. (2013). "Geotechnical stability analysis". In: *Geotechnique* 63.7, pp. 531–572 (cit. on p. 62).

Son, Q. T. (2009). "Développements théorique et numérique d'un modèle multiphasique pour le calcul des ouvrages renforcés par inclusions". PhD thesis. Ecole Nationale des Ponts et Chaussées (cit. on p. 60).

Soubra, A.-H. (1999). "Upper-Bound Solutions for Bearing Capacity of Foundations". In: *Journal of Geotechnical and Geoenvironmental Engineering* 125.1, pp. 59–68 (cit. on p. 148).

Steenfelt, J. S., B. Foged, A. H. Augustesen, and K. Lyngby (2015). "Izmit Bay Bridge-Geotechnical challenges and innovative solutions". In: *International Journal of Bridge Engineering* 3.3, pp. 53–68 (cit. on p. 17).

Terrasol (2023). *TALREN: méthode de calcul des ouvrages en terre renforcée*. Paris (cit. on pp. 157, 175).

Timoshenko, S. P. (1921). "On the correction for shear of the differential equation for transverse vibrations of prismatic bars". In: *The London, Edinburgh, and Dublin Philosophical Magazine and Journal of Science* 41.245, pp. 744–746 (cit. on p. 256).

Vamvatsikos, D. and C. A. Cornell (2002). "Incremental dynamic analysis". In: *Earthquake Engineering and Structural Dynamics* 31.3, pp. 491–514 (cit. on p. 260).

Vamvatsikos, D. and C. A. Cornell (2004). "Applied incremental dynamic analysis". In: *Earthquake Spectra* 20.2, pp. 523–553 (cit. on p. 260).

Vandeputte, D., P. Billion, A. Courtois, P. Labbé, and G. Devésa (2010). "Impedance Calculations for Foundations on Soil Reinforced With Concrete Inclusions". In: *Proceedings of the CSNI workshop on soil structure interaction (SSI)-knowledge and effect on the seismic assessment of NPPs structures and components*. Ottawa, pp. 375–383 (cit. on p. 35).

Van Eekelen, S. J. M., A. Bezuijen, and O. Oung (2003). "Arching in piled embankments; experiments and design calculations". In: *BGA International Conference on Foundations: Innovations, observations, design and practice*. Dundee, Scotland, pp. 885–894 (cit. on p. 25).

Veletsos, A. and J. Meek (1974). "Dynamic of structure-foundation systems". In: *Earthquake Engineering and Structural Dynamics* 3, pp. 121–138 (cit. on p. 250).

Wuttke, F., B. Kafle, Y. Lins, and T. Schanz (2013). "Macroelement for statically loaded shallow strip foundation resting on unsaturated soil". In: *International Journal of Geomechanics* 13.5, pp. 557–564 (cit. on pp. 46–48).

Yang, Y., Y. P. Cheng, W. Gong, H. Fan, and G. Dai (2023). “Effect of cushion types on the seismic response of structure with disconnected pile raft foundation”. In: *Structures* 48.2023, pp. 1333–1345 (cit. on pp. 29, 38).

Yang, Y., H. Fan, Y. P. Cheng, W. Gong, G. Dai, F. Liang, and Y. Jia (2022). “Seismic response of nuclear power station with disconnected pile-raft foundation using dynamic centrifuge tests”. In: *Journal of Cleaner Production* 379.2022, p. 134572 (cit. on pp. 34, 38).

Zienkiewicz, O. C. and R. L. Taylor (2000). *The Finite Element Method*. Elsevier (cit. on p. 232).

List of Figures

List of Tables

List of Acronyms

Notation	Description
ASIRI	Amélioration des Sols par Inclusions RIgides.
BIE	Boundary integral equation.
CAV	Cumulative absolute velocity.
DM	Damage measure.
EDP	Engineering demand parameter.
FELA	Finite element limit analysis.
FEM	Finite element method.
IDA	Incremental dynamic analysis.
IM	Intensity measure.
LTP	Load Transfer Platform = *Plate-forme de Transfert de Charge*.
PGA	Peak ground acceleration.
PGV	Peak ground velocity.
PSA	Pseudo-acceleration.
SDOF	Single-Degree-Of-Freedom system.
SFSI	Soil-Foundation-Structure Interaction = *Interaction Sol-Fondation-Structure*.
SSI	Soil-Structure Interaction = *Interaction Sol-Structure*.

List of Symbols

Notation	Description
B	Diameter of circle foundation or small dimension of rectangular foundation.
D	Dynamic magnification factor.
E_H	Horizontal load transfer efficiency.
E_V	Vertical load transfer efficiency.
E_p	Young's modulus of pile or rigid inclusion element.
E_s	Frontal reaction modulus per unit length or Young's modulus of soil.
E	Young's modulus.
F	Dimensionless frequency for ground motion modification.
G	Shear modulus.
I_p	Quadratic moment of area.
I_u	Displacement kinematic interaction factor.
I_{PSA}	Pseudo-acceleration kinematic interaction factor.
L_{ext}	Length outside the kinematic failure mechanism.
L_{int}	Length within the kinematic failure mechanism.
L	Length of pile or inclusion.
V_s	Shear Wave Velocity.
α	Coverage area ratio.
η	ratio of shear wave propagation velocity at an interface of two soil layers.
ν	Poisson's ratio.
ω	Angular frequency.
ρ	Mass density.
ξ	Damping ratio.
a_0	Dimensionless frequency.
d	Diameter of pile or inclusion.
f_c	Fundamental vertical frequency of the soil column.
f_s	Fundamental horizontal frequency of the soil column.
l_0	Transfer length.
p_l^*	Standard net limit pressure.
q_s	Limit value of skin friction.

Notation	Description
s	Axe-to-axe spacing of piles or inclusions.

Résumé en français

A

Objectif du projet

L'utilisation des inclusions rigides pour le renforcement du sol a suscité un intérêt en raison de leur potentiel à améliorer la capacité portante de la fondation, à réduire les tassements et à renforcer la stabilité globale de l'ouvrage. Comprendre les phénomènes d'interaction sol-structure (ISS) qui régissent de telles fondations sous chargement sismique est essentiel pour garantir leur performance sécurisée et fiable dans les zones sujettes aux séismes.

Dans la pratique, la conception sismique des fondations renforcées par inclusions rigides repose principalement sur les approches pseudo-statiques introduites par le projet national ASIRI (ASIRI, 2012). Cependant, la fiabilité de ces méthodes de calcul largement utilisées dans des contextes sismiques reste incertaine. Par conséquent, il devient impératif d'étudier la différence entre les résultats obtenus à partir d'un modèle pseudo-statique simplifié et d'un modèle dynamique sophistiqué. Cette exploration s'étend également à l'examen du potentiel d'amélioration des approches de calcul pseudo-statique proposée.

Il est aussi nécessaire de quantifier la contribution des inclusions rigides à l'amélioration de la capacité portante. Cependant, une méthode pratique fait défaut. Ainsi, la prise en compte de l'inertie du sol devient cruciale dans les scénarios sismiques. Dans le contexte de l'amélioration du sol par inclusions rigides, la quantification des effets de renforcement à l'aide de la théorie de la conception à la rupture (Salençon, 1983) constitue une motivation essentielle pour cette recherche.

De plus, la réponse dynamique des structures fondées sur une fondation améliorée par inclusions rigides présente un problème complexe d'ISS qui nécessite l'utilisation de méthodes de calcul adaptées. Dans le cadre de la conception basée sur les performances, les codes de conception contemporains tels que l'Eurocode 8 (AFNOR, 2007) reconnaissent l'influence de l'ISS et la dissipation d'énergie non-linéaire lors de séismes intenses (Pérez-Herreros, 2020).

L'approche la plus directe, connue sous le nom d'approche globale, consiste à modéliser le sol, les éléments de fondation et la superstructure pour prendre en compte le comportement non-linéaire du système de fondation-superstructure. Cependant, cette méthode requiert des ressources informatiques importantes. Pour réduire la complexité et les coûts informatiques, le concept d'un macro-élément, introduit initialement par Nova and Montrasio (1991) et plus tard appliqué de manière efficace aux fondations superficielles

et profondes, permet de consolider les effets d'ISS linéaires et non-linéaires au sein d'un élément non-linéaire multidirectionnel. Le macro-élément intègre une loi constitutive non-linéaire définie en termes de forces généralisées et de déplacements dans le cadre de la théorie de la plasticité ou de l'hypoplasticité, capable de coupler les comportements dynamiques linéaires et non-linéaires (Pérez-Herreros, 2020).

Dans ce contexte, l'objectif principal de ce travail de thèse est d'explorer à la fois les aspects linéaires et non-linéaires de l'ISS pour les fondations renforcées par inclusions rigides sous chargement sismique. L'objectif final est de développer un modèle de macro-élément capable de représenter ces comportements.

Par conséquent, la recherche vise à aborder les aspects fondamentaux suivants :

- Revue des études expérimentales et numériques existantes

  Une revue exhaustive des études expérimentales et numériques existantes dans la littérature offre des informations précieuses sur le comportement des fondations renforcées par inclusions rigides sous diverses conditions de charge. Plusieurs études ont déjà été menées dans la littérature existante, et dans certains cas, les observations des études liées à d'autres systèmes de fondation peuvent être extrapolés et appliqués aux inclusions rigides. Néanmoins, un écart important persiste entre les investigations orientées vers la recherche et leur application pratique dans l'ingénierie.

- Comportement de l'ISS linéaire

  Cette étude se concentre sur l'investigation du comportement de l'ISS des fondations renforcées par inclusions rigides dans le domaine linéaire élastique. L'étude explore les effets de l'interaction inertielle et cinématique, dans le but de comprendre la réponse dynamique du système lorsqu'il est soumis à des charges sismiques. Cette analyse devrait fournir des informations sur le comportement linéaire de ces fondations et leur réponse au mouvement du sol induit par les séismes.

- Stabilité sismique des fondations

  L'exploration du domaine non-linéaire commence par une évaluation de la stabilité sismique des fondations grâce à la mise en œuvre de la théorie du calcul à la rupture. Plus précisément, l'approche cinématique par l'extérieur de la théorie du calcul à la rupture est utilisée pour établir un domaine de stabilité.

  L'objectif de cette approche est de fournir une compréhension approfondie sur les mécanismes de rupture que les fondations sur inclusions rigides peuvent rencontrer sous des charges sismiques et la capacité portante associée.

- Développement et validation du macro-élément

  L'accent principal est mis sur le développement d'un modèle de macro-élément qui représente précisément le comportement des fondations renforcées par inclusions rigides et intègre les effets d'ISS identifiés par l'analyse linéaire et le calcul à la rupture. Ce macro-élément est censé offrir un outil efficace pour analyser la réponse de ces systèmes de fondation sous chargement sismique. La recherche comprend également l'incorporation de la modélisation numérique pour valider l'approche proposée du macro-élément. Des études paramétriques peuvent être menées à l'aide du modèle de macro-élément pour obtenir une compréhension complète des effets d'ISS sur de telles fondations.

Conclusion principale

Cette thèse de doctorat examine les phénomènes d'ISS dynamique des fondations renforcées par inclusions rigides sous chargement sismique en utilisant plusieurs approches complémentaires, y compris différents modèles numériques, stratégies de modélisation et solution analytiques. L'étude est complétée par un examen de la capacité portante de telles fondations, en utilisant l'approche cinématique par l'extérieur de la théorie du calcul à la rupture. De plus, un nouveau macro-élément a été développé pour traiter le problème d'ISS dynamique non-linéaire des fondations renforcées par inclusions rigides sous chargement sismique.

Les principales contributions et conclusions de ce travail sont exposées ci-dessous.

La **revue de la littérature** se concentre sur différents effets d'ISS dynamique et leur impact sur la réponse de la fondation, soit au niveau global sur la fondation entière, soit au niveau local sur le comportement individuel des inclusions rigides, de la plate-forme de transfert de charge, etc. À ce jour, il existe encore peu d'études expérimentales portant sur le comportement dynamique des fondations sur sol renforcé par des inclusions rigides, mais les travaux existants permettent déjà d'observer des caractéristiques intéressantes de ce type de fondation sous chargement sismique. Les méthodes numériques disponibles aujourd'hui peuvent répondre à la plupart des questions concernant les problèmes dynamiques d'ISS dans le domaine linéaire (c'est-à-dire l'interaction cinématique, l'effet de groupe, etc.). Cependant, il est encore nécessaire de disposer d'outils informatiques appropriés pour mieux comprendre les spécificités impliquées dans la réponse non-linéaire de ces fondations.

Les principales conclusions des études numériques et expérimentales mises en évidence dans la revue de la littérature peuvent être résumées comme suit :

- L'introduction d'inclusions rigides atténue le tassement des fondations lors de séismes;
- Comparées aux fondations sur pieux, les inclusions rigides subissent des efforts inertiels plus faibles, principalement en raison de la déconnexion entre la dalle et les inclusions;
- Des effets d'isolation sismique sont observés dans les fondations renforcées par inclusions rigides sous chargements sismiques de haute intensité. La plate-forme de transfert de charge offre la possibilité de développer un mécanisme de glissement à l'interface entre la fondation et la plate-forme de transfert de charge, isolant la structure du sol renforcé qui la supporte. Ce mécanisme non-linéaire empêche une partie de l'énergie sismique arrivant à la base de la structure.

La deuxième partie de cette thèse s'est concentrée sur les principaux effets dynamiques d'ISS développés dans les fondations renforcées par inclusions rigides à travers une **étude d'ISS dans le domaine élastique linéaire**. Les principales observations de cette étude peuvent être résumées comme suit :

- Comparé aux fondations sur pieux, la modification du mouvement sismique à la base de la structure due au phénomène d'interaction cinématique est généralement moins significative. Cet effet est pratiquement imperceptible dans la plage de basses fréquences et ne devient perceptible qu'à des fréquences élevées, bien que l'amplitude soit relativement faible pour la plupart des configurations pratiques. Du point de vue de la conception, cela implique généralement une réduction du mouvement d'entrée par rapport aux conditions en champ libre;
- La présence des inclusions rigides a un impact négligeable sur les impédances dynamiques de la fondation dans les directions horizontales. Dans la direction verticale et de rotation, la raideur dynamique se situe entre celle des fondations superficielles et des fondations sur pieux;
- L'efficacité du transfert de charge verticale dans un système de fondation renforcée par inclusions rigides est observée comme étant supérieure à celle horizontale. Le sol récupère principalement la plupart des forces horizontales transférées par la dalle, ce qui affecte la direction des contraintes dans le sol. Ainsi, l'inclinaison des charges transmises à travers le sol autour des renforcements est plus importante que celle appliquée à la fondation;
- En ce qui concerne les moments fléchissants cinématiques dans les inclusions rigides, les observations sont cohérentes avec celles déjà trouvées pour les fondations sur pieux, le moment fléchissant maximal étant situé aux interfaces entre différentes couches de sol de caractéristiques différentes. Son amplitude est principalement contrôlée par le contraste de rigidité à l'interface. Des différences par rapport aux fondations sur pieux peuvent être observées en tête des inclusions rigides, ce qui

est lié aux différentes conditions aux limites à cet endroit (sans connexion rigide entre les inclusions et la dalle). Enfin, aucun effet de groupe n'est observé lorsqu'un groupe d'inclusions rigides est soumis à une charge cinématique. Cela est également cohérent avec les observations habituelles faites pour les fondations sur pieux.

La capacité portante de la fondation renforcée par inclusions rigides est examinée dans la partie III en utilisant l'approche extérieure cinématique. L'**étude de la stabilité sismique de la fondation** prend en compte le développement des forces d'inertie dans le sol ainsi que l'inclinaison et l'excentricité des charges appliquées par la superstructure à la fondation. Les points suivants servent de résumé les principales contributions :

- Ce travail étend l'application de l'approche cinématique par l'extérieur aux fondations renforcées par inclusions rigides. La validation est réalisée grâce à des comparaisons avec les résultats dans la littérature pour les configurations non renforcées et à une analyse par éléments finis pour les configurations renforcées;
- Pour estimer avec précision la contribution des inclusions dans le cadre de l'approche cinématique par l'extérieur, un multicritère pour les inclusions rigides est proposé, prenant en compte différents modes de rupture;
- Plusieurs facteurs influençant la capacité portante de la fondation sont explorés, révélant que la capacité portante augmente systématiquement avec le taux de substitution. La capacité portante d'une fondation renforcée dépasse constamment celle d'une fondation non renforcée dans les mêmes conditions de chargement : intensité sismique, inclinaison et excentricité;
- Pour les fondations renforcées présentant un facteur de sécurité significatif (c'est-à-dire plus de 3) sous une charge statique centrée verticalement, l'impact de l'inertie du sol peut souvent être négligé. Cependant, lorsque le facteur de sécurité initial de la fondation est déjà faible, une perte significative de capacité portante peut survenir en raison des forces d'inertie du sol.

Un **nouveau macro-élément pour les fondations renforcées par inclusions rigides** sous chargement sismique a été développé dans la partie IV, permettant de prendre en compte à la fois les phénomènes d'ISS linéaire et non-linéaire dans l'étude de la stabilité de structures fondées sur le sol renforcé par inclusions rigides soumises à des charges sismiques.

La surface de rupture déterminée par le calcul à la rupture et les impédances dynamiques de la fondation sont intégrées dans la formulation du macro-élément. Des vérifications de cohérence, des validations par des logiciels tiers et des comparaisons avec des solutions analytiques vérifient la validité des différents composants de ce macro-élément.

Le modèle de macro-élément validé est ensuite utilisé pour mener une étude paramétrique sur une structure simplifiée et une analyse dynamique incrémentale d'un bâtiment de 22

étages. Ces applications démontrent l'utilité et l'efficacité de l'approche du macro-élément d'ISS dans la conception pratique.

Perspectives

Les futures recherches pourraient se concentrer sur les aspects suivants :

Étude dans le domaine linéaire élastique

- Comparaison avec des études expérimentales

  Une analyse comparative peut être menée avec des études expérimentales telles que ICEDA (EDF, 2008a) pour vérifier la validité de l'approche de modélisation numérique.

- Étude de configurations plus complexes

  L'étude se concentre principalement sur des fondations de dimensions relativement modestes, et l'exploration de fondations plus grandes reste inexplorée. Combler cette lacune pourrait répondre à des besoins d'ingénierie spécifiques, tels que les réservoirs de GNL ou les centrales nucléaires.

- Amélioration de la méthode pseudo-statique conventionnelle pour la détermination des charges cinématiques dans les inclusions

  Le travail devrait également se concentrer sur l'amélioration de l'approche pseudo-statique conventionnelle utilisée pour estimer les moments fléchissants cinématiques, dans le but d'améliorer ses performances et de réduire les différences observées avec l'approche dynamique. Ce travail s'appliquerait non seulement aux inclusions rigides, mais aussi aux fondations sur pieux.

Capacité portante sismique

- Effet 3D pour la capacité portante

  Il est également intéressant d'étudier l'effet tridimensionnel sur la capacité portante, car l'étude actuelle de la capacité portante sismique est menée dans un plan en 2D. Des recherches supplémentaires pourraient proposer un facteur de forme pour tenir compte adéquatement de l'effet tridimensionnel, en utilisant soit la modélisation numérique soit un champ de vitesse virtuel en 3D.

- Considération de la contribution de plate-forme de transfert de charge

  L'étude peut être améliorée en considérant la contribution du matelas de transfert de charge dans le mécanisme de rupture intersectant les inclusions rigides, ce qui est actuellement négligé pour faciliter l'utilisation des mécanismes de rupture existants

développés pour les fondations superficielles non renforcées. Cette amélioration pourrait impliquer l'application d'un champ de vitesse cinématiquement admissible.

- Profil homogénéisé

  Suivant l'approche d'homogénéisation, un profil homogénéisé peut être proposé avec des paramètres de résistance équivalents (c-φ) par le biais d'une analyse approfondie de diverses configurations. Une série de graphiques pourrait être établie pour indiquer les corrélations potentielles entre les paramètres de résistance équivalents (c-φ), les propriétés du sol mou et le taux de substitution.

Approche de macro-élément

- Abaque de conception

  Un ensemble de courbes peut être produit à l'aide de cet outil pour offrir des compréhensions sur la réponse d'ISS linéaire et non-linéaire des structures fondées sur des inclusions rigides, en termes de plusieurs paramètres adimensionnels.

- Comparaison croisée

  Une étude comparative supplémentaire pourrait être réalisée en utilisant une modélisation numérique 3D non-linéaire, des résultats expérimentaux issus de essais en centrifugeuse et de mesures sismiques réelles (par exemple, le pont Rion-Antirion) afin d'enrichir l'application du modèle macro-élément et de recueillir davantage d'informations.

- Réponse dépendante de la fréquence

  Dans le modèle macro-élément actuel, le champ lointain est caractérisé par un ensemble de ressorts et d'amortisseurs calibrés à l'aide de fonctions d'impédance dynamique. Cependant, la formulation actuelle ne tient pas compte de la réponse dépendante de la fréquence. Pour remédier à cette limitation, les effets dépendant de la fréquence peuvent être intégrés dans le modèle de macro-élément proposé grâce à des méthodes numériques avancées, telles que l'approche Laplace-Temps.

B

Analogue modelling of the dynamic response of a soil column

The soil displacement profile $g(z)$ is assumed to replicate the shape of the fundamental eigenmode of the soil column, with an amplitude equal to d_{max} at the soil surface. This amplitude corresponds to the maximum free-field displacement at the ground surface, and in this context, it is obtained as the average value of the peak ground displacements from the five artificial accelerograms. The fundamental eigenmode can be obtained through a discrete model, as illustrated in Figure B.1.

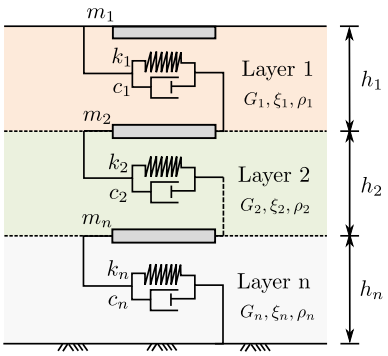

Fig. B.1. Discrete model to assessing the fundamental model of a soil column (Brûlé and Cuira, 2018)

The behaviour of a soil column consisting of n layers can be approximated by representing it as an equivalent model composed of a series arrangement of n simple oscillators. Each oscillator comprises concentrated surface masses m_i linked to an analogue Kelvin-Voigt model. Each layer is defined by its shear modulus G_i, density ρ_i and material damping ratio ξ_i.

The concentrated masses m_i that define this analogue model are determined using Equations B.1 and B.2.

- For the first layer:

$$m_1 = \frac{h_1 \rho_1}{2} \tag{B.1}$$

- For layers other than the first one:

$$m_i = \frac{h_i \rho_i + h_{i-1} \rho_{i-1}}{2} \tag{B.2}$$

The stiffness of this analogue model is represented by Equation B.3.

$$k_i = \frac{G_i}{h_i} \tag{B.3}$$

Solving Equation B.4 in matrix form for this discretised system provides the displacement profile $g(z)$ at each node i for all the eigenmodes.

$$\underline{\underline{K}}.\underline{U_i} = \omega_i^2 \underline{\underline{M}}.\underline{U_i} \tag{B.4}$$

where $\underline{\underline{K}}$ is the stiffness matrix, $\underline{\underline{M}}$ is the mass matrix, $\underline{U_i}$ represents the i^{th} mode, and ω_i is the i^{th} modal angular frequency.

C

Complementary results for dynamic impedances

The detailed comparisons of the reinforced foundation with the configuration A01 with the corresponding shallow foundations and pile foundations are provided in Section 5.3 of Chapter 5. The other configurations of the reinforced foundation, listed in Table C.1, are also compared with the shallow foundations and the pile foundations with LTP.

Tab. C.1. Main characteristics of the studied configurations

Group	Case	f_s* (Hz)	f_c** (Hz)	B/L	L/d	E_p/E_s	s/d	α	Figure
B	01	2.42	4.76	1	23.8	517	4.76	3.46%	Figure C.1
	02	4.43	8.72	"	"	129	"	"	Figure C.2
C	01	3.50	6.89	1	31.3	230	6.25	2.01%	Figure C.3
	02	"	"	"	19.2	"	3.85	5.31%	Figure C.4
D	01	3.50	6.89	1	23.8	230	3.57	6.16%	Figure C.5
	02	"	"	"	"	"	5.95	2.22%	Figure C.6
E	01	3.50	6.89	0.33	23.8	230	4.76	3.46%	Figure C.7
	02	"	"	2	"	"	"	"	Figure C.8

* f_s is horizontal fundamental frequency of soil column
** f_c is vertical fundamental frequency of soil column

The main characteristics of different groups are listed as follows:

- Group A: reference configuration (α = 3.46 %);
- Group B: shear wave velocity V_s, 100 m/s for B01 and 200 m/s for B02;
- Group C: coverage area ratio α, α = 2.01 % for C01, α = 5.31 % for C02 and α = 7.54 % for C03 ;
- Group D: centre-to-centre spacing, 1.5 m for D01 and 2.5 m for D02, as depicted in Figure 4.7;
- Group E: foundation dimension B, 3 m for E01 and 20 m for E02, as depicted in Figure 5.2.

The comparisons are conducted concerning dynamic stiffness, damping ratio, and dynamic magnification factor. The dynamic stiffness values are normalised by the static stiffness of the shallow foundation with the LTP for each direction. The damping is expressed in the form of a damping ratio, with a maximum value of 1. Additionally, the dynamic magnification factor is also examined.

The observations from the comparisons remain consistent with the results presented in Section 5.3 as the parameters of the foundation systems are varied. These parameters include soil stiffness, coverage area ratio, number of rigid inclusions, inclusion spacing, and foundation dimension.

To briefly recap, the conclusions from the comparison with different foundation systems are provided.

Regarding dynamic stiffness, the following observations emerge:

- In the horizontal direction, the dynamic stiffness of a reinforced foundation is comparable to that of a shallow foundation with LTP;
- In the vertical and rotational directions, the dynamic stiffness of a reinforced foundation falls between that of a shallow foundation with LTP and a pile foundation with LTP.

Concerning the damping ratio, the conclusions are as follows:

- In the horizontal direction, the damping of a reinforced foundation resembles that in a shallow foundation with LTP;
- In the vertical and rotational directions, the damping characteristics in a reinforced foundation align with those of a pile foundation with LTP.

In terms of the dynamic magnification factor, the key findings are as follows:

- In the horizontal direction, the dynamic magnification factor of a reinforced foundation mirrors that of a shallow foundation with LTP;
- In the vertical and rotational directions, the dynamic magnification factor of a reinforced foundation is akin to that of a pile foundation with LTP, and the maximum amplification of a reinforced foundation is smaller than of a shallow foundation.

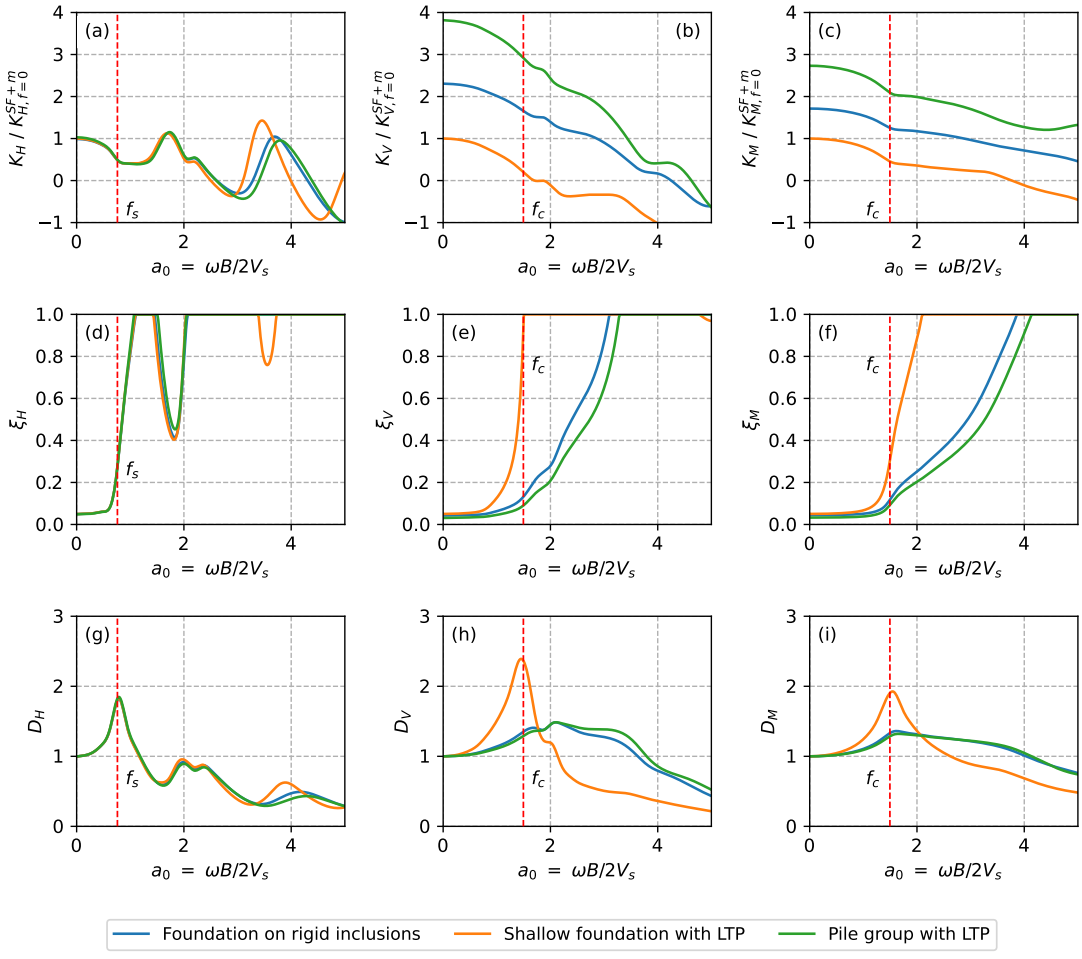

Fig. C.1. Dynamic stiffness and damping ratio of configuration B01 ($V_{s,soft\ soil}$=100 m/s)

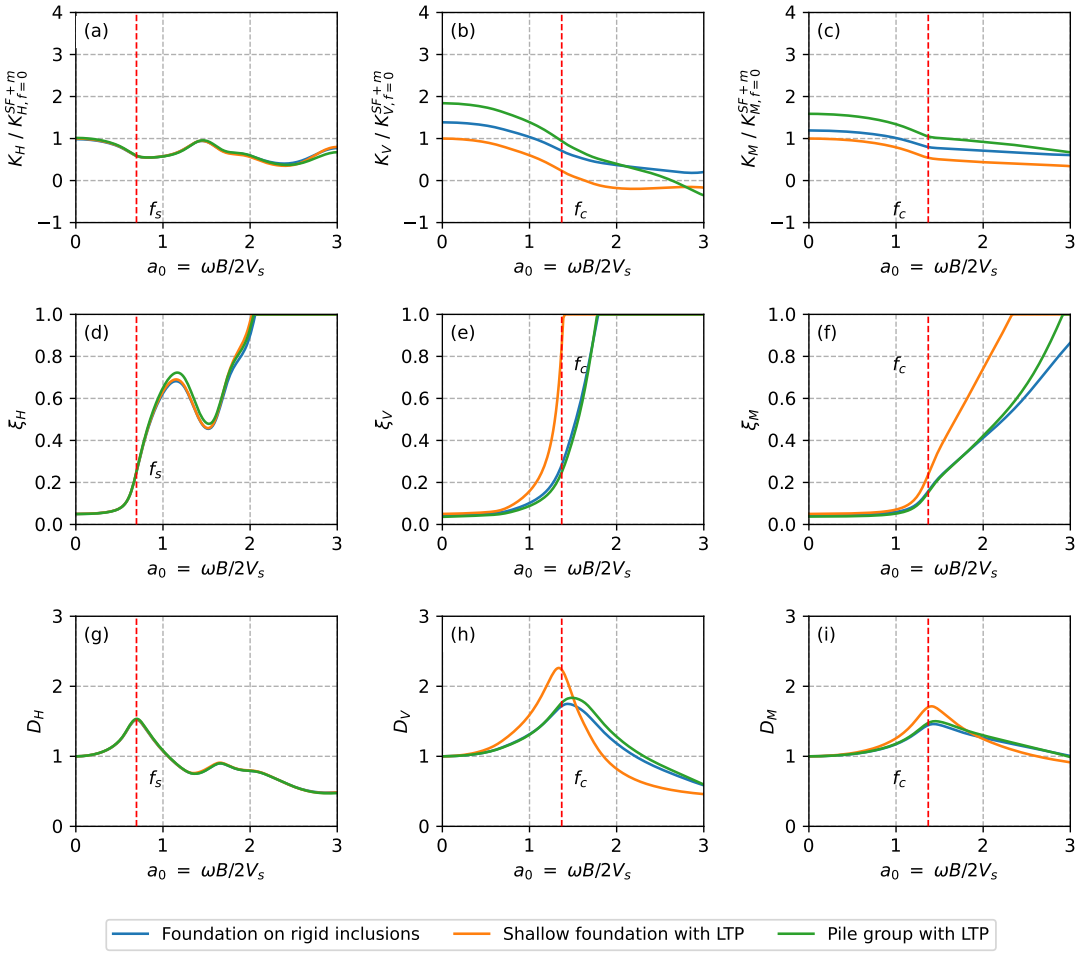

Fig. C.2. Dynamic stiffness and damping ratio of configuration B02 ($V_{s,soft\ soil}$=200 m/s)

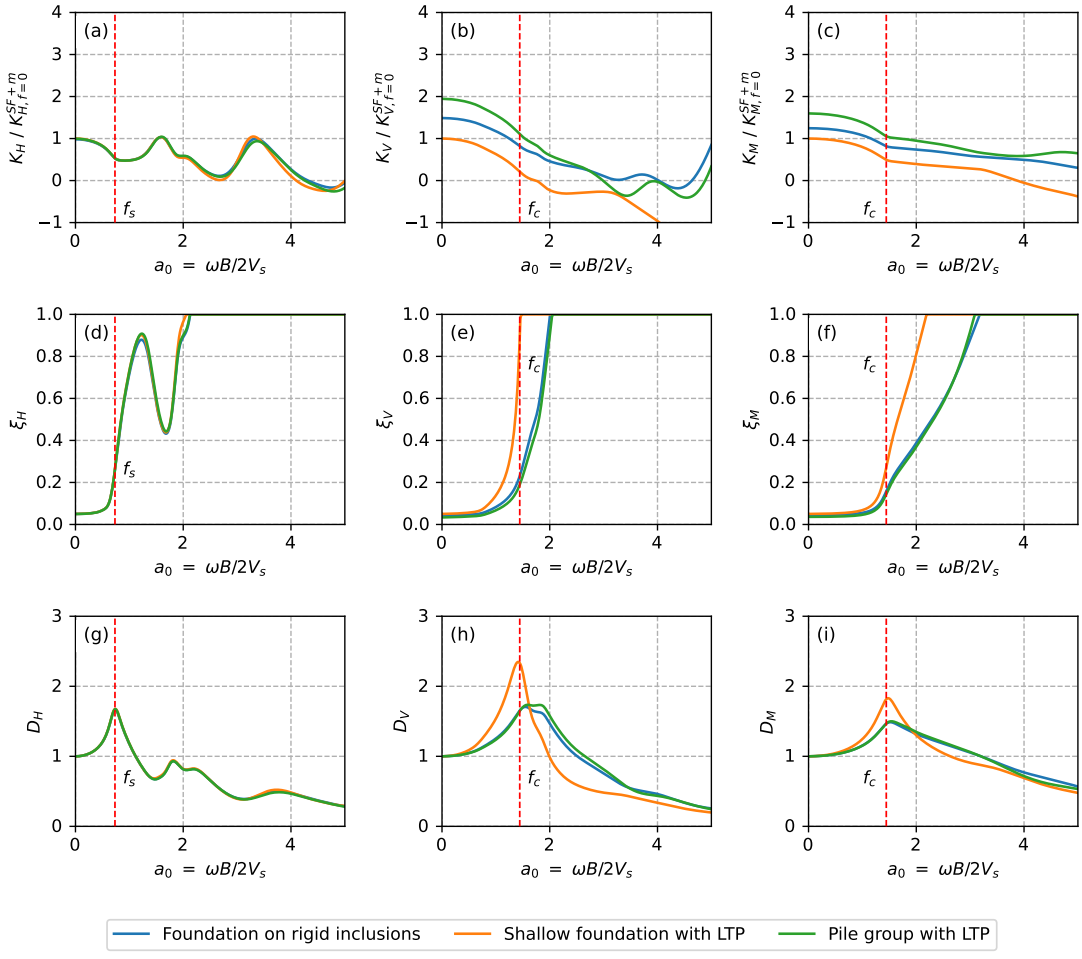

Fig. C.3. Dynamic stiffness and damping ratio of configuration C01 ($\alpha = 2.01\%$)

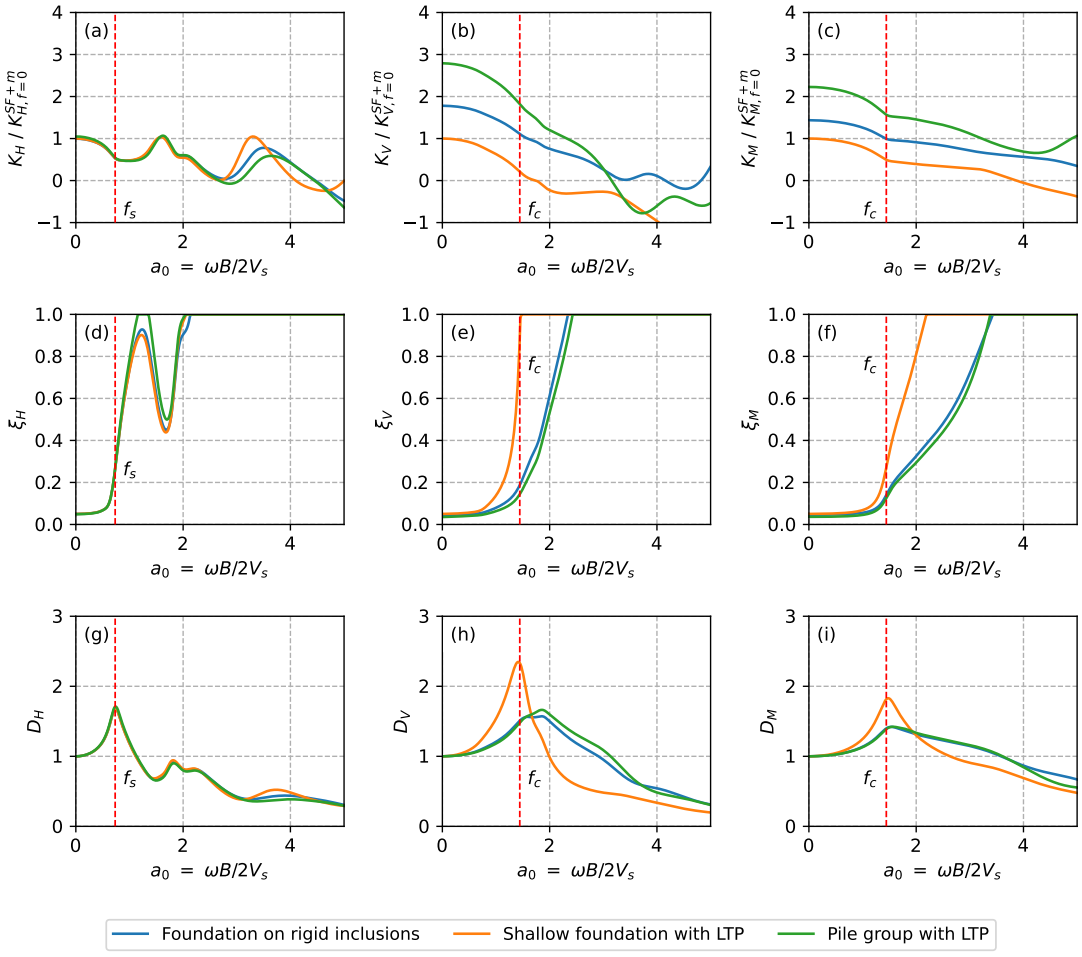

Fig. C.4. Dynamic stiffness and damping ratio of configuration C02 ($\alpha = 5.31\%$)

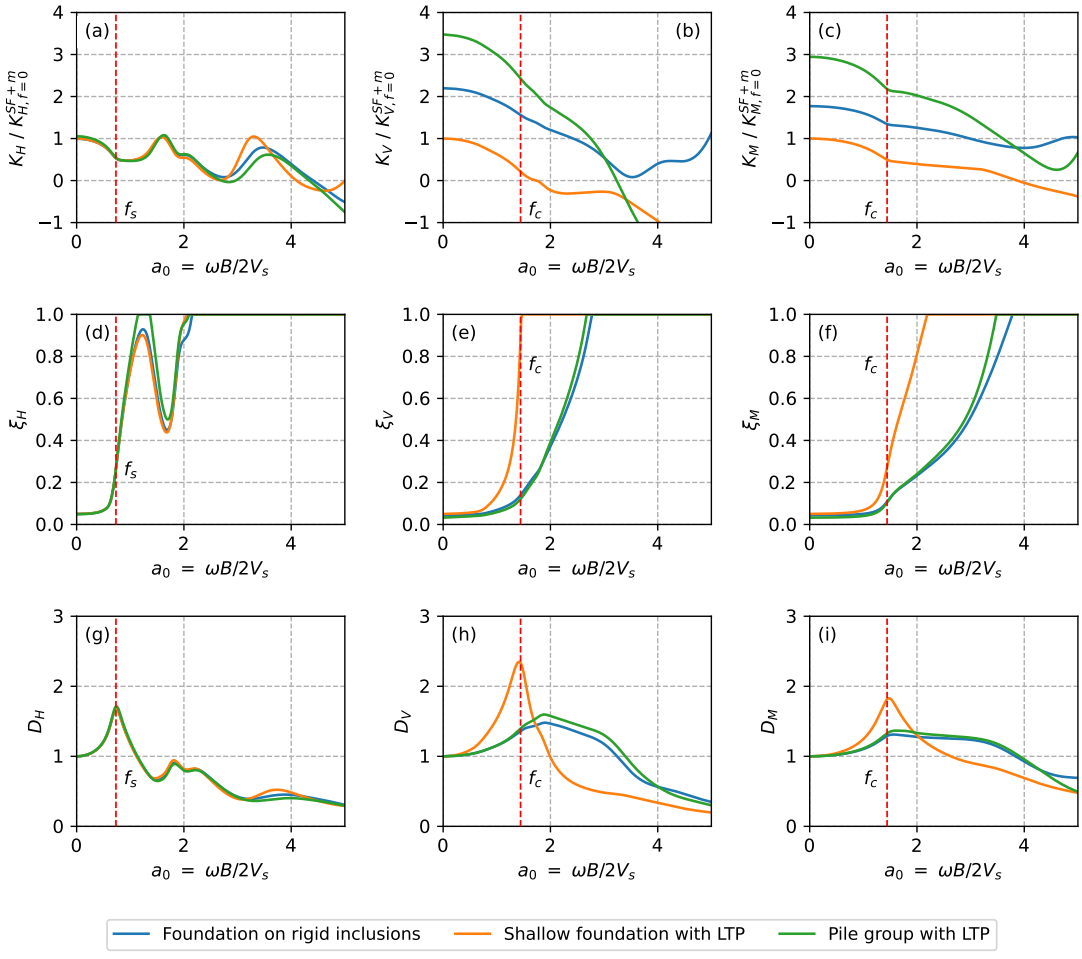

Fig. C.5. Dynamic stiffness and damping ratio of configuration D01 ($s = 1.5\ m, N_{RI} = 49$)

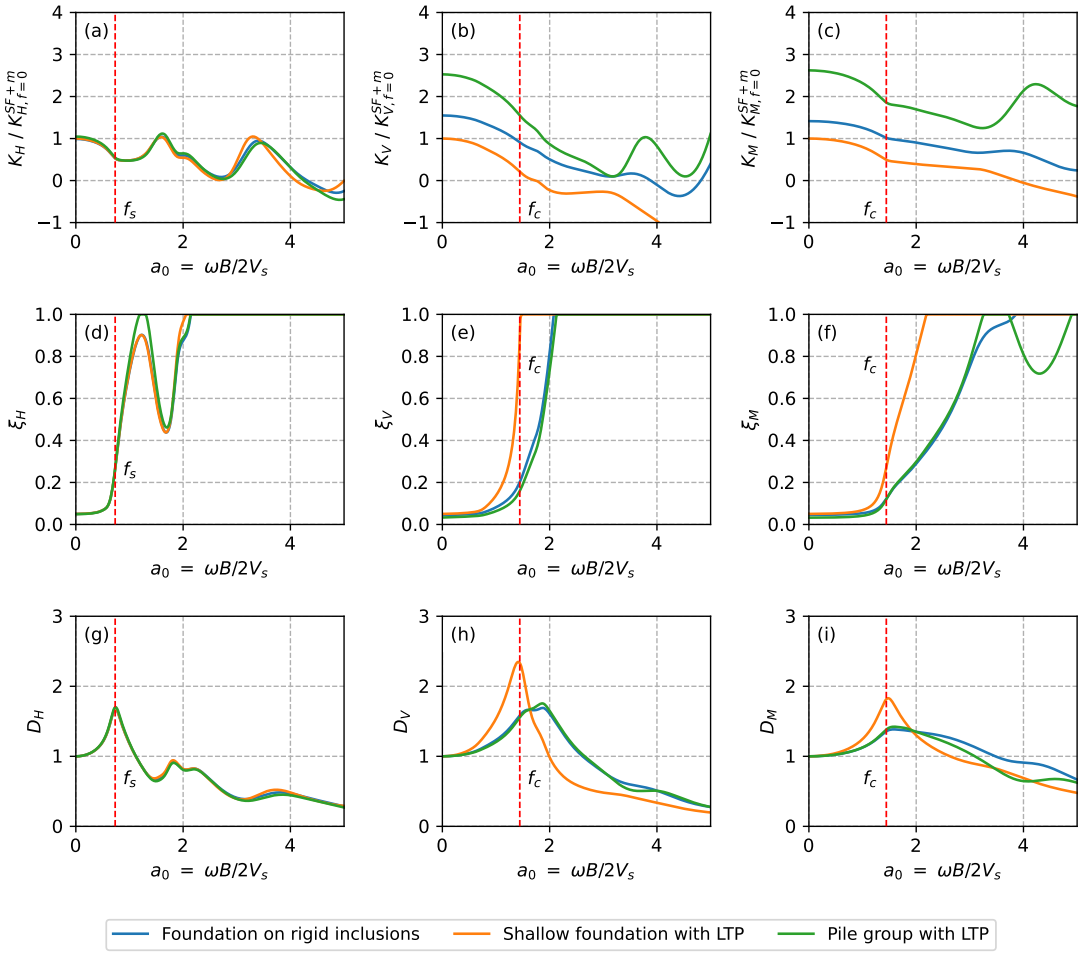

Fig. C.6. Dynamic stiffness and damping ratio of configuration D02 ($s = 2.5\ m, N_{RI} = 25$)

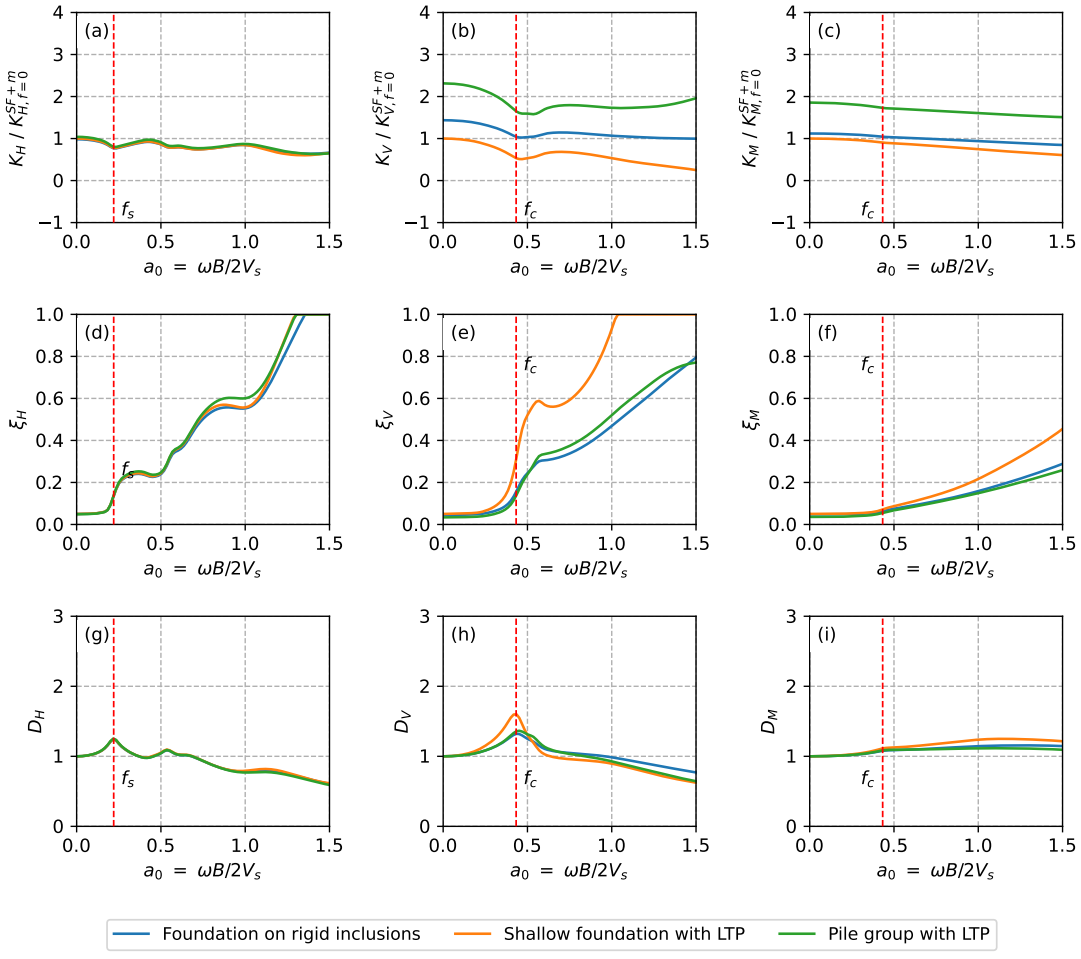

Fig. C.7. Dynamic impedances of configuration E01 ($B = 3\ m$)

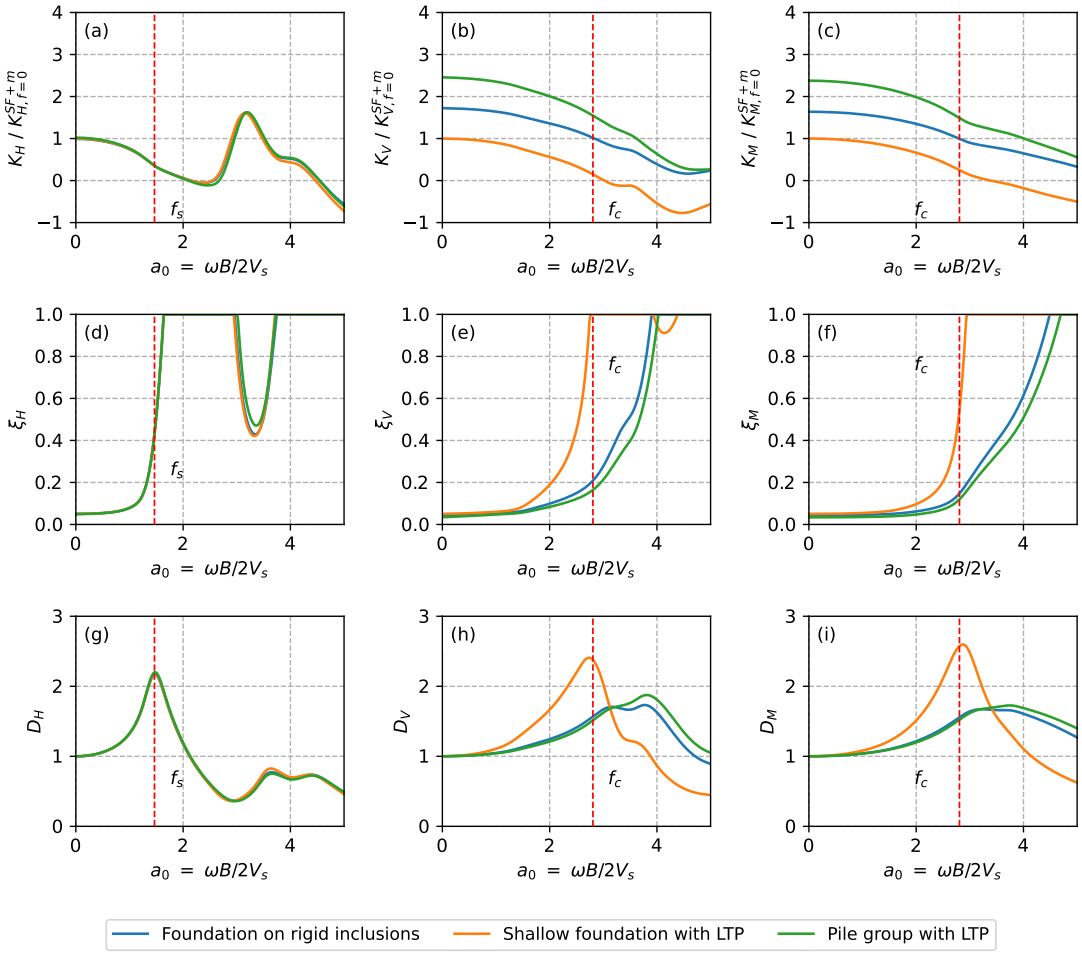

Fig. C.8. Dynamic impedances of configuration E02 ($B = 20\ m$)

D

Maximum resisting rate functions for the usual criteria

Maximum resisting rate functions π for the usual criteria are presented in this Appendix.

For a Tresca criterion:

- In the volume:

$$\pi(\underline{\underline{\widehat{d}}}) = \begin{cases} +\infty & \text{if} \quad tr(\underline{\underline{\widehat{d}}}) \neq 0 \\ C(|\widehat{d}_1| + |\widehat{d}_2|) & \text{if} \quad tr(\underline{\underline{\widehat{d}}}) = 0 \end{cases} \tag{D.1}$$

- Along the lines of velocity discontinuity, with normal vector $\underline{n}$:

$$\pi(\underline{n}, \|\underline{\widehat{U}}\|) = \begin{cases} +\infty & \text{if} \quad \|\underline{\widehat{U}}\| \cdot \underline{n} \neq 0 \\ C|\|\underline{\widehat{U}}\|| & \text{if} \quad \|\underline{\widehat{U}}\| \cdot \underline{n} = 0 \end{cases} \tag{D.2}$$

For a Tresca criterion without tensile strength:

- In the volume:

$$\pi(\underline{\underline{\widehat{d}}}) = \begin{cases} +\infty & \text{if} \quad tr(\underline{\underline{\widehat{d}}}) \neq 0 \\ C(|\widehat{d}_1| + |\widehat{d}_2| - tr(\underline{\underline{\widehat{d}}})) & \text{if} \quad tr(\underline{\underline{\widehat{d}}}) = 0 \end{cases} \tag{D.3}$$

- Along the lines of velocity discontinuity, with normal vector $\underline{n}$:

$$\pi(\underline{n}, \|\underline{\widehat{U}}\|) = \begin{cases} +\infty & \text{if} \quad \|\underline{\widehat{U}}\| \cdot \underline{n} \neq 0 \\ C(|\|\underline{\widehat{U}}\|| - \|\underline{\widehat{U}}\| \cdot \underline{n}) & \text{if} \quad \|\underline{\widehat{U}}\| \cdot \underline{n} = 0 \end{cases} \tag{D.4}$$

For a Coulomb criterion:

- In the volume:

$$\pi(\underline{\underline{\widehat{d}}}) = \begin{cases} \dfrac{C}{tan\varphi} tr(\underline{\underline{\widehat{d}}}) & \text{if} \quad tr(\underline{\underline{\widehat{d}}}) > (|\widehat{d}_1| + |\widehat{d}_2|) sin\varphi \\ +\infty & \text{otherwise} \end{cases} \tag{D.5}$$

- Along the lines of velocity discontinuity, with normal vector $\underline{n}$:

$$\pi(\underline{n}, \|\widehat{\underline{U}}\|) = \begin{cases} +\infty & \text{if} \quad \|\widehat{\underline{U}}\| \cdot \underline{n} \neq 0 \\ C|\|\widehat{\underline{U}}\|| & \text{if} \quad \|\widehat{\underline{U}}\| \cdot \underline{n} = 0 \end{cases} \tag{D.6}$$

E

Numerical resolution of the macro-element

E.1 Dynamic numerical integration

The time response of the system can be obtained using the Newmark-Beta algorithm. In the formulation of the Newmark-Beta algorithm, the integral equations for velocity and displacement are expressed as follows:

$$\underline{\dot{U}}_1 = \underline{\dot{U}}_0 + (1-\gamma)\Delta t\underline{\ddot{U}}_0 + \gamma\Delta t\underline{\ddot{U}}_1 \tag{E.1}$$

$$\underline{U}_1 = \underline{U}_0 + \Delta t\underline{\dot{U}}_0 + (1-\beta)\Delta t^2\underline{\ddot{U}}_0 + \beta\Delta t^2\underline{\ddot{U}}_1 \tag{E.2}$$

The index 0 denotes the initial step with known acceleration, velocity, and displacement, while the index 1 corresponds to the next step to be determined.

It is evident that the factors γ and β describe the evaluation between the influence of the initial acceleration and the final acceleration in a time step Δt. The stability conditions for the Newmark-beta algorithm are introduced as follows:

- $\gamma < \frac{1}{2}$: unstable;
- $\gamma \geq \frac{1}{2}$ and $\beta \geq \frac{\gamma}{2}$: unconditionally stable;
- $\gamma \geq \frac{1}{2}$ and $\beta < \frac{\gamma}{2}$: conditionally stable if the time step is sufficiently small.

Therefore, the combination of $\gamma = \frac{1}{2}$ and $\beta = \frac{1}{4}$, which results in an unconditionally stable scheme with the best accuracy, is the most widely used scheme in structural mechanics.

This scheme is employed to solve the equation of motion described by Equation 11.45. Using the notations $n_0 = \gamma\Delta t$, $n_1 = \beta\Delta t^2$, $n_2 = (1-\gamma)\Delta t$, and $n_3 = (\frac{1}{2}-\beta)\Delta t^2$, the dynamic equation can be simplified as follows:

$$(\underline{\underline{M}} + n_0\underline{\underline{C}} + n_1\underline{\underline{K}})\underline{\ddot{U}}_1 = \underline{P} + \underline{\underline{C}}(\underline{\dot{U}}_0 + n_2\underline{\ddot{U}}_0) + \underline{\underline{K}}(\underline{U}_0 + \Delta t\underline{\dot{U}}_0 + n_3\underline{\ddot{U}}_0) \tag{E.3}$$

E.2 Global stiffness matrix assembly

The global stiffness matrix assembly is illustrated in Figure E.1.

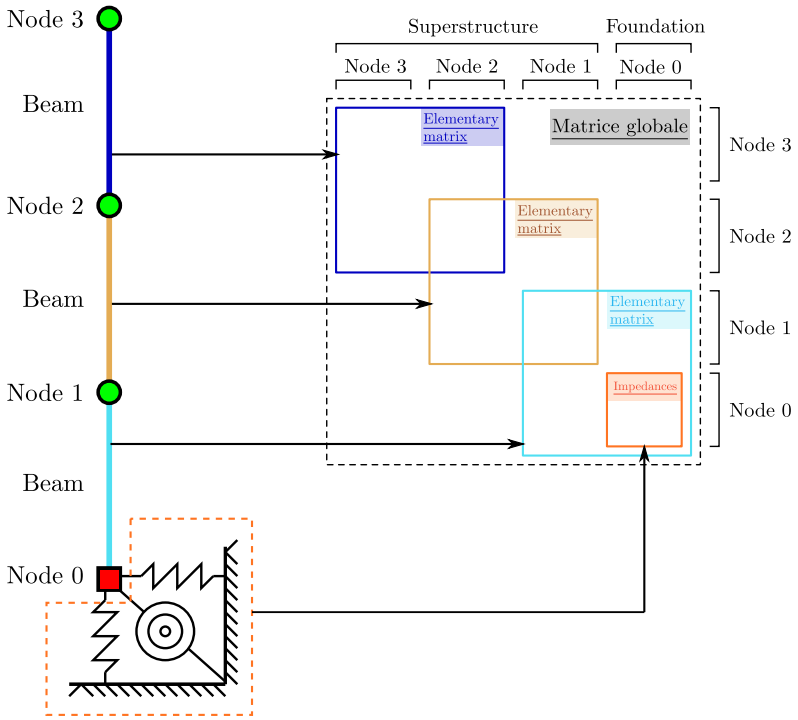

Fig. E.1. Illustration of the global stiffness matrix assembly

E.3 Numerical resolution scheme

The numerical resolution scheme can be found in Figure E.2.

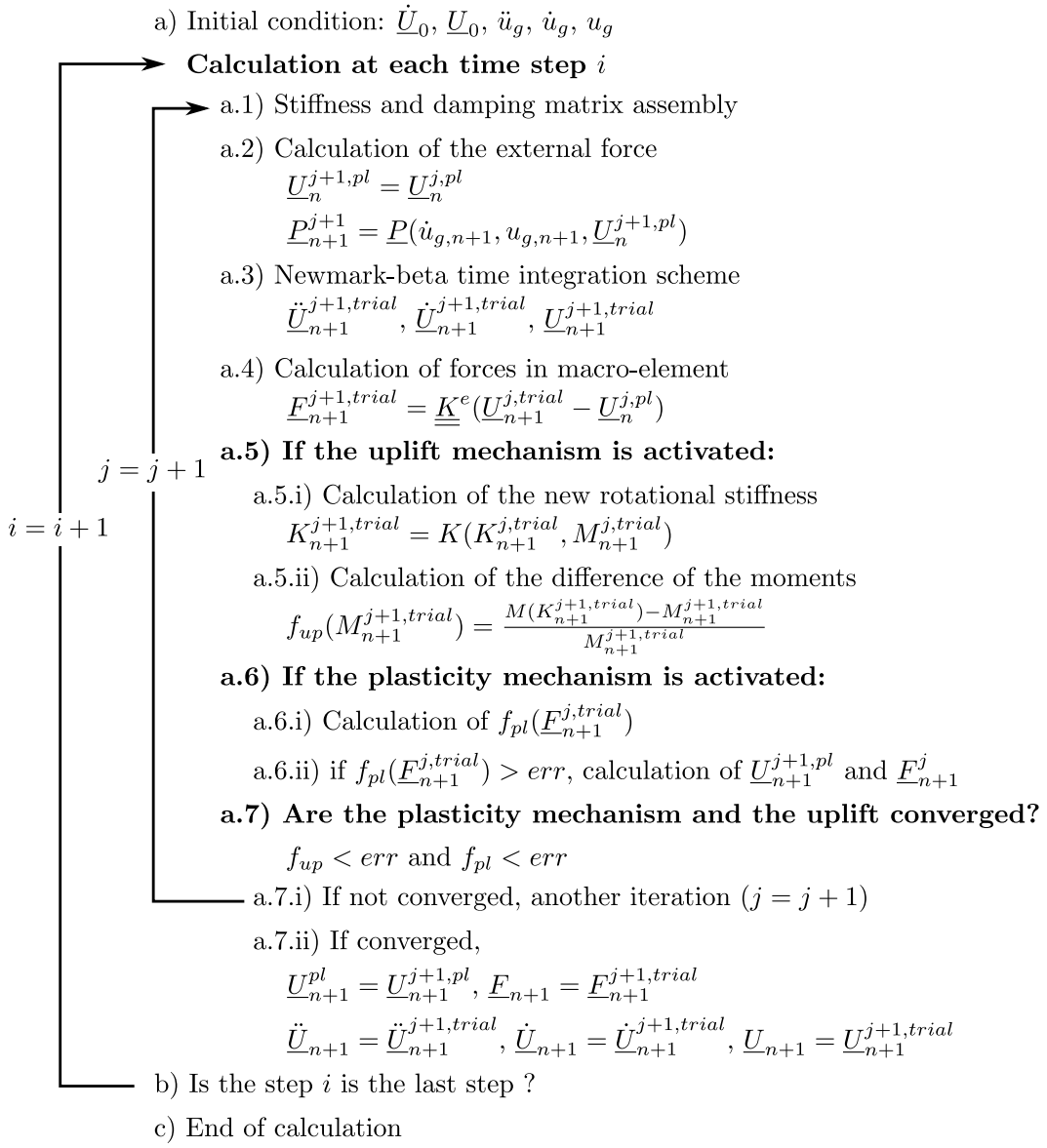

Fig. E.2. Macro-element numerical resolution scheme

Macro-element validation

F

F.1 Superstructure and assembly with SSI springs

The characteristics of the models to validate the superstructure and the assembly with SSI springs are listed as follows. The models are depicted in Figure F.1.

- PFC01: an Euler-Bernoulli beam with a fixed base under horizontal forces;
- PFC02: a Timoshenko beam with a fixed base under horizontal forces;
- PFC03: an Euler-Bernoulli beam with SSI springs under horizontal forces and moments;
- PFC04: an Timoshenko beam with SSI springs under horizontal forces and moments;
- RMP01: Vibration mode analysis for a structure composed of an Euler-Bernoulli beam, two lumped masses with SSI springs;
- RMP02: Vibration mode analysis for a fixed base structure composed of four Timoshenko beams, five lumped masses;
- RMP03: Vibration mode analysis for a structure composed of four Timoshenko beams, five lumped masses with SSI springs.

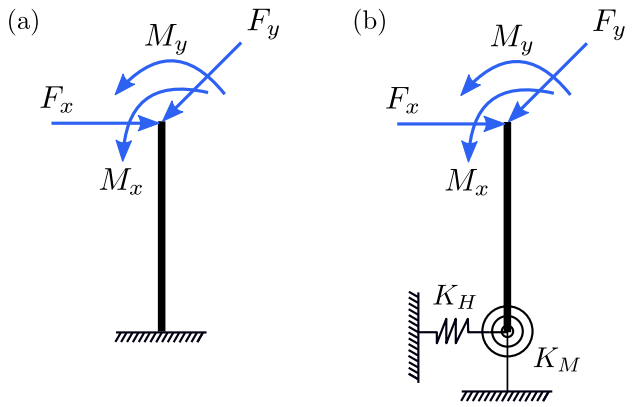

Fig. F.1. Tested structure model under static load: (a) fixed based model and (b) model combined with SSI springs

F.2 Dynamic integration algorithm

The characteristics of the models to validate the dynamic integration algorithm are listed as follows. The models are depicted in Figure F.2.

- PEB01: A fixed base Euler-Bernoulli beam with a lumped mass subjected to a rectangular impulse;
- PEB02: A Euler-Bernoulli beam with a lumped mass and SSI springs subjected to a rectangular impulse;
- PEB03: A fixed base Euler-Bernoulli beam with a distributed mass subjected to a rectangular impulse;
- PEB04: A Euler-Bernoulli beam with a distributed mass and SSI springs subjected to a rectangular impulse;
- PEB05: A Euler-Bernoulli beam with a distributed mass and SSI springs and damping subjected to a rectangular impulse.
- PTB01: A fixed base Timoshenko beam with a lumped mass subjected to a rectangular impulse;
- PTB02: A Timoshenko beam with a lumped mass and SSI springs and damping subjected to a rectangular impulse;
- PTB03: A fixed base Timoshenko beam with a lumped mass subjected to a rectangular impulse;
- PTB04: A Timoshenko beam with a lumped mass and SSI springs and damping subjected to a rectangular impulse;

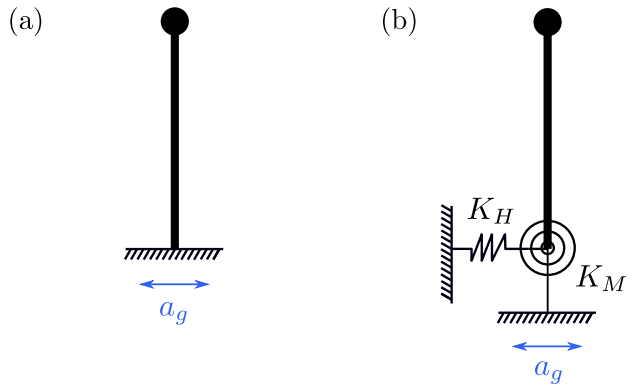

Fig. F.2. Tested structure model under dynamic impulse: (a) fixed based model and (b) model combined with SSI springs

F.3 Non-linear elastic resolution: uplift

The descriptions of the models to validate the non-linear elastic resolution are listed as follows.

- DEP01: System subjected to a sinusoidal signal at 1 Hz with a maximum acceleration of 0.5 m/s^2;
- DEP02: System subjected to a sinusoidal signal at 2 Hz with a maximum acceleration of 0.6 m/s^2;
- DEP03: System subjected to a sinusoidal signal at 1 Hz with a maximum acceleration of 0.6 m/s^2;
- DEP04: System subjected to an accelerogram (Chi-chi HWA033-000) with a maximum acceleration of 0.6 m/s^2;

F.4 Plasticity resolution

The descriptions of the models to validate the plasticity resolution are listed as follows.

- ANL01: Sliding of a rigid block subjected to a rectangular impulse compared with the analytical solution;
- ANL02: Sliding of a rigid block subjected to a rectangular impulse for different safety factors compared with the analytical solution;
- SLA01 - SLA03: Sliding of a rigid block subjected to an accelerogram compared with SLAMMER. Three earthquake records are selected: Tabs BOS-L1, Coalinga C03-000, and Chichi HWA033-000;
- GLP01 - GLP03: Sliding of a structure subjected to an accelerogram compared with Plaxis 2D. Three earthquake records are selected: Tabs BOS-L1, Kobe TAK-090, and Chichi HWA033-000.

F.5 Combination of non-linear elastic resolution and plasticity resolution

The descriptions of the models to validate the combination of non-linear elastic resolution and plasticity resolution are listed as follows.

- VGD01: Macro-element model with the sliding and uplift behaviours subjected to the seismic excitation in X and Z direction;
- VGD02: Macro-element model with the sliding and uplift behaviours subjected to the seismic excitation in X, Y and Z direction.

F.6 Consistency checks

The descriptions of the models used in consistency checks are listed as follows. The studied model is depicted in Figure F.3.

- TCD01 - TCD03: uplift behaviour with different structure heights with the earthquake record Kobe TAK-090;
- TCG01 - TCG04: sliding behaviour with different frictional angles and dilatancy angles with the earthquake record Kobe TAK-090;
- TCC01: Combination of resolution of non-linear elasticity (uplift) resolution and plasticity (sliding) resolution with the earthquake record Kobe TAK-090;

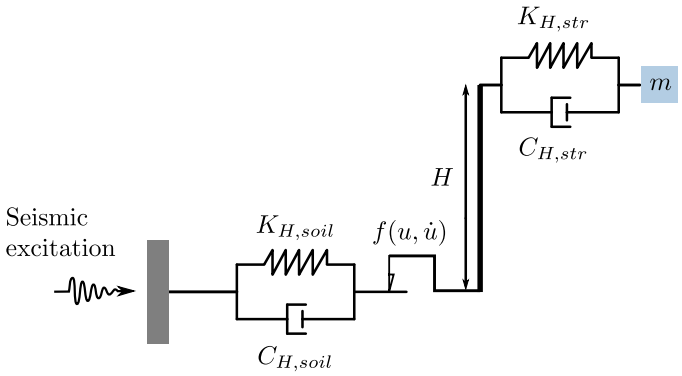

Fig. F.3. Tested structure model in consistency checks

G

Calibrated stiffness and damping

The calibrated stiffness and damping for each tested configuration used in Section 12.2 are listed in the following tables.

Tab. G.1. Calibrated stiffness and damping terms for the configurations with safety factor $F = 6$

F	V_s (m/s)	h_{eq} (m)	f_h (Hz)	K_x (MN/m)	K_z (MN/m)	K_{ry} (MNm/rad)	C_x (MNs/m)	C_z (MNs/m)	C_{ry} (MNms/rad)
6	100	3	2	717	2778	43869	58	81	3581
6	150	3	2	1784	4550	70967	144	128	5715
6	200	3	2	3044	6737	102832	244	186	8244
6	100	5	2	723	2778	43897	59	81	3601
6	150	5	2	1788	4550	70985	144	128	5736
6	200	5	2	3046	6737	102844	245	186	8266
6	100	7.5	2	735	2778	43950	60	81	3643
6	150	7.5	2	1794	4550	71017	146	128	5777
6	200	7.5	2	3050	6737	102867	246	186	8309
6	100	10	2	750	2778	44019	62	81	3706
6	150	10	2	1801	4550	71062	148	128	5834
6	200	10	2	3055	6737	102898	248	186	8366
6	100	12.5	2	766	2778	44096	65	81	3797
6	150	12.5	2	1811	4550	71116	150	128	5908
6	200	12.5	2	3061	6737	102935	251	186	8437
6	100	15	2	783	2778	44179	69	81	3932
6	150	15	2	1821	4550	71175	153	128	6006
6	200	15	2	3068	6737	102979	254	186	8525
6	100	3	4	395	2156	41190	20	45	2127
6	150	3	4	1045	3070	67697	47	60	3034
6	200	3	4	2310	4420	99412	98	82	4201
6	100	5	4	396	2156	41441	21	45	2196
6	150	5	4	1074	3070	67896	49	60	3106
6	200	5	4	2350	4420	99578	101	82	4277
6	100	7.5	4	396	2156	41848	22	45	2320
6	150	7.5	4	1139	3070	68232	54	60	3240
6	200	7.5	4	2422	4420	99874	107	82	4426
6	100	10	4	403	2156	42271	23	45	2478
6	150	10	4	1234	3070	68619	62	60	3416
6	200	10	4	2507	4420	100224	116	82	4627
6	100	12.5	4	430	2156	42647	27	45	2665
6	150	12.5	4	1347	3070	69031	71	60	3628
6	200	12.5	4	2593	4420	100593	126	82	4876
6	100	15	4	483	2156	42980	33	45	2887
6	150	15	4	1453	3070	69439	81	60	3864
6	200	15	4	2674	4420	100954	137	82	5157

Tab. G.2. Calibrated stiffness and damping terms for the configurations with safety factor $F = 3$

F	V_s (m/s)	h_{eq} (m)	f_h (Hz)	K_x (MN/m)	K_z (MN/m)	K_{ry} (MNm/rad)	C_x (MNs/m)	C_z (MNs/m)	C_{ry} (MNms/rad)
3	100	5	2	753	2880	44030	63	90	3718
3	150	5	2	1799	4703	71051	147	139	5819
3	200	5	2	3053	6853	102887	247	196	8345
3	100	7.5	2	770	2880	44112	66	90	3820
3	150	7.5	2	1810	4703	71112	150	139	5902
3	200	7.5	2	3060	6853	102929	250	196	8425
3	100	10	2	789	2880	44212	70	90	3999
3	150	10	2	1823	4703	71187	154	139	6028
3	200	10	2	3069	6853	102984	254	196	8536
3	100	12.5	2	808	2880	44317	77	90	4284
3	150	12.5	2	1837	4703	71272	160	139	6221
3	200	12.5	2	3079	6853	103049	259	196	8695
3	100	15	2	825	2880	44419	87	90	4707
3	150	15	2	1851	4703	71361	168	139	6513
3	200	15	2	3090	6853	103119	267	196	8916
3	100	5	4	426	2411	42612	26	58	2645
3	150	5	4	1246	3445	68663	63	76	3438
3	200	5	4	2489	5129	100151	114	103	4582
3	100	7.5	4	466	2411	42890	31	58	2822
3	150	7.5	4	1360	3445	69077	72	76	3653
3	200	7.5	4	2586	5129	100564	125	103	4855
3	100	10	4	534	2411	43199	39	58	3059
3	150	10	4	1480	3445	69550	84	76	3936
3	200	10	4	2687	5129	101014	139	103	5207
3	100	12.5	4	622	2411	43517	48	58	3323
3	150	12.5	4	1584	3445	70003	97	76	4312
3	200	12.5	4	2779	5129	101447	153	103	5601
3	100	15	4	703	2411	43813	57	58	3543
3	150	15	4	1666	3445	70380	114	76	4801
3	200	15	4	2857	5129	101839	170	103	6062

Tab. G.3. Calibrated stiffness and damping terms for the configurations with safety factor $F = 1.5$

F	V_s (m/s)	h_{eq} (m)	f_h (Hz)	K_x (MN/m)	K_z (MN/m)	K_{ry} (MNm/rad)	C_x (MNs/m)	C_z (MNs/m)	C_{ry} (MNms/rad)
1.5	100	10	2	832	3128	44455	92	109	4903
1.5	150	10	2	1854	4923	71377	170	157	6578
1.5	200	10	2	3091	7045	103127	268	214	8948
1.5	100	12.5	2	852	3128	44570	109	109	5655
1.5	150	12.5	2	1872	4923	71489	188	157	7193
1.5	200	12.5	2	3106	7045	103225	283	214	9410
1.5	100	15	2	869	3128	44672	126	109	6394
1.5	150	15	2	1889	4923	71594	214	157	8113
1.5	200	15	2	3120	7045	103322	305	214	10126
1.5	100	10	4	732	2773	43934	60	79	3629
1.5	150	10	4	1682	4112	70453	118	103	4917
1.5	200	10	4	2867	5910	101888	173	135	6135
1.5	100	12.5	4	789	2773	44214	71	79	4002
1.5	150	12.5	4	1756	4112	70817	137	103	5510
1.5	200	12.5	4	2946	5910	102296	200	135	6935
1.5	100	15	4	827	2773	44431	89	79	4772
1.5	150	15	4	1810	4112	71115	150	103	5906
1.5	200	15	4	3007	5910	102618	228	135	7762

Tab. G.4. Calibrated stiffness and damping terms for the configurations with safety factor $F = 1.2$

F	V_s (m/s)	h_{eq} (m)	f_h (Hz)	K_x (MN/m)	K_z (MN/m)	K_{ry} (MNm/rad)	C_x (MNs/m)	C_z (MNs/m)	C_{ry} (MNms/rad)
1.2	100	10	2	846	3224	44537	104	117	5421
1.2	150	10	2	1865	5006	71450	181	166	6941
1.2	200	10	2	3100	7125	103187	276	223	9208
1.2	100	12.5	2	866	3224	44650	122	117	6239
1.2	150	12.5	2	1884	5006	71566	206	166	7832
1.2	200	12.5	2	3116	7125	103295	298	223	9889
1.2	100	15	2	883	3224	44748	137	117	6877
1.2	150	15	2	1901	5006	71669	239	166	8996
1.2	200	15	2	3132	7125	103397	331	223	10931
1.2	100	10	4	775	2847	44141	67	87	3865
1.2	150	10	4	1733	4338	70698	131	115	5323
1.2	200	10	4	2919	6155	102155	189	147	6612
1.2	100	12.5	4	820	2847	44387	84	87	4559
1.2	150	12.5	4	1797	4338	71039	147	115	5804
1.2	200	12.5	4	2991	6155	102532	220	147	7541
1.2	100	15	4	852	2847	44575	110	87	5692
1.2	150	15	4	1844	4338	71315	163	115	6346
1.2	200	15	4	3045	6155	102835	244	147	8249

ECOLE DOCTORALE

Titre : Développement d'un macro-élément de fondations sous charge dynamique : Application au cas des sols renforcés par inclusions rigides

Mots clés : Macro-élément, Fondation, Inclusions rigides, Interaction dynamique soil-structure, Capacité portante, Chargement sismique, ASIRI+

Résumé : La réponse dynamique d'une fondation renforcée par inclusions rigides représente un problème complexe d'interaction sol-structure (ISS). Cependant, le nombre d'études s'intéressant à ce type de fondations reste encore limité, et il est nécessaire d'explorer les phénomènes d'ISS impliqués dans leur réponse sous l'action des séismes et d'améliorer les méthodes d'analyse.
Sur la base des connaissances acquises à partir des études expérimentaux et numériques disponibles, ce travail de recherche s'intéresse aux phénomènes d'ISS dynamique des fondations renforcées par inclusions rigides. L'étude vise à fournir une meilleure compréhension du comportement sismique de ce type de fondation en utilisant plusieurs approches complémentaires comprenant divers modèles numériques, stratégies de résolution et approches analytiques. Les effets des phénomènes d'interaction inertiel et cinématique à la fois sur la réponse globale de la fondation et sur la réponse des différents éléments du système sont examinés en détail.
La capacité portante sismique des fondations renforcées par inclusions rigides est étudiée en utilisant l'approche cinématique par l'extérieur dans le cadre de la théorie du calcul à la rupture. Une approche analytique permettant d'explorer plusieurs mécanismes de rupture de la fondation est proposée et validée par des analyses numériques en éléments finis. L'évolution des facteurs de réduction est également explorée pour plusieurs configurations de renforcement.
Un nouveau macro-élément pour les fondations renforcées par inclusions rigides sous chargement sismique est développé et validé numériquement. Il permet la modélisation de la réponse linéaire et non-linéaire de la fondation, incluant les mécanismes de décollement, de glissement et de perte de la capacité portante. Ce modèle est ensuite utilisé pour conduire une étude paramétrique à l'aide d'un modèle de structure simplifiée et l'analyse dynamique incrémentale d'une tour R+22, démontrant l'efficacité et l'utilité de l'approche proposée dans une démarche de conception parasismique basée sur la performance.
Cette recherche est menée dans le cadre du Projet National français ASIRI+ et du projet ANR ASIRIplus_SDS.

Title : Development of a macro-element of foundations under dynamic load: Application in the case of soils reinforced by rigid inclusions

Keywords : Macro-element, Foundation, Rigid inclusion, Dynamic soil-structure interaction, Bearing capacity, Seismic loading, ASIRI+

Abstract : The dynamic response of a rigid inclusion-reinforced foundation represents a complex Soil-Structure Interaction (SSI) problem. Considering the limited existing studies, there is a clear necessity to explore the SSI phenomena involved in the response of such foundations under seismic conditions and to enhance the corresponding design methodologies.
Building upon insights from a limited number of dynamic experimental and numerical studies, this research focuses on the dynamic SSI phenomena of foundations reinforced by rigid inclusions. The study aims to understand the seismic behaviour of such foundations better using several complementary approaches, including various numerical models, resolution strategies, and analytical analyses. The effects of inertial and kinematic interaction phenomena on the response of both the overall foundation and individual elements within the system are examined in detail.
The seismic bearing capacity of foundations reinforced by rigid inclusions is further investigated, using the kinematic exterior approach within the framework of yield design theory. A multi-subsystem analytical approach based on the kinematic exterior approach is introduced and validated through FEM analyses. The evolution of the reduction factors is also explored for several configurations of the reinforcement.
A novel macro-element for rigid inclusion-reinforced foundations under seismic loading is developed and numerically validated. It allows the modelling of both the linear and non-linear response of the foundation, including uplift, sliding and loss of bearing capacity mechanisms. The validated macro-element model is used to perform a parametric study using a lumped mass model and the Incremental Dynamic Analysis of a 22-storey building, demonstrating the effectiveness and usefulness of the proposed approach in a performance-based design approach.
This research is conducted within the framework of the French National project ASIRI+ and French National Research (ANR) project ASIRIplus_SDS.

Institut Polytechnique de Paris
91120 Palaiseau, France